Technische Universität München
TUM School of Natural Sciences

On Coexistence Dynamics and Its Theoretical Principles: Chimeras in Networks of Networks

Seungjae Lee

Vollständiger Abdruck der von der TUM School of Natural Sciences der Technischen Universität München zur Erlangung des eines

Doktors der Naturwissenschaften (Dr. rer. nat)

genehmigten Dissertation.

Vorsitz: Prof. Dr. Menno Poot

Prüfer*innen der Dissertation:

1. Prof. Dr. Katharina Krischer
2. Prof. Dr. Arkardy Pikovsky
3. Prof. Dr. Christian Kühn

Die Dissertation wurde am 19.09.2023 bei der Technischen Universität München eingereicht und durch die TUM School of Natural Sciences am 09.01.2024 angenommen.

Technical University of Munich
School of Natural Sciences
Department of Physics
Supervisor: Prof. Dr. rer. nat. habil. Katharina Krischer

I would like to dedicate this thesis to my beloved parents[1].

[1] Note that this is not a sentence in a LaTex template but my sincere confession.

I would rather wear out than rust out.

GEORGE WHITEFIELD

Abstract

In 1665, Christiaan Huygens observed the so-called *odd sympathy* of the coupled pendulum of two clocks. Such a collective behavior of coupled oscillators, which cannot be understood in terms of the laws for individual oscillators, has been under consideration in various scientific fields. Having passed more than 300 years since that observation in Holland, one of the most intriguing collective dynamics of coupled oscillators came into observation in 2002: A symmetric oscillator system can spontaneously split into the simultaneous coexistence of coherent and incoherent oscillations via the breaking of the system's symmetry. Such coexistence patterns of the incongruity in the oscillator system were highlighted in 2004 when the term, *chimera states*, was first introduced. In this thesis, we discuss some theoretically interesting and important chimera dynamics of coupled phase oscillators, starting with the simplest model and then gradually introducing topological complexity to a network of networks where the oscillators are stationed. More specifically, a system of identical Kuramoto-Sakaguchi phase oscillators is considered setting on the background topology, ranging from two-population networks, a triangular network of three populations, to a ring of six populations. In two-population networks, we investigate the dynamical and spectral properties of what we coin a Poisson chimera state, which is known to be neutrally stable. Then, two ways that give rise to the attracting Poisson chimeras are discussed based on the Lyapunov stability analysis. Next, as a configuration of higher topological complexity, we consider a triangular network of three oscillator populations. Thereby, we elucidate the dynamical properties of symmetric- and symmetry-broken chimera states. Particularly, a tri-stability of chimera attractors is discussed, including chaotic chimera states, periodic antiphase chimeras, and steady chimera states. Thirdly, considering a ring of six oscillator populations, we therein study heteroclinic switching dynamics between saddle chimera states such as unstable steady, breathing, and quasiperiodic chimera states, respectively. We demonstrate that the structure of the unstable manifold of each saddle chimera state can form such a heteroclinic cycle between saddle chimeras. Finally, to take into account higher-dimensional complexity, the Kuramoto-Sakaguchi phase oscillators defined usually on a unit circle are extended to the generalized KS oscillators on the surface of a higher-dimensional unit sphere. Thereby, we study the scenario of the emergence of observable chimera states in

two-population networks. Due to the higher-dimensional nature of the oscillators, we observe more complex chimera states such as periodic alternating chimeras and component-wise aperiodic chimera dynamics than those, e.g., stationary and breathing chimeras in the usual KS oscillators in two-population networks. Not only for those phenomenological observations and their explanations, but we also provide all the necessary theoretical principles for the exploration of the aforementioned chimera dynamics.

Abstract

Im Jahr 1665 beobachtete Christiaan Huygens die sogenannte "seltsame Sympathie" der gekoppelten Pendel zweier Uhren. Ein solches kollektives Verhalten gekoppelter Oszillatoren, das nicht mit den Gesetzen für einzelne Oszillatoren erklärt werden kann, wurde in verschiedenen wissenschaftlichen Bereichen untersucht. Mehr als 300 Jahre nach dieser Beobachtung in Holland wurde im Jahr 2002 eine der faszinierendsten kollektiven Dynamiken gekoppelter Oszillatoren beobachtet: Ein symmetrisches Oszillator-System kann spontan in die gleichzeitige Koexistenz von kohärenten und inkohärenten Schwingungen übergehen, indem die Symmetrie des Systems gebrochen wird. Solche Koexistenzmuster der Unvereinbarkeit im Oszillator-System wurden 2004 hervorgehoben, als der Begriff "Chimäre-Zustände" erstmals eingeführt wurde. In dieser Arbeit diskutieren wir einige theoretisch interessante und wichtige Chimären-Dynamiken gekoppelter Phasen-Oszillatoren, beginnend mit dem einfachsten Oszillator-Modell und allmählich eine topologische Komplexität in das gekoppelte Oszillator-Netzwerk einführend. Konkret wird ein System identischer Kuramoto-Sakaguchi-Phasen-Oszillatoren betrachtet, das auf der zugrunde liegenden Topologie basiert, angefangen von Zweipopulationsnetzwerken über ein dreieckiges Netzwerk aus drei Populationen bis hin zu einem Ring aus sechs Populationen. In Zweipopulationsnetzwerken untersuchen wir die dynamischen und spektralen Eigenschaften eines sogenannten Poisson-Chimäre-Zustands, der als neutral stabil bekannt ist. Anschließend werden zwei Möglichkeiten diskutiert, die zu den anziehenden Poisson-Chimären führen, basierend auf der Lyapunov-Stabilitätsanalyse. Als Konfiguration mit höherer topologischer Komplexität betrachten wir ein dreieckiges Netzwerk aus drei Oszillator-Populationen. Dabei klären wir die dynamischen Eigenschaften von symmetrischen und symmetriebrechenden Chimäre-Zuständen auf. Insbesondere wird eine Tri-Stabilität von Chimäre-Attraktoren diskutiert, einschließlich chaotischer Chimäre-Zustände, periodischer gegenphasiger Chimären und stabiler Chimäre-Zustände. Drittens untersuchen wir ein Ringnetzwerk aus sechs Oszillator-Populationen und studieren darin die heterokline Schalt-Dynamik zwischen Sattel-Chimäre-Zuständen wie instabilen, stationären, atmenden und quasiperiodischen Chimäre-Zuständen. Wir zeigen, dass die Struktur des instabilen Mannigfaltigkeitsbereichs jedes Sattel-Chimäre-Zustands solch einen heteroklinen Zyklus zwischen den Sattel-Chimären bilden kann. Schließlich werden,

um eine höherdimensionale Komplexität zu berücksichtigen, die üblicherweise auf einem Einheitskreis definierten Kuramoto-Sakaguchi-Phasen-Oszillatoren auf die generalisierten KS-Oszillatoren auf der Oberfläche einer höherdimensionalen Einheitssphäre erweitert. Dabei untersuchen wir das Szenario des Auftretens beobachtbarer Chimäre-Zustände in Zweipopulationsnetzwerken. Aufgrund der höherdimensionalen Natur der Oszillatoren beobachten wir komplexere Chimäre-Zustände wie periodische abwechselnde Chimären und komponentenweise aperiodische Chimäre-Dynamiken im Vergleich zu den üblichen KS-Oszillatoren in Zweipopulationsnetzwerken, wie z.B. stationäre und atmende Chimären. Wir bieten nicht nur für diese phänomenologischen Beobachtungen und deren Erklärungen, sondern auch für die Erforschung der genannten Chimären-Dynamiken alle notwendigen theoretischen Prinzipien.

Table of contents

Chapter 1

Introduction

In 1996, perhaps, I spent most of my day-time in a kindergarten learning many things for myself to be prepared to study in an elementary school. The kindergarten had a few classes named after flowers, although I do not remember which flower I belonged to, unfortunately. During those times, all children therein learned basic arithmetic, refined their Korean expressions, and undertook many activities. Some of them, especially those in advanced classes, to which I did not belong, studied multiplication tables and English. As adorable children in a typical Korean preschool, we spent some of our days learning children's songs, and we practiced the lyrics and dance routines to have a small stage in a kindergarten festival every year, showing the profound innocence of our childhood to our parents. I believe it brought great joy to my parents amidst the Korean currency crisis in 1997, which was a national bankruptcy that brought tough times to all families, in particular, for young parents. As of now, I do not remember every song that *I knew completely when I wore a younger man's clothes*. Many things have grown dim in my memory and I remember those days less and less as time goes by. Still, one song has burned into my memory and even today I know it by heart. The song is simple and thus suitable for little children to enhance not only their vocabulary but also their emotional quotient (EQ). The name of the song is '*Rocks and Water*'[1]. It has been literally a long time since I sang this song (note that this was in the last century!).

[1] I was not able to find any official English translation of this song. Thus, it was translated by myself.

Rocks and Water

Breaking a big boulder, a stone
Breaking a stone, a cobble
Breaking a cobble, a pebble
Breaking a pebble, grains of sand
La la la la la la la la
La la la la la la la la

Gathering ditch water, it becomes a stream
Gathering stream water, it becomes a brook
Gathering brook water, it becomes a large river
Gathering river water, it becomes the sea
La la la la la la la la
La la la la la la la la

Seok-Jung Yun (1911–2003)

Although this song was originally written in order to help children learn the concepts of certain vocabulary words, I believe the song teaches us more than this. It consists of two verses. The first verse deals with rocks such as a boulder, pebbles, and grains of sand and goes to ever smaller sizes of the original object. In the second verse, the size of the objects is increased, here different kinds of water combine to ever larger structures. Two verses classify the objects according to increasing/decreasing scales while decreasing/increasing complexity. At that time, I did not notice the true meaning of what the song tells us. I think nobody in my class realized it. We just noticed that the word 'boulder' indicates something bigger than a stone whereas the river is larger than the ditch water. However, I now see something deeper than this. It reminds me of something in my physics studies. The song actually teaches us an important lesson, which brings us to the main motivation of this thesis. The two verses display two different flows when it comes to the development of physics or methods of physical science. To understand this, we first take a squint at the unique characteristics of physics by comparing it with other scientific studies.

A scientific study can be defined or characterized by a particular focus on *the objects within its scale* that an observer (or a researcher) wants to explore. For example, the American Heritage Dictionary of the English Language (AHD) describes chemistry:

> The science of the composition, structure, properties, and reactions of *matter, especially of atomic and molecular systems* [1]

while the AHD says about biology:

> The science of *life and of living organisms*, including their structure, function, growth, origin, evolution, and distribution [1].

Note that the italic phrases above indicate the objects that chemistry and biology deal with, respectively. Also, we know that geology mainly deals with the composition and the structure of the earth and astronomy is the study of celestial bodies. They all are characterized by having their own specific target objects. We can say without loss of generality that chemistry is the science of atoms and molecules, biology is the one of living things, geology is the study of the earth, and astronomy is the one of celestial bodies. Hence, in the school of natural science, one can concentrate one's interest on a specific physical object or a group of materials, and then disclose their predictable behavior and elucidate their properties.

If so, how does physics go on? I learned an important lesson about the unique characteristics of physics from an open course lecture by Prof. Dr. Sang-Jin Sin[2]: Physics is defined or characterized by *the methods*, not the specific objects. Therefore, the objects under its scope are everything in the universe, i.e., physics is the study of everything. The AHD describes physics:

> The science of matter and energy and of interactions between the two, *grouped in traditional fields* such as acoustics, optics, mechanics, thermodynamics, and electromagnetism, as well as in modern extensions including quantum mechanics, relativity theory, cryogenics, solid-state physics, particle physics, and plasma physics [1].

The definition speaks about matter (especially of which system?) and energy (of what?). However, all physical objects are matter, and hence they have energy. The so-called *fields* described above are not restricted to the specific physical *objects* or a group of physical materials, such as molecules, atoms, celestial bodies, or living things but rather they are the methods to describe *the laws of physics* by which all materials are governed, such as mechanics or dynamics, and theories like $\boldsymbol{X}$-physics where $\boldsymbol{X}$ could be any of physical objects, e.g., solid-state physics, particle physics, or plasma physics. In this perspective, there could be so-called chemical physicists, biological physicists, geological physicists, or astronomical physicists. To clarify this, we have to recall the old description of physics. The AHD says physics is also:

[2]The lecture is given here (only Korean version available): `https://www.youtube.com/playlist?list=PLGF0JqQbSvJpesmPJfHSmvfcjV5FTFzyb`. The tile of lectures can be translated as 'Principles of Physical Phenomena: Utility of Physics and Worldviews'

> (Archaic) The study of the natural or material world and phenomena; natural philosophy [1].

Physics is the study of **the laws** that govern **everything in every scale**, whatever they may be, and of **the methods** used to describe them. In terms of our song, everything in all the different scales, from the boulders down to grains of sand, or from the ditch water up to the sea, is governed by **the laws of physics** and they lie under the framework of **the physical methods**. This explains why the department of physics in a university covers all the scales of objects from the Planck scale to the galaxy unit[3]. I would say it is a *scale-free* science. Not only all scales but also all physical objects, from subatomic particles, chemical and biological objects to celestial bodies, can be explored using the methods or theories of physics since all their properties and motions are governed by the laws of physics[4]. This raises important questions: How have the laws of physics been constructed? Which method has led physics in the history of modern science? Or is it possible to understand the entire nature by investigating each scale of objects? In particular, is it possible to explain all natural phenomena just in terms of properties of those on the simplest level and their extrapolation? If not, why is it? And, how then can we understand natural phenomena that cannot be described in terms of a simple extrapolation of properties of each scale? Those questions lead to the overarching concepts of this thesis, and we will answer them below.

The lesson of the song answers those questions and is relevant to the main idea of this thesis, or its philosophical background. The first verse and the second verse of the song depict two conceptually different routes, along which physicists have understood natural phenomena in the history of modern science. The first verse directly teaches us ***to break*** the objects into simpler units on smaller scales; breaking the boulder into a stone, the stone into a cobble, the cobble into pebble, and the pebble into grains of sand. In this process, the scale of the objects usually (but not necessarily) gets smaller, and more importantly, the objects necessarily become simpler and easier to deal with. The concept behind this approach is called '*reductionism*', which is well described in a lecture by S. Haro:

> The reductionism (or reduction) is often used to imply *the whole is nothing but the sum of its part* [2].

[3] See, for example, `https://www.ph.tum.de/research/groups/?language=en`

[4] In this perspective, physics sometimes seems useless to some laypeople. Prof. Sang-Jin Sin said in his lecture "physics is a discipline that encompasses all things, which is why physics students graduate without learning as much about molecules and atoms as chemistry students. Similarly, they graduate without learning as much about celestial bodies as astronomy students. It can be said that there is nothing they learn more than students in other fields." However, physics is the study of the laws that govern everything and the methods used to describe all things in the universe. Hence, I would say we can apply, in principle, our knowledge to every problem in every field. From this point of view, it is the most useful and instructive study.

More practically, in performing physical science, J. C. Lennox pointed out:

> One obvious thing to try to do is to split the problem up into separate parts or aspects, and thus *reduce* it to simpler components that are individually easier to investigate [3].

The message of the reductionism is clear and simple: **The whole is nothing but the sum of its parts.** It then implies that we are *only* required to understand the properties of simple building blocks that constitute the whole and this is necessary and sufficient for a complete understanding of the entire system. In fact, it is not an exaggeration to say the major trajectory of physics has been led by reductionism since Galileo challenged Aristotle's natural philosophy, and the advent of Sir Isaac Newton's *Principia* [4, 5], followed by Kepler [6]. For example, note that calculus itself is the method of breaking a complicated curve into simpler straight segments that make the system much easier to explore. Up to the middle of the 20th century, reductionism has dominated the world of physical science and also efficiently enhanced our understanding of natural phenomena in our universe or specific physical systems according to the interests of each scientist. From the perspective of the extreme reductionists, in order to *completely* understand, for example, a stone that looks complicated, they have broken the stone, and further and further split it into silicon dioxide, oxygen atoms, and finally into subatomic particles[5], which looks much simpler to investigate[6]. Thus, we reach the knowledge of the building blocks of the system, simpler and easier to investigate, and that is all. If we understood the properties of the building blocks, then we are done at this stage since the original complex physical phenomenon is nothing more than the sum of the properties of those building blocks. The reductionism in physical science can be encapsulated in the below quote by S. Weinberg who said:

> The reason we give the impression that we think that elementary particle physics is *more fundamental* than other branches of physics is because it is [9].

In this saying, his philosophy describes well the holy prophecy of reductionism to the secular world of science. The study of building blocks, i.e., elementary particles, is all for physics and moreover all for science since (once again) the whole is nothing but the sum of its parts. Then,

[5] depending on readers, it could be a string or loop [7]

[6] In this perspective, we have one humorous metaphor for highly simplified or reduced physical methods of the exploration of complex phenomena: Milk production at a dairy farm was low, so the farmer wrote to the local university, asking for help from academia. A multidisciplinary team of professors was assembled, headed by a theoretical physicist, and two weeks of intensive on-site investigation took place. The scholars then returned to the university, notebooks crammed with data, where the task of writing the report was left to the team leader. Shortly thereafter the physicist returned to the farm, saying to the farmer, "I have the solution, but it works only in the case of spherical cows in a vacuum.", quoted from Ref. [8].

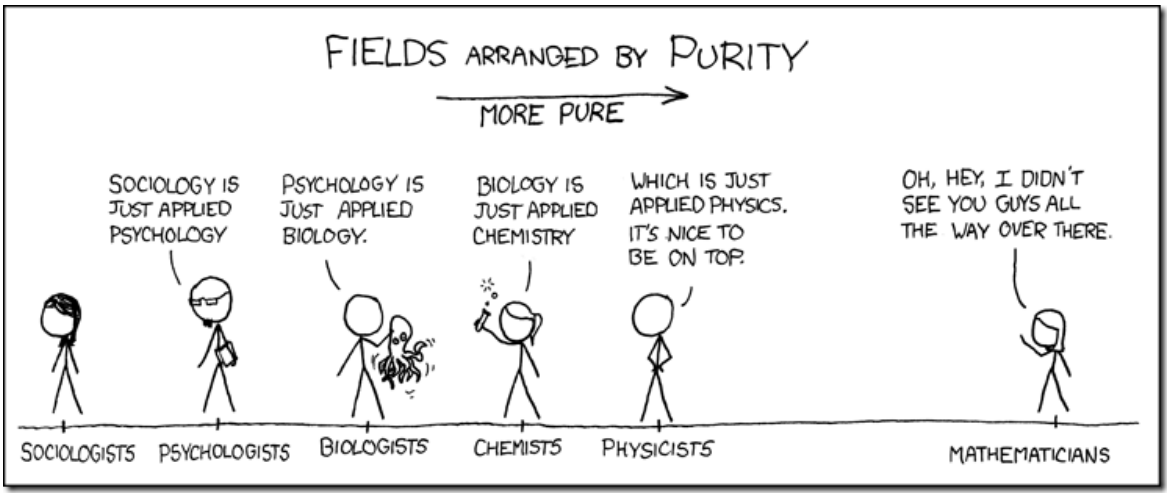

Fig. 1.1 A cartoon depicts the hierarchy of knowledge in terms of reductionism. See the main text. From `https://larspsyll.wordpress.com/2013/09/08/probabilistic-reductionism/`

it follows from the assumption of S. Weinberg that there exists the so-called *fundamental study* which explores the building blocks and we can completely explain everything in nature by simply extrapolating their properties. In this light, i.e., the existence of the most fundamental study, the creed of reductionism sometimes appears as the saying, for example, by J. Watson: "There is only one science, physics: everything else is social work [10]".

On the other hand, reductionism sometimes can be represented by the philosophical trend of defining a higher-level concept by breaking it down into lower-level elements. Thus, it follows that there is a hierarchical structure of knowledge. In Fig. 1.1, one aspect of reductionism is well described. It tells **X** is nothing more than, or nothing but, slightly complex **Y**. In other words, **X** can be reduced just to an application of **Y**. Here,

$$(\mathbf{X},\mathbf{Y}) \in \{(\text{sociology},\text{psychology}),(\text{psychology},\text{biology}), \\ (\text{biology},\text{chemistry}),(\text{chemistry},\text{physics}),\cdots\} =: S \tag{1.1}$$

At the last step, the reductionists can say that physics is nothing but a slightly complex application, described in the language of mathematics, to acquire knowledge about the entire natural phenomena in the universe, i.e., $(\text{physics},\text{math}) \in S$. Thus, as J. C. Lennox pointed out, a reductionist could say "There is the way in which the language of mathematics is used to reduce or compress the description of often very complex phenomena into short and elegant equations." This reduction method has been accompanied by the development of physics. For example, phenomenological observations by Tycho Brahe led Kepler to the reduced statements of his observations, which inspired Sir Isaac Newton to further

compress Kepler's work into some mathematical statements [3]. Then, in the history of modern science, theoretical physicists and mathematicians have tried to reduce and compress complex phenomena into a single mathematical statement or simple equations like the so-called *theory of everything* [9]. This trend, the dream of reductionists, reached its zenith in this context when David Hilbert, more specifically, the *Hilbert program* tried to reduce all the mathematics into some general algorithmic process based on sets of formal statements using a finite set of symbols, axioms, and rules of inference [3]. Hence, one can say $(\text{math}, \text{Hilbert}) \in S$ in Eq. (1.1).

Do we really need only the properties of fundamental particles, to understand every natural phenomenon? At this point, it is time to invoke what R. Dawkins said[7]: "Next time somebody tells you that something is true, why not say to them: 'What kind of evidence is there for that?' And if they can't give you a good answer, I hope you'll think very carefully before you believe a word they say" [11]. We should ask something important: Can building blocks indeed explain everything? Does nature evidence only the phenomenon that can be explained by the simple sum of the building blocks? Let Sir Isaac Newton speak [12] and this is what the second verse of the song tells:

> *What we know is a drop,*
> *what we don't know is an ocean.*

First of all, we all know that the Hilbert program turned out to be failed by Gödel's incompleteness theorems [3]. There exist true statements that cannot be proven in the framework of finite sets of symbols, axioms, and inference rules. As Freeman Dyson, a theoretical physicist, said in Ref. [13] "Gödel proved that in mathematics **the whole is always greater than the sum of the parts**." Secondly, we all know that many phenomena in nature cannot be explained only in terms of the building blocks or a simple extrapolation of their properties. Let us consider two extreme examples, with a particular focus on how the interaction works between building blocks.

On the one hand, the simple extrapolation of the properties of the building blocks works well, e.g., when the system holds the superposition principle due to the linear governing equations. Consider a charged particle interacting with another charged particle (and ignore all the other interactions). In this system, the electric field, i.e., the interaction between them, is governed by a linear differential equation of electrostatics and the superposition

[7] I must say I do not follow all his philosophy. However, the statement itself is instructive to follow.

principle holds: The introduction of the third charged particle to the system does not change the interaction between the two, originally set in the system. It is due to the linearity and this system can be understood in terms of the properties of building blocks and a simple sum of the interaction between them. On the other hand, where nonlinearity works, something different can happen. Let us consider an extreme example of a system of nonlinearly interacting agents. Consider a system of a young couple. The interaction between a man and a woman does not follow the superposition principle. To prove this, just introduce the third party, who particularly *had* a close relationship to one of the two. The introduction of that third party makes completely different the interaction between the two preexisting people. This reminds us of what S. Strogatz said in Ref. [14]: "the term 'many-body problem' takes on new meaning." Thus, we know this system and its phenomenon cannot be understood in terms of a simple extrapolation of properties of building blocks. Assuming that we understand all the particles consisting of our bodies, it does not guarantee anything about our behaviors as a simple sum of the properties of those particles. Let Sir Isaac Newton speak once again: "I can calculate the motion of heavenly bodies, but not the madness of people" [12].

Such phenomena beyond the sum of its parts are called '*emergent phenomena*'. The emergent phenomenon is something emerging on a higher level that cannot be reduced to the lower-level properties of the building blocks. More specifically, as P. W. Anderson brought it to the point:

> The behavior of large and complex aggregates of elementary particles, it turns out, is not to be understood in terms of a simple extrapolation of the properties of a few particles [15]

since we know that:

> At each level of complexity entirely new properties appear, and the understanding of new behaviors requires research which is as fundamental in its nature as any other [15].

The message of this way of physical science can be encapsulated in one simple sentence:

> *More is different*

by P. W. Anderson [15] or *More than the sum* by S. Strogatz [16]. The doctrine of this is that the understanding of the building blocks is *not equivalent* to the understanding of the entire system. There is something more than the sum of its parts. In mathematics, it was proved by K. Gödel as we saw above. In natural phenomena, there are countlessly many emergent phenomena around us such as self-organization, evolution of networks, pattern formation,

phase transition, and so on, in complex systems [17–20]. One of the most well-known emergent phenomena is the collective behavior of a large system. A complex system, which consists of numerous objects with nonlinear interactions, easily shows entirely new collective properties which are not to be understood in terms of a simple extrapolation of the properties of the individuals at the lowest level of the building blocks. The importance of collective phenomena of complex systems was highlighted by S. Hawking, saying "I think the next century will be the century of complexity" [21]. We see that contemporary physics is *de facto* full of boundary-free and complexity-ridden studies. Contemporary research brings more and more complexity and takes fewer and fewer boundaries.

Now, we can answer what brings us to the topic of this thesis. In 1665, Christiaan Huygens in Holland observed something strange when he played with two pendulum clocks. This strange behavior emerges in a system of two-coupled pendulum clocks hung on the same rigid board. He observed the so-called '*odd sympathy*' where one pendulum clock is swung to the right while at the same time the other to the left, forming exactly 180 degrees out of phase [22–24]. This phenomenon is one important example of emergent phenomena that cannot be understood in terms of the laws for individual pendulum clocks [16]. Particularly, it is the collective dynamics of *a system of coupled oscillators*, or oscillating objects. In the history of modern science, oscillations or oscillators have been under consideration in various scientific fields in order to understand some natural phenomena. For example, one can approximate the dynamics as a simple harmonic oscillation (see Chap. 2 for details), near a local minimum of a given potential in a physical system. Likewise, we can understand some important emergent phenomena in nature by exploring the collective behavior of coupled oscillator ensembles [25, 26]. Especially within the realm of modern interdisciplinary studies, the collective dynamics of a network of interconnected oscillators are becoming increasingly significant [25, 26]. Here, the network (or the system) consists of numerous oscillators that are nonlinearly interacting with each other. Such systems are well known to exhibit a variety of emergent/collective phenomena, with various applications in laser physics [27, 28] or Josephson junctions [29, 30] and also in biology [31–33], neural science [34–37], and atomic physics [38, 39] or engineering application [40, 41]. Note that collective behavior, *by definition*, cannot be understood in terms of the uncoupled or intrinsic dynamics of each oscillator, a building block of the system. S. Strogatz highlighted such a collective behavior of systems of coupled oscillators, concerning the observation of Christiaan Huygens, saying

> even though we know the laws for individual pendulum clocks, that isn't enough to tell us how two or more of them will behave together [16].

Hence, we are required to *not only* understand the microscopic individual oscillators (building blocks) of the system *but also* to study the macroscopic dynamics of the oscillator ensembles. This motivates and leads us to the following chapters in the thesis.

From the observation of Huygens in 1665, researchers have been exploring and investigating various emergent/collective behaviors in a system of coupled oscillators. For example, Y. Kuramoto suggested a simple model, now called the Kuramoto model, to study a transition from incoherence to partially locked states [42] where oscillators with heterogeneous intrinsic frequencies exhibit self-organized order depending on interaction strength [43]. Subsequently, a variety of collective behaviors in a system of coupled oscillators has been under consideration such as properties of incoherent oscillators [44], cluster patterns with higher order interactions [45] or in a network [46–48], macroscopic chaos of limit-cycle oscillators [49, 50], a discontinuous transition from incoherence to coherence [51], and synchronization in a complex networks [52]. There are numerous examples of collective motions of coupled oscillators in nature and man-made systems [25, 26]. A system of coupled oscillators results in a self-organized collective behavior, and thus researchers have explored dynamical characteristics or properties of oscillator ensembles resulting from a given interaction among the oscillators. After such a long history of emergent/collective behaviors in coupled oscillator ensembles, one intriguing phenomenon was observed in a system of identical oscillators stationed along a ring geometry in 2002 [53]. Despite the system's translational invariance due to its composition of identical oscillators, the ensuing collective dynamics is quite remarkable. Note that the above-mentioned collective phenomena can each be characterized by a unique essential property such as synchronization of a system. In contrast, this novel observation does not just exhibit the anticipated uniform oscillation or complete synchronization of identical oscillators. Instead, depending on a given initial condition, it spontaneously self-organizes into two distinct groups, and the dynamics or characteristics within these two groups do not show a straightforward relationship but rather display entirely different behaviors. The observed collective dynamics of this system can be characterized by **coexistence of coherence and incoherence** via the symmetry-breaking mechanism. What does that *coexistence* mean? The system of given oscillators splits spontaneously into a synchronously oscillating part and the other part consisting of incoherent oscillators. Thus, **the disparate parts**, i.e., coherence and incoherence, **coexist** in a network of coupled oscillators. This intriguing dynamical state arises from the breaking of the system's symmetry: here, the translational invariance of identical oscillators is broken along the ring geometry. Such coexistence patterns or dynamics manifests itself as a spatiotemporal pattern, wherein the system demonstrates both a coherently oscillating portion and an incoherently oscillating portion along the ring. Later in 2004, it was coined

a **chimera state** to highlight its peculiarity, i.e., the simultaneous presence of incongruous parts [54].

The first chimera states, as mentioned above, were studied in a spatially extended ring geometry with a *nonlocal coupling function* where the interaction strength between the oscillators is decreased as a function of the distance between them [59–71]. However, simpler configurations, such as **a network of networks**, have also revealed fundamental properties of chimera states. Here, a network of networks means that the system consists of some populations within which there are numerous oscillators with a given interaction rule between populations. Then, chimera states in a network of networks arise due to the breaking of permutation symmetries of the network topology of populations. To gain more insights into its fundamental characteristics, D. Abrams *et al.* [72] and E. Montbrió *et al.* [73] exploited a simplified model where a system of identical or heterogeneous Kuramoto-Sakaguchi (KS) phase oscillators is arranged in two-population networks, respectively[8]. In these studies, the connections within and between populations are assumed to be all-to-all, with different coupling strengths where the former is stronger than the latter to emulate the nonlocal coupling as in a ring geometry. Subsequently, systems of coupled oscillators have been extensively investigated in a network of networks. More specifically, the two-population network was considered for the system of identical [72, 74, 55] and heterogeneous [75–77] Kuramoto-Sakaguchi oscillators. Also, numerous other variations were taken into account, including phase oscillators under higher-order interaction and planar oscillators [78–85], or a nonlocal intra-population network topology [86, 87]. In addition, researchers have investigated chimera states by considering more complex topological setups such as three- and multi-population networks [88, 89, 56, 90–93, 57, 94].

The success of such models for the study of macroscopic dynamics relied on two main pillars (for details, see Chap. 2): First, the system of identical Kuramoto-Sakaguchi oscillators in a network of networks, a so-called *sinusoidally coupled* system [95]. This means each oscillator is sinusoidally influenced by an external forcing term or an effective force that depends only on the macroscopic observable. Here, the macroscopic observable is the Kuramoto order parameter that measures the degree of coherence of the oscillators in each population, requiring the whole information from all the microscopic individual oscillators. Second, dimension reduction methods allow for the description of the system's collective dynamics in terms of a few macroscopic variables rather than directly studying all the microscopic individual oscillators. Particularly, in the thermodynamic limit, the collective

The contents of the following paragraphs in part were described previously in more detail in Refs. [55–58].

[8] For those who are not familiar with Kuramoto-Sakaguchi oscillators, see Chap. 2

dynamics of infinitely many oscillators can be confined to low-dimensional dynamics on an invariant manifold called Ott-Antonsen (OA) manifold [96, 97]. In this manifold, the dynamics of the Kuramoto order parameter can be written in a closed form with only two variables (not an infinite number of degrees of freedom), provided that the mean-field force is given by the Kuramoto order parameter. For finite-sized ensembles, the so-called Watanabe-Strogatz (WS) transformation [98, 99], which is a linear fractional transformation [100], conformally maps the microscopic individual oscillators of each population to three macroscopic variables and $N-3$ independent constants of motion [101–103]. In the following chapters, we will discuss them in detail.

This thesis raises several important questions on chimera states in a network of networks. As mentioned above, such chimeras emerge via the breaking of permutation symmetries of a given network topology. Thus, in the following chapters, we will ask how different topologies of networks of populations will affect chimera states and their macroscopic dynamics. To this end, we will first discuss how to deal with the system's macroscopic dynamics, not just exploring all the individual degrees of freedom. Then, we consider *two-population networks* to ask how the observable macroscopic dynamics of chimera states is affected by different complexities such as initial conditions, intra-population network topology, and higher-dimensional dynamics. Next, how a simple transition from two- to *three-population networks* gives rise to various chimera dynamics in terms of their collective motion. Moving further, we will ask how a specific complexity of a network of populations, i.e., a ring of six oscillator populations, and its permutation symmetries change chimera dynamics, compared to those in two- and three-population networks. Finally, how about considering the dimensional complexity of oscillators? Does the system of higher-dimensional oscillators defined on the surface of the unit sphere of higher-dimensional complex spaces bring forth different chimera dynamics?

To answer those questions, we follow the below steps.

[1] Introduction and motivation were given in Chap. 1.

[2] In Chap. 2, we will discuss one part of the title of this thesis, that is, theoretical principles. Therein, we will discuss all the theoretical ingredients for the exploration of the coexistence dynamics, being the main issues of the following chapters. Starting from a single oscillator, we revisit ensembles of identical Kuramoto-Sakaguchi oscillators and study the dynamics of their macroscopic behavior. Next, we discuss how to deal with the macroscopic dynamics of the system using the dimension reduction methods, i.e., the Ott-Antonsen and the Watanabe-Strogatz ansatz. Then, we extend a KS phase

oscillator defined on a unit circle to a unit vector oscillator, called a generalized KS oscillator on the surface of the higher-dimensional unit sphere. Both usual and generalized Kuramoto-Sakaguchi oscillators will be dealt with in a network of networks for the study of chimera states. Finally, the theoretical tools for the study of stability will be given.

[3] In Chap. 3, a thorough investigation is given for chimera states of identical Kuramoto-Sakaguchi oscillators in two-population networks. Therein, the spectral properties of finite-sized chimeras in two-population networks are discussed. We classify chimera states as Poisson or Non-Poisson chimeras based on the collective dynamics of the incoherent oscillators. Then, a Lyapunov analysis is performed, confirming the neutral stability of Poisson chimeras. By introducing *perturbations* to the system of identical phase oscillators, either in the form of topological variations or of amplitude degrees of freedom, we will demonstrate that Poisson chimeras can be rendered attracting.

[4] In Chap. 4, the chimera states of identical Kuramoto-Sakaguchi oscillators are studied in three-population networks. We investigate the full phase space dynamics of the system beyond the symmetry-reduced manifold and discover the existence of macroscopic chaotic chimera attractors. These chaotic chimera states, characterized by aperiodic antiphase dynamics of the order parameters, are observed in both finite-sized systems inside the Poisson submanifold and the thermodynamic limit outside the OA manifold, respectively. Furthermore, the chaotic chimera states coexist with a periodic antiphase chimera solution in the OA manifold and a stationary symmetric-chimera solution, resulting in the tri-stability of chimera attractors.

[5] In Chap. 5, we focus on chimera states in a network of six populations of identical Kuramoto-Sakaguchi phase oscillators arranged in a ring. Although many configurations of synchronized and desynchronized populations are possible, they are found to be linearly unstable in almost all parameter ranges. Nevertheless, some unstable chimera states, characterized by one incoherent and five synchronized populations, are observed in a wide parameter range and for random initial conditions. The structure of the saddle chimera in phase space is relevant to the formation of a heteroclinic cycle of symmetric variants of the saddle chimera, resulting in switching dynamics. Small natural-frequency heterogeneities make the heteroclinic switching dynamics asymptotically attracting, while large heterogeneities lead to a variety of attracting chimera states replacing the heteroclinic switching between saddle chiemras.

[6] In Chap. 6, we will explore the generalized Kuramoto oscillators defined on a higher-dimensional unit sphere, rather than being confined to the unit circle of the complex plane. Using the extended Watanabe-Strogatz transformation [104], the macroscopic dynamics of chimera states is investigated in both real and complex spaces. More specifically, chimera states in two-population networks are studied in terms of the motion of order parameter vectors, varying the intra-population coupling strength. The results show stationary and breathing chimeras for strong coupling, periodic alternation of order parameters for weaker coupling, and a transition to aperiodic chimera dynamics as the coupling weakens further via the breaking of the conserved quantities. This scenario of the emergence of various chimera states will be validated both for $\mathbb{C}^2$ and $\mathbb{R}^4$ cases.

[7] Finally, in Chap. 7, we will make a conclusion of this thesis.

[8] In Append. A, an example of collective dynamics of coupled oscillator systems different from a chimera state is given. See Chap. 2 for details.

Chapter 2

Theoretical Principles

Since Y. Kuramoto introduced a simple model to demonstrate a transition from disorder to self-organized order in a system of coupled oscillators [42], numerous authors have examined and discussed a variety of oscillator ensembles to investigate collective behaviors that arise in ensembles of nonlinearly coupled self-sustained oscillators. [25, 26, 105, 32]. The aim of this chapter is to provide the theoretical principles for the description of the macroscopic dynamics of oscillator ensembles as needed to follow the main results of the thesis. As stated in Chap. 1, our goal in this thesis is the exploration of **the coexistence dynamics of a system of identical Kuramoto-Sakaguchi oscillators in a network of networks**. To give the theoretical background, we first discuss how to construct a system of identical Kuramoto-Sakaguchi oscillators in a single network (or one population), starting from an individual oscillator, i.e., a building block of the system. Then, the macroscopic behavior of the system of identical Kuramoto-Sakaguchi oscillators is discussed based on the investigation of the Kuramoto order parameter. Note that the Kuramoto order parameter is defined and obtained from the sum of the microscopic individual oscillators, which requires us to investigate a numerous number of degrees of freedom. Next, we study how to describe the macroscopic dynamics of the ensemble using dimension reduction methods. In this chapter, we provide all the practical steps for the utilization of the Ott-Antonsen (OA) ansatz and the Watanabe-Strogatz (WS) transformation. Then, we will construct a system of Kuramoto-Sakaguchi oscillators in a network of networks, and show how one can describe it in terms of the WS and the OA variables. The aforementioned process will be given for both the usual and the generalized Kuramoto-Sakaguchi oscillators, respectively. Finally, we discuss the theoretical background of Lyapunov stability analysis, which we will exploit throughout the thesis for the study of the stability of chimera dynamics.

2.1 From a Building Block to an Ensemble

The simplest, yet the most important oscillating behavior both in nature and man-made systems is, without any doubt, *a simple harmonic oscillator* (SHO) [106–108]. In physics, this model is often used to approximate the local behavior of a physical system by considering a linear oscillation. For example, consider a complicated potential of a given physical system that is concave up at some point, i.e., it has a local minimum, then in the vicinity of the local minimum of the potential, the dynamics of the system can be approximated as a simple harmonic oscillator problem in the vicinity of the local minimum point of the potential. We readily encounter many instances of such a harmonic oscillation in diverse physical systems, including mechanical systems and electrical circuits [109]. In the complex plane, the SHO is described as $W(t) = W(0)e^{\mathrm{i}\omega_0 t}$ which is a solution of initial value problem of the ODE:

$$\partial_t W(t) = \mathrm{i}\omega_0 W(t) \tag{2.1}$$

where $\partial_t := \frac{d}{dt}$ and $\forall t$: $W(t) = W(t-T) \in \mathbb{C}$ fully depicts a periodic motion in the complex plane with the period $T = \frac{2\pi}{\omega_0}$. Here, $\omega_0 \in \mathbb{R}$ is called a natural frequency determined by intrinsic properties of the system such as the length of a pendulum, a spring constant, or the capacitance/inductance, according to the physical nature of the system under consideration. Equation (2.1) is linear so that the rotational symmetry can be considered, i.e., the system is invariant under the transformation $W \mapsto We^{\mathrm{i}\theta_0}$ where $\theta_0 \in \mathbb{R}$. Hence, there is no preferred phase value in this periodic motion [110]. Note that the simple harmonic oscillator represents one periodic trajectory whose amplitude is determined by the initial condition. Thus, there exists a continuous band of periodic orbits around a *center* [111–113]. An SHO is not an isolated closed trajectory in the phase space.

As described above, the SHO is the simplest linear oscillator. In Chap. 1, we learned that nonlinearity is necessary to observe the collective behavior in a complex system. How then can we describe a simple *nonlinear* oscillator? To this end, we impose the simplest nonlinear term in Eq. (2.1) that preserves the rotational symmetry [110]. This leads to

$$\partial_t W = \mathrm{i}\omega_0 W + f(W, \overline{W}) \tag{2.2}$$

where $f(W, \overline{W})$ characterizes the nonlinearity and satisfies

$$f(We^{\mathrm{i}\theta_0}, \overline{W}e^{-\mathrm{i}\theta_0}) = f(W, \overline{W})e^{\mathrm{i}\theta_0}. \tag{2.3}$$

Hereafter, the symbol with an overbar indicates the complex conjugate. Among many other ways to satisfy Eq. (2.3), the simplest nonlinear term doing so is $f(W, \overline{W}) = W\overline{W}W = |W|^2 W$.

The nonlinear oscillator constructed from the above is called *a Stuart-Landau oscillator* (SLO) and is governed by

$$\partial_t W = c_1 W + c_2 |W|^2 W \tag{2.4}$$

where $c_1, c_2 \in \mathbb{C}$. As the simple harmonic oscillation represents a universal local behavior of any linear oscillation, likewise, Eq. (2.4) represents the normal form of *Hopf bifurcation*, i.e., the universal local behavior of nonlinear oscillation near the emergence of a limit-cycle oscillation [114]. The periodic motion of Eq. (2.4) is an isolated closed trajectory in the phase space. To be more specific, let us assume that $c_1 = \mu + \mathrm{i}$ and $c_2 = \alpha + \mathrm{i}\beta$. Then, $\mu \in \mathbb{R}$ is the bifurcation parameter and $\alpha \in \mathbb{R}$ is called the *first Lyapunov coefficient* [112] that determines the stability of the limit-cycle generated in the Hopf bifurcation at $\mu = 0$: If $\alpha < 0$, the limit-cycle described by $W(t) = \sqrt{-\mu/\alpha} e^{\mathrm{i}(1-\beta\mu/\alpha)t}$, is stable for $\mu > 0$ and the bifurcation is then called *supercritical*. Otherwise, if $\alpha > 0$, an unstable limit-cycle emerges for $\mu < 0$ in a so-called *subcritical* Hopf bifurcation[1].

The Stuart-Landau oscillator could be a good candidate for a building block of a generic system of coupled oscillators. Let us extend an oscillator to an ensemble of coupled oscillators, of which we are to study the collective dynamics. First of all, we consider a system of infinitely many oscillators since we have the *digitus minimus* of physicists[2]. We assume that oscillators are interacting with others according to a given coupling scheme, which will be specified in this chapter. To give a concrete shape to this idea, we here consider a continuous oscillatory medium. The system is described by an oscillator field $W(x,t) \in \mathbb{C}$ over a spatiotemporal domain, depending on $x \in [0,L] =: \mathbb{D} \subseteq \mathbb{R}$ and $t \in \mathbb{R}$[3]. At a certain point $x \in \mathbb{D}$, the oscillator field $W(x,t)$ can be interpreted as a single oscillator $W(x,t)$ that is coupled with other oscillators at other points on $\mathbb{D}$ via a given coupling function. Note that, for simplicity, we only deal with a 1D geometry of length $|\mathbb{D}| = L$ with periodic boundary conditions. The simplest spatiotemporal dynamical system of such a continuous oscillatory field is a *reaction-diffusion equation* which reads

$$\frac{\partial}{\partial t} W(x,t) = \mathscr{F}(W) + D \frac{\partial^2}{\partial x^2} W. \tag{2.5}$$

[1] Cf. the SHO is one of a continuous band of (i.e., an infinite number of) periodic orbits near a *center*, and hence it is a non-isolated neutrally stable orbit, not a limit-cycle. In fact, the analytic planar system ($\partial_t \mathbf{x} = \mathbf{f}(\mathbf{x})$ where $\mathbf{x} \in \mathbb{R}^2$ and $\mathbf{f}$ is analytic in $\mathbb{R}^2$) has at most a finite number of limit-cycles in any bounded region in $\mathbb{R}^2$ (Dulac) [112].

[2] We know that physicists have five fingers to count the number of degrees of freedom: one, two, three, finite-N, and infinity.

[3] A dynamical system is a triplet $(X, \mathscr{T}, \varphi_t)$, where X is a topological space, called the phase space, with an appropriate structure such as a metric, $\mathscr{T}$ is the time domain and $\varphi_t : X \to X$ for $t \in \mathscr{T}$ is the family of evolution operators satisfying $\varphi_0 = \mathrm{id}$ and $\varphi_s \circ \varphi_t = \varphi_{t+s}$ $\forall t, s \in \mathscr{T}$ [115]. Throughout this thesis, we consider $\mathscr{T} = \mathbb{R}_+$ without loss of generality.

where D is a diffusion coefficient. In Eq. (2.5), the reaction term $\mathscr{F}(W)$ governs the (decoupled) local dynamics by which the single oscillator behaves independently of the others. The coupling term, i.e., the diffusion term $D\partial_x^2 W(x,t)$ specifies a pure-local interaction through which each oscillator (i.e., the oscillator field at a certain point x in the domain) can be considered as coupled only with the nearest neighbors due to the property of the Laplacian operator[4]. Equation (2.5) is a general reaction-diffusion equation. Now, we can specify the reaction term using the building block that we had, i.e., the Stuart-Landau oscillator in Eq. (2.4). This leads to the reaction-diffusion equation given by

$$\frac{\partial}{\partial t}W(x,t) = \underbrace{(1+\mathrm{i}\omega_0)W(x,t) - (1+\mathrm{i}c_2)|W(x,t)|^2 W(x,t)}_{\text{intrinsic dynamics of building block, i.e., SLO}} + \underbrace{(1+\mathrm{i}c_1)\frac{\partial^2}{\partial x^2}W(x,t)}_{\text{purely local coupling}} \tag{2.6}$$

where $\omega_0, c_1, c_2 \in \mathbb{R}$ [5]. Equation (2.6) is called the *Complex Ginzburg-Landau Equation* (CGLE). The CGLE is known to exhibit a variety of spatiotemporal collective patterns depending on the parameter values, examples ranging from a nearly uniform oscillation to chaotic dynamics [110, 116]. Note that the local dynamics of Eq. (2.6) is still the Stuart-Landau oscillator, which is our building block that constitute the ensemble.

The diffusion term in Eq. (2.6) describes a purely local interaction between neighboring oscillators. In fact, we can consider a rather general spatial coupling function in the oscillatory medium. For this, we replace the Laplacian operator (local coupling) with an integral operator which reads

$$\frac{\partial}{\partial t}W(x,t) = (1+\mathrm{i}\omega_0)W(x,t) - (1+\mathrm{i}c_2)|W(x,t)|^2 W(x,t) + \varepsilon e^{-\mathrm{i}\alpha}(\mathscr{G}W)(x,t) \tag{2.7}$$

where $\varepsilon \in \mathbb{R}$ is the coupling strength and $\alpha \in [0, 2\pi]$ is the so-called phase-lag parameter. Note that here we write $1+\mathrm{i}c_1 \mapsto \varepsilon e^{-i\alpha} \in \mathbb{C}$. The coupling term can be written as an integral convolution operator defined by

$$(\mathscr{G}W)(x,t) := \int_{\mathbb{D}} G(x-x')W(x',t)dx' \tag{2.8}$$

where $\mathbb{D} := [0, L]$ is the spatial domain of the medium and $G(y)$ with $|y| \leq L/2$ is a coupling function that will be specified later in this chapter. Note that in general the integral in Eq. (2.8)

[4] This can be easily understood by, for example, considering a finite difference discretization of the Laplacian operator $\partial_x^2 W \sim W_{j+1} + W_{j-1} - 2W_j$. Thus, each oscillator j interacts only with the nearest neighbors $j-1$ and $j+1$ in a ring geometry.

[5] Here, the constants c_1 and c_2 have different meanings from those in Eq. (2.4)

is not treated in a Riemannian sense but rather in a Lebesgue sense since the continuity of $W(x,t)$ as a function of x is not guaranteed in general [117, 118].

Although Equation (2.7) is defined *ab initio* in a continuous oscillatory medium described by the oscillator field $W(x,t)$, we interpreted the oscillatory field $W(x,t)$ at a certain point x as an oscillator coupled with other oscillators situated in the domain of the medium. In this perspective, we can view (not rigorously but practically) this continuous system as a continuum limit of a finite-sized ensemble[6]. The governing equation of the finite-sized ensemble is given by

$$\partial_t W_j = (1+\mathrm{i}\omega_0)W_j - (1+\mathrm{i}c_2)|W_j|^2 W_j + \varepsilon e^{-\mathrm{i}\alpha}\left(\frac{L}{N}\sum_{k=1}^{N} G_{jk}W_k\right) \tag{2.9}$$

where $W_j(t) := W(x,t)$ at $x = x_j := \frac{L(j-1)}{N}$ and G_{jk} for $j,k = 1,\ldots,N$. Here, N is the number of oscillators in the finite-sized ensemble.

Both continuous and discrete systems of coupled Stuart-Landau oscillators can display a variety of collective dynamics, depending on the specifics of the coupling function $G(y)$. For discrete systems, we consider the following four cases:

[1] For $G_{jk} \sim \delta_{j,k+1} + \delta_{j,k-1}$, the purely local interaction of diffusive coupling is recovered, as discussed above for the CGLE [110, 116];

[2] $G_{jk} = \frac{1}{L}$ for all $j,k = 1,\ldots,N$ results in a global (all-to-all) coupling in the system where each oscillator is coupled with all the others through the mean-field force [119];

[3] A network structure of oscillators is obtained when G_{jk} represents its weighted adjacency matrix, which has zero entries for all pairs of oscillators j,k that are uncoupled [52, 120] and all non-zero values represent the interaction strength between oscillators j and k.

[4] $G_{jk} = G(x_j - x_k)$ with non-constant, piece-wise smooth and even function $G(y)$ [61, 60] yields an ensemble of nonlocally coupled Stuart-Landau oscillators in a spatially extended system [53, 64];

In this thesis, in order to study chimera states, we will exploit the second case [2], however, with a structure of a network of networks. In Appendix. A, we consider collective behavior in a system with spatially nonlocal coupling as an example of the case [4]. More precisely, we will discuss a traveling wave solution of nonlocally coupled Stuart-Landau oscillators in a ring geometry [121].

[6] or one can interpret this finite-sized ensemble as a finite-size approximation of the continuous medium.

2.2 Ensemble of Kuramoto Phase Oscillators

Depending on the coupling scheme, an ensemble of coupled Stuart-Landau oscillators in Eq. (2.9) can exhibit various collective dynamics including chimera states. Yet, it is not an easy task to deal with planar oscillators since they have two degrees of freedom, the phase and the amplitude. In this section, we focus on the collective behavior of so-called phase-oscillators with the phase being the only degree of freedom.

The Stuart-Landau oscillator in Eq. (2.4) represents a limit-cycle in the phase space ($\mathbb{R}^2$) around the origin, i.e., an isolated periodic trajectory on a circle with radius $\sqrt{-\mu/\alpha}$ centered at the origin. Here, the amplitude dynamics governs the transversal direction to the periodic motion on the limit-cycle whereas the phase variable describes the tangential motion of the periodic orbit [25]. However, since the amplitude shows constant motion, we are tempted to ignore it and consider only the phase dynamics meaningful. Let us see how we can justify such a treatment. In Sec. 2.1, we discussed that a Stuart-Landau oscillator can be either stable or unstable, depending on a given parameter set. The stability of the limit-cycle oscillation can be investigated by measuring Lyapunov exponents [122–124]. The Lyapunov exponents provide the local information on the exponential growth/shrinkage rate of a given perturbation in the tangent space dynamics along a reference trajectory. For the details, see Sec. 2.6. In the case of a stable limit-cycle, we can easily find that the amplitude dynamics has a negative Lyapunov exponent with a finite order of magnitude. This means that transversal perturbations shrink exponentially fast to zero, so that the stable limit-cycle trajectory is restored. How rapidly it settles down to the original trajectory is characterized by the magnitude of the Lyapunov exponent. On the other hand, the phase degree of freedom is characterized by a zero Lyapunov exponent, which confirms that tangentially to or along the periodic motion, the dynamics is neutrally stable. The neutrally stable phase dynamics gives rise to collective motion when the oscillator phases are coupled with the phases of others in an appropriate condition [25]. Since the Lyapunov exponents characterizing the dynamics of the two variables have different orders of magnitude, i.e., the expansion/contraction rate of local perturbations, we observe a separation of time scales. Starting from an initial condition near the stable limit-cycle, the trajectory falls into the limit-cycle trajectory asymptotically and fast. Then, the trajectory evolves according to the phase dynamics along the limit-cycle with $|W(t)| \to \sqrt{-\mu/\alpha}$. For details on the reduction with the center manifold theorem, see Ref. [125].

In a system of identical Stuart-Landau oscillators coupled through a sufficiently weak coupling strength, the amplitude variables likewise approach the amplitude value of the

given uncoupled SLO on a fast time scale, i.e., $|W(x,t)| \approx 1$ for all $x \in \mathbb{D}$[7]. This leads the amplitude variables of the oscillator ensemble to a nearly homogeneous distribution. The small fluctuations around the homogeneous amplitude distribution can be ignored in this context[8]. In contrast, on the slow time scale, the phase variables adjust their dynamics through the interaction between the oscillators due to their (nearly) neutral stability. Hence, a system of weakly coupled oscillators can display a nontrivial (inhomogeneous) collective motion in their phase degrees of freedom while the amplitude variables settle down to the trivial behavior, i.e., the homogeneous distribution. Hence, we can consider only the phase dynamics of the ensemble.

Such phase-only dynamics of a system of nearly identical oscillators can be validated in general as long as the coupling strength is sufficiently weak [126, 42, 25]. In other words, this reduction method is generally applicable for other nearly identical planar oscillators, such as van der Pol oscillators when they are weakly coupled [127]. But, here we focus on the system of Stuart-Landau oscillators in Eq. (2.7). Let us first assume that the coupling strength is sufficiently weak, i.e., $\varepsilon \ll 1$. Then, in polar coordinates where $W(x,t) = r(x,t)e^{\mathrm{i}\phi(x,t)}$ for $r(x,t) \in \mathbb{R}$ and $\phi(x,t) \in \mathbb{T} := [0, 2\pi]$, Equation (2.7) can be written as

$$\begin{aligned}\frac{\partial}{\partial t} r(x,t) &= r(x,t) - r(x,t)^3 + \varepsilon \int_{\mathbb{D}} G(x-x') r(x',t) \cos(\phi(x',t) - \phi(x,t) - \alpha) dx' \\ &= r(x,t)(1 - r(x,t)^2) + O(\varepsilon)\end{aligned} \tag{2.10}$$

and

$$\begin{aligned}\frac{\partial}{\partial t} \phi(x,t) &= \omega_0 - c_2 r(x,t)^2 + \frac{\varepsilon}{r(x,t)} \int_{\mathbb{D}} G(x-x') r(x',t) \sin(\phi(x',t) - \phi(x,t) - \alpha) dx' \\ &= \omega_0 - c_2 r(x,t)^2 + O(\varepsilon) \\ &\mapsto c_2 (1 - r(x,t)^2) + O(\varepsilon)\end{aligned} \tag{2.11}$$

for the amplitude and phase variables, respectively. Note that the last line of Eq. (2.11) arises from the phase shift invariance $\phi \mapsto \phi + (\omega_0 - c_2)t$ since the system has the continuous rotational symmetry. For $\varepsilon \ll 1$, the system has two time scales [59]: The amplitude dynamics falls first into its homogeneous arrangement within the fast time scale such that $r(x,t) = 1$ for all $x \in \mathbb{D}$. On the slow time scale, the system dwells in a manifold with a uniform amplitude distribution such that only the phase dynamics is nontrivial via $O(\varepsilon)$ term

[7] Note that in Eq. (2.7), the corresponding amplitude is given as $\sqrt{-\mu/\alpha} = 1$.

[8] Note that we cannot ignore the amplitude dynamics if the coupling strength is not sufficiently weak. For example, see Appendix. A.

in Eq. (2.11). Therefore, the phase-reduced dynamics reads

$$\frac{\partial}{\partial t}\phi(x,t) = \omega + \varepsilon \int_{\mathbb{D}} G(x-x') \sin(\phi(x',t) - \phi(x,t) - \alpha) dx' \tag{2.12}$$

where ω results from an appropriate rotating reference frame, and can be interpreted as a natural (intrinsic) frequency of the phase oscillator. This phase-only equation is called in general a *phase-reduced model* or a *phase model* [127, 128].

In the finite-sized approximation, each phase oscillator $\phi_j(t) \in \mathbb{T}$ is governed by

$$\partial_t \phi_j = \omega + \varepsilon \frac{L}{N} \sum_{k=1}^{N} G(x_j - x_k) \sin(\phi_k - \phi_j - \alpha) \tag{2.13}$$

for $j = 1, ..., N$. This set of coupled equations is called *an ensemble of Kuramoto-Sakaguchi phase oscillators*. In contrast, it is called Kuramoto-Battogtokh model [53] when the coupling function represents the (spatially extended) nonlocal coupling on a ring geometry. A chimera state was initially observed in the Kuramoto-Battogtokh model [53]. However, in this thesis, our main concern is the study of chimera states in a network of networks, where intra- and inter-population coupling is all-to-all, yet with different coupling strengths. Hence, as the first step, here we study systems of globally coupled Kuramoto phase oscillators in a single network and then construct a network of networks. To this end, we discuss the details of a system of identical *Kuramoto-Sakaguchi oscillators* below, which reads

$$\partial_t \phi_j(t) = \omega + \frac{\varepsilon}{N} \sum_{k=1}^{N} \sin(\phi_k - \phi_j - \alpha) \tag{2.14}$$

for $j = 1, ..., N$. Due to the phase shift invariance in Eq. (2.14), we can set $\omega = 0$. Note that Eq. (2.14) can be obtained from Eq. (2.13) when $G_{jk} = \frac{1}{L}$ for $j, k = 1, ..., N$, i.e., the (all-to-all) globally coupled system. For the sake of simplicity, we set ε to unity.

So far, we have prepared the building blocks of our main system (Kuramoto-Sakaguchi oscillators) and an ensemble of them. To study the collective dynamics of the system, we need one more necessary ingredient. We have to find a ruler to measure the macroscopic behavior from the information of the individual oscillators $\{\phi_j(t)\}_{j=1}^{N}$. Such a ruler is given by the Kuramoto order parameter. It is defined as [129]

$$\Gamma(t) = R(t) e^{\mathrm{i}\Theta(t)} := \frac{1}{N} \sum_{k=1}^{N} e^{\mathrm{i}\phi_k(t)} \in \mathbb{C}^1 \tag{2.15}$$

where $\Gamma(t) \in \mathbb{C}$, $R(t) \in \mathbb{R}$ and $\Theta(t) \in \mathbb{T}$. To understand its physical meaning, suppose that each oscillator moves according to Eq. (2.14) on a unit circle in the complex plane, i.e., the motion follows $e^{i\phi_k(t)}$ as a function of time for $k = 1, ..., N$ [9]. Then, the Kuramoto order parameter corresponds to the centroid of the oscillator phases on the unit circle [43]. The modulus $|\Gamma(t)| = R(t)$ measures the degree of coherence of the phase variables, and the argument $\arg\Gamma(t) = \Theta(t)$ gives the average phase of the oscillators on the unit circle. Therefore, a completely incoherent state where all the oscillators are distributed uniformly on the unit circle (we assume $N \gg 1$) is characterized by $R = 0$. On the other hand, the synchronized state results in $R = 1$. An intermediate value $0 < R < 1$ indicates partial coherence of the oscillator phases. Thus, the Kuramoto order parameter is a good ruler that measures the collective behavior of the system. However, so far, the Kuramoto order parameter in Eq. (2.15) is calculated from a numerous number of microscopic phases, i.e., we have to obtain all $\phi_j(t)$ as a function of time for $j = 1, ..., N$. Furthermore, the Kuramoto order parameter in Eq. (2.15) only provides us with a phenomenological observation of the collective behavior, not the governing equation of the order parameter. Recall that our goal is the description of the collective *dynamics*, which means we would like to investigate the governing equation of the Kuramoto order parameter if it exists. In Sec. 2.4, we will discuss this aspect in more detail.

Now we introduce a more concrete approach to the system of Kuramoto-Sakaguchi oscillators. Here, we show another simple way to Eq. (2.14) that includes important concepts for the study of oscillator systems. Let us first discuss an obvious concept, a *phase* on a limit-cycle trajectory in the state space[10]. The single nonlinear oscillator can be generally written as [42, 130, 25]

$$\partial_t \mathbf{X} = \mathbf{F}(\mathbf{X}) \tag{2.16}$$

where $\mathbf{X} \in E \subseteq \mathbb{R}^M$, $\mathbf{F} \in C^1(E)$ and E is an open subset of $\mathbb{R}^M$. Assume that Eq. (2.16) has a stable limit-cycle trajectory such that $\mathbf{X}_0(t+T) = \mathbf{X}_0(T)$ where T is its *period* and $\mathbf{X}_0 : \mathbb{R} \to E$ denotes the very stable limit-cycle in phase space. Next, we can introduce the *frequency*, $\omega = \frac{2\pi}{T}$, and define the limit set $\Gamma := \{\mathbf{X} \in E \mid \mathbf{X} = \mathbf{X}_0(t),\ t \in [0, T]\}$ that attracts nearby trajectories into itself. Since a limit-cycle is a periodic trajectory, whose phase evolves monotonically, gaining 2π in each cycle [25], and Γ is one-dimensional manifold embedded in $E \subseteq \mathbb{R}^M$, we can uniquely assign any point $\mathbf{X}_p \in \Gamma$ to a *phase* $\psi_p \in \mathbb{T} := [0, 2\pi]$, on which a diffeomorphism is defined as $\Psi : \Gamma \to \mathbb{T}$, called the *phase map* such that $\Psi(\mathbf{X}_p) = \psi_p$

[9] Note that the phase variable is the argument of $e^{i\phi_k(t)}$, and this fact will be needed again when we discuss the generalized Kuramoto oscillator in Sec. 2.5

[10] the phase space

and $\varphi_t(\mathbf{X}_p) := \mathbf{X}_0(t + \frac{T}{2\pi}\psi_p) = \mathbf{X}_0(t + \frac{\psi_p}{\omega})$ by setting $\Psi(\mathbf{X}_0(0)) = 0$ where $\varphi_t : E \to E$ (or $\varphi : \mathbb{R} \times E \to E \subseteq \mathbb{R}^M$) is a flow of Eq. (2.16) [112]. Therefore, the *phase variable* on a limit-cycle Γ is defined as $\theta : \mathbb{R} \to \mathbb{T}$ to satisfy $\theta(t) = \Psi(\varphi_t(\mathbf{X}_p)) = \Psi(\mathbf{X}_0(t + \omega^{-1}\psi_p))$. In fact, we can define the frequency as $\omega := \nabla_{\mathbf{X}}\Psi \cdot \frac{d\mathbf{X}}{dt} = \nabla_{\mathbf{X}}\Psi \cdot \mathbf{F}(\mathbf{X})$ without loss of generality. Note that the phase variable $\theta(t)$ is also T-periodic in time, and one can define it to be $\theta(t) = \omega t + \psi_p$, which results in $\dot{\theta}(t) = \omega$ without loss of generality [130, 131].

The concept of a phase can be extended to a trajectory outside the limit-cycle but asymptotically converging to the limit-cycle under a weak perturbation [25, 42, 130]. To define the phase outside the limit-cycle, we consider an open neighborhood $U(\Gamma) \subseteq E$ of the limit-cycle trajectory where an initial condition starting in $U(\Gamma)$ converges to Γ as $t \to \infty$. From an initial condition $\mathbf{X}_p \in U(\Gamma)$, the *asymptotic phase* $\psi_p \in \mathbb{T}$ is defined to fulfill

$$\lim_{t\to\infty} \left| \varphi_t(\mathbf{X}_p) - \mathbf{X}_0(t + \frac{1}{\omega}\psi_p) \right| = 0 \tag{2.17}$$

(compare this with the phase defined above on the limit-cycle). Likewise, the *asymptotic phase map* is defined as $\Psi : U(\Gamma) \to \mathbb{T}$ with $\Psi(\mathbf{X}_p) = \psi_p$ and the *asymptotic phase variable* as $\theta : \mathbb{R} \to \mathbb{T}$ such that $\theta(t) = \Psi(\varphi_t(\mathbf{X}_p))$ satisfies Eq. (2.17) [130]. Here, the asymptotic phase variable is also T-periodic and can be chosen to follow $\theta(t) = \omega t + \psi_p$ so that $\dot{\theta}(t) = \omega$. The collection of all points in $U(\Gamma)$ with the same asymptotic phase variable is called an *isochron* [132, 42]. The isochron is an $(M-1)$-dimensional hypersurface that is a level set of Ψ. If a given set of points belongs to $U(\Gamma)$ at a certain time, it will stay on the same isochron for all t as long as no perturbation is imposed on them [42].

The concept of an asymptotic phase variable is still valid in the presence of a weak perturbation as long as the trajectory starting in $U(\Gamma)$ asymptotically converges to Γ. First, we introduce a small perturbation to Eq. (2.16) such that

$$\partial_t \mathbf{X} = \mathbf{F}(\mathbf{X}) + \varepsilon \mathbf{P}(\mathbf{X}) \tag{2.18}$$

where $\mathbf{P} : E \to E$ and $\varepsilon \ll 1$ is a small parameter which determines the perturbation strength so that $\varepsilon\mathbf{P}(\mathbf{X})$ describes a small perturbation depending on $\mathbf{X}$. The periodic orbit still persists, however, with a period slightly changed. We can therefore study how to approximate the orbit in the lowest order of ε under a weak perturbation [130, 42]. From the above definitions, we can consider a time derivative of the phase map, which reads

$$\partial_t \Psi(\mathbf{X}) = \nabla_{\mathbf{X}}\Psi \cdot \frac{d\mathbf{X}}{dt} = \nabla_{\mathbf{X}}\Psi \cdot \left[\mathbf{F}(\mathbf{X}) + \varepsilon\mathbf{P}(\mathbf{X})\right] = \omega + \varepsilon\nabla_{\mathbf{X}}\Psi \cdot \mathbf{P}(\mathbf{X}) \tag{2.19}$$

where we define for the situation without perturbation $\nabla_{\mathbf{X}}\Psi \cdot \mathbf{F}(\mathbf{X}) =: \omega$. This exact equation does not give a closed form in Ψ. The RHS depends generally on the precise value of $\mathbf{X}$ on the isochron characterized by Ψ. However, we can introduce the lowest approximation to obtain the closed equation for the phase variable since $\mathbf{X} \in U(\Gamma)$ still lies near Γ so that $|\mathbf{X} - \mathbf{X}_0| \to 0$ as $\varepsilon \to 0$ and the asymptotic phase variable has the same value on an isochron [42]. Hence, replacing $\mathbf{X}$ by $\mathbf{X}_0(\Psi)$ [11] results in the approximated equation

$$\partial_t \Psi = \omega + \varepsilon \, \nabla_{\mathbf{X}}\Psi \Big|_{\mathbf{X}=\mathbf{X}_0(\Psi)} \cdot \mathbf{P}(\mathbf{X}_0(\Psi)) = \omega + \varepsilon \, \mathbf{Q}(\Psi) \cdot \mathbf{P}(\Psi) \tag{2.20}$$

where $\mathbf{Q}(\Psi) = \nabla_{\mathbf{X}}\Psi|_{\mathbf{X}=\mathbf{X}_0(\Psi)}$ is called the *phase sensitivity function* (or the *phase response curve*) and both functions $\mathbf{Q}$ and $\mathbf{P}$ are 2π-periodic in Ψ. Returning back to our usual notation, we can rewrite Eq. (2.20) as

$$\partial_t \phi(t) = \omega + \varepsilon \, Q(\phi) P(\phi) \tag{2.21}$$

where $Q(\phi)$ is the phase response curve. It determines how sensitively a single oscillator at phase ϕ responds to a weak external perturbation in the lowest order of ε [42].

Many dynamical systems in nature, for example, ensembles of biological individuals as coupled oscillators, appear as a *pulse-coupled* oscillator system [133, 31]. Each oscillator sees a sudden impact from other interacting oscillators in the system. Such a system can be described by the so-called *Winfree model*

$$\partial_t \phi_j(t) = \omega + \varepsilon \, Q(\phi_j) \frac{1}{N} \sum_{k=1}^{N} P(\phi_k), \quad j = 1, \ldots, N \tag{2.22}$$

where ε is the coupling strength, $Q(\phi)$ is the phase response curve, i.e., the phase sensitivity function, and $P(\phi)$ characterizes a smooth pulse-like coupling. This equation describes a system of coupled oscillators with the building block represented in Eq. (2.21). It is important to note that in Eq. (2.22), there is no phase shift invariance since the oscillators are pulse-coupled ($P(\phi_k)$), not pairwise phase-coupled ($H(\phi_k - \phi_j)$). More specifically, Ariaratnam and Strogatz [133] introduced a mathematically tractable model for such pulse-coupled oscillator ensembles with specific functions:

$$Q(\phi) = -\sin\phi, \quad P(\phi) = 1 + \cos\phi. \tag{2.23}$$

[11] note that the phase map Ψ on a limit-cycle $\mathbf{X}_0$ is defined to be bijective, so that one can consider $\mathbf{X}_0(\Psi)$

The smooth function $P(\phi)$ describes a pulse coupling since at $\phi = 0$, the function is so sharply peaked as to represent the sudden firing impulse from the other oscillators [133, 134, 80]. Furthermore, one can generalize these functions to obtain a more sharply peaked pulse:

$$Q(\phi) = \sigma - \sin(\phi + \alpha), \quad P(\phi) = a_n(1+\cos\phi)^n \tag{2.24}$$

where $n \in \mathbb{N}$ and $a_n = 2^n(n!)^2/(2n)!$. In this case, the larger n is, the more sharply peaked is $P(\phi)$, so that as $n \to \infty$, $P(\phi) = 2\pi\delta(\phi)$ [133, 80].

To obtain the relation between Winfree (2.22) and Kuramoto (2.13), we take the *method of averaging* [111, 135, 136]: Under a transformation $\phi_j \mapsto t + \phi_j$ and averaging both sides over t, i.e., taking $\langle\cdot\rangle_t = \frac{1}{2\pi}\int_0^{2\pi}\cdot\, dt$, we get

$$\begin{aligned}
\partial_t\langle\phi_j\rangle_t + 1 &= \omega + \frac{\varepsilon}{N}\sum_{k=1}^{N}\frac{1}{2\pi}\int_0^{2\pi}(1+\cos(t+\phi_k))(\sigma - \sin(t+\phi_j+\alpha))dt \\
&\Longrightarrow\ \partial_t\langle\phi_j\rangle = \omega - 1 + \varepsilon\sigma + \frac{\varepsilon}{N}\sum_{k=1}^{N}\frac{1}{2\pi}\Big(-\pi\sin(\phi_j - \phi_k + \alpha)\Big) \\
&\Longrightarrow\ \partial_t\varphi_j = \omega + \frac{\varepsilon}{N}\sum_{k=1}^{N}\sin(\varphi_k - \varphi_j - \alpha), \quad j = 1,\ldots,N
\end{aligned} \tag{2.25}$$

where the last line arises due to the approximation method of averaging for which $\phi_j = \langle\phi_j\rangle + O(\varepsilon)$ and $\varphi_j := \langle\phi_j\rangle$ with $\omega - 1 + \varepsilon\sigma \mapsto \omega$ and $\frac{\varepsilon}{2} \mapsto \varepsilon$ for $j = 1,\ldots,N$. The above equation is nothing but Eq. (2.14).

2.3 System of Identical Kuramoto-Sakaguchi Oscillators

In this section, we investigate a system of *identical* Kuramoto-Sakaguchi oscillators and study their collective behavior which looks rather trivial but is important. More specifically, looking at the macroscopic dynamics, we here exploit directly the Kuramoto order parameter, as a phenomenological observation from all the individual oscillators $\{\phi_j(t)\}_{j=1}^N$, i.e., no governing equation of the order parameter is considered in this section. The system can display either *complete phase synchronization* or the *completely incoherent state* [12] depending on the value of the phase-lag parameter $\alpha \neq 0$. The phase-lag parameter determines the Benjamin-Feir instability α_{BF}: for $\alpha < \alpha_{\mathrm{BF}}$, the synchronized state is stable whereas the (completely) incoherent state is unstable. In contrast, for $\alpha > \alpha_{\mathrm{BF}}$, the synchronized state is

[12] Note that this state is a complete phase desynchronization where the oscillators are fully locked at the common frequency Ω while uniformly distributed on the unit circle. However, in the thesis, we call it the completely incoherent state to follow terms in the literature, e.g., Ref. [99].

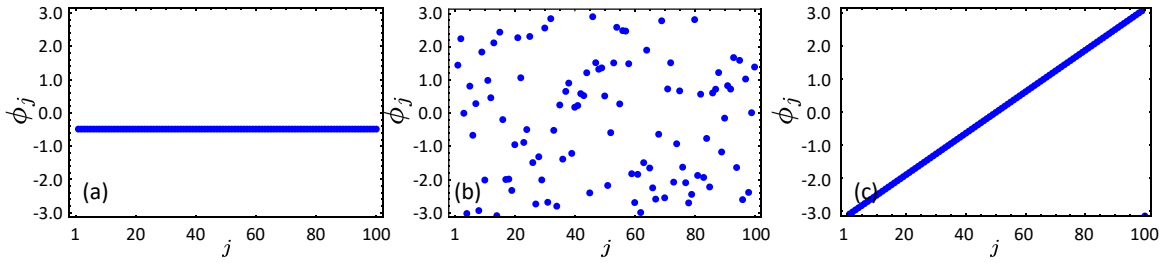

Fig. 2.1 Snapshots of the distribution of phases of different solutions of Eq. (2.14) with $N = 100$ oscillators at $t = 10,000$. (a) The synchronized state for $\alpha = \frac{\pi}{2} - 0.1$. (b) The completely incoherent state for $\alpha = \frac{\pi}{2} + 0.1$. Both results are obtained from random initial conditions. (c) The splay state for $\alpha = \frac{\pi}{2} + 0.1$ from an initial condition $\phi_j(0) = \frac{2\pi}{N} j$ for $j = 1, ..., N$. Note that when we rearrange the oscillator in ascending order of the phase values in (b), it does not exhibit a straight line with a constant slope as depicted in (c).

unstable and the incoherent state stable [110]. Below, we will show that the Benjamin-Feir instability occurs at $\alpha_{\mathrm{BF}} = \frac{\pi}{2}$ using linear stability analysis.

2.3.1 Complete Phase Synchronization

First of all, since we assume all the oscillators are identical, *complete phase synchronization* is expected to occur where $\phi_j(t) = \phi_0 + \Omega t$ for $j = 1, ..., N$ (see Fig. 2.1 (a)). All the oscillators have the same phase value and they are locked at the same collective frequency Ω. The (completely) synchronized state has unit modulus of the Kuramoto order parameter in Eq. (2.15):

$$\Gamma(t) = \frac{1}{N} \sum_{j=1}^{N} e^{\mathrm{i}\phi_j(t)} = \frac{1}{N} \sum_{j=1}^{N} e^{\mathrm{i}\phi_0} e^{\mathrm{i}\Omega t} = e^{\mathrm{i}\phi_0} e^{\mathrm{i}\Omega t} \tag{2.26}$$

for all t. Hence, $|\Gamma(t)| = 1$ for all $t \in \mathbb{R}$. In an appropriate rotating reference frame, for example, $\phi \mapsto \phi + \Omega t$, the synchronized state is a fixed point solution to Eq. (2.14) with $\phi_j = \phi_0$ for $j = 1, ..., N$. Thus, we can apply linear stability analysis straightforwardly by calculating the eigenvalues of the Jacobian matrix evaluated at the synchronized state. The Jacobian matrix reads

$$\begin{aligned} J_{ij} &:= \left. \frac{\partial \dot{\phi}_i}{\partial \phi_j} \right|_{\phi_0} = \left. \frac{\partial}{\partial \phi_j} \left(\frac{\varepsilon}{N} \sum_{k=1}^{N} \sin(\phi_k - \phi_i - \alpha) \right) \right|_{\phi_0} = \left. \frac{\varepsilon}{N} \sum_{k=1}^{N} \cos(\phi_k - \phi_i - \alpha)(\delta_{kj} - \delta_{ij}) \right|_{\phi_0} \\ &= \frac{\varepsilon}{N} \cos(-\alpha) - \delta_{ij} \left(\sum_{k=1}^{N} \cos(\phi_0 - \phi_0 - \alpha) \right) = \frac{\varepsilon}{N} \cos\alpha - \delta_{ij}\, \varepsilon \cos\alpha \end{aligned} \tag{2.27}$$

where δ_{ij} is a Kronecker's delta for $i, j = 1, ..., N$. For the eigenvalues, we obtained

$$\lambda_i = \begin{cases} 0, & \text{if } i = 1 \\ -\varepsilon \cos\alpha, & \text{if } i = 2, ..., N \end{cases}. \tag{2.28}$$

Hence, the stability of the synchronized state is determined by the phase-lag parameter α: If $\alpha > \frac{\pi}{2}$, then the eigenvalue $\lambda_{i\geq 2} = -\varepsilon \cos\alpha > 0$ so that the sync state is unstable. On the contrary, if $\alpha < \frac{\pi}{2}$, it becomes stable. Note that there is always one zero eigenvalue, $\lambda_1 = 0$, which arises from the phase-shift invariance with the corresponding eigenvector $v_1 \sim (1, ..., 1)^\top$. On the other hand, there are $(N-1)$-fold degenerate negative eigenvalues with corresponding eigendirections transverse to the synchronized manifold, i.e., $v_i = (v_i^{(1)}, ..., v_i^{(N)})^\top$ with $\sum_{k=1}^{N} v_i^{(k)} = 0$ for $i = 2, ..., N$.

2.3.2 Completely Incoherent State: Splay State

Secondly, one can obtain a set of oscillators distributed uniformly on the unit circle of $\mathbb{C}^1$ while all the oscillators are rotating with the common frequency Ω. This incoherent state is characterized by the Kuramoto order parameter in Eq. (2.15) being zero. An example is depicted in Fig. 2.1 (b). In fact, there are many realizations of such incoherent states for large N with

$$\frac{1}{N}\sum_{j=1}^{N} \sin\phi_j = \frac{1}{N}\sum_{j=1}^{N} \cos\phi_j = 0 \tag{2.29}$$

that leads to $|\Gamma(t)| = 0$. Here, we focus on a very specific example of an incoherent state, which shows equally spaced phases along the unit circle when arranged in ascending order of the phase value. This incoherent state is called a *splay state* (see Fig. 2.1 (c)) [137][13] and is considered the core of all the completely incoherent states [99]. Thus, we next concentrate on the splay state as a representative of all the realization of the incoherent states. The splay state satisfies

$$\phi_j(t) = \frac{2\pi}{N} j + \Omega t \tag{2.30}$$

where Ω is the common frequency at which every oscillator is fully locked, i.e., it describes the uniform ratotion of the phases.

In Eq. (2.30), we defined and then observed the splay state, which consists of equally spaced phases on the unit circle [137, 138]. Furthermore, all the oscillators are uniformly rotating with the same common collective frequency Ω, i.e., they are fully-locked. Hence, in

[13] Some authors call this state *ponies on a merry-go-round* [138] due to its shape on the unit circle.

a suitable rotating reference frame, a splay state also can be treated as a fixed point solution of Eq. (2.14). The Jacobian matrix evaluated at the splay state solution $\boldsymbol{\phi}^* := \{\phi_j = \frac{2\pi}{N} j | j = 1,...,N\}$ reads

$$\begin{aligned} J_{ij} := \left.\frac{\partial \dot{\phi}_i}{\partial \phi_j}\right|_{\boldsymbol{\phi}^*} &= \left.\frac{\partial}{\partial \phi_j}\left(\frac{\varepsilon}{N}\sum_{k=1}^{N}\sin(\phi_k - \phi_i - \alpha)\right)\right|_{\phi^*} \\ &= \frac{\varepsilon}{N}\cos\left(\frac{2\pi}{N}(j-i) - \alpha\right) - \delta_{ij}\,\frac{\varepsilon}{N}\sum_{k=1}^{N}\cos\left(\frac{2\pi}{N}(k-i) - \alpha\right) \quad (\to 0) \\ &= \frac{\varepsilon}{N}\cos\left(\frac{2\pi}{N}(j-i) - \alpha\right) \end{aligned} \tag{2.31}$$

for $i, j = 1,...,N$. In fact, due to the equally spaced phases, the Jacobian matrix in Eq. (2.31) becomes a *circulant matrix* with zero row-sum. In a matrix form, it reads [139, 140]

$$J = \begin{pmatrix} c_0 & c_{N-1} & \cdots & c_2 & c_1 \\ c_1 & c_0 & c_{N-1} & \cdots & c_2 \\ \vdots & c_1 & c_0 & \ddots & \vdots \\ c_{N-2} & \ddots & \ddots & \ddots & c_{N-1} \\ c_{N-1} & c_{N-2} & \cdots & c_1 & c_0 \end{pmatrix}. \tag{2.32}$$

Hence, the eigenvalues of the Jacobian matrix are given by

$$\lambda_j = c_0 + c_{N-1}w^j + c_{N-2}w^{2j} + \cdots + c_1 w^{(N-1)j} \tag{2.33}$$

with corresponding eigenvectors $v_j = (1, w^j, w^{2j}, ..., w^{(N-1)j})^\top$ where $w = e^{\mathrm{i}\frac{2\pi}{N}}$ for $j = 0,...,N-1$ [139, 140]. Among the eigenvalues, there are two non-zero eigenvalues $\lambda_2 = \frac{\varepsilon}{2}e^{\mathrm{i}\alpha}$ and $\lambda_{N-1} = \frac{\varepsilon}{2}e^{-\mathrm{i}\alpha}$. Apart from these two, there are $N-2$ neutrally stable directions with zero eigenvalues. One of them arises from the phase-shift invariance of the system. The other $N-3$ neutral stabilities arise from the fact that there are many realizations of the incoherent states that satisfy the condition $\sum_{k=1}^{N} e^{\mathrm{i}\phi_k} = 0$, and the perturbations among these realizations bring about the neutrally stable directions [99]. We will discuss the details of the neutral stability on the ground of Watanabe-Strogatz transformation later in this chapter. As a consequence, the linear stability of the splay state is determined by the real part of the two non-zero eigenvalues, i.e., $\mathrm{Re}\left[\frac{\varepsilon}{2}e^{\pm\mathrm{i}\alpha}\right] = \frac{\varepsilon}{2}\cos\alpha$: if $\alpha > \frac{\pi}{2}$, then the real parts of these two eigenvalues are negative. The splay state is found to be stable. On the contrary, it is unstable as long as $\alpha < \frac{\pi}{2}$.

In conclusion, the Benjamin-Feir instability of the system of identical Kuramoto-Sakaguchi oscillators occurs at $\alpha_{\mathrm{BF}} = \frac{\pi}{2}$.

2.4 Macrosopic Dynamics: Watanabe-Strogatz and Ott-Antonsen Ansatz

In this section, we revisit a remarkable rather recently developed result, which allows us to describe the macroscopic dynamics of ensembles of coupled phase oscillators. Let us begin with the simplest system, i.e., the identical Kuramoto-Sakaguchi oscillators in Eq. (2.14). The identical KS oscillators in Eq. (2.14) can be written in the following general form

$$\partial_t \phi_j = g + \mathrm{Im}\left[f e^{-\mathrm{i}\phi_j}\right], \quad j = 1, \ldots, N \tag{2.34}$$

where g is determined from the (decoupled) local information of each oscillator, and f governs how the oscillators are coupled in a mean-field manner, i.e., it describes an all-to-all coupling. Equation (2.14) is obtained with

$$f = \varepsilon \Gamma(t) e^{-\mathrm{i}\alpha} := \varepsilon e^{-\mathrm{i}\alpha} \frac{1}{N} \sum_{k=1}^{N} e^{\mathrm{i}\phi_k(t)} \quad \text{and} \quad g = \omega \tag{2.35}$$

Then, each oscillator is *effectively* decoupled and influenced by the mean-field forcing only, i.e., the Kuramoto order parameter $\Gamma(t)$. This is a typical example of *sinusoidally* coupled systems. What does '*sinusoidally*' mean? As one can easily notice, the governing equation of each oscillator depends on its own index j only through the first harmonics, e.g., $e^{\pm \mathrm{i}\phi_j(t)}$ while the other terms are the same for all the oscillators acting like an external forcing and constitute the mean-field coupling. Such a system is called a sinusoidally coupled system of identical phase oscillators [95].

In 1993-1994, S. Watanabe and S. Strogatz reported remarkable results. They stated that a system of N sinusoidally coupled *identical* phase oscillators can be reduced to 3D dynamics and all the other degrees of freedom are just constants of motion [98, 99]. They introduced a time-dependent transformation between the microscopic phase variables $\{\phi_j(t)\}_{j=1}^{N}$ and the microscopic constants of motion $\{\psi_j\}_{j=1}^{N}$ plus three macroscopic variables $\{\rho(t), \Phi(t), \Psi(t)\}$. The transformation is called the *Watanabe-Strogatz transformation* after their discoverers.

In 2008, E. Ott and T. Antonsen worked also on various sinusoidally coupled phase oscillator ensembles in the thermodynamic limit, but in contrast to Watanabe and Strogatz

they considered heterogeneous natural frequencies [96, 97]. They proposed a 2D invariant manifold to which the infinite-dimensional system can be reduced when a certain condition is met. Later, Marvel, Mirollo and Strogatz [95] and Pikovsky and Rosenblum [101, 102], respectively, demonstrated the relation between the Watanabe-Strogatz transformation and the Ott-Antonsen ansatz. Thereafter, many researchers have exploited those two approaches so as to understand a variety of collective dynamics including a chimera state [62]. In this chapter, we revisit their works in a practical way which will help us explore the *coexistence dynamics* in the following chapters.

In describing the collective behavior of the system, a ruler to measure its macroscopic feature was introduced. In our context, the Kuramoto order parameter is a perfect quantity to measure the degree of coherence of oscillator phases. For example, in the identical KS model in Sec. 2.3, the Kuramoto order parameter distinguishes between phase synchronization ($|\Gamma(t)|=1$) and the incoherent state ($|\Gamma(t)|=0$). In this measuring process, first of all, one has to obtain the microscopic information, i.e., $\{\phi_j(t)\}_{j=1}^N$ from the governing equations (2.34). Then, $\{\phi_j(t)\}_{j=1}^N$ can be substituted into the definition of the Kuramoto order parameter in Eq. (2.15). Can we think about the governing dynamics of the macroscopic observable? Can we find a governing equation of the order parameter? The Watanabe-Strogatz (WS) transformation [98, 99, 141] and Ott-Antonsen (OA) ansatz [96, 97, 142] give answers to such questions.

Below, we follow all the important steps of both the WS and the OA ansatz. A system of sinusoidally coupled oscillators is, in general, governed by

$$\partial_t \phi_j(t) = \omega + \mathrm{Im}\left[H(t)e^{-\mathrm{i}\phi_j(t)}\right] \tag{2.36}$$

for $j=1,\ldots,N$. Here, $H(t)$ could be any forcing function acting on an oscillator, e.g., it could determine the mean-field forcing like the Kuramoto order parameter. The Watanabe-Strogatz transformation is a time-dependent analytic automorphism of linear fractional transformation [100] onto the unit disk such that [95, 102]

$$e^{\mathrm{i}\phi_j(t)} = M_t(e^{\mathrm{i}\psi_j}) := e^{\mathrm{i}\Phi(t)}\frac{\rho(t)+e^{\mathrm{i}(\psi_j-\Psi(t))}}{1+\rho(t)e^{\mathrm{i}(\psi_j-\Psi(t))}} \tag{2.37}$$

for $j=1,\ldots,N$ where $\rho(t)\in[0,1)$, and $\Phi(t),\Psi(t)\in\mathbb{R}$. This transformation is equivalent to another form that reads

$$\tan\left(\frac{\phi_j(t)-\Phi(t)}{2}\right) = \frac{1-\rho(t)}{1+\rho(t)}\tan\left(\frac{\psi_j-\Psi(t)}{2}\right) \tag{2.38}$$

for $j = 1,...,N$ (for the detailed derivation between them, see Refs. [95, 102]). It is a one-parameter family of linear fractional transformations and its inverse maps the time-independent phases $\{\psi_j\}_{j=1}^N$ onto the time-dependent phase variables $\{\phi_j(t)\}_{j=1}^N$. In other words, the microscopic phases $\{\phi_j(t)\}_{j=1}^N$ are transformed to one time-dependent macroscopic radial variable $\rho(t) \in \mathbb{R}$ and two time-dependent macroscopic angular (or phase) variables $\Psi(t), \Phi(t) \in \mathbb{R}$ plus the time-independent microscopic constants of motion $\{\psi_j\}_{j=1}^N$. The constants of motion are determined by a given initial condition $\{\phi_j(0)\}_{j=1}^N$ with three constraints [99]. There are only $N-3$ independent constants of motion in $\{\psi_j\}_{j=1}^N$. Two of the constraints are imposed by

$$\frac{1}{N}\sum_{k=1}^{N}\cos\psi_k = \frac{1}{N}\sum_{k=1}^{N}\sin\psi_k = 0 \tag{2.39}$$

and the other one can be relatively freely chosen such as $\sum_{k=1}^N \psi_k = 0$ or $\sum_{k=1}^N \cos(2\psi_k) = 0$ [102]. We will explain why these constraints are imposed later in this section. After having introduced these three constraints, it is possible to determine $\phi_j(0)$ from the macroscopic variables $\rho(0), \Psi(0), \Phi(0)$ and ψ_j for $j = 1,...,N$, and vice versa.

To describe how the WS variables govern the macroscopic behavior of the system, we need to find the relation between the Kuramoto order parameter $\Gamma(t)$ and the macroscopic WS variables. Therefore, the WS transformation in Eq. (2.37) is substituted into the Kuramoto order parameter such that

$$\begin{aligned}\Gamma(t) &= \frac{1}{N}\sum_{k=1}^{N} e^{\mathrm{i}\phi_k(t)} = \frac{1}{N}\sum_{k=1}^{N} e^{\mathrm{i}\Phi(t)}\frac{\rho(t)+e^{\mathrm{i}(\psi_k-\Psi(t))}}{1+\rho(t)e^{\mathrm{i}(\psi_k-\Psi(t))}} \\ &= \rho(t)e^{\mathrm{i}\Phi(t)}\left(\frac{1}{N\rho(t)}\sum_{k=1}^{N}\frac{\rho(t)+e^{\mathrm{i}(\psi_k-\Psi(t))}}{1+\rho(t)e^{\mathrm{i}(\psi_k-\Psi(t))}}\right) =: \rho(t)e^{\mathrm{i}\Phi(t)}\gamma(\rho,\Psi)\end{aligned} \tag{2.40}$$

where $\gamma(\rho,\Psi) \in \mathbb{C}$ and $|\gamma| \leq 1$. This relation gives physical meanings of the macroscopic WS variables. The radial variable $\rho(t)$ and the angular variable $\Phi(t)$ act similarly (not exactly since $\gamma(\rho,\Psi)$) like the Kuramoto order parameter $\Gamma(t) = R(t)e^{\mathrm{i}\Theta(t)}$. As the modulus of the Kuramoto order parameter measures the degree of coherence of the oscillators, so does the WS radial variable. For $\rho = R = 0$, the completely incoherent state is captured while $\rho = R = 1$ indicates complete phase synchronization. Furthermore, $0 < \rho < 1$ represents partial coherence of the system although $\rho e^{\mathrm{i}\Phi}$ does not exactly coincide with the Kuramoto order parameter due to $\gamma(\rho,\Psi)$. The angular variable $\Phi(t)$ measures the mean phase value of the ensemble, just as $\Theta(t)$ does. The other angular variable $\Psi(t)$ characterizes how the individual oscillators behave with respect to $\Phi(t)$ [102]. Furthermore, the group action of the

Watanabe-Strogatz transformation in Eq. (2.37) gives an orbit partition of the phase space. The N-dimensional phase space now can be partitioned into a set of 3D invariant subspaces which are characterized by $N-3$ constants of motion determined by the initial condition. Hence, the reduced 3D macroscopic dynamics resides in the $(N-3)$-parameter family of invariant manifolds as long as the constants of motion are given [95, 99].

Our main task in this section is to find the governing equations for the Kuramoto order parameter. For this, we can obtain a hint from Eq. (2.40). The macroscopic WS variables $\rho(t)e^{i\Phi(t)}$ are linked to the Kuramoto order parameter $\Gamma(t) = R(t)e^{i\Theta(t)}$. Now, the task appears clear: If one can find (i) the governing equations for WS variables and (ii) some conditions where $\gamma = 1$ so that $\Gamma = \rho e^{i\Phi}$, then the WS variables exactly describe the dynamics of the Kuramoto order parameter. Below, we follow some steps that lead us to the governing equations of the WS variables and the conditions for $\gamma = 1$.

Following the steps reported in Ref. [99] and previously discussed in Ref. [56], we below obtain the governing equations of the WS variables. Starting with Eq. (2.38) and its time derivative, we obtain

$$\begin{aligned}
\frac{d}{dt}(\phi_j - \Phi) &= 2\frac{d}{dt}\left[\tan^{-1}\left(g\tan\left(\frac{\psi_j-\Psi}{2}\right)\right)\right] \\
&= \frac{2}{1+g^2\tan^2\left(\frac{\psi_j-\Psi}{2}\right)}\left[\dot{g}\tan\left(\frac{\psi_j-\Psi}{2}\right) + \frac{g}{\cos\left(\frac{\psi_j-\Psi}{2}\right)}\left(-\frac{1}{2}\dot{\Psi}\right)\right] \\
&= \frac{g}{\cos^2\left(\frac{\psi_j-\Psi}{2}\right)+g^2\sin^2\left(\frac{\psi_j-\Psi}{2}\right)}\left(\frac{\dot{g}}{g}\sin(\psi_j-\Psi) - \dot{\Psi}\right)
\end{aligned} \tag{2.41}$$

for $j = 1,\ldots,N$ and $g := \frac{1-\rho}{1+\rho} \in \mathbb{R}$. Using the trigonometric identity, the denominator can be written as

$$\begin{aligned}
\cos^2\left(\frac{\psi_j-\Psi}{2}\right) + g^2\sin^2\left(\frac{\psi_j-\Psi}{2}\right) &= \frac{1+\cos(\psi_j-\Psi)}{2} + g^2\frac{1-\cos(\psi_j-\Psi)}{2} \\
&= \frac{1+\rho^2}{(1+\rho)^2} + \frac{2\rho}{(1+\rho)^2}\cos(\psi_j-\Psi) \\
&= \frac{1+\rho^2+2\rho\cos(\psi_j-\Psi)}{(1+\rho)^2}
\end{aligned} \tag{2.42}$$

The time derivative of g is

$$\frac{\dot{g}}{g} = \frac{-\dot{\rho}(1+\rho)-\dot{\rho}(1-\rho)}{(1+\rho)^2}\frac{1+\rho}{1-\rho} = \frac{-2\dot{\rho}}{1-\rho^2}. \tag{2.43}$$

Substituting Eqs. (2.42-2.43) into Eq. (2.41), the phase velocity reads

$$\frac{d}{dt}\phi_j = \dot{\Phi} + \frac{1-\rho^2}{1+\rho^2+2\rho\cos(\psi_j-\Psi)}\left(\frac{-2\dot{\rho}}{1-\rho^2}\sin(\psi_j-\Psi) - \dot{\Psi}\right) \tag{2.44}$$

for $j = 1,...,N$. On the other hand, the same velocity is given by

$$\begin{aligned}\frac{d}{dt}\phi_j &= \omega + \mathrm{Im}\left[H(t)e^{-\mathrm{i}\phi_j}\right] \\ &= \omega + \frac{1}{2\mathrm{i}}\left(He^{-\mathrm{i}\phi_j} - \overline{H}e^{\mathrm{i}\phi_j}\right) \\ &= \omega - \sin\phi_j\,\mathrm{Re}H + \cos\phi_j\,\mathrm{Im}H\end{aligned} \tag{2.45}$$

for $j = 1,...,N$. To compare these two equations, we need to describe $(\cos\phi_j, \sin\phi_j)^\top$ in terms of the macroscopic WS variables. To do so, we use Eq. (2.37), and obtain

$$\begin{aligned}e^{\mathrm{i}(\phi_j-\Phi)} &= \cos(\phi_j-\Phi) + \mathrm{i}\sin(\phi_j-\Phi) \\ &= \frac{2\rho+(1+\rho^2)\cos(\psi_j-\Psi)}{1+\rho^2+2\rho\cos(\psi_j-\Psi)} + \mathrm{i}\frac{(1-\rho^2)\sin(\psi_j-\Psi)}{1+\rho^2+2\rho\cos(\psi_j-\Psi)}\end{aligned} \tag{2.46}$$

for $j = 1,...,N$. Now, we can express $(\cos\phi_j, \sin\phi_j)^\top$ in terms of the WS variables

$$\begin{pmatrix}\cos\phi_j \\ \sin\phi_j\end{pmatrix} = \frac{1}{1+\rho^2+2\rho\cos(\psi_j-\Psi)}\begin{pmatrix}-\sin\Phi & \cos\Phi \\ \cos\Phi & \sin\Phi\end{pmatrix}\begin{pmatrix}(1-\rho^2)\sin(\psi_j-\Psi) \\ 2\rho+(1+\rho^2)\cos(\psi_j-\Psi)\end{pmatrix}. \tag{2.47}$$

From the last equation, the meaning of the three constraints on the constants of motion becomes clear. For $\rho = 0$, the completely incoherent state occurs as $\Gamma = 0$ in Eq. (2.40). The complete incoherence is characterized by Eq. (2.29). Furthermore, at $\rho = 0$, Equation (2.47) reads

$$\begin{aligned}\cos\phi_j &= -\sin\Phi\sin(\psi_j-\Psi) + \cos\Phi\cos(\psi_j-\Psi) = \cos(\psi_j-\Psi+\Phi) \\ \sin\phi_j &= \cos\Phi\sin(\psi_j-\Psi) + \sin\Phi\cos(\psi_j-\Psi) = \sin(\psi_j-\Psi+\Phi)\end{aligned} \tag{2.48}$$

for $j = 1,...,N$. Substituting this into Eq. (2.29), one recovers the constraints on the constants of motion as in Eq. (2.39). The third constraint tells the relation between the constants of motion and Ψ in a rather arbitrary way [102]. Inserting Eq. (2.47) into Eq. (2.45) and then

comparing Eq. (2.45) to Eq. (2.44), we obtain

$$\begin{aligned}
&\dot{\Phi}\Big(1+\rho^2+2\rho\cos(\psi_j-\Psi)\Big)+(1-\rho^2)\left(\frac{-2\dot{\rho}}{1-\rho^2}\sin(\psi_j-\Psi)-\dot{\Psi}\right)\\
&=\omega\Big(1+\rho^2+2\rho\cos(\psi_j-\Psi)\Big)\\
&\quad-\mathrm{Re}H\Big[(1-\rho^2)\cos\Phi\sin(\psi_j-\Psi)+2\rho\sin\Phi+(1+\rho^2)\sin\Phi\cos(\psi_j-\Psi)\Big]\\
&\quad+\mathrm{Im}H\Big[-(1-\rho^2)\sin\Phi\sin(\psi_j-\Psi)+2\rho\cos\Phi+(1+\rho^2)\cos\Phi\cos(\psi_j-\Psi)\Big] \qquad (2.49)
\end{aligned}$$

Arranging then both sides with respect to the linearly independent functions $\{1,\sin(\psi_j-\Psi),\cos(\psi_j-\Psi)\}$, the three governing equations for the macroscopic WS variables are obtained in the form of [102]

$$\begin{aligned}
\partial_t\rho(t)&=\frac{1-\rho^2}{2}\mathrm{Re}\Big[H(t)e^{-\mathrm{i}\Phi}\Big]\\
\partial_t\Psi(t)&=\frac{1-\rho^2}{2\rho}\mathrm{Im}\Big[H(t)e^{-\mathrm{i}\Phi}\Big]\\
\partial_t\Phi(t)&=\omega+\frac{1+\rho^2}{2\rho}\mathrm{Im}\Big[H(t)e^{-\mathrm{i}\Phi}\Big]. \qquad (2.50)
\end{aligned}$$

Furthermore, these equations can be rewritten by introducing $z(t):=\rho(t)e^{\mathrm{i}\Phi(t)}$ and $\xi(t):=\Phi(t)-\Psi(t)$ as

$$\begin{aligned}
\partial_t z(t)&=\mathrm{i}\omega z+\frac{1}{2}H(t)-\frac{1}{2}z^2\overline{H(t)}\\
\partial_t\xi(t)&=\omega+\mathrm{Im}\Big[\bar{z}H(t)\Big]. \qquad (2.51)
\end{aligned}$$

So far, we have done the first task, i.e., finding the governing equations for the WS variables. Next, to complete our task, we need to find the condition for which $\gamma(\rho,\Psi)$ is unity.

Up to now, the constants of motion, after being defined with three constraints, did not take any role in the description. Now we consider them more closely. In Eq. (2.40), γ depends on the constants of motion $\{\psi_j\}_{j=1}^N$. How do they affect the macroscopic dynamics? Let us play with the definition of γ. Using the geometric series expansion, we can write [101]

$$\gamma=\frac{1}{N}\sum_{k=1}^{N}\frac{1+\rho^{-1}e^{\mathrm{i}(\psi_k-\Psi)}}{1+\rho e^{\mathrm{i}(\psi_k-\Psi)}}=1+(1-\rho^{-2})\sum_{l=2}^{\infty}C_l(-\rho e^{\mathrm{i}\Psi})^l \qquad (2.52)$$

where $C_l := \frac{1}{N}\sum_{k=1}^{N} e^{il\psi_k}$ with $C_1 = 0$ due to the constraints on the constant of motion. Note that γ is written as a sum of 1 plus an additional term. This additional term vanishes as long as $C_l = 0$ for all $l \geq 2$. Taking a close look at C_l, it depends on the structure (distribution) of the constants of motion since it is defined as the l-th Daido order parameter on the constants of motion [143]. Therefore, in order for C_l to be zero for some l's, we first consider *uniformly distributed* constants of motion that make $|C_l| = 1$ and $\arg C_l = \psi_1 l$ for $l = N, 2N, \ldots$ and $C_l = 0$ otherwise [102]. Assuming uniformly distributed constants of motion $\{\psi_j = -\pi + 2\pi\frac{j-1}{N}\}_{j=1}^{N}$ leads us to

$$\gamma = 1 + (1-\rho^{-2})\sum_{l=2}^{\infty} C_l(-\rho e^{\mathrm{i}\Psi})^l = 1 + (1-\rho^{-2})\frac{[-\rho e^{\mathrm{i}(\psi_1-\Psi)}]^N}{1-[-\rho e^{\mathrm{i}(\psi_1-\Psi)}]^N}. \tag{2.53}$$

The second term gives rise to an oscillation of the Kuramoto order parameter and it goes to zero as $N \to \infty$ since $\rho < 1$ [55]. Thus, we obtain the condition for which we are looking: *uniformly distributed constants of motion in the thermodynamic limit*, i.e., $N \to \infty$.

Under the two conditions, i.e., (i) uniformly distributed constants of motion and (ii) the thermodynamic limit, the Kuramoto order parameter reads

$$\Gamma(t) := r(t)e^{\Theta(t)} = \rho(t)e^{\mathrm{i}\Phi(t)} =: z(t) \tag{2.54}$$

and $z(t)$ is governed by Eq. (2.51). We will call the manifold where this condition holds the *Ott-Antonsen manifold* [102, 95].

What does this manifold mean for the behavior of our phase oscillators? In the thermodynamic limit with the conservation of the number of oscillators, the governing equation of the system is the continuity equation of the phase density function $f(\phi,t)$ in terms of the continuous variable ϕ. Here, the constants of motion are also read as continuous parameters ψ. We already considered the thermodynamic limit. So, we assume uniform distribution of constants of motion $d\mu(\psi) = \frac{1}{2\pi}d\psi$ together with the Watanabe-Strogatz transformation $\phi = T(\psi) := -\mathrm{i}\log M_t(e^{i\psi})$ for a fixed t [95]. This transformation pushes-forward a measure μ to $T_*\mu$. Therefore, $d(T_*\mu)(\phi) = f(\phi)d\phi$ where the phase density function

$$\begin{aligned} f(\phi) &:= \frac{1}{2\pi}\partial_\phi T^{-1}(\phi) = \frac{1}{2\pi}\frac{1-\rho^2}{1-2\rho\cos(\phi-\Phi)+\rho^2} \\ &= \frac{1}{2\pi}\frac{1-|z|^2}{1-2|z|\cos(\phi-\arg z)+|z|^2} \end{aligned} \tag{2.55}$$

is the normalized Poisson kernel [95]. Note that $z(t) = \rho(t)e^{\mathrm{i}\Phi(t)}$. This fact reveals that the oscillators' phases are distributed according to the Poisson kernel in the OA manifold [62].

In fact, the Poisson kernel interprets the Kuramoto order parameter in the thermodynamic limit as

$$\begin{aligned}\Gamma(t) &= \int_{\mathbb{T}} M_t(e^{\mathrm{i}\psi}) d\mu(\psi) = \int_{\mathbb{T}} e^{\mathrm{i}\phi} d(T_*\mu)(\phi) \\ &= \int_{\mathbb{T}} e^{\mathrm{i}\phi} \frac{1}{2\pi} \frac{1-|\rho|^2}{1-2|\rho|\cos(\phi-\Phi)+|\rho|^2} d\phi \\ &= \rho(t) e^{\mathrm{i}\Phi(t)} = z(t). \end{aligned} \tag{2.56}$$

This also reveals that the macroscopic behavior (i.e, the dynamics of the Kuramoto order parameter) of the system is equivalent to the dynamics of the WS (or OA) variables in the Ott-Antonsen manifold [102, 95].

To characterize the Ott-Antonsen manifold further, we again consider the continuity equation

$$\frac{\partial}{\partial t} f(\phi,t) + \frac{\partial}{\partial \phi}\Big(f(\phi,t) v(\phi,t) \Big) = 0 \tag{2.57}$$

where the continuous velocity reads

$$v(\phi,t) := \omega + \mathrm{Im}\Big[H(t) e^{-\mathrm{i}\phi} \Big] \tag{2.58}$$

Then, the phase density function, which is 2π-periodic in ϕ, is Fourier-expanded

$$f(\phi,t) = \frac{1}{2\pi}\Big[1 + \sum_{n=1}^{\infty} \big(a_n(t) e^{-\mathrm{i}n\phi} + c.c. \big) \Big] \tag{2.59}$$

where $c.c.$ stands for the complex conjugate. Note that we need to investigate infinitely many Fourier coefficients, i.e., $\{a_n(t)\}_{n\in\mathbb{N}}$. The Fourier coefficient in this case is nothing but the n-th Daido order parameter [143] in the thermodynamic limit which is defined by

$$\Gamma_n(t) := \int_{-\pi}^{\pi} f(\phi,t) e^{\mathrm{i}n\phi} d\phi = a_n(t) \tag{2.60}$$

where $n \in \mathbb{N}$ and its finite-sized version is $\Gamma_n(t) := \frac{1}{N}\sum_{k=1}^{N} e^{\mathrm{i}n\phi_k(t)}$. The Kuramoto order parameter is $\Gamma(t) = \Gamma_1(t)$. Substituting Eq. (2.59) into the continuity equation, one obtains [102]

$$\partial_t \Gamma_n(t) = \mathrm{i}\omega\Gamma_n(t) + \frac{n}{2} H(t)\Gamma_{n-1}(t) - \frac{n}{2}\overline{H(t)}\Gamma_{n+1}(t) \tag{2.61}$$

for $n \in \mathbb{N}$. The dynamics of the Kuramoto order parameter and the Daido order parameters are governed by infinitely many equations [77]. Nevertheless, the difficulty can be lifted using the conditions on the distribution of constants of motion. First, we use the finite-sized

system for the sake of simplicity. The Daido order parameter can be written in terms of the WS variables. It then follows [144]

$$\begin{aligned}\Gamma_n(t) &:= \frac{1}{N}\sum_{k=1}^{N} e^{\mathrm{i}n\phi_k(t)} = \rho^n(t)e^{\mathrm{i}n\Phi(t)}\frac{1}{N}\sum_{k=1}^{N}\left(\frac{1+\rho^{-1}e^{\mathrm{i}(\psi_k-\Psi)}}{1+\rho e^{\mathrm{i}(\psi_k-\Psi)}}\right)^n \\ &=: \rho^n(t)e^{\mathrm{i}n\Phi(t)}\gamma_n(\rho,\Psi) = z^n\gamma_n \end{aligned} \tag{2.62}$$

where $z(t) = \rho(t)e^{\mathrm{i}\Phi(t)}$. The uniform distribution of constants of motion gives $\gamma_n = 1$, and then leads to $\Gamma_n = z^n = \Gamma^n$ for all n. In the thermodynamic limit with uniformly distributed constants of motion $d\mu(\psi) = \frac{1}{2\pi}d\psi$, this can be written as

$$\begin{aligned}\Gamma_n(t) &= \rho^n(t)e^{\mathrm{i}n\Phi(t)}\int_{-\pi}^{\pi}\left(\frac{1+\rho^{-1}e^{\mathrm{i}(\psi-\Psi)}}{1+\rho e^{\mathrm{i}(\psi-\Psi)}}\right)^n\frac{1}{2\pi}d\psi \\ &= \rho^n(t)e^{\mathrm{i}n\Phi(t)}\int_{-\pi}^{\pi}\left(1+\rho^{-1}e^{\mathrm{i}(\psi-\Psi)}\right)^n\left[1+\sum_{l=1}^{\infty}\left(-\rho e^{\mathrm{i}(\psi-\Psi)}\right)^l\right]^n\frac{1}{2\pi}d\psi \\ &= \rho^n(t)e^{\mathrm{i}n\Phi(t)} = z^n(t)\end{aligned} \tag{2.63}$$

where we used $\int_{-\pi}^{\pi}e^{\mathrm{i}k\psi}\frac{1}{2\pi}d\psi = 0$ for $k \in \mathbb{Z}\setminus\{0\}$. Consequently, for a uniform distribution of the constants of motion, the Daido order parameter is nothing but the n-th power of the Kuramoto order parameter:

$$\Gamma_n(t) = z^n(t) = \Gamma^n(t) \tag{2.64}$$

and all the Fourier coefficients (higher Daido order parameters) in Eq. (2.59) can be written in terms of the first coefficient (Kuramoto order parameter):

$$a_n(t) = z^n(t) = \Gamma^n(t) \tag{2.65}$$

for $n \in \mathbb{N}$. Furthermore, the infinitely many equations in Eq. (2.61) can be reduced to just one equation

$$\begin{aligned}\partial_t\Gamma(t) &= \mathrm{i}\omega\Gamma(t) + \frac{1}{2}H(t) - \frac{1}{2}\Gamma^2(t)\overline{H(t)} \quad \text{or} \\ \partial_t z(t) &= \mathrm{i}\omega z(t) + \frac{1}{2}H(t) - \frac{1}{2}z^2(t)\overline{H(t)}.\end{aligned} \tag{2.66}$$

The invariant manifold defined by Eq. (2.65), i.e., $\{a_n(t) = \Gamma^n(t)\}_{n\in\mathbb{N}}$, is called *Ott-Antonsen manifold* and Eq. (2.66) is called *Ott-Antonsen equation* [96, 97]. Note that this equation is

exactly the same as the first equation of Eqs. (2.51), and in the OA manifold where $\gamma = 1$, the second equation of Eq. (2.51) is irrelevant since it is decoupled from $z(t)$ [144]. Furthermore, the Ott-Antonsen equation can be written in a closed form as long as the forcing $H(t)$ is represented in terms of $z(t)$, i.e., depends on the Kuramoto order parameter (the mean-field forcing) [72].

Finally, the Ott-Antonsen ansatz (Eq. (2.65)) also leads to the normalized Poisson kernel for the phase distribution [96, 97]:

$$\begin{aligned} f(\phi,t) &= \frac{1}{2\pi}\left[1+\sum_{n=1}^{\infty}\left(a_n(t)e^{-in\phi}+c.c.\right)\right] \\ &= \frac{1}{2\pi}\left[1+\sum_{n=1}^{\infty}\left(z^n(t)e^{-in\phi}+c.c.\right)\right] = \frac{1}{2\pi}\frac{1-|z|^2}{1-2|z|\cos(\phi-\arg z)+|z|^2} \end{aligned} \tag{2.67}$$

for $|z|<1$. Thus, for the (partially) incoherent states, the oscillators are distributed according to the normalized Poisson kernel peaked around $\arg z(t)$. Note that as $|z| \to 1^-$, the phase distribution becomes $f(\phi,t) = \delta(\phi - \arg z)$, and then all the oscillators have the same phase value as $\arg z(t)$ [95].

2.4.1 The Identical Kuramoto-Sakaguchi Model Revisited

In this section, we apply the WS and OA ansatz to a familiar example, the identical Kuramoto-Sakaguchi phase oscillator ensembles from Sec. 2.3. The system reads

$$\partial_t \phi_j(t) = \omega + \mathrm{Im}\left[\Gamma(t)e^{-\mathrm{i}\phi_j(t)}e^{-i\alpha}\right], \quad j = 1,\ldots,N \tag{2.68}$$

where $\Gamma(t) := \frac{1}{N}\sum_{k=1}^{N} e^{\mathrm{i}\phi_k(t)}$ is the Kuramoto order parameter and $\alpha \in [0,2\pi]$ is the phase-lag parameter. Each oscillator is affected by the common mean-field forcing $H(t) := \Gamma(t)e^{-\mathrm{i}\alpha}$, and the governing equation can equivalently be expressed as

$$\partial_t \phi_j(t) = \omega + \mathrm{Im}\left[H(t)e^{-\mathrm{i}\phi_j(t)}\right] \tag{2.69}$$

for $j = 1,\ldots,N$. Here, it is apparent that each oscillator depends only on the mean-field coupling through the Kuramoto order parameter; the dependence on its own index j appears only through the first harmonics $e^{\pm\mathrm{i}\phi_j}$. It is the sinusoidally coupled system.

For the identical Kuramoto-Sakaguchi phase oscillators, the mean-field forcing $H(t) = \Gamma(t)e^{-\mathrm{i}\alpha}$ is already written in terms of the Kuramoto order parameter $\Gamma(t)$, which is not in

general the case. Therefore, the OA equation in Eq. (2.66) is written in a closed form as

$$\begin{aligned}\partial_t z(t) &= \mathrm{i}\omega z + \frac{1}{2}\Gamma e^{-\mathrm{i}\alpha} - \frac{1}{2}z^2\overline{\Gamma}e^{\mathrm{i}\alpha} \\ &= \mathrm{i}\omega z + \frac{1}{2}ze^{-\mathrm{i}\alpha} - \frac{1}{2}|z|^2 ze^{\mathrm{i}\alpha}.\end{aligned} \tag{2.70}$$

This equation governs the dynamics of the Kuramoto order parameter, and can be solved easily. Let us study the magnitude of the order parameter, which sufficiently characterizes the order parameter behavior. The magnitude dynamics reads

$$\partial_t |z|^2 = z\frac{d\overline{z}}{dt} + \overline{z}\frac{dz}{dt} = |z|^2(1-|z|^2)\cos\alpha. \tag{2.71}$$

Putting $r(t) = |z(t)|^2$, we obtain a simple ODE that reads

$$\partial_t r = r(1-r)\cos\alpha. \tag{2.72}$$

There are two fixed points $r_* = 0$ and $r^* = 1$, which correspond to the completely incoherent state and the fully synchronized state, respectively. The linear stability of the state is easily obtained: If $\cos\alpha < 0$ ($\alpha > \pi/2$), then r_* is stable whereas r^* is unstable. However, r_* becomes unstable and r^* stable when $\cos\alpha > 0$, i.e., $\alpha < \frac{\pi}{2}$. This result is consistent with the finite-sized system result that we discussed in Sec. 2.3.

Furthermore, recall that when the linear stability analysis was performed for the splay state, we found many neutrally stable directions. According to the WS transformation, there are $N-3$ constants of motion that give rise to $N-3$ neutrally stable directions. As we already discussed, for large enough N, there are many ways to give a completely incoherent state. The core of them is a splay state. Both the splay state and all the other incoherent states should satisfy $\Gamma = 0$. Then, the phase space of the incoherent states characterized by $\Gamma = 0$ consists of the $(N-3)$-parameter family of invariant subspaces (characterized by $N-3$ constants of motion). Each of them corresponds to a realization of the incoherent states. The perturbations among these $N-3$ subspaces give rise to $N-3$ neutrally stable directions [99]. On the other hand, the synchronized state can be represented only in one way, i.e., $\phi_j = \text{const.}$, except for the phase shift invariance, for $j = 1, ..., N$. Thus, the synchronization takes a role of a hinge at which all the invariant subspaces of the incoherent states meet [99]. Hence, there is only one perturbation within the synchronization manifold (phase shift invariance along the sync manifold) and no further neutrally stable directions exist. Again, the Benjamin-Feir instability occurs at $\alpha_{\mathrm{BF}} = \frac{\pi}{2}$.

2.4.2 System of Coupled Oscillators in a Network of Networks

Thus far we have taken a look at the description of the system's macroscopic motion for a single network of globally coupled Kuramoto-Sakaguchi phase oscillators. In this section, we introduce a set of such populations, *a network of networks*, and give a general description of the system based on the WS and OA ansatz. In the following chapters, we will discuss chimera states in this network of networks as the main theme of the thesis.

The governing equations are [101, 102]

$$\begin{aligned}
\partial_t \phi_j^{(a)} &= \omega_a + \mathrm{Im}\left[H_a(t)e^{-\mathrm{i}\phi_j^{(a)}}\right], \\
H_a(t) &:= \sum_{b=1}^{M} G_{ab}\Gamma_b(t)e^{-\mathrm{i}\alpha}, \\
\Gamma_a(t) &= R_a(t)e^{\mathrm{i}\Theta_a(t)} := \frac{1}{N}\sum_{k=1}^{N} e^{\mathrm{i}\phi_k^{(a)}(t)}
\end{aligned} \tag{2.73}$$

for $j = 1,...,N$ and for $a,b = 1,...,M$ where M is the number of populations and N is the number of oscillators in each population (same for all the populations). Also, G_{ab} is a coupling strength matrix between populations and Γ_a denotes the Kuramoto order parameter within the individual populations. Equation (2.73) describes the system of sinusoidally coupled oscillators in a network of networks, and hence we exploit the WS and OA dimension reduction methods to investigate the macroscopic dynamics of the entire system. Note that each subpopulation only includes identical oscillators whose natural frequencies are the same as ω_a within the population but they might have different values for the different populations [101]. For a finite number of populations, the population index takes a role as a discrete parameter. We first consider the Watanabe-Strogatz transformation for each population such that [101]

$$\tan\left(\frac{\phi_j^{(a)}(t) - \Phi_a(t)}{2}\right) = \frac{1-\rho_a(t)}{1+\rho_a(t)}\tan\left(\frac{\psi_j^{(a)} - \Psi_a(t)}{2}\right) \tag{2.74}$$

for $j = 1, ..., N$ and $a = 1, ..., M$. Then, the macroscopic WS variables of each population are governed by [102]

$$\begin{aligned}
\partial_t \rho_a &= \frac{1-\rho_a}{2} \mathrm{Re}\left[H_a e^{-\mathrm{i}\Phi_a} \right] \\
\partial_t \Psi_a &= \frac{1-\rho_a^2}{2\rho_a} \mathrm{Im}\left[H_a e^{-\mathrm{i}\Phi_a} \right] \\
\partial_t \Phi_a &= \omega_a + \frac{1+\rho_a^2}{2\rho_a} \mathrm{Im}\left[H_a e^{-\mathrm{i}\Phi_a} \right]
\end{aligned} \tag{2.75}$$

for $a = 1, ..., M$ with constants of motion $\{\psi_j^{(a)}\}_{j=1}^N$ for $a = 1, ..., M$ with constraints discussed previously. In other forms, these equations are written as [144]

$$\begin{aligned}
\partial_t z_a &= \mathrm{i}\omega_a z_a + \frac{1}{2} H_a - \frac{1}{2} z_a^2 \overline{H_a}, \\
\partial_t \xi_a &= \omega_a + \mathrm{Im}\left[\overline{z_a} H_a \right]
\end{aligned} \tag{2.76}$$

where $z_a = \rho_a e^{\mathrm{i}\Phi_a}$ and $\xi_a = \Phi_a - \Psi_a$ for $a = 1, ..., M$. As we discussed in Sec. 2.4, the WS transformation gives the relation between the Kuramoto order parameter and the WS variables, which reads

$$\Gamma_a(t) = \rho_a(t) e^{\mathrm{i}\Phi_a(t)} \gamma_a(\rho_a, \Psi_a; t) \tag{2.77}$$

where γ_a is defined by

$$\begin{aligned}
\gamma_a &= \frac{1}{\rho_a}(\zeta_a + \mathrm{i}\eta_a) \\
&:= \frac{1}{\rho_a N} \sum_{k=1}^{N} \frac{2\rho_a + (1+\rho_a^2)\cos(\psi_k^{(a)} - \Psi_a)}{1 + 2\rho_a \cos(\psi_k^{(a)} - \Psi_a) + \rho_a^2} + \mathrm{i} \frac{1}{\rho_a N} \sum_{k=1}^{N} \frac{(1-\rho_a^2)\sin(\psi_k^{(a)} - \Psi_a)}{1 + 2\rho_a \cos(\psi_k^{(a)} - \Psi_a) + \rho_a^2}
\end{aligned} \tag{2.78}$$

where $\zeta_a = \mathrm{Re}\gamma_a$ and $\eta_a = \mathrm{Im}\gamma_a$ for $a = 1,...,M$. Using the above equations, we can rewrite Eq. (2.126) as [101, 102, 74]

$$\begin{aligned}
\partial_t \rho_a &= \frac{1-\rho_a^2}{2} \sum_{a'=1}^{M} G_{aa'} \big(\zeta_{a'} \cos(\Phi_{a'} - \Phi_a - \alpha) - \eta_{a'} \sin(\Phi_{a'} - \Phi_a - \alpha) \big), \\
\partial_t \Psi_a &= \frac{1-\rho_a^2}{2\rho_a} \sum_{a'=1}^{M} G_{aa'} \big(\zeta_{a'} \sin(\Phi_{a'} - \Phi_a - \alpha) + \eta_{a'} \cos(\Phi_{a'} - \Phi_a - \alpha) \big), \\
\partial_t \Phi_a &= \omega_a + \frac{1+\rho_a^2}{2\rho_a} \sum_{a'=1}^{M} G_{aa'} \big(\zeta_{a'} \sin(\Phi_{a'} - \Phi_a - \alpha) + \eta_{a'} \cos(\Phi_{a'} - \Phi_a - \alpha) \big)
\end{aligned} \tag{2.79}$$

for $a = 1,...,M$.

In Sec. 2.4, we showed that the OA dynamics assumes that the following two conditions are met: (i) uniform constants of motion $\psi_j^{(a)} = -\pi + \frac{2\pi(j-1)}{N}$ for $j = 1,...,N$, and (ii) the thermodynamic limit $N \to \infty$. Under these conditions, the Kuramoto order parameter is exactly described by $\Gamma_a(t) = \rho_a(t) e^{i\Phi_a(t)}$ since $\gamma_a = 1$ for $a = 1,...,M$ and the governing equations of the OA variables read [88, 101, 102]

$$\begin{aligned}
\partial_t \rho_a &= \frac{1-\rho_a^2}{2} \sum_{a'=1}^{M} G_{aa'} \rho_{a'} \cos(\Phi_{a'} - \Phi_a - \alpha), \\
\partial_t \Phi_a &= \omega_a + \frac{1+\rho_a^2}{2\rho_a} \sum_{a'=1}^{M} G_{aa'} \rho_{a'} \sin(\Phi_{a'} - \Phi_a - \alpha)
\end{aligned} \tag{2.80}$$

for $a = 1,...,M$. These equations are equivalent to

$$\partial_t z_a(t) = \mathrm{i}\omega_a z_a + \frac{1}{2} H_a(t) - \frac{1}{2} z_a^2 \overline{H_a(t)} \tag{2.81}$$

for $a = 1,...,M$. Here, the forcing fields read

$$\begin{aligned}
H_a(t) &:= e^{-\mathrm{i}\alpha} \sum_{a'=1}^{m} G_{aa'} \Gamma_{a'} = e^{-\mathrm{i}\alpha} \sum_{a'=1}^{M} G_{aa'} \int_{\mathbb{T}} f_{a'}(\phi^{(a')}, t) e^{\mathrm{i}\phi^{(a')}} d\phi^{(a')} \\
&= e^{-\mathrm{i}\alpha} \sum_{a'=1}^{m} G_{aa'} z_{a'} = e^{-\mathrm{i}\alpha} \sum_{a'=1}^{m} G_{aa'} \rho_{a'} e^{\mathrm{i}\Phi_{a'}}
\end{aligned} \tag{2.82}$$

for $a = 1,...,M$ where $f_a(\phi^{(a)}, t)$ is the phase distribution function for each population, which follows the normalized Poisson kernel.

2.5 System of Generalized Kuramoto Oscillators

Thus far, we have discussed the collective behavior of systems of identical Kuramoto-Sakaguchi oscillators. The investigation of them relied on the utilization of dimension reduction methods such as the Watanabe-Strogatz transformation [98, 99, 95] and the Ott-Antonsen ansatz [96, 97]. These methods were applicable since the Kuramoto oscillator systems are sinusoidally coupled phase oscillators defined on the unit circle in $\mathbb{C}^1$ or $\mathbb{R}^2$. In recent developments, the Kuramoto phase oscillators have been extended to the so-called generalized Kuramoto oscillators [145–150]. In these models, each oscillator is represented by a unit vector defined on the surface of a higher-dimensional unit sphere. Dimension reduction methods like the OA or the WS ansatz, which we discussed in Sec. 2.4, also have been developed and employed to study the collective dynamics of these higher-dimensional oscillators [151–157, 104]. In this section, we present some theoretical principles for ensembles of generalized Kuramoto-Sakaguchi oscillators. Likewise, we review the dimension reduction method, i.e., the generalized Watanabe-Strogatz transformation as a vector form of a linear fractional transformation. This projection map provides a way for the investigation of the macroscopic dynamics of the vector oscillator system in the thermodynamic limit, considering both real ($\mathbb{R}^M$) and complex ($\mathbb{C}^M$) spaces. Later on, in Chap. 6, we will investigate the chimera states of generalized Kuramoto-Sakaguchi oscillators in two-population networks.

2.5.1 Identical Generalized Kuramoto-Sakaguchi Oscillator Ensemble

The system of Kuramoto-Sakaguchi oscillators (2.68) defined on a unit circle in $\mathbb{C}^1$ or $\mathbb{R}^2$ has a sinusoidal form and therefore can be extended to a system of generalized Kuramoto oscillators. In this higher-dimensional model, the oscillators are defined on the surface of a unit sphere in M-dimensional real and complex spaces, respectively [104]. To get a brief glimpse of this, we can write Eq. (2.68) with an appropriate time rescaling as

$$\begin{aligned}\partial_t e^{\mathrm{i}\phi_j} &= \mathrm{i}\dot{\phi}_j e^{\mathrm{i}\phi_j} = \mathrm{i}\omega e^{\mathrm{i}\phi_j} + 2\mathrm{i}e^{\mathrm{i}\phi_j}\mathrm{Im}\left[H(t)e^{-\mathrm{i}\phi_j}\right] \\ &= \mathrm{i}\omega e^{\mathrm{i}\phi_j} + e^{\mathrm{i}\phi_j}\left(H(t)e^{-\mathrm{i}\phi_j} - \overline{H(t)}e^{\mathrm{i}\phi_j}\right) = -e^{\mathrm{i}\phi_j}\overline{H(t)}e^{\mathrm{i}\phi_j} + \mathrm{i}\omega e^{\mathrm{i}\phi_j} + H(t) \qquad (2.83)\end{aligned}$$

The contents of this section were in part published previously in S. Lee and K. Krischer, J. Phys. A: Math. Theor. **56**, 405001 (2023) [58]. All figures and their captions are reproduced from those in it.

for $j = 1,...,N$. Let us take $e^{\mathrm{i}\phi_j(t)} \in \mathbb{C}^1 \mapsto \boldsymbol{x}_j(t) \in \mathbb{K}^M$ with a constraint $\boldsymbol{x}_j(t)^\dagger \boldsymbol{x}_j(t) = \langle \boldsymbol{x}_j(t) | \boldsymbol{x}_j(t) \rangle = 1$ for all t and $j = 1,...,N$ where $\mathbb{K} = \mathbb{R}$ or $\mathbb{C}$ is a ground field, and $\dagger$ denotes a Hermitian adjoint [158]. Then, one can treat $\boldsymbol{x}_j(t)$ as a unit vector oscillator defined on the surface of the unit sphere denoted by $\mathbb{S}^M := \{\boldsymbol{x} \in \mathbb{K}^M | \boldsymbol{x}^\dagger \boldsymbol{x} = 1\}$ either for $\mathbb{K} = \mathbb{R}$ or $\mathbb{C}$. Then one can assume that the oscillator $\boldsymbol{x}_j$ is governed by

$$\partial_t \boldsymbol{x}_j = -\boldsymbol{x}_j \boldsymbol{H}^\dagger \boldsymbol{x}_j + \Omega \boldsymbol{x}_j + \boldsymbol{H} \tag{2.84}$$

for $j = 1,...,N$. Here, the mean-field forcing $\boldsymbol{H}(t) \in \mathbb{K}^M$ generally can be any arbitrary vector that characterizes an external forcing function or the global (mean-field) coupling of the system corresponding to $H(t)$ in Eq. (2.83). Also, $\Omega \in \mathbb{K}^{M\times M}$, corresponding to $\mathrm{i}\omega$ in Eq. (2.83), with $\Omega^\dagger = -\Omega$ is an anti-hermitian natural frequency matrix that we will set to zero throughout this thesis. In this system, the Kuramoto order parameter serves as the center of mass of the oscillators on $\mathbb{S}^M$, which is defined by

$$\boldsymbol{\Gamma}(t) := \frac{1}{N} \sum_{k=1}^{N} \boldsymbol{x}_k(t) \in \mathbb{K}^M. \tag{2.85}$$

In Ref. [104], the generalized Watanabe-Strogatz transformation[14] was introduced as a vector form of a linear fractional transformation, defined by

$$\boldsymbol{x}_j(t) = M_t(\boldsymbol{x}_{0,j}) := \frac{\boldsymbol{A}\boldsymbol{x}_{0,j} + \boldsymbol{\psi}}{\boldsymbol{\psi}^\dagger \boldsymbol{A}\boldsymbol{x}_{0,j} + 1} \tag{2.86}$$

for $j = 1,...,N$ where $\boldsymbol{A}(t) \in \mathbb{K}^{M\times M}$ and $\boldsymbol{\psi}(t) \in \mathbb{K}^M$ are the WS variables that describe the macroscopic dynamics of the system. In this context, the initial conditions $\boldsymbol{x}_j(0) =: \boldsymbol{x}_{0,j}$ act as the constants of motion. Furthermore, the WS variable $\boldsymbol{\psi}$ characterizes the degree of coherence of the oscillators on the unit sphere, as similar to the Kuraomto order parameter in Eq. (2.85). To see this, consider

$$\boldsymbol{\Gamma} = \frac{1}{N} \sum_{k=1}^{N} \boldsymbol{x}_k = \frac{1}{N} \sum_{k=1}^{N} \frac{\boldsymbol{A}\boldsymbol{x}_{0,k} + \boldsymbol{\psi}}{\boldsymbol{\psi}^\dagger \boldsymbol{A}\boldsymbol{x}_{0,k} + 1} \tag{2.87}$$

If $|\boldsymbol{\psi}| = 1$, Equation (2.87) gives $\boldsymbol{\psi}^\dagger \boldsymbol{\Gamma} = 1$, i.e., $|\boldsymbol{\Gamma}| = 1$ (synchronization). On the other hand, if $\boldsymbol{\psi} = \boldsymbol{0}$, we obtain

$$\boldsymbol{\Gamma} = \boldsymbol{A}\left(\frac{1}{N} \sum_{k=1}^{N} \boldsymbol{x}_{0,k}\right) = 0 \quad \text{(completely incoherent)} \tag{2.88}$$

[14] For more details, see Ref. [159].

provided that the initial conditions are distributed uniformly on $\mathbb{S}^M$ ensuring $\frac{1}{N}\sum_{k=1}^{N}\boldsymbol{x}_{0,k}=\boldsymbol{0}$. For the intermediate values $0<|\boldsymbol{\psi}|<1$, it indicates the partially incoherent state as the Kuramoto order parameter does, yet both variables do not necessarily coincide with each other. This behavior is reminiscent of the relation between the Kuramoto order parameter and the WS variables of the Kuramoto phase oscillators, discussed in Sec. 2.4.

As we did in Sec. 2.4, the Kuramoto order parameter $\Gamma(t)$ can be described by solely the WS variable $\boldsymbol{\psi}$ as long as we take uniform constants of motion and the thermodynamic limit. In the thermodynamic limit, the governing equation for the continuous oscillator is given by

$$\partial_t\boldsymbol{x}=-\boldsymbol{x}\boldsymbol{H}^\dagger\boldsymbol{x}+\boldsymbol{\Omega}\boldsymbol{x}+\boldsymbol{H}. \tag{2.89}$$

Note that the oscillator vector should satisfy $\langle\boldsymbol{x}|\boldsymbol{x}\rangle=1$ to be confined to $\mathbb{S}^M$. From Eq. (2.86) and Eq. (2.89), we obtain

$$\partial_t\boldsymbol{x}=\frac{(\dot{\boldsymbol{A}}\boldsymbol{x}_0+\dot{\boldsymbol{\psi}})(\boldsymbol{\psi}^\dagger\boldsymbol{A}\boldsymbol{x}_0+1)-(\boldsymbol{A}\boldsymbol{x}_0+\boldsymbol{\psi})\partial_t(\boldsymbol{\psi}^\dagger\boldsymbol{A})\boldsymbol{x}_0}{(\boldsymbol{\psi}^\dagger\boldsymbol{A}\boldsymbol{x}_0+1)^2} \tag{2.90}$$

and the inverse transformation reads

$$\begin{aligned}\boldsymbol{x}_0&=(\boldsymbol{A}-\boldsymbol{x}\boldsymbol{\psi}^\dagger\boldsymbol{A})^{-1}(\boldsymbol{x}-\boldsymbol{\psi})\\&=\frac{1}{1-\boldsymbol{\psi}^\dagger\boldsymbol{x}}(\boldsymbol{A}^{-1}-\boldsymbol{\psi}^\dagger\boldsymbol{x}\boldsymbol{A}^{-1}+\boldsymbol{A}^{-1}\boldsymbol{x}\boldsymbol{\psi}^\dagger)(\boldsymbol{x}-\boldsymbol{\psi}).\end{aligned} \tag{2.91}$$

Note that the last line is due to Ref. [160]. For the sake of simplicity, we introduce some useful notations:

$$\begin{aligned}\boldsymbol{Q}\boldsymbol{x}_0+\boldsymbol{q}&=I^{-1}\big(\boldsymbol{Q}(\boldsymbol{A}^{-1}-\boldsymbol{\psi}^\dagger\boldsymbol{x}\boldsymbol{A}^{-1}+\boldsymbol{A}^{-1}\boldsymbol{x}\boldsymbol{\psi}^\dagger)(\boldsymbol{x}-\boldsymbol{\psi})+I\boldsymbol{q}\big)\\&=I^{-1}\big(\boldsymbol{Q}\boldsymbol{A}^{-1}(\boldsymbol{x}-\boldsymbol{\psi})+\boldsymbol{Q}(\boldsymbol{\psi}^\dagger\boldsymbol{x}\boldsymbol{A}^{-1}-\boldsymbol{A}^{-1}\boldsymbol{x}\boldsymbol{\psi}^\dagger)\boldsymbol{\psi}_I+\boldsymbol{q}\big)\end{aligned} \tag{2.92}$$

where $I=1-\boldsymbol{\psi}^\dagger\boldsymbol{x}$. Then, $\boldsymbol{\psi}^\dagger\boldsymbol{A}\boldsymbol{x}_0+1=\kappa I^{-1}$ where $\kappa=1-\boldsymbol{\psi}^\dagger\boldsymbol{\psi}$. Using these quantities, we can rewrite the first term of Eq. (2.90) as

$$(\dot{\boldsymbol{A}}\boldsymbol{x}_0+\dot{\boldsymbol{\psi}})(\boldsymbol{\psi}^\dagger\boldsymbol{A}\boldsymbol{x}_0+1)=\kappa I^{-2}\Big(\dot{\boldsymbol{A}}\boldsymbol{A}^{-1}(\boldsymbol{x}-\boldsymbol{\psi})+\dot{\boldsymbol{A}}(\boldsymbol{\psi}^\dagger\boldsymbol{x}\boldsymbol{A}^{-1}-\boldsymbol{A}^{-1}\boldsymbol{x}\boldsymbol{\psi}^\dagger)\boldsymbol{\psi}+I\dot{\boldsymbol{\psi}}\Big) \tag{2.93}$$

and the second term as

$$-(\boldsymbol{A}\boldsymbol{x}_0+\boldsymbol{\psi})\partial_t(\boldsymbol{\psi}^\dagger\boldsymbol{A})\boldsymbol{x}_0=\kappa I^{-2}\boldsymbol{x}\Big(\partial_t(\boldsymbol{\psi}^\dagger\boldsymbol{A})\boldsymbol{A}^{-1}(\boldsymbol{x}-\boldsymbol{\psi})+\partial_t(\boldsymbol{\psi}^\dagger\boldsymbol{A})(\boldsymbol{\psi}^\dagger\boldsymbol{x}\boldsymbol{A}^{-1}-\boldsymbol{A}^{-1}\boldsymbol{x}\boldsymbol{\psi}^\dagger)\boldsymbol{\psi}\Big). \tag{2.94}$$

Finally, Equation (2.90) can be rewritten as

$$\partial_t \boldsymbol{x} = \frac{1}{\kappa}\Big(\boldsymbol{x}(-\kappa\partial_t(\boldsymbol{\psi}^\dagger\boldsymbol{A}) - \partial_t(\boldsymbol{\psi}^\dagger\boldsymbol{A})\boldsymbol{A}^{-1}\boldsymbol{\psi}\boldsymbol{\psi}^\dagger\boldsymbol{A})\boldsymbol{A}^{-1}\boldsymbol{x} \\ + (\kappa\dot{\boldsymbol{A}} + \dot{\boldsymbol{A}}\boldsymbol{A}^{-1}\boldsymbol{\psi}\boldsymbol{\psi}^\dagger\boldsymbol{A} - \dot{\boldsymbol{\psi}}\boldsymbol{\psi}^\dagger\boldsymbol{A} + \partial_t(\boldsymbol{\psi}^\dagger\boldsymbol{A})\boldsymbol{A}^{-1}\boldsymbol{\psi}\boldsymbol{A})\boldsymbol{A}^{-1}\boldsymbol{x} - \dot{\boldsymbol{A}}\boldsymbol{A}^{-1}\boldsymbol{\psi} + \dot{\boldsymbol{\psi}}\Big). \tag{2.95}$$

Comparing this equation with Eq. (2.89) under the condition $\boldsymbol{x} \in \mathbb{S}^M$, we obtain for the dynamics of the WS variables

$$\begin{aligned} \partial_t \boldsymbol{A} &= \boldsymbol{H}\boldsymbol{\psi}^\dagger\boldsymbol{A} - \boldsymbol{H}^\dagger\boldsymbol{\psi}\boldsymbol{A} \\ \partial_t \boldsymbol{\psi} &= -\boldsymbol{\psi}\boldsymbol{H}^\dagger\boldsymbol{\psi} + \boldsymbol{H}. \end{aligned} \tag{2.96}$$

Furthermore, T. Tanaka [104] showed that $\boldsymbol{A} = \boldsymbol{P}^{1/2}\boldsymbol{U}$ (polar decomposition) where $\boldsymbol{U} \in \mathbb{K}^{M\times M}$ is a unitary matrix and $\boldsymbol{P}^{1/2} = \boldsymbol{V}\Sigma^{1/2}\boldsymbol{V}^\dagger$ with $\Sigma^{1/2} := (\sqrt{\Sigma_{ij}})$. Here, $\boldsymbol{V}\Sigma\boldsymbol{V}^\dagger$ is a singular value decomposition of $\boldsymbol{P} := (1-|\boldsymbol{\psi}|^2)I_M + \boldsymbol{\psi}\boldsymbol{\psi}^\dagger$ where $I_M \in \mathbb{R}^{M\times M}$ is the identity matrix and thus it follows that $\boldsymbol{P}^{1/2}\boldsymbol{\psi} = \boldsymbol{\psi}$ holds [104]. This information will be used later in this section.

In the thermodynamic limit, without loss of generality, it is possible to set $\boldsymbol{U} = I_M$ as long as all $\boldsymbol{x}_0$ are uniformly distributed on $\mathbb{S}^M$. Then, the Kuramoto order parameter can be expressed in terms of the WS variables[15] as in Eq. (2.56). To obtain this, we use the same method as in Sec. 2.4, which is somewhat different from Ref. [104]. Consider the Kuramoto order parameter defined in Eq. (2.85) with the WS transformation in Eq. (2.86):

$$\boldsymbol{\Gamma}(t) = \frac{1}{N}\sum_{k=1}^{N}\boldsymbol{x}_k(t) = \frac{1}{N}\sum_{k=1}^{N}\frac{\boldsymbol{A}\boldsymbol{x}_{0,k} + \boldsymbol{\psi}}{\boldsymbol{\psi}^\dagger\boldsymbol{A}\boldsymbol{x}_{0,k} + 1}. \tag{2.97}$$

[15] Here, we call $\boldsymbol{\psi}$ the WS variable even though it is taken from the uniform constants of motion and the thermodynamic limit.

Substituting $\boldsymbol{A} = \boldsymbol{P}^{1/2}\boldsymbol{U}$ and $\boldsymbol{P}^{1/2}\boldsymbol{\psi} = \boldsymbol{\psi}$ into the above equation, we obtain

$$\begin{aligned}
\boldsymbol{\psi}^\dagger\boldsymbol{\Gamma} &= \frac{1}{N}\sum_{k=1}^{N}(\boldsymbol{\psi}^\dagger\boldsymbol{H}^{1/2}\boldsymbol{U}\boldsymbol{x}_{0,k} + |\boldsymbol{\psi}|^2)\frac{1}{1+\boldsymbol{\psi}^\dagger\boldsymbol{U}\boldsymbol{x}_{0,k}} \\
&= \frac{1}{N}\sum_{k=1}^{N}(\boldsymbol{\psi}^\dagger\boldsymbol{U}\boldsymbol{x}_{0,k} + |\boldsymbol{\psi}|^2)\sum_{\ell=0}^{\infty}(-1)^\ell(\boldsymbol{\psi}^\dagger\boldsymbol{U}\boldsymbol{x}_{0,k})^\ell \\
&= -\frac{1}{N}\sum_{k=1}^{N}\sum_{\ell=0}^{\infty}(-1)^{\ell+1}(\boldsymbol{\psi}^\dagger\boldsymbol{U}\boldsymbol{x}_{0,k})^{\ell+1} + |\boldsymbol{\psi}|^2\frac{1}{N}\sum_{k=1}^{N}\sum_{\ell=0}^{\infty}(-1)^\ell(\boldsymbol{\psi}^\dagger\boldsymbol{U}\boldsymbol{x}_{0,k})^\ell \\
&= |\boldsymbol{\psi}|^2\left(1+(1-|\boldsymbol{\psi}|^{-2})\sum_{\ell=2}^{\infty}(-1)^\ell C_\ell\right)
\end{aligned} \tag{2.98}$$

where $C_\ell := \frac{1}{N}\sum_{k=1}^{N}(\boldsymbol{\psi}^\dagger\boldsymbol{U}\boldsymbol{x}_{0,k})^\ell$ and $C_1 = 0$. Taking the thermodynamic limit with uniformly distributed constants of motion, we can set $\boldsymbol{U} = I_M$ and write C_ℓ as

$$C_\ell = \begin{cases} \dfrac{1}{S_M}\displaystyle\int_{|\boldsymbol{x}_0|=1}(\boldsymbol{\psi}^\dagger\boldsymbol{x}_0)^\ell d\boldsymbol{x}_0, & \text{for } \mathbb{K}=\mathbb{R} \\ \\ \dfrac{1}{S_{2M}}\displaystyle\int_{|\boldsymbol{x}_0|=1}(\boldsymbol{\psi}^\dagger\boldsymbol{x}_0)^\ell d\boldsymbol{x}_0, & \text{for } \mathbb{K}=\mathbb{C} \end{cases} \tag{2.99}$$

where $S_M = \frac{2\pi^{M/2}}{\Gamma(M/2)}$ is the surface area of the $(M-1)$-sphere. Let us first consider the real space, i.e., $\mathbb{K} = \mathbb{R}$. Using the spherical coordinate systems, one can write a position of an oscillator on the surface of the unit ball in $\mathbb{R}^M$ as $x_1 = \sin\theta_1\sin\theta_2\cdots\sin\theta_{M-2}\cos\phi$, $x_2 = \sin\theta_1\sin\theta_2\cdots\sin\theta_{M-2}\sin\phi$, ..., $x_{M-2} = \sin\theta_1\sin\theta_2\cos\theta_3$, $x_{M-1} = \sin\theta_1\cos\theta_2$, and $x_M = \cos\theta_1$ where $\theta_1,...,\theta_{M-2} \in [0,\pi]$ and $\phi \in [0,2\pi]$. Here, x_M corresponds to the z-axis, for example, in the 3D space. We call this axis the M-axis and we refer to the plane perpendicular to the M-axis as the $M^\perp$-(hyper)plane throughout this thesis. Without loss of generality, we can assume that $\boldsymbol{\psi}$ is aligned along the M-axis, i.e., $\boldsymbol{\psi} = |\boldsymbol{\psi}|\hat{x}_M$. Consequently, this yields

$$\begin{aligned}
C_\ell &= \frac{1}{S_M}|\boldsymbol{\psi}|^\ell\int_{|\boldsymbol{x}_0|=1}\cos^\ell\theta_1 d^M V = \frac{|\boldsymbol{\psi}|^\ell}{S_M}S_{M-1}\int\cos^\ell\theta_1\sin^{M-2}\theta_1 d\theta_1 \\
&= |\boldsymbol{\psi}|^\ell\frac{1+(-1)^\ell}{2\sqrt{\pi}}\frac{\Gamma\left(\frac{\ell+1}{2}\right)\Gamma\left(\frac{M}{2}\right)}{\Gamma\left(\frac{\ell+M}{2}\right)}
\end{aligned} \tag{2.100}$$

which leads to

$$\sum_{\ell=2}^{\infty}(-1)^{\ell}C_{\ell}=|\boldsymbol{\psi}|^{2}\frac{\Gamma\left(\frac{M}{2}\right)}{2\Gamma\left(1+\frac{M}{2}\right)}{}_{2}F_{1}(1,\frac{3}{2};\frac{M+2}{2};|\boldsymbol{\psi}|^{2}) \tag{2.101}$$

where ${}_2F_1$ is the ordinary hypergeometric function [161]. Finally, Equation (2.98) can be written as

$$\begin{aligned}\boldsymbol{\psi}^{\dagger}\boldsymbol{\Gamma}&=|\boldsymbol{\psi}|^{2}\left(1+\frac{|\boldsymbol{\psi}|^{2}-1}{M}{}_{2}F_{1}(1,\frac{3}{2};\frac{M+2}{2};|\boldsymbol{\psi}|^{2})\right)\\&=\boldsymbol{\psi}^{\dagger}\boldsymbol{\psi}\frac{M-1}{M}{}_{2}F_{1}(\frac{1}{2},1;\frac{M+2}{2};|\boldsymbol{\psi}|^{2})=\boldsymbol{\psi}^{\dagger}h(|\boldsymbol{\psi}|^{2},M)\boldsymbol{\psi}\end{aligned} \tag{2.102}$$

where $h(|\boldsymbol{\psi}|^2,M):=\frac{M-1}{M}{}_2F_1(\frac{1}{2},1;\frac{M+2}{2};|\boldsymbol{\psi}|^2)$. Hence, we can assume that

$$\boldsymbol{\Gamma}(t)=\frac{M-1}{M}{}_{2}F_{1}(\frac{1}{2},1;\frac{M+2}{2};|\boldsymbol{\psi}|^{2})\boldsymbol{\psi}(t)=h(|\boldsymbol{\psi}|^{2},M)\boldsymbol{\psi}(t). \tag{2.103}$$

For $\mathbb{K}=\mathbb{C}$, obtaining $\boldsymbol{\Gamma}(t)=\boldsymbol{\psi}(t)$ is straightforward as the coefficients $C_\ell=0$ for $\ell\neq 0$[16].

To explore chimera states in a system of generalized Kuramoto-Sakaguchi oscillators in two-population networks, as we did in Sec. 2.3 for the usual KS model, we here introduce a suitable coupling matrix, which corresponds to the phase-lag parameter α in Eq. (2.14). Moreover, the Benjamin-Feir instability point becomes relevant to this coupling matrix.

In line with Eq. (2.14), we define in Eq. (2.84) $\boldsymbol{H}(t)=\boldsymbol{K}\boldsymbol{\Gamma}(t)$ where $\boldsymbol{K}\in\mathbb{K}^{M\times M}$ is a coupling matrix. Then, the microscopic dynamics of the oscillators are given by [104]

$$\begin{aligned}\partial_t\boldsymbol{x}_j&=-\boldsymbol{x}_j\boldsymbol{H}^{\dagger}\boldsymbol{x}_j+\boldsymbol{H}\\&=-\boldsymbol{x}_j\boldsymbol{\Gamma}^{\dagger}\boldsymbol{K}^{\dagger}\boldsymbol{x}_j+\boldsymbol{K}\boldsymbol{\Gamma}\end{aligned} \tag{2.104}$$

for $j=1,\ldots,N$. In Eq. (2.14), the phase-lag parameter induces phase rotations of $-\alpha$ to each phase on the unit circle. Similarly, we introduce a rotation matrix as the coupling matrix [150, 157]. First, we consider the real space $\mathbb{R}^M$. For a rotation in the real space, we need to distinguish between even and odd dimensional cases [153, 148]. For odd M, we set the M-axis as the rotational axis, and then the $M^{\perp}$-plane is isoclinically rotating with the

[16] T. Tanaka in Ref. [104] obtained $\boldsymbol{\Gamma}(t)=\int_{|\boldsymbol{x}_0|=1}M_t(\boldsymbol{x}_0)d\mu(\boldsymbol{x}_0)=\frac{1}{S_M}\int_{|\boldsymbol{x}_0|=1}\boldsymbol{x}(t)d\boldsymbol{x}_0=\frac{M-1}{M}{}_2F_1(\frac{1}{2},1;\frac{M+2}{2};|\boldsymbol{\psi}|^2)\boldsymbol{\psi}(t)=h(|\boldsymbol{\psi}|^2,M)\boldsymbol{\psi}(t)$ and $\boldsymbol{\Gamma}(t)=\frac{1}{S_{2M}}\int_{|\boldsymbol{x}_0|=1}\boldsymbol{x}(t)d\boldsymbol{x}_0=\boldsymbol{\psi}(t)$.

same angle. An example is

$$\boldsymbol{K} = \begin{pmatrix} \cos\alpha & -\sin\alpha & 0 & 0 & 0 \\ \sin\alpha & \cos\alpha & 0 & 0 & 0 \\ 0 & 0 & \cos\alpha & -\sin\alpha & 0 \\ 0 & 0 & \sin\alpha & \cos\alpha & 0 \\ 0 & 0 & 0 & 0 & 1 \end{pmatrix} \tag{2.105}$$

for $\mathbb{R}^5$. For even M, there is no rotational axis and hence we exploit planes of rotation, in particular, an isoclinic rotation with the same rotational angle for each plane. An example is

$$\boldsymbol{K} = \begin{pmatrix} \cos\alpha & -\sin\alpha & 0 & 0 \\ \sin\alpha & \cos\alpha & 0 & 0 \\ 0 & 0 & \cos\alpha & -\sin\alpha \\ 0 & 0 & \sin\alpha & \cos\alpha \end{pmatrix} \tag{2.106}$$

which holds in $\mathbb{R}^4$.

To determine the Benjamin-Feir instability, we take a look at the macroscopic dynamics in the thermodynamic limit determined by the WS variable from Eq. (2.96):

$$\begin{aligned} \partial_t \boldsymbol{\psi} &= -\boldsymbol{\psi}\boldsymbol{H}^\dagger\boldsymbol{\psi} + \boldsymbol{H} \\ &= h(|\boldsymbol{\psi}|^2, M)\left(-\boldsymbol{\psi}\boldsymbol{\psi}^\dagger\boldsymbol{K}^\dagger\boldsymbol{\psi} + \boldsymbol{K}\boldsymbol{\psi} \right) \end{aligned} \tag{2.107}$$

where the order parameter $\boldsymbol{\Gamma}$ is replaced by $h(|\boldsymbol{\psi}|^2, M)\boldsymbol{\psi}$ as in Eq. (2.103). Using Eq. (2.107), the dynamics of the magnitude of the WS variable is given by

$$\begin{aligned} \partial_t |\boldsymbol{\psi}|^2 &= \partial_t (\boldsymbol{\psi}^\dagger\boldsymbol{\psi}) \\ &= h(|\boldsymbol{\psi}|^2, M)\left((-\boldsymbol{\psi}^\dagger\boldsymbol{K}\boldsymbol{\psi}\boldsymbol{\psi}^\dagger + \boldsymbol{\psi}^\dagger\boldsymbol{K}^\dagger)\boldsymbol{\psi} + \boldsymbol{\psi}^\dagger(-\boldsymbol{\psi}\boldsymbol{\psi}^\dagger\boldsymbol{K}^\dagger\boldsymbol{\psi} + \boldsymbol{K}\boldsymbol{\psi}) \right) \\ &= 2h(|\boldsymbol{\psi}|^2, M)(1 - |\boldsymbol{\psi}|^2)\left\langle \boldsymbol{\psi} \middle| \frac{\boldsymbol{K} + \boldsymbol{K}^\dagger}{2} \middle| \boldsymbol{\psi} \right\rangle . \end{aligned} \tag{2.108}$$

For even M, the last term becomes $\left\langle \boldsymbol{\psi} \middle| \frac{\boldsymbol{K}+\boldsymbol{K}^\dagger}{2} \middle| \boldsymbol{\psi} \right\rangle = \cos\alpha |\boldsymbol{\psi}|^2$. Thus, Equation (2.108) is simply written as

$$\partial_t |\boldsymbol{\psi}|^2 = 2h(|\boldsymbol{\psi}|^2, M)(1 - |\boldsymbol{\psi}|^2)|\boldsymbol{\psi}|^2 \cos\alpha \tag{2.109}$$

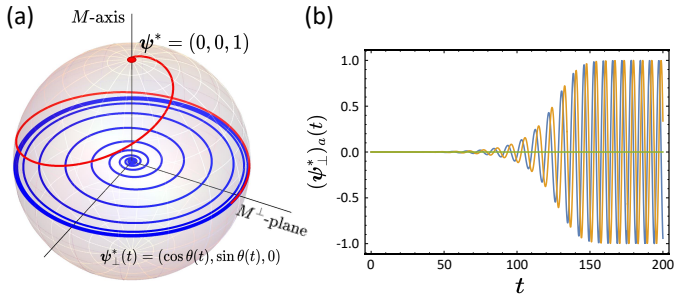

Fig. 2.2 (a) The time-parametric plot showcases a trajectory initiated close to the origin on the $M^\perp$-plane (blue). This trajectory gradually converges towards a limit-cycle solution on the unit circle within the $M^\perp$-plane, indicating a synchronized solution. If a slight perturbation is introduced along the M-axis, the trajectory is abruptly redirected towards the north pole (red). (b) The plot illustrates the time evolution of the components of the WS variable $\boldsymbol{\psi}^*_\perp(t)$. The rotation occurs at a tangential speed of $\sin\alpha$. Blue: $(\boldsymbol{\psi}^*_\perp)_1$, Orange: $(\boldsymbol{\psi}^*_\perp)_2$ and Green: $(\boldsymbol{\psi}^*_\perp)_3 = 0$.

which resembles Eq. (2.72). There exist two fixed points: $\rho_* = |\boldsymbol{\psi}| = 0$ representing the incoherent state, and $\rho^* = |\boldsymbol{\psi}| = 1$ indicating the synchronized state. The stability of these fixed points depends on the value of α. Specifically, the synchronized state ρ^* is stable while the incoherent state ρ_* is unstable for $\alpha < \frac{\pi}{2}$. Opposite to this, the incoherent state ρ_* is stable while the synchronized state ρ^* becomes unstable for $\alpha > \frac{\pi}{2}$. Therefore, the Benjamin-Feir instability occurs at $\alpha_{\mathrm{BF}} = \frac{\pi}{2}$ for even M.

For odd M, the last term of Eq. (2.108) reads $\left\langle \boldsymbol{\psi} \middle| \frac{\boldsymbol{K}+\boldsymbol{K}^\dagger}{2} \middle| \boldsymbol{\psi} \right\rangle = |\boldsymbol{\psi}|^2 \cos\alpha + (1-\cos\alpha) x_M^2$ where x_M is the coordinate of $\boldsymbol{\psi}$ along the rotational axis, i.e., the M-axis. In this case, the synchronized state manifests in two distinct spaces: either on the M-axis or on the $M^\perp$-plane. In the former case, the synchronized state is always stable regardless of the value of α since on the M-axis it is governed by $\partial_t |\boldsymbol{\psi}|^2 = 2h(|\boldsymbol{\psi}|^2, M)(1-|\boldsymbol{\psi}|^2)|\boldsymbol{\psi}|^2$. Note $\boldsymbol{\psi} = (0,\ldots,0,x_M)^\top$ and $|\boldsymbol{\psi}| = x_M$ along the M-axis. In the latter case, the stability of the synchronized state is determined by the parameter α. Equation (2.108) on the $M^\perp$-plane can be expressed as $\partial_t |\boldsymbol{\psi}|^2 = 2h(|\boldsymbol{\psi}|^2, M)(1-|\boldsymbol{\psi}|^2)|\boldsymbol{\psi}|^2 \cos\alpha$ (where $x_M = 0$ on the $M^\perp$-plane). As a result, the synchronized state is stable for $\alpha < \frac{\pi}{2}$ and unstable for $\alpha > \frac{\pi}{2}$. Thus, the Benjamin-Feir instability also occurs at $\alpha_{\mathrm{BF}} = \frac{\pi}{2}$. However, the synchronized state on the $M^\perp$-plane is always unstable to perturbations along the M-axis, as the synchronized states at the poles are globally attracting in each hemisphere of the unit ball except for the $M^\perp$-plane, regardless of the value of α.

As an example, we consider the 3D real space for the stability analysis of the synchronized state. First, consider the synchronized state on the M-axis $\boldsymbol{\psi}^* = (0,0,\pm 1)$, i.e., the north and the south poles, respectively. In fact, the dynamics asymptotically approaches this solution as $t \to \infty$ since $h(|\boldsymbol{\psi}|^2,3) = \frac{|\boldsymbol{\psi}|-(1-|\boldsymbol{\psi}|^2)\tanh^{-1}|\boldsymbol{\psi}|}{|\boldsymbol{\psi}|^3}$ and $\tanh^{-1}(1) = \infty$ while $h(|\boldsymbol{\psi}|^2,3) \to 1$ as $|\boldsymbol{\psi}| \to 1^-$. To study the stability of this solution, let $\boldsymbol{\psi}^* = (0,0,\pm 1 \mp \delta)$. Then, the trajectory starting on the upper/lower hemisphere approaches this fixed point solution on the north/south pole: $\lim_{\delta\to 0^+} F(\boldsymbol{\psi}^*) = (0,0,0)^\top$ where $F(\boldsymbol{\psi}) := -\boldsymbol{\psi}\boldsymbol{H}^\dagger\boldsymbol{\psi} + \boldsymbol{H}$. The Jacobian matrix evaluated at this solution is given by

$$\lim_{\delta\to 0^+} J\Big|_{\boldsymbol{\psi}^*} = \begin{pmatrix} -1+\cos\alpha & -\sin\alpha & 0 \\ \sin\alpha & -1+\cos\alpha & 0 \\ 0 & 0 & -2 \end{pmatrix} \tag{2.110}$$

and its eigenvalues are $\lambda_1 = -2, \lambda_\pm = -1 + e^{\pm i\alpha}$. Hence, the synchronized solution on the poles is always a stable solution regardless of α. Each pole is a globally attracting fixed point of the corresponding hemisphere (not including the $M^\perp$-plane). If the trajectory starts slightly outside the $M^\perp$-plane, the solution asymptotically approaches the north pole or the south pole, depending on whether it initiates above or below the plane. as time goes on (Fig. 2.2 (a)).

Subsequently, we observe that a trajectory precisely starting on the $M^\perp$-plane for $\alpha < \frac{\pi}{2}$ asymptotically approaches a limit-cycle solution, which rotates around the great circle on the x_1x_2-plane, as depicted in Fig. 2.2 (a). This limit-cycle solution also represents the synchronized state, as the magnitude of the WS variable is equal to unity. By considering $\boldsymbol{\psi}^\perp(t) = \varepsilon(\cos\theta(t), \sin\theta(t), 0)^\top$ and taking the limit as $\varepsilon \to 1^-$, we find that $\lim \varepsilon \to 1^- F(\boldsymbol{\psi}^\perp) = \sin\alpha(-\sin\theta(t), \cos\theta(t), 0)^\top$. This demonstrates that the trajectory asymptotically converges to the synchronized limit-cycle trajectory, which rotates counterclockwise along the unit circle with a tangential speed of $\sin\alpha$. Due to the rotational symmetry of the system, we can set the synchronized solution as a fixed point on the unit circle, which then reads $\boldsymbol{\psi}^* \perp = \lim_{\varepsilon\to 1^-} \varepsilon(1,0,0)$. To study its stability, we obtain the eigenvalue of the Jacobian matrix, evaluated at this solution, with the corresponding eigendirection along the M-axis. The eigenvalue is given by $\lambda_3 = 1 - \cos\alpha$, confirming that the synchronized limit-cycle solution is always unstable along the M-axis. Note that it remains stable on the $M^\perp$-plane for $\alpha < \alpha_{\mathrm{BF}}$ as we discussed earlier.

Next, for the complex space $\mathbb{K} = \mathbb{C}$, we choose the coupling matrix as $\boldsymbol{K} = e^{-i\alpha} I_M$ for all M. Then, the WS variable is governed by

$$\partial_t \boldsymbol{\psi} = -\boldsymbol{\psi}\boldsymbol{H}^\dagger\boldsymbol{\psi} + \boldsymbol{H} = -\boldsymbol{\psi}\boldsymbol{\psi}^\dagger\boldsymbol{K}^\dagger\boldsymbol{\psi} + \boldsymbol{K}\boldsymbol{\psi}. \tag{2.111}$$

where the WS variable equals the Kuramoto order parameter, i.e., $\boldsymbol{\Gamma}(t) = \boldsymbol{\psi}(t)$ for $\mathbb{C}^M$. Consequently, the magnitude dynamics of the Kuramoto order parameter reads

$$\partial_t |\boldsymbol{\psi}|^2 = 2(1-|\boldsymbol{\psi}|^2)\left\langle \boldsymbol{\psi}\left|\frac{\boldsymbol{K}+\boldsymbol{K}^\dagger}{2}\right|\boldsymbol{\psi}\right\rangle = 2(1-|\boldsymbol{\psi}|^2)|\boldsymbol{\psi}|^2\cos\alpha \tag{2.112}$$

Note that this equation is the same as Eq. (2.72). Therefore, the synchronized state $|\boldsymbol{\psi}| = 1$ is stable for $\alpha < \frac{\pi}{2}$ whereas unstable for $\alpha > \frac{\pi}{2}$, and thus, again $\alpha_{\mathrm{BF}} = \frac{\pi}{2}$.

Here, we make an additional remark regarding the distribution of oscillators on $\mathbb{S}^M$. In Sec. 2.4, we demonstrated that the phase distribution in the Ott-Antonsen manifold follows the normalized Poisson kernel. For the generalized Kuramoto oscillators, we can also guess the distribution of the oscillators on the surface of unit sphere. Considering the Watanabe-Strogatz transformation in Eq. (2.86), it is anticipated that the oscillators on $\mathbb{S}^M$ are distributed according to the higher-dimensional Poisson kernel in $\mathbb{C}^M$. Let us first consider the complex spaces. Assume that the oscillators on $\mathbb{S}^M$ are distributed by

$$f_{\mathrm{complex}}(\boldsymbol{x},\boldsymbol{\psi};t) = \frac{1}{S_{2M}}\frac{1-|\boldsymbol{\psi}|^2}{|\boldsymbol{\psi}-\boldsymbol{x}|^{2M}} \tag{2.113}$$

for $\boldsymbol{\psi} \in \mathbb{C}^M$ and for $\boldsymbol{x} \in \mathbb{S}^M$. Then, we can calculate the Kuramoto order parameter as

$$\begin{aligned}
\boldsymbol{\Gamma}(t) &= \int_{|\boldsymbol{x}|=1} \boldsymbol{x} f(\boldsymbol{x},\boldsymbol{\psi};t) d\boldsymbol{x} \\
&= \frac{1-|\boldsymbol{\psi}|^2}{S_{2M}} \int_{|\boldsymbol{x}|=1} \frac{\boldsymbol{x}}{(1+|\boldsymbol{\psi}|^2 - 2\mathrm{Re}\,\langle\boldsymbol{\psi}|\boldsymbol{x}\rangle)^M} d\boldsymbol{x} \\
&= \frac{1-|\boldsymbol{\psi}|^2}{S_{2M}} \int_{|\eta|\le 1} \int_{|\boldsymbol{n}|=\sqrt{1-|\eta|^2}} \frac{\eta\hat{\boldsymbol{\psi}}+\boldsymbol{n}}{(1+|\boldsymbol{\psi}|^2 - 2\mathrm{Re}\,\langle\boldsymbol{\psi}|\boldsymbol{x}\rangle)^M} d\boldsymbol{n} \frac{1}{\sqrt{1-|\eta|^2}} d\eta
\end{aligned} \tag{2.114}$$

where $\hat{\boldsymbol{\psi}} := \frac{\boldsymbol{\psi}}{|\boldsymbol{\psi}|}$ is a unit vector and $\langle \boldsymbol{n}|\boldsymbol{\psi}\rangle = 0$. Here, we decompose the unit vector on the sphere into $\boldsymbol{x} = \eta\hat{\boldsymbol{\psi}} + \boldsymbol{n}$ [104]. Then, the integral can be written as

$$\begin{aligned}
\boldsymbol{\Gamma}(t) &= \frac{1-|\boldsymbol{\psi}|^2}{S_{2M}}\hat{\boldsymbol{\psi}} \int_{|\eta|\le 1} \int_{|\boldsymbol{n}|=\sqrt{1-|\eta|^2}} \frac{\eta}{(1+|\boldsymbol{\psi}|^2 - 2|\boldsymbol{\psi}|\mathrm{Re}\eta)^M} d\boldsymbol{n} \frac{1}{\sqrt{1-|\eta|^2}} d\eta \\
&= \frac{S_{2M-2}}{S_{2M}}(1-|\boldsymbol{\psi}|^2)\hat{\boldsymbol{\psi}} \int_{|\eta|\le 1} \frac{\eta}{(1+|\boldsymbol{\psi}|^2 - 2|\boldsymbol{\psi}|\mathrm{Re}\eta)^M} d\boldsymbol{n} \frac{(1-|\eta|^2)^{\frac{2M-3}{2}}}{\sqrt{1-|\eta|^2}} d\eta \\
&= \frac{S_{2M-2}}{S_{2M}}(1-|\boldsymbol{\psi}|^2)\hat{\boldsymbol{\psi}} \int_0^1 \int_0^{2\pi} \frac{re^{i\theta}}{(1+|\boldsymbol{\psi}|^2 - 2|\boldsymbol{\psi}|r\cos\theta)^M} (1-r^2)^{M-2} r d\theta dr \\
&= \boldsymbol{\psi}(t)
\end{aligned} \tag{2.115}$$

which is consistent with the result above, i.e., $\boldsymbol{\Gamma}(t) = \boldsymbol{\psi}(t)$ for the complex space. Thus, we can expect that the oscillators for the complex spaces are distributed according to Eq. (2.113), i.e., the higher-dimensional normalized Poisson kernel. However, for the real spaces, $\mathbb{R}^M$, the normalized Poisson kernel is given by

$$f_{\text{real}}(\boldsymbol{x}, \boldsymbol{\psi}; t) = \frac{1}{S_M} \frac{1 - |\boldsymbol{\psi}|^2}{|\boldsymbol{\psi} - \boldsymbol{x}|^M} \tag{2.116}$$

which leads to the following relation for the Kuramoto order parameter

$$\begin{aligned}
\boldsymbol{\Gamma}(t) &= \frac{1 - |\boldsymbol{\psi}|^2}{S_M} \int_{|\boldsymbol{x}|=1} \frac{\boldsymbol{x}}{(1 + |\boldsymbol{\psi}|^2 - 2\langle \boldsymbol{\psi} | \boldsymbol{x} \rangle)^{M/2}} d\boldsymbol{x} \\
&= \frac{1 - |\boldsymbol{\psi}|^2}{S_M} \int_{-1}^{1} \int_{|\boldsymbol{n}|=\sqrt{1-\eta^2}} \frac{\eta \hat{\boldsymbol{\psi}} + \boldsymbol{n}}{(1 + |\boldsymbol{\psi}|^2 - 2\langle \boldsymbol{\psi} | \boldsymbol{x} \rangle)^{M/2}} d\boldsymbol{n} \frac{d\eta}{\sqrt{1-\eta^2}} \\
&= \frac{S_{M-1}}{S_M} (1 - |\boldsymbol{\psi}|^2) \hat{\boldsymbol{\psi}} \int_{-1}^{1} \frac{\eta}{(1 + |\boldsymbol{\psi}|^2 - 2|\boldsymbol{\psi}|\eta)^{M/2}} \frac{(1-\eta^2)^{\frac{M-2}{2}}}{\sqrt{1-\eta^2}} d\eta \\
&= \boldsymbol{\psi}(t)
\end{aligned} \tag{2.117}$$

which is inconsistent with Eq. (2.103), i.e., $\boldsymbol{\Gamma}(t) = h(|\boldsymbol{\psi}|, M)\boldsymbol{\psi}(t)$. This suggests that the distribution of higher-dimensional real oscillators on $\mathbb{S}^M$ does not follow the higher-dimensional normalized Poisson kernel given by Eq.(2.116) with the given $\boldsymbol{\psi}$. Previous studies have reported that in the thermodynamic limit, higher-dimensional real oscillators distributed according to the higher-dimensional Poisson kernel satisfy the Ott-Antonsen (OA) equations introduced in Refs.[152, 153]. In those works, the authors employed the spherical harmonics expansion (for 3D real space) of the oscillator distribution function[17], similar to how Ott and Antonsen used the Fourier series expansion for 2D real space in Eq. (2.59). The oscillator distribution, e.g., for 3D real spaces, is assumed to be [152]

$$\begin{aligned}
f_{\text{real}}(\theta, \phi, t) &= \sum_{l=0}^{\infty} \sum_{m=-l}^{l} f_{lm} Y_{lm}(\theta, \phi) \\
&= \frac{1}{S_3} \left(1 + 4\pi \sum_{l=0}^{\infty} \sum_{m=-l}^{l} \rho^l \overline{Y_{lm}}(\Theta, \Phi) Y_{lm}(\theta, \phi) \right)
\end{aligned} \tag{2.118}$$

[17] For higher dimensions, a generalized spherical harmonics expansion was utilized [153].

where $f_{lm} = \rho^l \overline{Y_{lm}}(\Theta,\Phi)$ is taken as a generalied OA ansatz and $Y_{lm}(\theta,\phi)$ are spherical harmonics [161, 162]. To obtain the phase distribution function, we can use [152]

$$\frac{4\pi}{2l+1}\sum_{m=-l}^{l} Y_{lm}(\hat{y})\overline{Y_{lm}}(\hat{x}) = P_l(\hat{x}\cdot\hat{y}) \tag{2.119}$$

where $P_l(x)$ are Legendre polynomials and

$$\sum_{l=0}^{\infty} y^l P_l(x) = \frac{1}{\sqrt{1+y^2-2xy}}. \tag{2.120}$$

Using the above relations, we obtain

$$\begin{aligned} f_{\text{real}}(\theta,\phi,t) &= \frac{1}{S_3}\left(1+4\pi\sum_{l=1}^{\infty}\frac{2l+1}{4\pi}\rho^l P_l(\hat{r}\cdot\hat{\rho})\right) = \frac{1}{S_3}\left(2\sum_{l=0}^{\infty} l\rho^l P_l(\hat{r}\cdot\hat{\rho}) + \sum_{l=0}^{\infty}\rho^l P_l(\hat{r}\cdot\hat{\rho})\right) \\ &= \frac{1}{S_3}\left(2\rho\frac{\partial}{\partial\rho}\sum_{l=0}^{\infty}\rho^l P_l(\hat{r}\cdot\hat{\rho}) + \sum_{l=0}^{\infty}\rho^l P_l(\hat{r}\cdot\hat{\rho})\right) \\ &= \frac{1}{S_3}\left(2\rho\frac{\partial}{\partial\rho}\frac{1}{\sqrt{1+\rho^2-2\hat{r}\cdot\hat{\rho}}} + \frac{1}{\sqrt{1+\rho^2-2\hat{r}\cdot\hat{\rho}}}\right) \end{aligned} \tag{2.121}$$

where $\boldsymbol{\rho} = \rho(\sin\Theta\cos\Phi, \sin\Theta\sin\Phi, \cos\Theta)^\top \in \mathbb{R}^3$ is the OA variable[18] and the microscopic oscillator is represented by $\boldsymbol{r} = (\sin\theta\cos\phi, \sin\theta\sin\phi, \cos\theta)^\top \in \mathbb{S}^3$ with $\boldsymbol{r}^\dagger\boldsymbol{r} = 1$ in the thermodynamic limit. Finally, the oscillator distribution is given by [152]

$$f_{\text{real}}(\theta,\phi,t) = \frac{1}{4\pi}\frac{1-\rho^2}{(1+\rho^2-2\rho\hat{\rho}\cdot\hat{r})^{3/2}} = \frac{1}{S_3}\frac{1-|\boldsymbol{\rho}|^2}{|\boldsymbol{\rho}-\boldsymbol{r}|^3} \tag{2.122}$$

as in Eq. (2.116). However, the OA variable consistent with the normalized Poisson kernel as above is governed by

$$\partial_t\boldsymbol{\rho} = \boldsymbol{\Omega}\boldsymbol{\rho} + \frac{1}{2}(1+|\boldsymbol{\rho}|^2)(\boldsymbol{K}\boldsymbol{\Gamma}) - \left[\boldsymbol{\rho}^\top(\boldsymbol{K}\boldsymbol{\Gamma})\right]\boldsymbol{\rho} \tag{2.123}$$

which is different from Eq. (2.96). In conclusion, for both higher-dimensional complex and real spaces, the distribution of oscillators follows the higher-dimensional Poisson kernel in the Ott-Antonsen manifold. In the case of complex oscillators, the model and the generalized WS transformation described in Ref.[104] provide the correct approach, and the Kuramoto order parameter precisely coincides with the OA variable. However, to obtain the Poisson kernel distribution in real spaces, we need to consider the spherical harmonics expansion and

[18] In our notation, it corresponds to $\boldsymbol{\psi}$

the governing equations introduced in Refs.[152, 153]. In this manifold, the Kuramoto order parameter exactly matches the OA variable.

2.5.2 System of Coupled Oscillators in a Network of Networks

In the previous subsection, we studied the generalized Kuramoto-Sakaguchi oscillator systems in a single network, and therein we revisited the dimension reduction methods, i.e., the generalized Watanabe-Strogatz transformation. In the thermodynamic limit with uniformly distributed initial conditions, the WS variable itself can fully depict the Kuramoto order parameter and their dynamical equations, the Ott-Antonsen dynamics. In this section, we construct a system of generalized Kuramoto-Sakaguchi oscillators in a network of networks as we did in Sec. 2.4.2 for a system of classical Kuramoto-Sakaguchi oscillators.

The governing equations of the microscopic individual oscillators can be written as

$$\partial_t \boldsymbol{x}_j^{(a)} = -\boldsymbol{x}_j^{(a)} \boldsymbol{H}_a^\dagger \boldsymbol{x}_j^{(a)} + \boldsymbol{H}_a, \quad \boldsymbol{H}_a(t) := \boldsymbol{K} \cdot \sum_{b=1}^{L} G_{ab} \boldsymbol{\Gamma}_b(t), \quad \boldsymbol{\Gamma}^{(a)}(t) := \frac{1}{N} \sum_{k=1}^{N} \boldsymbol{x}_k^{(a)} \tag{2.124}$$

for $j = 1, ..., N$ and for $a, b = 1, ..., L$ where L is the number of populations and N is the number of oscillators in each population (same for all the populations). Also, G_{ab} is a coupling strength matrix between populations and $\boldsymbol{\Gamma}^{(a)}(t)$ denotes the Kuramoto order parameter for population a, as the center of mass of the oscillators on $\mathbb{S}^M$. For this system, we can also think about a set of Watanabe-Strogatz transformations given by

$$\boldsymbol{x}_j^{(a)}(t) = M_t(\boldsymbol{x}_{0,j}^{(a)}) := \frac{\boldsymbol{A}(t)_a \boldsymbol{x}_{0,j}^{(a)} + \boldsymbol{\psi}_a(t)}{\boldsymbol{\psi}_a(t)^\dagger \boldsymbol{A}_a(t) \boldsymbol{x}_{0,j}^{(a)} + 1} \tag{2.125}$$

for $j = 1, ..., N$ and $a = 1, ..., L$. From Eq. (2.96), we know that the macroscopic WS variables of each population are governed by

$$\begin{aligned} \partial_t \boldsymbol{A}_a(t) &= \boldsymbol{H}_a \boldsymbol{\psi}_a^\dagger \boldsymbol{A}_a - \boldsymbol{H}_a^\dagger \boldsymbol{\psi}_a \boldsymbol{A}_a \\ \partial_t \boldsymbol{\psi}_a(t) &= -\boldsymbol{\psi}_a \boldsymbol{H}_a^\dagger \boldsymbol{\psi}_a + \boldsymbol{H}_a \end{aligned} \tag{2.126}$$

with uniformly distributed initial conditions $\boldsymbol{x}_{0,j}^{(a)}$ on $\mathbb{S}^M$ for $j = 1, ..., N$ and for $a = 1, ..., M$.

In the thermodynamic limit, the Kuramoto order parameter can be written only in terms of the WS variables. Hence, the forcing field can be written as

$$\begin{aligned}\boldsymbol{H}_a(t) &:= \boldsymbol{K}\cdot\sum_{b=1}^{L} G_{ab}\boldsymbol{\Gamma}_b(t) = \boldsymbol{K}\cdot\sum_{b=1}^{L} G_{ab}\int_{|\boldsymbol{x}_b|=1}\boldsymbol{x}_b f_b(\boldsymbol{x}_b,t)d\boldsymbol{x}_b \\ &= \boldsymbol{K}\cdot\sum_{b=1}^{L} G_{ab}\int_{|\boldsymbol{x}_b|=1}\boldsymbol{x}_b\frac{1}{S_{2M}}\frac{1-|\boldsymbol{\psi}_b|^2}{|\boldsymbol{\psi}_b-\boldsymbol{x}_b|^{2M}}d\boldsymbol{x}_b \\ &= \boldsymbol{K}\cdot\sum_{b=1}^{L} G_{ab}\frac{1-|\boldsymbol{\psi}_b|^2}{S_{2M}}\int_{|\boldsymbol{x}_b|=1}\frac{\boldsymbol{x}_b}{(1+|\boldsymbol{\psi}_b|^2-2\mathrm{Re}\,\langle\boldsymbol{\psi}_b|\boldsymbol{x}_b\rangle)^M}d\boldsymbol{x}_b \\ &= \boldsymbol{K}\cdot\sum_{b=1}^{L} G_{ab}\boldsymbol{\psi}_b(t)\end{aligned} \tag{2.127}$$

for $a=1,...,L$ for the complex space $\mathbb{K}=\mathbb{C}$. On the other hand, as we discussed in Sec. 2.5, the forcing field of the real spaces $\mathbb{K}=\mathbb{R}$ reads

$$\begin{aligned}\boldsymbol{H}_a(t) &:= \boldsymbol{K}\cdot\sum_{b=1}^{L} G_{ab}\boldsymbol{\Gamma}_b(t) = \boldsymbol{K}\cdot\sum_{b=1}^{L} G_{ab}h(|\boldsymbol{\psi}_b|^2,M)\int_{|\boldsymbol{x}_b|=1}\boldsymbol{x}_b f_b(\boldsymbol{x}_b,t)d\boldsymbol{x}_b \\ &= \boldsymbol{K}\cdot\sum_{b=1}^{L} G_{ab}h(|\boldsymbol{\psi}_b|^2,M)\int_{|\boldsymbol{x}_b|=1}\boldsymbol{x}_b\frac{1}{S_M}\frac{1-|\boldsymbol{\psi}_b|^2}{|\boldsymbol{\psi}_b-\boldsymbol{x}_b|^{M}}d\boldsymbol{x}_b \\ &= \boldsymbol{K}\cdot\sum_{b=1}^{L} G_{ab}h(|\boldsymbol{\psi}_b|^2,M)\frac{1-|\boldsymbol{\psi}_b|^2}{S_M}\int_{|\boldsymbol{x}_b|=1}\frac{\boldsymbol{x}_b}{(1+|\boldsymbol{\psi}_b|^2-2\mathrm{Re}\,\langle\boldsymbol{\psi}_b|\boldsymbol{x}_b\rangle)^{M/2}}d\boldsymbol{x}_b \\ &= \boldsymbol{K}\cdot\sum_{b=1}^{L} G_{ab}h(|\boldsymbol{\psi}_b|^2,M)\boldsymbol{\psi}_b(t)\end{aligned} \tag{2.128}$$

for $a=1,...,L$. Therefore, the OA dynamics of generalized Kuramoto-Sakaguchi oscillators in multi-population networks read

$$\partial_t\boldsymbol{\psi}_a = -\boldsymbol{\psi}_a\boldsymbol{H}_a^\dagger\boldsymbol{\psi}_a+\boldsymbol{H}_a = -\boldsymbol{\psi}_a\left(\sum_{b=1}^{L} G_{ab}\boldsymbol{\psi}_b^\dagger\boldsymbol{K}^\dagger\right)\cdot\boldsymbol{\psi}_a+\boldsymbol{K}\cdot\sum_{b=1}^{L} G_{ab}\boldsymbol{\psi}_b \tag{2.129}$$

for $a=1,...,L$ for the complex spaces $\mathbb{C}^M$, while the OA dynamics for $\mathbb{R}^M$ can be written as

$$\begin{aligned}\partial_t\boldsymbol{\psi}_a &= -\boldsymbol{\psi}_a\boldsymbol{H}_a^\dagger\boldsymbol{\psi}_a+\boldsymbol{H}_a \\ &= -\boldsymbol{\psi}_a\left(\sum_{b=1}^{L} G_{ab}h(|\boldsymbol{\psi}_b|^2,M)\boldsymbol{\psi}_b^\top\boldsymbol{K}^\top\right)\cdot\boldsymbol{\psi}_a+\boldsymbol{K}\cdot\sum_{b=1}^{L} G_{ab}h(|\boldsymbol{\psi}_b|^2,M)\boldsymbol{\psi}_b\end{aligned} \tag{2.130}$$

for $a=1,...,L$.

2.6 Lyapunov Exponent and Covariant Lyapunov Vector

In Sec. 2.3, we studied the stability of the synchronized state and the completely incoherent state for the system of identical Kuramoto-Sakaguchi oscillators. In those two cases, the dynamical states are fixed points in a rotating reference frame, and the linear stability is readily obtained from the eigenvalues of the Jacobian matrix evaluated at the fixed point. In this section, we briefly take a look at a practical tool for the general exploration of the stability of dynamical states. It is called Lyapunov stability analysis. Along a given trajectory in phase space, we can investigate the stability of the trajectory by imposing local perturbations. This is done by measuring how rapidly a local perturbation grows (unstable) or shrinks (stable). The local growth rate is characterized by the *Lyapunov exponents* and the local perturbation directions of expansion/contraction are given by the *covariant Lyapunov vectors* [122–124]. Here, we give the mathematical background of such a Lyapunov analysis.

Let us consider a set of ordinary differential equations $\partial_t \mathbf{x} = \mathbf{f}(\mathbf{x})$ with an initial condition $\mathbf{x}(0) = \mathbf{x}_0$ where $\mathbf{x} \in \mathbb{R}^M$ and $\mathbf{f} : \mathbb{R}^M \to \mathbb{R}^M$ is the vector field of the system. The initial condition determines a reference trajectory $\mathbf{x}_{\mathrm{ref}}(t)$. Along the reference trajectory, we dive into the tangent space $T_{\mathbf{x}_{\mathrm{ref}}(t)}\mathbb{R}^M$ where the local perturbation vector $\delta\mathbf{x}(t) \in T_{\mathbf{x}_{\mathrm{ref}}(t)}\mathbb{R}^M$ resides. The local perturbation vectors are governed by the Jacobian matrix evaluated along the reference trajectory such that

$$\partial_t \delta\mathbf{x}(t) = \mathbf{J}(\mathbf{x}_{\mathrm{ref}}(t);t)\delta\mathbf{x}(t) \tag{2.131}$$

for $\delta\mathbf{x}(t) \in T_{\mathbf{x}_{\mathrm{ref}}(t)}\mathbb{R}^M$ where $(\mathbf{J}(t))_{ij} := \left.\frac{\partial \mathbf{f}_i}{\partial \mathbf{x}_j}\right|_{\mathbf{x}_{\mathrm{ref}}(t)}$. From Eq. (2.131), the tangent linear propagator can be constructed from the fundamental matrix solution, which is obtained by

$$\partial_t \mathbf{O}(t) = \mathbf{J}(\mathbf{x}_{\mathrm{ref}}(t);t)\mathbf{O}(t) \tag{2.132}$$

for the initial condition $\mathbf{O}(0) = I_M$. Therefore, the tangent linear propagator is given by

$$\mathbf{M}(t_0,t) = \mathbf{O}(t)\mathbf{O}(t_0)^{-1} \tag{2.133}$$

for $t_0 < t$. The tangent linear propagator *propagates* the local perturbation vector at the time point t_0, i.e., $\delta\mathbf{x}(t_0) \in T_{\mathbf{x}_{\mathrm{ref}}(t_0)}\mathbb{R}^M$, to the perturbation vector $\delta\mathbf{x}(t) \in T_{\mathbf{x}_{\mathrm{ref}}(t)}\mathbb{R}^M$ at the future

The contents of this section were in part published previously in S. Lee and K. Krischer, Chaos **31**, 113101 (2021) [55].

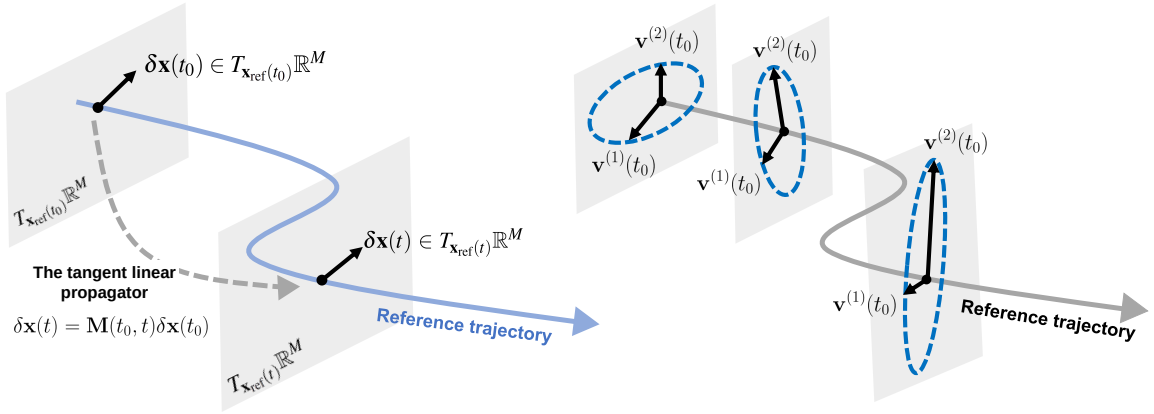

Fig. 2.3 (Left) A schematic figure of the dynamical system. Along the reference trajectory, the local perturbation vector which lives on the tangent space evloves according to the tangent linear propagator. (Right) A schematic figure of the covariant Lyapunov vectors. The first Lyapunov exponent is assumed to be negative (contracting CLV) and the second LE is assumed to be positive (expanding CLV).

time point, which means

$$\delta\mathbf{x}(t) = \mathbf{M}(t_0,t)\delta\mathbf{x}(t_0). \tag{2.134}$$

In 1965, Valery Oseledets proved the so-called *multiplicative ergodic theorem* or *Oseledets theorem* [163]. It says that with the tangent linear propagators, we can construct the forward/backward Oseledets matrices according to

$$\begin{aligned}
\mathbf{\Xi}^{+}(t) &= \lim_{t_2\to\infty}\left[\mathbf{M}(t,t_2)^{\top}\mathbf{M}(t,t_2)\right]^{1/(2(t_2-t))} \\
\mathbf{\Xi}^{-}(t) &= \lim_{t_1\to-\infty}\left[\mathbf{M}(t_1,t)^{-\top}\mathbf{M}^{-1}(t_1,t)\right]^{1/(2(t_1-t))}
\end{aligned} \tag{2.135}$$

where $-\top$ indicates the transpose and inverse of a matrix. The Oseledets theorem proves that the limits in Eq. (2.135) exist and share the same real positive eigenvalues denoted by $\mu_1 > \mu_2 > ... > \mu_M$[19]. The Lyapunov exponents are defined by $\lambda_i = \log\mu_i$ for $i = 1,...,M$. The meaning of the Lyapunov exponents will be clear later in this section. The forward/backward Oseledets matrix explores the future/past dynamics along the reference trajectory $\mathbf{x}_{\rm ref}(t)$. The eigenvalues μ_i for $i = 1,...,M$ have corresponding eigenvectors, which are called the *forward/backward Lyapunov vectors* $\mathbf{d}_{\pm}^{(i)}(t)$. Nevertheless, the forward/backward Lyapunov vectors are not covariant under the dynamics. Hence, those vectors are not related to the information on the local expansion/contraction of the perturbation vectors along the reference trajectory. To study the correct local perturbation directions, V. Oseledets suggested

[19]Here, we only consider the nondegenerate case. Hence, there are M eigenvalues.

decomposing the tangent space according to the local expansion/contraction behavior along the reference trajectory [123, 124, 163, 164], which is called the *Oseledets splitting*. Define the nested subspaces as

$$(\mathbf{\Gamma}^{(i)}(t))^{+} := \bigoplus_{j=i}^{M} (\mathbf{U}^{(j)}(t))^{+}$$
$$(\mathbf{\Gamma}^{(i)}(t))^{-} := \bigoplus_{j=1}^{i} (\mathbf{U}^{(j)}(t))^{-} \tag{2.136}$$

where $(\mathbf{U}^{(j)}(t))^{\pm}$ are the eigenspaces of the forward/backward Oseledets matrices spanned by $\{\mathbf{d}_{\pm}^{(j)}(t)\}_{j=1}^{M}$. Therefore, the tangent space is decomposed into $\mathbf{T}_{\mathbf{x}_{\mathrm{ref}}(t)}(\mathbb{R}^M) = \bigoplus_{j=1}^{M} \mathbf{\Omega}^{(j)}(t)$, where $\mathbf{\Omega}^{(i)}(t) := (\mathbf{\Gamma}^{(i)}(t))^{+} \cap (\mathbf{\Gamma}^{(i)}(t))^{-}$ is called the Oseledets' splitting. In contrast to the eigenspaces of the forward/backward Lyapunov matrices, the Oseledets' splitting is covariant under the dynamics such that $\mathbf{\Omega}^{(i)}(t) = \mathbf{M}(t_0,t)\mathbf{\Omega}^{(i)}(t_0)$. The spanning vectors $\{\mathbf{v}^{(i)}(t)\}_{i=1}^{M}$ of the Oseledets' splittings are called the *Covariant Lyapunov Vectors* (CLVs) [123, 124]. The information on the local expansion/contraction direction is given by the Oseledets' splitting since they are norm-independent and also covariant under the given dynamics. Now the Lyapunov exponents get their meaning. The Lyapunov exponents are the exponential growth/shrinking rates of the local perturbations along the direction of the CLVs (see Fig. 2.3). They are defined by

$$\Lambda_i = \lim_{t\to\infty} \frac{1}{t} \log \frac{||\mathbf{M}(t_0,t)\mathbf{u}(t_0)||}{||\mathbf{u}(t_0)||} \tag{2.137}$$

for $\mathbf{u}(t_0) \in (\mathbf{\Gamma}^{(i)}(t_0))^{+} \backslash (\mathbf{\Gamma}^{(i+1)}(t_0))^{+}$ where the nested subspaces are $\mathbb{R}^M = (\mathbf{\Gamma}^{(1)}(t))^{+} \supset (\mathbf{\Gamma}^{(2)}(t))^{+} \supset \ldots \supset (\mathbf{\Gamma}^{(M)}(t))^{+}$. In conclusion, for the study of the stability of a dynamical state, we measure the Lyapunov exponents characterizing the exponential asymptotic growth rate $||\mathbf{M}(t_0,t)\mathbf{v}^{(i)}(t_0)|| \sim ||\mathbf{v}^{(i)}(t_0)||\exp(\Lambda_i t)$, and we also investigate the covariant Lyapunov vectors indicating the stable/unstable directions of the perturbation vectors in the phase space [122].

Chapter 3

Coexistence Dynamics I: Attracting Poisson Chimera

In this chapter, we discuss the first and the simplest *coexistence dynamics of identical Kuramoto-Sakaguchi oscillators in a network of networks*, that is, a chimera state in a two-population network. This system and its observable chimera states were originally studied in Refs. [72, 74]. Our main task in this chapter is to provide details on (a) how the chimera states behave as the system size increases, (b) how the chimeras in a finite-sized ensemble are linked to the chimeras in the OA manifold, and (c) their spectral properties based on the Lyapunov analysis that we discussed in Sec. 2.6. As introduced in Chap. 1, after the first observation of chimera states in a ring geometry with a nonlocal coupling function, chimera states in two-population networks have been investigated with various oscillator systems in numerous papers to emulate a nonlocal coupling in a simpler setting that allows for a deeper understading both in the thermodynamic limit and in finite-sized ensembles [72, 74, 78, 79, 87, 75, 76, 80, 101, 73, 86, 77, 165–167]. In the thermodynamic limit, the chimera states of Kuramoto-Sakaguchi oscillators can be studied using the Ott-Antonsen ansatz described in Sec. 2.4.2. We know that the oscillators are distributed according to the normalized Poisson kernel in the OA manifold and the dynamics in the OA manifold can be written in a closed form that enables one to easily investigate the essential properties of chimeras. Furthermore, chimeras in the OA manifold are known to be neutrally stable when the oscillators are strictly identical [97]. In contrast, when the oscillators are slightly heterogeneous, the asymptotic dynamics even starting slightly off the OA manifold was found to be attracted to the OA manifold in the long time limit [97, 168, 78, 169]. On the other hand, in the finite-sized

The contents of this chapter were in part published previously in S. Lee and K. Krischer, Chaos **31**, 113101 (2021) [55]. Note all figures and figure captions are reproduced or regenerated from those in it.

system, the behavior of the chimera states exhibits a strong dependence on initial conditions (ICs) [73, 77, 167, 101, 102, 168]. Below, we will demonstrate that the strong dependence on the ICs of the finite-sized chimeras is due to their neutral stability. Depending on initial conditions, their macroscopic observables may exhibit simple and regular dynamics or irregular, complicated motions. The simplest chimera dynamics of the finite-sized ensemble can be obtained when the initial phases of the incoherent population are distributed according to the normalized Poisson kernel. In the following, we will call such ICs *Poisson initial conditions* (PIC), in order to start the dynamics for small N as close as possible to the OA manifold, which will be called the *Poisson submanifold* throughout this thesis. All the other initial conditions generated outside the Poisson submanifold are referred to as *non-Poisson initial conditions* (n-PIC), i.e., a set of initial phases randomly and independently generated from the uniform distribution of $\mathbb{T}$. In the case of PICs, previous works showed that for large N the dynamics of the Kuramoto order parameter are indistinguishable from that observed in the OA manifold in the thermodynamic limit [72, 74]. However, the PIC-started chimera states for small-N exhibited prominently different order parameter dynamics from that of the large-sized populations or the OA dynamics, which has been attributed to finite-size fluctuations [74].

In this chapter, we demonstrate the dynamical and spectral properties of finite-sized chimeras in two-population networks. Considering the two different initial conditions described above, the initial condition dependence of chimera states is thoroughly discussed. Moreover, we increase the system size N to elucidate how the finite-sized chimera is connected to that of the OA dynamics in the thermodynamic limit. Next, we demonstrate the neutral stability of the chimera states in finite-sized ensembles, employing Lyapunov analysis. Finally, we impose a 'perturbation' to the identical Kuramoto-Sakaguchi oscillators. To this end, we consider either a nonlocal intra-population network as a topological variation or an ensemble of identical Stuart-Landau oscillators as a dynamical variation. We demonstrate that both variations could induce small heterogeneities to the phase dynamics that render Poisson chimeras attracting.

3.1 Chimeras in Two-population Network

3.1.1 Governing Equations and Observable Chimera Dynamics

Consider a set of identical Kuramoto-Sakaguchi phase oscillators arranged in a two-population network topology. In each population, the oscillators are all-to-all coupled with each other as well as to the oscillators in the other population. However, the strength of the inter-population

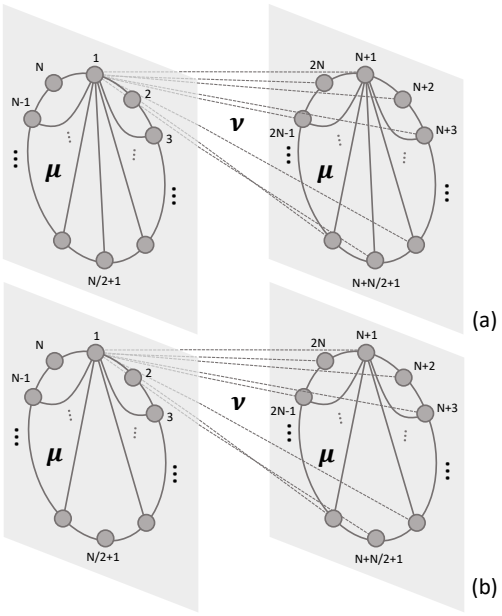

Fig. 3.1 Schematics of the two-population network topologies considered in this paper. (a) Global intra- and inter- population topology, and (b) global inter- and nonlocal intra-population coupling. Here, only the connections from the first oscillator are fully depicted. The solid connections indicate the intra-population coupling with strength μ, and the dashed ones the inter-population connections with strength ν. Note that in the nonlocal intra-population topology, each oscillator is connected to all the other oscillators except of the opposite one.

coupling is weaker than the intra-population coupling strength. This situation is depicted in Fig. 5.1 (a). Note that this model can be obtained from Eq. (2.73) with $M = 2$, i.e., two-population networks with each population consisting of N oscillators. As we discussed in Chap. 2, the dynamics of each oscillator is fully described by its phase $\phi_j^{(a)}(t) \in \mathbb{T} = [-\pi, \pi)$ for $j = 1, ..., N$ and $a = 1, 2$. Then, the oscillators are governed by

$$\partial_t \phi_j^{(a)} = \omega_a + \mathrm{Im}\left[H_a(t) e^{-i\phi_j^{(a)}} \right] \tag{3.1}$$

for $a = 1, 2$. Here, the forcing field that affects each oscillator in population a is defined by

$$H_a(t) := \sum_{b=1}^{M} G_{ab} \Gamma_b(t) e^{-i\alpha} \tag{3.2}$$

where the Kuramoto order parameter is given by

$$\Gamma_a(t) = r_a(t)e^{i\Theta_a(t)} := \frac{1}{N}\sum_{k=1}^{N} e^{i\phi_k^{(a)}(t)} \tag{3.3}$$

for $a = 1,2$ and the coupling strength matrix reads $G_{11} = G_{22} = \mu$ and $G_{12} = G_{21} = \nu$ with $\mu > \nu$. The parameter ν and μ are the inter- and intra-population coupling strengths, respectively (see Fig. 5.1). Notice that all the oscillators are identical within each population, i.e., they have the same intrinsic frequency $\omega_a = 0$ for $a = 1,2$ and the same phase-lag parameter $\alpha = \pi/2 - \beta$ where β is small enough for chimera states to exist [170]. More specifically, the governing equations can be rewritten as

$$\partial_t \phi_j^{(1)}(t) = \omega_1 + \frac{\mu}{N}\sum_{k=1}^{N}\sin(\phi_k^{(1)} - \phi_j^{(1)} - \alpha) + \frac{\nu}{N}\sum_{k=1}^{N}\sin(\phi_k^{(2)} - \phi_j^{(1)} - \alpha) \tag{3.4}$$

for the oscillators $\phi_j^{(1)}$ in the first population for $j = 1,...,N$, and those of the second population read

$$\partial_t \phi_j^{(2)}(t) = \omega_2 + \frac{\mu}{N}\sum_{k=1}^{N}\sin(\phi_k^{(2)} - \phi_j^{(2)} - \alpha) + \frac{\nu}{N}\sum_{k=1}^{N}\sin(\phi_k^{(1)} - \phi_j^{(2)} - \alpha) \tag{3.5}$$

for $j = 1,...,N$. For the sake of simplicity, we rescale time to set $\mu + \nu = 1$ and define $A = \mu - \nu$ as the control parameter. Throughout this work, we fix $\beta = 0.08$ and A to be either 0.2 (stationary chimera states) or 0.35 (breathing chimera states) [72]. In this system, a chimera state is characterized by one perfectly synchronized oscillator population with $r_{\text{sync}}(t) = 1$ and one (partially) incoherent oscillator population, i.e., $0 < r_{\text{incoh}}(t) < 1$ [74].

Numerical integration of Eqs. (3.4-3.5) shows that the chimera trajectories can be classified according to the type of initial conditions as well as to the motion of the order parameter. If a trajectory starts from a PIC[1], the modulus of the order parameter dynamics of the chimera state shows a simple, regular motion, as depicted in Fig. 3.2. More specifically, for large N as in Fig. 3.2 (b,d), the modulus of the Kuramoto order parameter for the incoherent population, i.e., $r_{\text{incoh}}(t)$, is either stationary in time (Fig. 3.2 (b)) or exhibits a periodic oscillation (Fig. 3.2 (d)), depending on the value of A. These chimera dynamics were termed stationary and breathing chimeras, respectively [72]. Note that for large sized N, $r_{\text{incoh}}(t)$ is virtually indistinguishable from the OA dynamics in the thermodynamic limit (see Ref. [72, 74]). For

[1]The detailed description of ICs and how one can obtain it will be given in the next section.

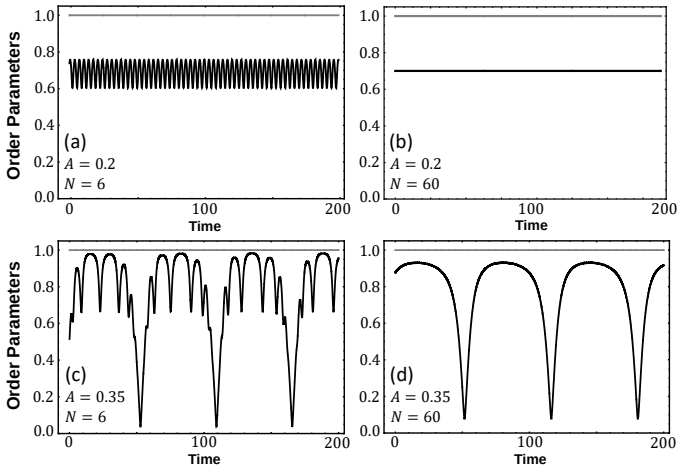

Fig. 3.2 The magnitudes of Kuramoto order parameters $r(t)$ of the coherent and incoherent populations of chimera states in the two-population network starting from PICs after transients have died out ($t \geq 10^5$). For each figure, the gray solid line indicates the order parameter for the perfectly synchronized population $(r(t) = 1)$ and the black solid line the incoherent population $(r(t) < 1)$: (a-b) Stationary chimera states with $A = 0.2$ and (c-d) breathing chimera states with $A = 0.35$ for the system sizes $N = 6$ (left) and $N = 60$ (right), respectively.

small N, as in Fig. 3.2 (a,c), $r_{\text{incoh}}(t)$ is composed of two contributions: the motion of the OA dynamics and a superimposed secondary oscillation along the OA dynamics[2].

In contrast, a chimera trajectory initiated from an n-PIC shows a rather complicated motion of $r_{\text{incoh}}(t)$, strongly depending on the given initial condition (Fig. 3.3). This initial condition dependence of $r_{\text{incoh}}(t)$ has been pointed out previously [73, 101, 72, 88], and many authors have exploited rather special initial conditions for their chimera studies [72, 74]. Below, we will address the initial condition dependence of chimera states in more detail, and classify the chimera states according to the concept of *Poisson and non-Poisson chimeras*.

3.1.2 Poisson and Non-Poisson Chimeras

To obtain a PIC for a finite-sized ensemble, we first consider the thermodynamic limit where the Ott-Antonsen ansatz works. The OA manifold can be approached by considering uniformly distributed constants of motion with $N \to \infty$ and applying the WS transformation. Then, the phase density function can be written as a Fourier series expansion where the n-th coefficient is the n-th power of the first coefficient, i.e., the Kuramoto order parameter. Hence, for each population and $|z_a| < 1$, the phase density function in the OA manifold can

[2]Note that throughout this chapter, we name each chimera state according to its dynamics in the thermodynamic limit at the given parameter set for the sake of simplicity.

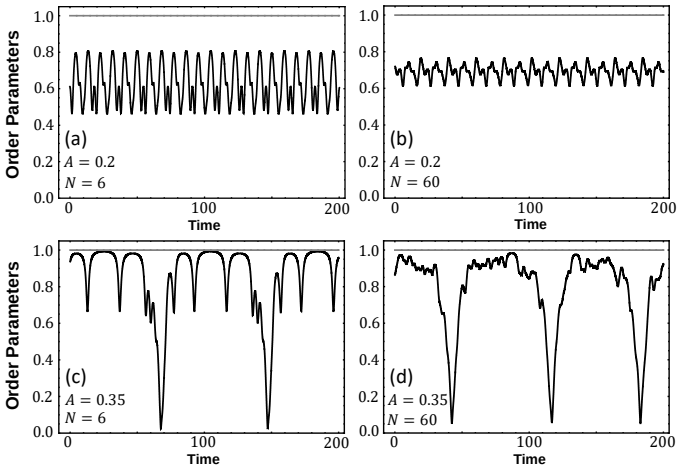

Fig. 3.3 The magnitudes of Kuramoto order parameters $r(t)$ of the coherent and incoherent populations of chimera states in the two-population network starting from n-PICs after transients have died out ($t \geq 10^5$). For each figure, the gray solid line indicates the order parameter for the perfectly synchronized population $(r(t) = 1)$ and the black solid line the incoherent population $(r(t) < 1)$: (a-b) $A = 0.2$ (for which with PICs stationary chimeras are obtained) and (c-d) $A = 0.35$ (for which with PICs breathing chimeras are obtained) for the system sizes $N = 6$ (left) and $N = 60$ (right), respectively.

be written as

$$f_a(\phi^{(a)},t) = \frac{1}{2\pi}\left[1+\sum_{n=1}^{\infty}\left(z_a^n(t)e^{-in\phi^{(a)}}+c.c.\right)\right] = \frac{1}{2\pi}\frac{1-|z_a|^2}{1-2|z_a|\cos(\phi-\arg z_a)+|z_a|^2} \tag{3.6}$$

for $a = 1,2$. Note that for $|z_a| \to 1^-$ the phase distribution function $f_a(\phi^{(a)},t) = \delta(\phi^{(a)} - \arg z_a)$ is the Dirac delta distribution, reflecting synchronization (see Sec. 2.4). The Ott-Antonsen equation can then be written as

$$\partial_t z_a(t) = i\omega_a z_a(t) + \frac{1}{2}H_a(t) - \frac{1}{2}z_a(t)^2\overline{H_a(t)} \tag{3.7}$$

for $a = 1,2$. Here, we can write H_a in terms of z_a

$$\begin{aligned} H_2 e^{i\alpha} &= \mu\Gamma_2 + \nu\Gamma_1 = \mu\int_{\mathbb{T}} f_2(\phi^{(2)},t)e^{i\phi^{(2)}}d\phi^{(2)} + \nu\int_{\mathbb{T}} f_1(\phi^{(1)},t)e^{i\phi^{(1)}}d\phi^{(1)} = \mu z_2 + \nu z_1 \\ H_1 e^{i\alpha} &= \mu\Gamma_1 + \nu\Gamma_2 = \mu\int_{\mathbb{T}} f_1(\phi^{(1)},t)e^{i\phi^{(1)}}d\phi^{(1)} + \nu\int_{\mathbb{T}} f_2(\phi^{(2)},t)e^{i\phi^{(2)}}d\phi^{(2)} = \mu z_1 + \nu z_2. \end{aligned} \tag{3.8}$$

Finally, the OA equation can be rewritten in a closed form

$$\begin{aligned}\partial_t z_2 &= i\omega z_2 + \frac{e^{-i\alpha}}{2}(\mu z_2 + \nu z_1) - \frac{e^{i\alpha}}{2} z_2^2(\mu \overline{z_2} + \nu \overline{z_1}) \\ \partial_t z_1 &= i\omega z_1 + \frac{e^{-i\alpha}}{2}(\mu z_1 + \nu z_2) - \frac{e^{i\alpha}}{2} z_1^2(\mu \overline{z_1} + \nu \overline{z_2}).\end{aligned} \tag{3.9}$$

If we restrict the dynamics to a chimera state with $|z_1| = 1$, $|z_2| = \rho$, and $\varphi := \Phi_1 - \Phi_2$, the governing equations become a set of ODEs in terms of the radial and the phase variables which reads

$$\begin{aligned}\partial_t \rho &= \frac{1-\rho^2}{2}\big(\mu\rho\cos\alpha + \nu\cos(\varphi-\alpha)\big), \\ \partial_t \varphi &= \frac{1+\rho^2}{2\rho}\big(\mu\rho\sin\alpha - \nu\sin(\varphi-\alpha)\big) - \nu\sin\alpha - \nu\rho\sin(\varphi+\alpha).\end{aligned} \tag{3.10}$$

This equation has a fixed point solution corresponding to a stationary chimera state at the given parameter set, e.g., $A = 0.2$ and $\alpha = \frac{\pi}{2} - 0.08$.

As discussed above, for finite N, we need a specific initial condition, called a PIC, to study the simpler dynamics of the chimera state as depicted in Fig. 3.2. The PIC is defined and obtained as follows. The incoherent phases are generated from the normalized Poisson kernel (Eq. (3.6)) that corresponds to the Poisson submanifold for N initial phases. Thus, we first solve the 2D Ott-Antonsen reduced equations in Eq. (3.10) for the incoherent population. In this chapter, we consider the stationary chimera state with the parameter set $A = 0.2$ and $\beta = 0.08$ that results in $\rho = 0.69998$ and $\varphi = 6.11918$ from Eq. (3.10). Then, consider the Poisson kernel

$$f(\phi;\rho,\varphi) = \frac{1}{2\pi}\left[1 + \sum_{n=1}^{\infty}\left(\left(ze^{-i\phi}\right)^n + \text{c.c.}\right)\right] = \frac{1}{2\pi}\frac{1-\rho^2}{1-2\rho\cos(\phi-\varphi)+\rho^2} \tag{3.11}$$

where $z = \rho e^{i\varphi}$. For the finite-sized ensembles, we want the initial incoherent phase distribution $\{\phi_j(0)\}_{j=1}^N$ to be as close as possible to Eq. (3.11). To obtain such initial conditions, we use equally spaced probabilities as arguments of the inverse cumulative distribution function (CDF) of the normalized Poisson kernel. Then, the initial phases can be numerically obtained from

$$\frac{j-\frac{1}{2}}{N} = \int_{-\pi}^{\phi_j(0)} \frac{1}{2\pi}\frac{1-\rho^2}{1-2\rho\cos(\phi-\varphi)+\rho^2} d\phi \tag{3.12}$$

for $j = 1, ..., N$ where ρ and φ are the solutions to Eq. (3.10). For the perfectly synchronized population, the initial phases $\{\phi_j(0)\}_{j=1}^{N}$ are picked from the delta distribution $f(\phi) = \delta(\phi - \phi_0)$ where $\phi_0 \in \mathbb{T}$. In contrast, an n-PIC can be obtained by considering initial phases $\{\phi_i(0)\}_{i=1}^{2N}$ that are randomly and mutually independently picked up from the uniform distribution within $\mathbb{T}$.

Starting from PICs, the modulus of the Kuramoto order parameter exhibits different features, depending on the population size N. For large N, $r_{\text{incoh}}(t)$ is virtually nothing but the OA dynamics, i.e., the dynamics of the OA radial variable $|z_{\text{incoh}}| = \rho_{\text{incoh}}$ [72]. For small N, the motion of the Kuramoto order parameter $r_{\text{incoh}}(t)$ is comprised of the motion close to the OA dynamics plus the motion superimposed by a regular secondary oscillation (Fig. 3.2 a,c). It looks rather regular and does not seem to be comprised of irregular small-size fluctuations, as discussed in the literature Ref. [74]. We therefore conjecture that the secondary oscillation of the small-size chimera states has a deterministic origin.

To show the deterministic origin of the secondary oscillation of the small-sized PIC-started chimera dynamics, we first focus on the stationary chimera states with $A = 0.2$. For the small-sized ensembles, the Watanabe-Strogatz macroscopic dynamics is given by Eq. (2.126) or Eq. (2.79) with $M = 2$. Then, for $A = 0.2$, we obtain a stationary chimera state characterized by $\rho_1 = 1$, $\rho_2 = \rho < 1$, $\partial_t \Phi_a = \Omega$ for $a = 1, 2$, and $\partial_t \Psi_1 = 0$, $\partial_t \Psi_2 = \tilde{\Omega}$ when the constants of motion are uniformly distributed, i.e., $\psi_j^{(a)} = -\pi + \frac{2\pi(j-1)}{N}$ for $j = 1, ..., N$ and $a = 1, 2$. Note that a PIC of the microscopic dynamics corresponds to the uniform constants of motion in the WS dynamics, and both characterize the Poisson submanifold (a manifold as close as possible to the OA manifold for finite-N). For the moment, we assume that the second population is incoherent whereas the first population is synchronized. Using the relation between the Kuramoto order parameter and the WS variables in Eq. (2.77), we observe that the secondary oscillation occurs around the value of $\rho_2(t) = \rho$, as obtained from the Kuramoto order parameter measured from the microscopic individual oscillators (3.3). This secondary oscillation is suppressed as $N \to \infty$ since both the amplitude (Fig. 3.4 (a)) and the period (Fig. 3.4 (b)) of the secondary oscillation decrease with N increasing. This phenomenon can be understood as follows. First, pertaining to the decreasing amplitude, the

Kuramoto order parameter from Eq. (2.77) can be written as

$$\begin{aligned} r_2(t) &= |\Gamma_2(t)| = \rho_2(t)|\gamma_2(\rho_2,\Psi_2)| \\ &= \rho_2\left|1+(1-\rho_2^{-2})(-\rho_2)^N\frac{e^{i(2\pi-N\Psi_2)}}{1-(-\rho_2)^N e^{i(2\pi-N\Psi_2)}}\right| \\ &= \Bigg|\underbrace{\rho_2}_{\text{OA dynamics}} \underbrace{+\rho_2(1-\rho_2^{-2})(-\rho_2)^N\frac{e^{i(2\pi-N\Psi_2)}}{1-(-\rho_2)^N e^{i(2\pi-N\Psi_2)}}}_{\text{secondary oscillation}}\Bigg|. \end{aligned} \tag{3.13}$$

Thus, as $N\to\infty$, the amplitude of the secondary oscillation in the modulus of Kuramoto order parameter goes to zero since $(1-\rho_2^{-2})(-\rho_2)^N\to 0$ for $\rho_2<1$, and approaches the OA dynamics: $r_2(t)\to\rho_2=\rho$ (See Fig. 3.4 (d)).

Next, concerning the decreasing period, the inverse WS transformation in Eq. (2.38) directly produces a time derivative of each phase variable that reads

$$\dot\phi_j^{(a)}(t) = \dot\Phi_a - \frac{1-\rho_a^2}{1+\rho_a^2+2\rho_a\cos(\psi_j^{(a)}-\Psi_a)}\left(\dot\Psi_a+\frac{2\dot\rho_a}{1-\rho_a^2}\sin(\psi_j^{(a)}-\Psi_a)\right) \tag{3.14}$$

where the constants of motion $\psi_j^{(a)}$ are uniformly distributed in $[-\pi,\pi]$ for $a=1,2$ and $j=1,\ldots,N$. Plugging $\rho_2=\rho$, $\partial_t\Phi_2(t)=\Omega$ and $\Psi_2(t)=\tilde\Omega t+\Psi_2(0)$ from the WS dynamics into Eq. (3.14), we obtain the instantaneous phase velocities of the incoherent, i.e., second population as

$$\begin{aligned} \dot\phi_j^{(2)}(t) &= \Omega - \frac{\tilde\Omega(1-\rho_2^2)}{1+\rho_2^2+2\rho_2\cos(\psi_j^{(2)}-\tilde\Omega t-\Psi_2(0))} \\ &= \Omega - \frac{\tilde\Omega(1-\rho_2^2)}{1+\rho_2^2+2\rho_2\cos(\psi_j^{(2)}-\tilde\Omega(t-\frac{2\pi}{\tilde\Omega})+\Psi_2(0))} \\ &= \dot\phi_j^{(2)}(t-T) \quad \text{where } T:=\frac{2\pi}{|\tilde\Omega|} \end{aligned} \tag{3.15}$$

for $j=1,\ldots,N$. From the above equation, we find three properties of the instantaneous phase velocities of the incoherent oscillators:

- (i) The instantaneous phase velocity of each oscillator is a periodic function with the period $T=\frac{2\pi}{|\tilde\Omega|}$.
- (ii) All of them have the same functional form due to identical values of the three WS variables (ρ_0,Ω and $\tilde\Omega$).

- (iii) They are equally shifted within a period T due to the uniform constants of motion.

From this fact, we can assume $\dot{\phi}_i^{(2)}(t-\frac{j}{N}T)=\dot{\phi}_{i+j}^{(2)}(t)$ for an arbitrary $j\in\{1,...,N\}$, which gives $\phi_i^{(2)}(t-\frac{1}{N}T)=\phi_{i+1}^{(2)}(t)+C$ for $i=1,...,N$ with $\phi_{N+1}^{(2)}\equiv\phi_1^{(2)}$ where $C\in\mathbb{R}$ is a constant. This assumption leads to

$$\begin{aligned} r_2(t)=|\Gamma_2(t)| &= \left|\frac{1}{N}\sum_{k=1}^{N}e^{i\phi_{k+1}^{(2)}(t)}\right| = \left|\frac{e^{-iC}}{N}\sum_{k=1}^{N}e^{i\phi_k^{(2)}(t-\frac{T}{N})}\right| = \left|\frac{1}{N}\sum_{k=1}^{N}e^{i\phi_k^{(2)}(t-\frac{T}{N})}\right| \\ &= r_2\left(t-\frac{T}{N}\right)=r_2(t-\tau) \end{aligned} \tag{3.16}$$

where the period is given as $\tau=\frac{T}{N}=\frac{2\pi}{|\tilde{\Omega}|N}$. Numerical integration of Eqs. (3.4-3.5) with PICs reveals that the instantaneous velocity of each incoherent oscillator $\{\dot{\phi}_j^{(2)}(t)\}_{j=1}^N$ indeed satisfies the three properties depicted above (see Fig. 3.4 (e)). Thus, $r_{\rm incoh}(t)$ is indeed a periodic function and its period $\tau=\frac{2\pi}{|\tilde{\Omega}|N}$ is smoothly vanishing as N increases. In Fig. 3.4 (b), the numerically obtained period (τ) of the Kuramoto order parameter is plotted as a function of N together with the values predicted above ($\tau=\frac{T}{N}$). The good agreement of both values verifies that the period $\tau(N)$ of the regular oscillation in the Kuramoto order parameter is indeed decreasing with N following the curve T/N. Note that for $N\gtrsim 24$, the secondary oscillation does not appear prominently but rather $r_{\rm incoh}(t)$ displays a motion indistinguishable from that of the OA dynamics in the thermodynamic limit. We therefore classify chimeras with population sizes $N\gtrsim 24$ as large-size chimeras, and those with $N<24$ as small-size chimeras. In conclusion, we find a continuous change from the small-size to the large-size chimeras. Furthermore, the Poisson chimeras eventually approach the OA dynamics in the thermodynamic limit as $N\to\infty$, in that the period and the amplitude of the secondary oscillation of $r_{\rm incoh}(t)$ continuously decrease as the system size increases.

On the other hand, one can initiate the dynamics from an n-PIC. In this case, we observe that for the same parameter set ($A=0.2$ and β=0.08) which yields stationary chimera states the order parameter no longer exhibits a simple, regular dynamics, which is qualitatively different from that of the chimeras from a PIC. The specific irregular shape of the magnitude of the order parameter for the incoherent population depends on a given set of randomly generated initial phases. In Fig. 3.3, the time evolutions of the modulus of the Kuramoto order parameters are shown for n-PICs. The motion of $r_{\rm incoh}(t)$ looks more complicated in all four cases, compared to those in Fig. 3.4. In particular, the fluctuations of $r_{\rm incoh}(t)$ are no longer a combination of the OA dynamics and the superimposed secondary oscillation. Furthermore, such an irregularity does not disappear for large N. This is consistent with the observation that the instantaneous phase velocities of the incoherent oscillators $\{\dot{\phi}_j^{(2)}(t)\}_{j=1}^N$ do not

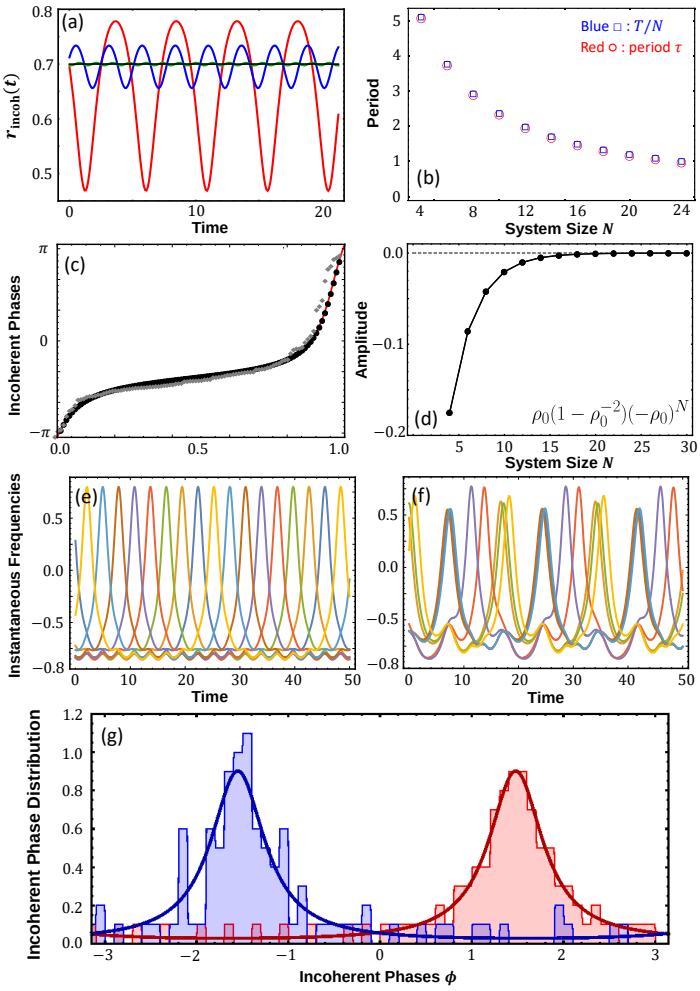

Fig. 3.4 (a) Oscillations of the magnitude of the order parameter for $A = 0.2$ and different system sizes: $N = 4$ (red), $N = 8$ (blue), $N = 16$ (green), and $N = 32$ (black). (b) Period of $r_{\mathrm{incoh}}(t)$ as determined numerically (red) and predicted from Eq. (3.16) as a function of the system size N. (c) Snapshot of the sorted incoherent phases in the numerical order with $N = 100$ as a function of the rescaled index after a time $t \geq 10^6$ for a Poisson chimera (black dots), a non-Poisson chimera (gray diamonds) and the theoretical curve of the inverse CDF of Poisson kernel (red solid curve). (d) Magnitude of the secondary oscillation as a function of system size. (e,f) Instantaneous frequencies of the incoherent oscillators of the system $N = 8$ for a Poisson chimera (e) and a non-Poisson chimera (f). (g) Snapshot of the incoherent phase distribution for a Poisson chimera (red) and the non-Poisson chimera (blue) for $t \geq 10^6$ with $N = 100$ oscillators. Each solid line indicates the theoretical Poisson kernel curve corresponding to ρ_0 within an appropriate rotating frame.

follow the above discussed three characteristics of chimeras starting from a PIC (Fig. 3.4 (f)). As discussed above, an n-PIC corresponds to nonuniform constants of motion. Thus, we conclude that the dynamics lives outside the Ott-Antonsen manifold in the thermodynamic

limit and the Poisson submanifold for the finite-sized ensemble, respectively. This is in line with literature results on the dynamics of chimera states in two-population networks of identical Kuramoto-Sakaguchi oscillators [101, 102, 72]. For example, with nonuniform constants of motion, a quasiperiodic chimera motion can be obtained, which does not exist in the OA manifold [72]. Hence, such a quasiperiodic chimera state can be classified as a non-Poisson chimera state.

We can numerically check whether a given chimera trajectory indeed lives on or outside the Poisson submanifold. In Fig. 3.4 (g), the red distribution illustrates that if the chimera trajectory starts from a PIC, then the incoherent phases of this chimera state remain distributed in the normalized Poisson kernel. This can be numerically confirmed by the observation that the incoherent phases sorted in ascending order of their values and plotted vs. the rescaled index (normalized to the total number of oscillators) coincide with the inverse CDF of Eq. (3.11) (Fig. 3.4 (c), black dots). This observation is in line with the fact that the OA manifold is invariant under the dynamics in the thermodynamic limit [95–97]. For the finite-sized chimeras, the numerical results verify that the finite-sized Poisson submanifold is also invariant under the dynamics along the PIC-started chimera dynamics. To show this, let us define

$$E(t) = \left| \langle e^{i\phi(t)} \rangle^2 - \langle e^{2i\phi(t)} \rangle \right| \tag{3.17}$$

where $\langle \cdot \rangle$ is the ensemble average, i.e., $\langle e^{im\phi(t)} \rangle := \frac{1}{N} \sum_{k=1}^{N} e^{im\phi_k(t)}$ for $m \in \mathbb{N}$. If a phase distribution follows the normalized Poisson kernel, this quantity is zero since the Poisson kernel is characterized by the fact that n-th Fourier coefficients (n-th Daido order parameter) are nothing but the n-th power of the first coefficient (the Kuramoto order parameter). Therefore, $E(t) = 0$ in the OA manifold for infinite-N or Poisson submanifold for finite-N. For large enough N, $E(t)$ of the PIC-started chimera trajectory is numerically found to be close to zero $E(t) \sim O(10^{-5})$, revealing that the incoherent phases of such chimeras remain in the normalized Poisson kernel. However, the n-PIC-started chimera trajectories do not have the incoherent phase distribution satisfying the normalized Poisson kernel (see Fig. 3.4 (c,g)). After a long enough transient time, we obtain $E(t) \sim O(10^{-1})$ for n-PICs.

So far, we demonstrated that PICs give rise to a particularly simple dynamics. This makes it worthwhile to go a step further and define a *Poisson chimera state* in two-population networks as follows: A chimera trajectory is called a Poisson chimera if the phases $\{\phi_i^{(a)}(t)\}_{i=1}^{N}$ of a given ensemble of oscillators satisfy the following two dynamical characteristics for $a = 1, 2$[3]:

[3]Note that the Poisson chimeras were originally characterized by three conditions in Ref. [55]. However, the third condition is not necessary to distinguish Poisson and non-Poisson chimera states in the context of this thesis.

Condition 1. One population is perfectly synchronized and invariant.

Condition 2. The other population consists of incoherent phases that remain distributed according to the normalized Poisson kernel or at least in a close vicinity of the Poisson submanifold.

Chimera states in two-population networks that do not fulfill **Conditions 1 - 2** are termed *a non-Poisson chimera state*. As demonstrated above, the Poisson chimera state can be obtained from a PIC for the finite-sized microscopic dynamics or uniform constants of motion for the WS dynamics, whose incoherent phases live in the Poisson submanifold since the Poisson submanifold is invariant. On the other hand, the non-Poisson chimera state can be obtained from an n-PIC or with nonuniform constants of motion, the incoherent oscillators of which reside outside the Poisson submanifold.

3.2 Stability of Poisson and Non-Poisson Chimeras

Thus far, we have discussed the dynamical properties of the observable chimera states and classified them according to the properties of the incoherent oscillators. In this section, we investigate the spectral properties of Poisson and non-Poisson chimeras. To this end, we consider the chimera state as the reference trajectory in the phase space, from which we will explore the tangent space dynamics. We numerically determine the Lyapunov exponents associated with the synchronized manifold and also the corresponding covariant Lyapunov vectors. Furthermore, we will classify them and approximate the values of the Lyapunov exponents exploiting the network symmetry analysis [47, 46]. For the incoherent oscillators, we will explain them by recalling the WS dynamics.

3.2.1 Network Symmetry Analysis: General Description

Let us first discuss how one can study the stability of the synchronized oscillators by taking a look at the structure of the network topology. The two-population network topology can be considered a finite-sized network with $2N$ nodes. Recently, many authors have focused on various network topologies to investigate the dynamics of a variety of coupled oscillators on a given finite-sized network with abundant discrete symmetries [171, 172, 48, 173–175]. For such symmetric network topologies, one can exploit the symmetries of the network to identify various cluster patterns of the coupled oscillators and determine their stability.

Such discrete network symmetries are represented by the automorphism group of a network [46, 47, 176, 177]. *The automorphism group* denoted by $\mathrm{Aut}(\mathscr{G})$ of the network

$\mathscr{G}$ is a mathematical group consisting of all the automorphisms. Here, *an automorphism* indicates a permutation σ of the set of nodes that preserve the adjacency relation between the nodes, i.e., $A_{ij} = A_{\sigma(i)\sigma(j)}$ for all i, j [177]. Then, we can consider the group action on the nodes under a subgroup $G \leq \mathrm{Aut}(\mathscr{G})$, which defines *an orbit partition* of a given network $\mathscr{G}$ under the subgroup G, i.e., $\varphi(G,i) = \{\sigma(i) | \sigma \in G\}$, which (mathematically) partitions the set of nodes according to $\varphi(G,i) = \varphi(G,j)$ for all $j \in \varphi(G,i)$, and $\varphi(G,i) \cap \varphi(G,j) = \emptyset$ if $j \notin \varphi(G,i)$. This partition of a network could be a candidate of a cluster synchronization (CS) pattern of the dynamical objects that are coupled via the network topology [46, 172, 47, 48][4]. It is due to an orbit partition of a network where each oscillator in the same orbit (cluster) should receive the same input from the others. Note that every orbit partition of a network is an *equitable partition*. However, there are equitable partitions of a network that are not orbit partitions [177].

For concrete examples, let us consider two different types of governing equations. The first one is called here the Pecora-type equation [47, 48, 172] and governed by

$$\partial_t \mathbf{x}_i(t) = \mathbf{F}(\mathbf{x}_i(t)) + K \sum_{j=1}^{N} A_{ij} \mathbf{H}(\mathbf{x}_j(t)) \tag{3.18}$$

and the other one is called the Kuramoto-type equation and is governed by

$$\partial_t \mathbf{x}_i(t) = \mathbf{F}(\mathbf{x}_i(t)) + K \sum_{j=1}^{N} A_{ij} \mathbf{H}(\mathbf{x}_j(t) - \mathbf{x}_i(t)) \tag{3.19}$$

for $i = 1, ..., N$ where N is the number of oscillators. Here, $\mathbf{x}_i(t) \in \mathbb{R}^n$ denotes the dynamical variable, $\mathbf{F}(\mathbf{x})$ characterizes the uncoupled local dynamics, i.e., the dynamics of a building block. The coupling function is denoted by $\mathbf{H}$, and K denotes the coupling strength. The network topology is given by the adjacency matrix A_{ij}.

Assume that we have a CS pattern candidate according to an orbit partition of the network. Then, we can denote the set of all clusters as $\{\varphi(i,G)\}_{i=1}^{N} = \{C_m\}_{m=1}^{M}$ where M is the total number of clusters, including *trivial clusters* that are composed of a single oscillator. Then, the coarse-grained CS dynamics is described by the variables $\{\mathbf{s}_m(t) = \mathbf{x}_i(t) | i \in C_m, 1 \leq m \leq M\}$ under the quotient adjacency matrix $\tilde{A}_{mm'} = \sum_{j \in C_{m'}} A_{ij}$ for an arbitrary node $i \in C_m$. The element of the quotient adjacency matrix $\tilde{A}_{mm'}$ is nothing but the number of links from an arbitrary node in C_m to all the nodes in $C_{m'}$. Note again that we can choose an arbitrary node in C_m since all the nodes in C_m receive the same input from $C_{m'}$. Hence, the quotient

[4] For the details, see the Supplemental Materials of Ref. [46].

(coarse-grained) dynamics of the CS pattern reads

$$\begin{aligned}\partial_t \mathbf{s}_m(t) &= \mathbf{F}(\mathbf{s}_m(t)) + K\sum_{m'=1}^{M}\tilde{A}_{mm'}\mathbf{H}(\mathbf{s}_{m'}(t)) \\ \partial_t \mathbf{s}_m(t) &= \mathbf{F}(\mathbf{s}_m(t)) + K\sum_{m'=1}^{M}\tilde{A}_{mm'}\mathbf{H}(\mathbf{s}_{m'}(t)-\mathbf{s}_m(t))\end{aligned} \tag{3.20}$$

for $m = 1,...,M$. Note that the dynamics of each cluster depends on all the other clusters that are connected through the quotient adjacency matrix $\tilde{A}$. This means that the stability of a cluster also could depend on the dynamics of other linked clusters. However, under an appropriate condition, one can study the stability of one cluster independently of others even though they are linked. To this end, we follow below the results of Ref. [46].

First, we introduce so-called *cluster-based coordinates* [46]. The set of N-dimensional orthonormal vectors $\{\mathbf{u}_\kappa^{(m)} \in \mathbb{R}^N\}_{\kappa=1}^{|C_m|}$ for $m = 1,...,M$ are called the *cluster-based coordinates* if they satisfy the following rules [46]:

- (i) $u_{\kappa i}^{(m)} = 0$ if $i \notin C_m$.
- (ii) For $\kappa = 1$, all the nonzero elements of $\mathbf{u}_1^{(m)}$ should be $1/\sqrt{|C_m|}$, which indicates the sync-manifold of the cluster C_m.
- (iii) The other vectors $\{\mathbf{u}_\kappa^{(m)}\}_{\kappa=2}^{|C_m|}$ are mutually orthogonal and also orthogonal to $\mathbf{u}_1^{(m)}$. Hence, they indicate the transverse directions to the sync-manifold of C_m.

Here, $|C_m|$ is the number of nodes in a C_m cluster. The cluster-based coordinates not only can block-diagonalize the adjacency matrix according to the given cluster pattern but also can be chosen to be eigenvectors of it [46].

To study the spectral properties of the quotient dynamics of each cluster, we consider the given CS pattern as the reference trajectory in phase space. Then, we add a small perturbation on them. This yields the following variational equation of an oscillator coupled to the oscillators in other clusters

$$\partial_t \delta\mathbf{x}_i(t) = D\mathbf{F}(\mathbf{s}_m)\delta\mathbf{x}_i + K\sum_{m'=1}^{M}\sum_{j\in C_{m'}} A_{ij}D\mathbf{H}(\mathbf{s}_{m'})\delta\mathbf{x}_j \tag{3.21}$$

for $i = 1,...,N$. Here, we consider the Pecora-type model where $\delta\mathbf{x}_i(t) = \mathbf{x}_i(t) - \mathbf{s}_m(t)$ for $i \in C_m$ and $D\mathbf{F}$ and $D\mathbf{H}$ indicate the Jacobian matrices of the given dynamical functions. Using the cluster-based coordinates such that $\boldsymbol{\eta}_\kappa^{(m)} = \sum_{i\in C_m} u_{\kappa i}^{(m)}\delta\mathbf{x}_i$ for $m = 1,...,M$ and $\kappa = 2,...,|C_m|$, we obtain $\boldsymbol{\eta}_\kappa^{(m)}$ for $\kappa \geq 2$, which represents the perturbation of the transverse

direction to the cluster C_m. Furthermore, in the cluster-based coordinates, the adjacency matrix takes a bock-diagonal form where each block corresponds to an ISC (independently synchronizable cluster, see Ref. 6.2) or an ISC set. Therefore, if the cluster C_m is an ISC, then the transversal variational equations of $\boldsymbol{\eta}_\kappa^{(m)}(t)$ become independent of $\boldsymbol{\eta}_\kappa^{(m')}$ for the other clusters $C_{m'}$. Thus, the $|C_m|-1$ transversal variational equations of the cluster C_m are given by [46]

$$\begin{aligned}\partial_t \boldsymbol{\eta}_\kappa^{(m)}(t) &= \left[D\mathbf{F}(\mathbf{s}_m) + K\lambda_\kappa^{(m)} D\mathbf{H}(\mathbf{s}_m)\right]\boldsymbol{\eta}_\kappa^{(m)}(t) \\ \partial_t \boldsymbol{\eta}_\kappa^{(m)}(t) &= \left[D\mathbf{F}(\mathbf{s}_m) - K\sum_{m'=1}^{M}\tilde{A}_{mm'} D\mathbf{H}(\mathbf{s}_{m'}-\mathbf{s}_m) + K\lambda_\kappa^{(m)} D\mathbf{H}(0)\right]\boldsymbol{\eta}_\kappa^{(m)}(t) \qquad (3.22)\end{aligned}$$

for $\kappa = 2,\ldots,|C_m|$, where $\lambda_\kappa^{(m)}$ is the eigenvalue of the adjacency matrix. The eigenvalues have corresponding eigenvectors $\mathbf{u}_\kappa^{(m)}$ associated with the cluster C_m since the cluster-based coordinates can be chosen to be the eigenvectors of the adjacency matrix [46, 172]. From the transversal variational equations, we can explore the spectral information, in particular, the stabilirt of the transverse direction of the synchronization manifold along our chimera trajectory.

3.2.2 Network symmetry Analysis: Application to Kuramoto-Sakaguchi Oscillators in Two-population Networks

In the following, we apply the above general description of network symmetry analysis to the system of identical Kuramoto-Sakaguchi oscillators in two-population networks. In particular, we will consider chimera states. Note that a chimera state can be interpreted as a CS pattern where the synchronized population is treated as one giant cluster C_0 while the incoherent population consists of N trivial clusters C_m with $m = 1,\ldots,N$. This leads us to the corresponding cluster-based coordinates $U^\top = [\mathbf{u}_1^{(0)}, \mathbf{u}_1^{(1)},\ldots,\mathbf{u}_1^{(N)}, \mathbf{u}_2^{(0)},\ldots,\mathbf{u}_N^{(0)}]$ for the chimera pattern discussed in Sec. 3.2.1. Here, $\mathbf{u}_1^{(0)}$ indicates the direction along the synchronized cluster C_0 of the chimera state, so that $u_{1j}^{(0)} = \frac{1}{\sqrt{N}}$ for $j \in C_0$ and $u_{1j}^{(0)} = 0$ if $j \notin C_0$. For the directions transverse to the sync-manifold, we obtain $\sum_{j\in C_0} u_{\kappa j}^{(0)} = 0$ and $u_{\kappa j}^{(0)} = 0$ if $j \notin C_0$ for $\kappa = 2,\ldots,N$. For the incoherent trivial clusters, we obtain $u_{1j}^{(m)} = 1$ if $j \in C_m$; otherwise $u_{1j}^{(m)} = 0$ for $m = 1,\ldots,N$. Hence, a possible candidate of the cluster-based

coordinates of a chimera pattern could be [178]

$$U^{\top} = \left(\begin{array}{c|c|c} \frac{1}{\sqrt{N}} & & \\ \vdots & \mathrm{O}_{N,N} & \mathrm{P} \\ \frac{1}{\sqrt{N}} & & \\ \hline 0 & & \\ \vdots & \mathrm{D} & \mathrm{O}_{N,N-1} \\ 0 & & \end{array}\right) \tag{3.23}$$

where the first column $\mathbf{u}_1^{(0)} = [\frac{1}{\sqrt{N}}, \cdots, \frac{1}{\sqrt{N}}, 0, \cdots, 0]^{\top}$ indicates the sync-manifold direction, $\mathrm{D} = \mathrm{diag}(1, ..., 1) \in \mathbb{R}^{N\times N}$ corresponds to the incoherent trivial clusters, each O is a zero-matrix, and $\mathrm{P} \in \mathbb{R}^{N\times N-1}$ represents the directions transverse to the sync manifold C_0. P is chosen to satisfy orthonormality and transversality conditions such as

$$\mathrm{P} = \begin{pmatrix} \frac{N-1}{\sqrt{N(N-1)}} & 0 & 0 & 0 \\ -\frac{1}{\sqrt{N(N-1)}} & \frac{N-2}{\sqrt{(N-1)(N-2)}} & 0 & 0 \\ -\frac{1}{\sqrt{N(N-1)}} & -\frac{1}{\sqrt{(N-1)(N-2)}} & \ddots & \vdots \\ \vdots & \vdots & \ddots & \frac{1}{\sqrt{2\cdot 1}} \\ -\frac{1}{\sqrt{N(N-1)}} & -\frac{1}{\sqrt{(N-1)(N-2)}} & \cdots & -\frac{1}{\sqrt{2\cdot 1}} \end{pmatrix} \tag{3.24}$$

Considering the chimera states in two-population networks and the corresponding CS pattern (C_0 for the sync population and $\{C_m\}_{m=1}^{N}$ for the incoherent population, respectively), the transversal Lyapunov exponents corresponding to the synchronized cluster C_0 can be analytically approximated. To do so, we first rewrite the governing equation (3.1) as

$$\partial_t \phi_i(t) = \mathrm{F}(\phi_i(t)) + \sum_{j=1}^{2N} K_{ij} B_{ij}^{(c)} \mathrm{H}(\phi_j(t) - \phi_i(t)) \tag{3.25}$$

for $i = 1, ..., 2N$ where the uncoupled dynamics is $\mathrm{F}(\phi) = -\frac{\mu}{N}\sin\alpha$ (here, just a constant as the local dynamics of the Kuramoto-Sakaguchi oscillator is a constant given by the natural frequency) and the coupling function is $\mathrm{H}(x) = \sin(x - \alpha)$. The adjacency matrix $B_{ij}^{(c)} \in \mathbb{R}^{2N\times 2N}$ stands for the complete graph with $2N$ nodes which reflect the topology of the all-to-all intra- and inter-population coupling. However, as we defined in Fig. 5.1, the coupling strengths are different between inter- and intra-populations, which leads us to introduce $K_{ij} = \frac{\mu}{N}$ if i, j belong to the same population, and $K_{ij} = \frac{\nu}{N}$ if i, j belong to different

populations, respectively, for $i,j=1,...,2N$. From the CS pattern $\{C_m\}_{m=0}^{N}$ of the chimera state, the quotient adjacency matrix is given as

$$\tilde{A}=\left(\begin{array}{c|ccc} N-1 & 1 & \cdots & 1 \\ \hline N & & & \\ \vdots & & A^{(c)} & \\ N & & & \end{array}\right) \tag{3.26}$$

where $A^{(c)}\in\mathbb{R}^{N\times N}$ is the adjacency matrix of the complete graph with N nodes that describes the all-to-all intra-population coupling[5]. Therefore, we obtain the (coarse-grained) quotient dynamics corresponding to the chimera pattern from Eq. (3.20) with the quotient variables denoted by $s_0(t)=\phi_i(t)$ (sync., C_0) and $s_m(t)=\phi_{i+N}(t)$ (incoh., C_m) for $m=i=1,...,N$:

$$\begin{aligned}\partial_t s_0(t) &= \mathrm{F}(s_0(t))+\frac{\mu}{N}\mathrm{H}(0)\tilde{A}_{00}+\frac{\nu}{N}\sum_{m'=1}^{N}\tilde{A}_{0m'}\mathrm{H}(s_{m'}(t)-s_0(t)) \\ &= -\mu\sin\alpha+\frac{\nu}{N}\sum_{m'=1}^{N}\sin(s_{m'}(t)-s_0(t)-\alpha)\end{aligned} \tag{3.27}$$

for the synchronized cluster (C_0), and $\mathrm{H}(0)=-\sin\alpha$. The variables of the N trivial clusters ($C_1,...,C_N$) for the incoherent population are governed by

$$\begin{aligned}\partial_t s_m(t) &= \mathrm{F}(s_m)+\frac{\nu}{N}\tilde{A}_{m0}\mathrm{H}(s_0-s_m)+\frac{\mu}{N}\sum_{m'=1}^{N}\tilde{A}_{mm'}\mathrm{H}(s_{m'}-s_m) \\ &= \nu\sin(s_0-s_m-\alpha)+\frac{\mu}{N}\sum_{m'=1}^{N}\sin(s_{m'}-s_m-\alpha)\end{aligned} \tag{3.28}$$

for $m=1,...,N$. Then, we consider the variational equations of the synchronized oscillators around the CS pattern as

$$\begin{aligned}\partial_t\delta\phi_i &= D\mathrm{F}(s_0)\delta\phi_i-\sum_{m'=0}^{N}\sum_{j\in C_{m'}}K_{ij}B_{ij}^{(c)}D\mathrm{H}(s_{m'}-s_0)\delta\phi_i+\sum_{m'=0}^{N}\sum_{k\in C_{m'}}K_{ik}B_{ik}^{(c)}D\mathrm{H}(s_{m'}-s_0)\delta\phi_k \\ &= D\mathrm{F}(s_0)\delta\phi_i-\frac{\mu}{N}\tilde{A}_{00}D\mathrm{H}(0)\delta\phi_i-\frac{\nu}{N}\sum_{m'=1}^{N}\tilde{A}_{0m'}D\mathrm{H}(s_{m'}-s_0)\delta\phi_i+\frac{\mu}{N}\sum_{k\in C_0}B_{ik}^{(c)}D\mathrm{H}(0)\delta\phi_k \\ &\quad+\frac{\nu}{N}\sum_{m'=1}^{N}\sum_{k\in C_{m'}}B_{ik}^{(c)}D\mathrm{H}(s_{m'}-s_0)\delta\phi_k\end{aligned} \tag{3.29}$$

[5]Note that for the quotient adjacency matrix $\tilde{A}\in\mathbb{R}^{(N+1)\times(N+1)}$ in Eq. (3.26), we take the index from 0 to N for the sake of simplicity: $\tilde{A}_{mm'}$ for $m,m'=0,1,...,N$. For example, $\tilde{A}_{00}=N-1$ and $\tilde{A}_{0m'}=1$ for $m'=1,...,N$

for each $i \in C_0$ where the small perturbation to the CS pattern is denoted by $\delta\phi_i(t) = \phi_i(t) - s_m(t)$ for $i \in C_m$ and $m = 0, 1, ..., N$. Next, in the cluster-based coordinate defined in Eq. (3.23), the transverse variables of the sync cluster can be written as $\eta_\kappa^{(0)}(t) = \sum_{i\in C_0} u_{\kappa i}^{(0)} \delta\phi_i(t)$ with $U = [\mathbf{u}_1^{(0)}, \mathbf{u}_1^{(1)}, ..., \mathbf{u}_1^{(N)}, \mathbf{u}_2^{(0)}, ..., \mathbf{u}_N^{(0)}]^\top$. Then, the variational equations transverse to the sync-cluster C_0 read

$$\begin{aligned}
\partial_t \eta_\kappa^{(0)} &= \sum_{i\in C_0} u_{\kappa i}^{(0)} \delta\dot{\phi}_i(t) \\
&= \sum_{i\in C_0} u_{\kappa i}^{(0)} \left(D\mathrm{F}(s_0) - \frac{\mu}{N}\tilde{A}_{00} D\mathrm{H}(0) - \frac{\nu}{N}\sum_{m'=1}^{N} \tilde{A}_{0m'} D\mathrm{H}(s_{m'} - s_0) \right) \delta\phi_i \\
&\quad + \frac{\mu}{N} D\mathrm{H}(0) \sum_{k\in C_0}\sum_{i\in C_0} u_{\kappa i}^{(0)} B_{ik}^{(c)} \delta\phi_k + \frac{\nu}{N}\sum_{m'=1}^{N}\sum_{i\in C_0}\sum_{k\in C_{m'}} u_{\kappa i}^{(0)} B_{ik}^{(c)} D\mathrm{H}(s_{m'} - s_0)\delta\phi_k \\
&= \left(D\mathrm{F}(s_0) - \frac{\mu}{N}\tilde{A}_{00} D\mathrm{H}(0) - \frac{\nu}{N}\sum_{m'=1}^{N} \tilde{A}_{0m'} D\mathrm{H}(s_{m'} - s_0) \right) \eta_\kappa^{(0)} \\
&\quad + \frac{\mu}{N} D\mathrm{H}(0) \sum_{k\in C_0}\sum_{i\in C_0}\sum_{\kappa'=1}^{|C_0|} u_{\kappa i}^{(0)} B_{ik}^{(c)} u_{\kappa' k}^{(0)} \eta_{\kappa'}^{(0)} \\
&\quad + \frac{\nu}{N}\sum_{m'=1}^{N}\sum_{i\in C_0}\sum_{k\in C_{m'}}\sum_{\kappa'=1}^{|C_{m'}|} u_{\kappa i}^{(0)} B_{ik}^{(c)} u_{\kappa' k}^{(m')} D\mathrm{H}(s_{m'} - s_0) \eta_{\kappa'}^{(m')}
\end{aligned} \tag{3.30}$$

for $\kappa = 2, ..., N$. Note that the adjacency matrix $B^{(c)}$ can be block-diagonalized by the cluster-based coordinates, so that the block corresponding to the sync-cluster C_0 can be represented by the matrix $\mathrm{diag}(\lambda_2^{(0)}, \lambda_3^{(0)}, ..., \lambda_N^{(0)}) \in \mathbb{R}^{(N-1)\times(N-1)}$ and the off-diagonal blocks are zero. Hence, the last term in Eq. (3.30) should be zero and we obtain

$$\sum_{i\in C_0}\sum_{k\in C_0} u_{\kappa i}^{(0)} B_{ik}^{(c)} u_{\kappa' k}^{(0)} = \lambda_\kappa^{(0)} \delta_{\kappa\kappa'} \tag{3.31}$$

for $\kappa, \kappa' = 2, ..., N$ where $\lambda_\kappa^{(0)}$ are the eigenvalues of the adjacency matrix and $\mathbf{u}_\kappa^{(0)}$ for $\kappa = 2, ..., N$ are the corresponding eigenvectors of the adjacency matrix [46, 178]. Finally, the transversal variational equations to the sync-manifold are given by

$$\begin{aligned}
\partial_t \eta_\kappa^{(0)} &= \left(D\mathrm{F}(s_0) - \frac{\mu}{N}\tilde{A}_{00} D\mathrm{H}(0) + \frac{\mu}{N}\lambda_\kappa^{(0)} D\mathrm{H}(0) - \frac{\nu}{N}\sum_{m'=1}^{N} \tilde{A}_{0m'} D\mathrm{H}(s_{m'} - s_0) \right) \eta_\kappa^{(0)} \\
&= \left(-\frac{\mu}{N}(N-1)\cos\alpha + \frac{\mu}{N}\lambda_\kappa^{(0)}\cos\alpha - \frac{\nu}{N}\sum_{m'=1}^{N} \cos(s_{m'} - s_0 - \alpha) \right) \eta_\kappa^{(0)}
\end{aligned} \tag{3.32}$$

for $\kappa = 2,...,N$. Notice that for the all-to-all intra- and inter- population network, we obtain the eigenvalues in Eq. (3.32) as $\lambda_{\kappa}^{(0)} = -1$ for all $\kappa = 2,...,N$. For example, the adjacency matrix of the system with $N = 4$ can be block-diagonalized as

$$UB^{(c)}U^{-1} = \left(\begin{array}{ccccc|ccc} 3 & 2 & 2 & 2 & 2 & & & \\ 2 & 0 & 1 & 1 & 1 & & & \\ 2 & 1 & 0 & 1 & 1 & & \mathrm{O}_{5,3} & \\ 2 & 1 & 1 & 0 & 1 & & & \\ 2 & 1 & 1 & 1 & 0 & & & \\ \hline & & & & & -1 & 0 & 0 \\ & \mathrm{O}_{3,5} & & & & 0 & -1 & 0 \\ & & & & & 0 & 0 & -1 \end{array}\right) \tag{3.33}$$

where the lower-right block corresponds to the sync-cluster C_0 and we obtain $\lambda_{\kappa}^{(0)} = -1$ for all κ for the all-to-all intra- and inter- population network. Hence, if we consider the summation term in Eq. (3.32) as an external forcing field [74], then it gives approximate values of the $(N-1)$-fold degenerate transverse LEs as

$$\Lambda_{\mathrm{trans},\kappa}^{(0)} = -\mu\cos\alpha - \frac{\nu}{N}\mathrm{Z} < 0 \tag{3.34}$$

for $\kappa = 2,...,N$ where $\mathrm{Z} = \sum_{m'=1}^{N}\cos(s_{m'} - s_0 - \alpha)$ is treated as an external forcing field.

So far, we have investigated the stability corresponding to the directions transverse to the sync-manifold. To study the stability of the synchronized population along the sync-manifold, we impose a perturbation along the sync-manifold: $s_0(t) \to s_0(t) + \delta s_0(t)$ where $|\delta s_0(t)| \ll 1$ is applied to Eq. (3.27). Then, the variational equation reads

$$\partial_t \delta s_0(t) = D\mathrm{F}(s_0)\delta s_0(t) - \frac{\nu}{N}\sum_{j=1}^{N} D\mathrm{H}(s_j - s_0)\delta s_0 = -\left(\frac{\nu}{N}\sum_{m'=1}^{N}\cos(s_{m'} - s_0 - \alpha)\right)\delta s_0(t) \tag{3.35}$$

from which we obtain

$$\Lambda_{\mathrm{perturb}}^{(0)} = -\frac{\nu}{N}\mathrm{Z} < 0 \tag{3.36}$$

provided that $Z = \frac{\nu}{N}\sum_{m'=1}^{N}\cos(s_{m'} - s_0 - \alpha)$ is regarded as external forcing function [74].

In Fig. 3.5, panels (a-b) display Lyapunov exponents along Poisson chimera trajectories for stationary (a) and breathing (b) chimeras from numerical experiments. Here, we also use the method described in Sec. 2.6 to obtain the Lyapunov exponents and the corresponding

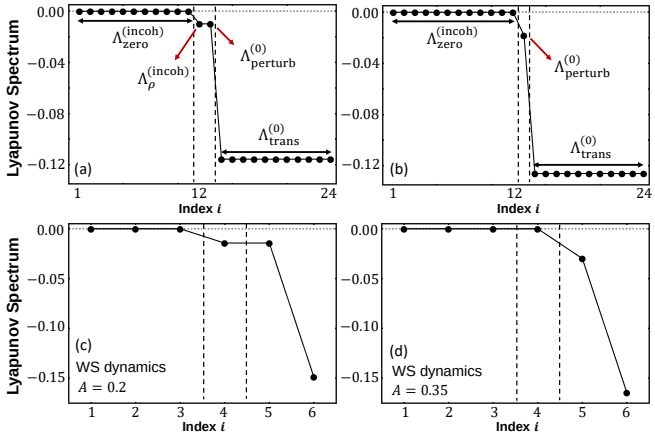

Fig. 3.5 (a-b) Lyapunov spectra of the full dynamics of Poisson chimera states with $N = 12$ for $A = 0.2$ (stationary chimeras) (a) and $A = 0.35$ (breathing chimeras) (b). For the meaning of the Λs see text. (c-d) Lyapunov spectra for the 6-dimensional Watanabe-Strogatz reduced dynamics of the chimera states in (a) and (b), respectively. The exponents marked by the black dashed lines indicate the LE corresponding to the radial WS variable.

covariant Lyapunov vectors. The Lyapunov exponents of a stationary chimera state (Fig. 3.5 (a)) are classified into four groups:

- (i) $(N-1)$-fold degenerate zero exponents denoted by $\Lambda^{(\mathrm{incoh})}_{\mathrm{zero}} = 0$,
- (ii) $(N-1)$-fold degenerate negative exponents denoted by $\Lambda^{(0)}_{\mathrm{trans}} < 0$,
- (iii) and (iv) two individual negative LEs, denoted by $\Lambda^{(0)}_{\mathrm{perturb}}$ and $\Lambda^{(\mathrm{incoh})}_{\rho}$.

The Lyapunov exponents obtained along a breathing Poisson chimera trajectory (Fig. 3.5 (b)) exhibit a similar classification of the Lyapunov exponents. However, we find just one individual non-degenerate negative exponent, $\Lambda^{(0)}_{\mathrm{perturb}}$ since one more zero Lyapunov exponent arises from the Hopf frequency, i.e., a periodic motion of the modulus of the order parameter.

Synchronized Population: $\Lambda^{(0)}_{\mathrm{trans}}$ and $\Lambda^{(0)}_{\mathrm{perturb}}$

In the previous section, we discussed analytically approximated Lyapunov exponents corresponding to the synchronized population: both transverse and parallel to the sync-manifold. In Fig. 3.5, Lyapunov exponents are depicted, which are obtained from numerical simulations. There are $(N-1)$-fold degenerate transverse Lyapunov exponents denoted by $\Lambda^{(0)}_{\mathrm{trans}}$, approximated in Eq. (3.34). The numerical analysis shows $-\mu\cos\alpha \ll -\frac{\nu}{N}Z < 0$. Thus, the degenerate transverse Lyapunov exponents in Eq. (3.34) are all negative, ensuring that

the chimera state is attracting in all directions transverse to the synchronized oscillators. Furthermore, numerically obtained covariant Lyapunov vectors corresponding to the LEs in Eq. (3.34) are of the form

$$\mathbf{v}_{\kappa}^{(0)} = [v_{\kappa 1}^{(\text{trans})}, ..., v_{\kappa N}^{(\text{trans})}, 0, ..., 0]^{\top} \in T_{\boldsymbol{\phi}_{\text{ch}}(t)}(\mathbb{T}^{2N}) \tag{3.37}$$

and $\sum_{i=1}^{N} v_{\kappa i}^{(\text{trans})} = 0$ for $\kappa = 2, ..., N$ where $\boldsymbol{\phi}_{\text{ch}}(t) \in \mathbb{T}^{2N}$ stands for the given chimera reference trajectory and $T_{\boldsymbol{\phi}_{\text{ch}}(t)}(\mathbb{T}^{2N})$ is the tangent space, as explained in Sec. 2.6. This result ensures that the LEs in Eq. (3.34) correspond indeed to the transverse Lyapunov exponents to the sync-manifold of the synchronized oscillators. In Fig. 3.5 (a-b) another negative Lyapunov exponent $\Lambda_{\text{perturb}}^{(0)}$ is depicted, which corresponds to the perturbation along the sync-manifold. Its analytically approximated value is given in Eq. (3.36). Its numerical value is also negative, confirming that a perturbation along the sync-manifold exponentially shrinks to zero. Note that $\Lambda_{\text{perturb}}^{(0)}$ depends strongly on the collective behavior of the incoherent oscillators $\{\phi_{i+N}(t) = s_m(t) | i = m = 1, ..., N\}$ (see Fig. 3.5 (f)) via the summation term in Eq. (3.36)). The numerical CLV corresponding to $\Lambda_{\text{perturb}}^{(0)}$ has the form $\mathbf{v}_{\text{perturb}}^{(0)} = [v, ..., v, v_1^{(\text{incoh})}, ..., v_N^{(\text{incoh})}]^{\top} \in T_{\boldsymbol{\phi}_{\text{ch}}(t)}(\mathbb{T}^{2N})$ where $\sum_{j=1}^{N} v_j^{(\text{incoh})} \neq 0$. Therefore, we conclude that the synchronized manifold is stable not only along the perturbations transverse to the sync-manifold but also for the perturbation along the sync-manifold.[6].

All the chimera states obtained in a two-population network, have the same 'pattern' of Lyapunov exponents, which is dictated by the structure of the network topology, namely; $(N-1)$-fold degenerate $\Lambda_{\text{trans},\kappa}^{(0)}$ for $\kappa = 2, ..., N$ and $\Lambda_{\text{perturb}}^{(0)}$. Thus, as can be seen from Fig. 3.5 (b), the same LEs associated with the synchronized population for the breathing chimera state were numerically detected, except for the additional zero LE.

Incoherent Population: $\Lambda_{\text{zero}}^{(\text{incoh})}$ and $\Lambda_{\rho}^{(\text{incoh})}$

Next, we examine the Lyapunov exponents associated with the incoherent population and consider first stationary Poisson chimera states. In Fig. 3.5 (a), the numerical results confirm that there are $(N-1)$-fold degenerate zero Lyapunov exponents $\Lambda_{\text{zero}}^{(\text{incoh})} = 0$ and one negative exponent $\Lambda_{\rho}^{(\text{incoh})} < 0$. To obtain more insight into this result, we consider the Watanabe-Strogatz transformation in Eq. (2.74) for $a = 1, 2$. The WS transformation leads to the 6D WS variables governed by Eq. (2.126) for $M = 2$. Here, the forcing field $H_a(t) = e^{-i\alpha} \sum_{a'=1}^{2} G_{aa'} \Gamma_{a'}(t)$ for $a = 1, 2$ and the Kuramoto order parameter are given by Eq. (2.77). Considering the 6D WS dynamics in the phase space together with the tangent space dynamics

[6]Note that the Lyapunov exponents obtained in Eq. (3.34) and Eq. (3.36) are consistent with previous results in Ref. [74].

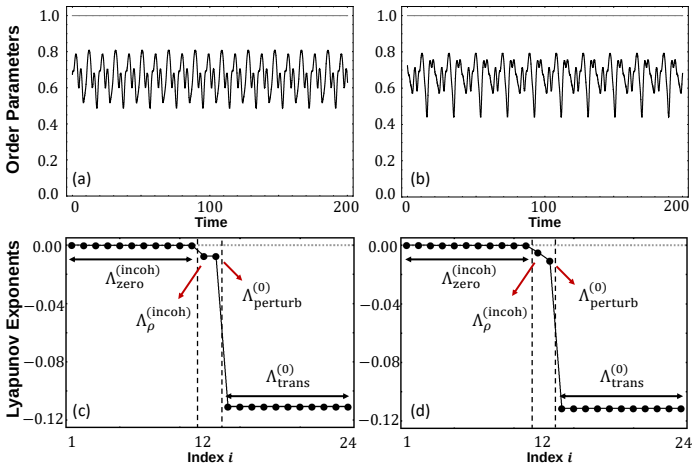

Fig. 3.6 (a-b) Temporal evolution of the magnitude of the Kuramoto order parameter obtained from non-Poisson chimera times series starting from different **n-PIC**s after a time $t \geq 10^6$ for $N = 12$ and $A = 0.2$. (c-d) Lyapunov spectra corresponding to the dynamics of (a-b).

along the corresponding chimera reference trajectory ($\rho_1(t) = 1$ and $\rho_2(t) < 1$), we also numerically determine the six Lyapunov exponents, as depicted in Fig. 3.5 (c-d). The results provide some insight into the classification of the Lyapunov exponents. As we discussed in Sec. 2.4, the WS variables (here, for the incoherent population) reside in an invariant subspace of the phase space, characterized by the $N-3$ constants of motion, i.e., by the initial condition [99]. The perturbations among those invariant subspaces yield $N-3$ neutrally stable directions, i.e., $N-3$ zero LEs. Apart from them, we observe two additional zero Lyapunov exponents associated with the incoherent population. These two zero LEs arise from the angular motions of the two angular WS variables [179]. In total, we obtain $N-1$ zero Lyapunov exponents. In addition to these zero LEs, we obtain one negative LE that corresponds to the stable WS radial dynamics whose value is determined by the parameter set. For the breathing chimera states, we numerically find N-fold degenerate zero Lyapunov exponents in the incoherent population. Here, an additional zero Lyapunov exponent results from the Hopf frequency since the breathing chimera arises at a supercritical Hopf bifurcation where the stationary chimera state loses its stability.

Non-Poisson Chimeras

We also numerically determine the Lyapunov exponents for non-Poisson chimera dynamics, shown in Fig. 3.6. As studied in Sec. 3.1.2, the incoherent population of non-Poisson chimera states strongly depends on a given initial condition. Here, we show two representative non-Poisson chimera motions at the same parameter set yet starting from different ICs, depicted

in Fig. 3.6 (a) and (b), respectively. In Fig. 3.6 (c-d), Lyapunov exponents are shown for the corresponding non-Poisson chimera trajectory in Fig. 3.6 (a-b). Note that a non-Poisson chimera state is also set on the same two-population network. Hence, we can expect that the Lyapunov exponents corresponding to the synchronized population exhibit the same features as those of the Poisson chimera state since they are dictated by the network structure. Figure 3.6 (c-d) shows that there are also $(N-1)$-fold degenerate transverse Lyapunov exponents $\Lambda^{(0)}_{\text{trans},\kappa}$ for $\kappa = 2,\ldots,N$ given by Eq. (3.34). Likewise, the CLV analysis confirms that their perturbation directions are indeed transverse to the sync-manifold as in Eq. (3.37). What is different from the Poisson chimeras, is that the LE arising from the perturbation along the sync-manifold (Eq. (3.36)) can take a different value depending on a given initial condition since $\Lambda^{(0)}_{\text{perturb}}$ strongly depends on the motion of the incoherent oscillators through Z in Eq. (3.36). Concerning the Lyapunov exponents of the incoherent population, they also follow the same characteristics as the Poisson chimera state, i.e., $N-1$ zero Lyapunov exponents and one negative LE, as discussed above.

3.3 Two Ways toward Attracting Poisson Chimeras

As discussed above, the identical Kuramoto-Sakaguchi oscillator system in the OA manifold is found to be neutrally stable [97, 102, 62]. Furthermore, in the previous section, we demonstrated that chimera states of identical KS oscillators in two-population, whether it is Poisson or non-Poisson, are neutrally stable with many zero Lyapunov exponents. To obtain attracting dynamics in the OA manifold, many authors have added a small heterogeneity, e.g., in the form of nonidentical natural frequencies or noisy oscillators, to the system of identical coupled oscillators. Such heterogeneity causes the dynamics to approach at least a close vicinity of the OA manifold or the Poisson submanifold. Furthermore, the stabilization of the OA manifold has been reported to be a generic consequence due to the presence of the small heterogeneity [101, 168, 180, 97, 169, 181, 62]. In this section, we suggest two simple systems that, according to the Lyapunov analysis, render Poisson chimeras in a network of identical and deterministic ensembles attracting. First, we consider a topological variation to Eq. (3.1), that is, nonlocal intra-population connectivity. For the second system, amplitude degrees of freedom of the oscillators will be introduced, i.e., we investigate a system of identical Stuart-Landau oscillators rather than Kuramoto-Sakaguchi phase oscillators in two-population networks. Below, we will see how those two variations introduce a small heterogeneity to the dynamics of phase variables, which then renders the Poisson chimeras attracting.

3.3.1 Topological Variation: Nonlocal Intra-population Network

The previous studies of the chimera dynamics of coupled oscillators, particularly, on nonlocal intra-population networks focused on randomly but systematically constructed topologies in the thermodynamic limit [87, 86]. We here consider the simplest regular and finite-sized nonlocal intra-population coupling while the inter-population coupling is all-to-all, as schematically depicted in Fig. 5.1(b). Compared to the global (all-to-all) connectivity of the intra-population, each oscillator loses one intra-population connection: it is not connected to the opposite oscillator on the ring[7].

The adjacency matrix of this nonlocal intra-population network is defined as

$$A = \begin{pmatrix} \overbrace{\begin{matrix} 0 & 1 & \cdots & 1 \\ 1 & 0 & \ddots & \vdots \\ \vdots & \ddots & \ddots & 1 \\ 1 & \cdots & 1 & 0 \end{matrix}}^{\mathrm{N/2}} & \overbrace{\begin{matrix} 0 & 1 & \cdots & 1 \\ 1 & 0 & \ddots & \vdots \\ \vdots & \ddots & \ddots & 1 \\ 1 & \cdots & 1 & 0 \end{matrix}}^{\mathrm{N/2}} \\ \begin{matrix} 0 & 1 & \cdots & 1 \\ 1 & 0 & \ddots & \vdots \\ \vdots & \ddots & \ddots & 1 \\ 1 & \cdots & 1 & 0 \end{matrix} & \begin{matrix} 0 & 1 & \cdots & 1 \\ 1 & 0 & \ddots & \vdots \\ \vdots & \ddots & \ddots & 1 \\ 1 & \cdots & 1 & 0 \end{matrix} \end{pmatrix} \tag{3.38}$$

where the i-th oscillator (node) is disconnected from the $(i+\frac{N}{2})$-th oscillator (node) in the same population.

The governing equations of the Kuramoto-Sakaguchi phase oscillators in the nonlocal intra-population topology are

$$\begin{aligned} \partial_t \phi_i^{(1)}(t) &= -\frac{\mu}{N}\sin\alpha + \frac{\mu}{N}\sum_{j=1}^{N} A_{ij}\sin(\phi_j^{(1)} - \phi_i^{(1)} - \alpha) + \frac{\nu}{N}\sum_{j=1}^{N}\sin(\phi_j^{(2)} - \phi_i^{(1)} - \alpha) \\ \partial_t \phi_i^{(2)}(t) &= -\frac{\mu}{N}\sin\alpha + \frac{\mu}{N}\sum_{j=1}^{N} A_{ij}\sin(\phi_j^{(2)} - \phi_i^{(2)} - \alpha) + \frac{\nu}{N}\sum_{j=1}^{N}\sin(\phi_j^{(1)} - \phi_i^{(2)} - \alpha) \end{aligned} \tag{3.39}$$

for $i = 1, ..., N$. Here, A_{ij} is the adjacency matrix of the nonlocal intra-population connectivity of each population defined in Eq. (3.38).

The nonlocally coupled system in Eq. (3.39) is no longer a sinusoidally coupled system, and therefore we cannot consider the OA or the WS dynamics to describe the macroscopic motions of the system. In spite of this, we found that chimera trajectories satisfy the

[7] To do so, we only consider even numbers of the oscillators for each population here

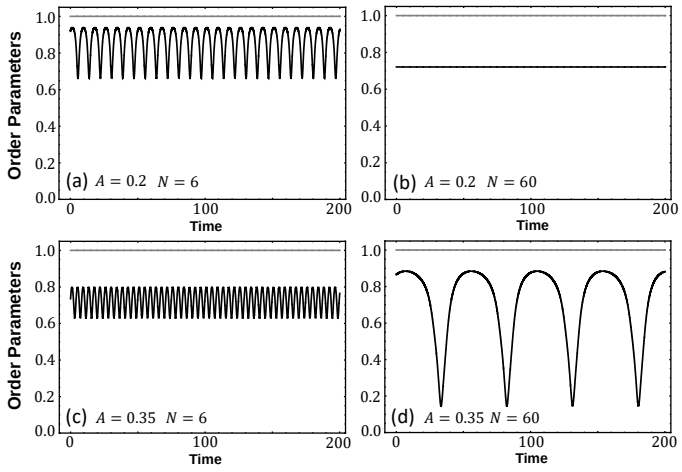

Fig. 3.7 The Kuramoto order parameters of the phase oscillators governed by the nonlocal intra-group coupling. (a,b) Chimera states with the parameter $A = 0.2$ and $\beta = 0.08$ corresponding to stationary chimeras for the system sizes $N = 6$ and $N = 60$, respectively. (c-d) Chimera sates with $A = 0.35$ corresponding to the breathing chimera states. Gray line: synchronized group ($r(t) = 1$), black line: incoherent order parameter ($r(t) < 1$).

dynamical characteristics of Poisson chimeras as defined in Sec. 3.1.2 as long as we started from a PIC. For this nonlocal Poisson chimera state[8], we observe that the distribution of the incoherent phases asymptotically approaches a close vicinity of the Poisson submanifold, regardless of whether the initial condition is a PIC or an n-PIC. In Fig. 3.7, the simple motion of the modulus of the Kuramoto order parameter for a stationary ((a-b) for$A = 0.2$) and a breathing ((c-d) for $A = 0.35$) Poisson chimera states is depicted. For the stationary chimera state (a-b), the modulus of the Kuramoto order parameter shows regular periodic motion for small N while it exhibits a stationary motion for large N, as expected for the stationary Poisson chimera state in Sec. 3.1.2. It follows from the fact that the nonlocal stationary chimera states also exhibit equally shifted, periodic phase velocities with the same functional form for the incoherent oscillators. Hence, we obtain the time-periodic order parameter for the small-sized stationary chimeras, and the oscillation gets suppressed as $N \to \infty$. For the breathing chimera states (c-d), the modulus of the Kuramoto order parameter displays periodic dynamics for large N, as anticipated for a typical breathing chimera motion after a supercritical Hopf bifurcation. However, for small N, the chimeras show no longer the main breathing motion superimposed by a secondary oscillation. We guess this might arise from the fact that the change of topology can vary the Hopf bifurcation point for small N, as it was reported in Ref. [87] for different nonlocal systems.

[8]To distinguish the two systems, we call them the global and the nonlocal chimera states, respectively.

3.3.2 Lyapunov Stability Analysis: Nonlocal Poisson Chimeras

In this section, we investigate the spectral properties of nonlocal Poisson chimera states, as we did for the global Poisson chimera state in Sec. 3.2.2. First, we analytically approximated the Lyapunov exponents associated with the synchronized population. Then, we compare our results with the numerically determined LEs and also discuss the LEs for the incoherent population.

Network symmetry Analysis: Application to Nonlocal Poisson Chimeras

For the Kuramoto-Sakaguchi phase oscillators in the nonlocal intra-population network, we employ the same method as in Sec. 3.2.1 where we treated the chimera state as a CS pattern dynamics. To do so, we rewrite Eq. (3.39) as

$$\partial_t \phi_i(t) = \mathrm{F}(\phi_i(t)) + \sum_{j=1}^{2N} K_{ij} B^{(\mathrm{n})}_{ij} \mathrm{H}(\phi_j(t) - \phi_i(t)) \tag{3.40}$$

for $i = 1, ..., 2N$ where $\mathrm{F}(\phi)$, K_{ij}, and $\mathrm{H}(x)$ are the same as defined in Eq. (3.25). However, the matrix $B^{(\mathrm{n})} \in \mathbb{R}^{2N\times 2N}$ is defined to reflect the nonlocal intra-population connectivity besides the all-to-all inter-population coupling, which therefore reads

$$B^{(\mathrm{n})} = \left(\begin{array}{c|c} A & J_N \\ \hline J_N & A \end{array}\right) \in \mathbb{R}^{2N\times 2N} \tag{3.41}$$

where $A \in \mathbb{R}^{N\times N}$ is defined in Eq. (3.38) and $J_N \in \mathbb{R}^{N\times N}$ is the unit matrix whose elements are all 1, i.e., $(J_N)_{ij} := 1$ for all $i, j = 1, ..., N$. In this setup, the (coarse-grained) quotient adjacency matrix is given by

$$\tilde{A}^{(\mathrm{n})} = \left(\begin{array}{c|ccc} N-2 & 1 & \dots & 1 \\ \hline N & & & \\ \vdots & & A & \\ N & & & \end{array}\right) \tag{3.42}$$

wherein $\tilde{A}^{(\mathrm{n})}_{00} = N-2$ and $\tilde{A}^{(\mathrm{n})}_{ij} = A_{mm'}$ for $m, m' = 1, ..., N$, again ensuring the nonlocal intra-population connectivity. The quotient dynamics is then obtained according to the CS pattern corresponding to the nonlocal Poisson chimeras. The quotient variables are defined by

$s_0(t)=\phi_i(t)$ (sync.) and $s_m(t)=\phi_{i+N}(t)$ (incoh.) for $i=m=1,...,N$, and are governed by

$$\begin{aligned}\partial_t s_0 &= \mathrm{F}(s_0)+\frac{\mu}{N}\tilde{A}^{(\mathrm{n})}_{00}\mathrm{H}(0)+\frac{\nu}{N}\sum_{m'=1}^{N}\tilde{A}^{(\mathrm{n})}_{0m'}\mathrm{H}(s_{m'}-s_0)\\ &= -\frac{\mu}{N}(N-1)\sin\alpha+\frac{\nu}{N}\sum_{m'=1}^{N}\sin(s_{m'}-s_0-\alpha)\end{aligned} \tag{3.43}$$

for the synchronized population, and

$$\begin{aligned}\partial_t s_m &= \mathrm{F}(s_m)+\frac{\nu}{N}\tilde{A}^{(\mathrm{n})}_{m0}\mathrm{H}(s_0-s_m)+\frac{\mu}{N}\sum_{m'=1}^{N}\tilde{A}^{(n)}_{mm'}\mathrm{H}(s_{m'}-s_m)\\ &= -\frac{\mu}{N}\sin\alpha+\nu\sin(s_0-s_m-\alpha)+\frac{\mu}{N}\sum_{m'=1}^{N}A_{mm'}\sin(s_{m'}-s_m-\alpha)\\ &= \tilde{\omega}_m(t)+\nu\sin(s_0-s_m-\alpha)+\frac{\mu}{N}\sum_{m'=1}^{N}\sin(s_{m'}-s_m-\alpha)\end{aligned} \tag{3.44}$$

with $\tilde{A}^{(\mathrm{n})}_{0m}=1$ and $\tilde{A}^{(\mathrm{n})}_{m0}=N$ for $m=1,...,N$ for the incoherent trivial clusters. Note that the summation term in the last line of Eq. (3.44) indicates the all-to-all mean-field coupling since we put the nonlocal term outside the summation, which leads us to the *topology-induced heterogeneity* defined by $\tilde{\omega}_m(t)=-\frac{\mu}{N}\sin(s_{m+N/2}-s_m-\alpha)$. This reminds us of the system of heterogeneous KS oscillators. However, here, the heterogeneity is induced by the topology in a system of identical oscillators. Does this render the dynamics attracting, as the heterogeneous natural frequency distribution does? This is our main concern in this section.

First, we need to study the stability of the synchronized cluster. To do so, consider the cluster-based coordinate vectors $\mathbf{u}^{(m)}_{\kappa}$, which are set to be the eigenvectors of the adjacency matrix. For the nonlocal population, the eigenvalues of the adjacency matrix are given as $\lambda^{(0)}_{\kappa}=0$ for $\kappa=2,...,N/2+1$ and $\lambda^{(0)}_{\kappa}=-2$ for $\kappa=N/2+2,...,N$. Note that due to the nonlocal connectivity, the eigenvalues are different from those of the all-to-all connectivity matrix[9]. This fact leads to the variational equations from Eq. (3.22), which read

$$\begin{aligned}\partial_t \eta^{(0)}_{\kappa} &= \left(D\mathrm{F}(s_0)-\frac{\mu}{N}\tilde{A}^{(n)}_{00}D\mathrm{H}(0)+\frac{\mu}{N}\lambda^{(0)}_{\kappa}D\mathrm{H}(0)-\frac{\nu}{N}\sum_{m'=1}^{N}\tilde{A}^{(n)}_{0m'}D\mathrm{H}(s_{m'}-s_0)\right)\eta^{(0)}_{\kappa}\\ &= \left(-\frac{\mu}{N}(N-2)\cos\alpha+\frac{\mu}{N}\lambda^{(0)}_{\kappa}\cos\alpha-\frac{\nu}{N}\mathrm{Z}\right)\eta^{(0)}_{\kappa}\end{aligned} \tag{3.45}$$

[9]Recall that $\lambda^{(0)}_{\kappa}=-1$ are the same for $\kappa=2,...,N$ for the global intra-population network.

for $\kappa = 2,...,N$. Substituting the eigenvalues above into Eq. (3.45), we obtain the splitting of the transversal (to the sync-manifold) Lyapunov exponents as

$$\begin{aligned}\Lambda^{(0)}_{\text{trans},\kappa} &= -\frac{\mu}{N}(N-2)\cos\alpha + \frac{\mu}{N}\lambda^{(0)}_{\kappa}\cos\alpha - \frac{\nu}{N}\mathrm{Z} \\ &= \begin{cases} -\frac{\mu}{N}(N-2)\cos\alpha - \frac{\nu}{N}\mathrm{Z} < 0, & \kappa = 2,...,N/2+1 \\ -\mu\cos\alpha - \frac{\nu}{N}\mathrm{Z} < 0, & \kappa = N/2+2,...,N \end{cases}\end{aligned} \tag{3.46}$$

provided that Z, defined in Eq. (3.34), is treated as an external forcing field. Likewise, another Lyapunov exponent of the synchronized population can be associated with a perturbation along the sync-manifold. Here, a small perturbation $s_0 \to s_0 + \delta s_0$ is imposed on Eq. (3.43) where $|\delta s_0| \ll 1$. This perturbation gives $\Lambda^{(0)}_{\text{sync}} = -\frac{\nu}{N}\mathrm{Z} < 0$ strongly depending on the motion of the incoherent oscillators.

Synchronized Population: $\Lambda^{(0)}_{\text{trans}}$ and $\Lambda^{(0)}_{\text{perturb}}$

For the nonlocal Poisson chimeras, the numerical Lyapunov analysis shows that nonlocal Poisson chimera states have qualitatively different LEs from those of the global Poisson chimeras, as shown in Fig. 3.8. We numerically obtain $N-1$ transverse Lyapunov exponents split into two different values, which is consistent with Eq. (3.46) that analytically approximates the $N-1$ transverse Lyapunov exponents. The splitting of the values of $\Lambda^{(0)}_{\text{trans}}$ arises from the transversal variational equations in Eq. (3.45), which include two different eigenvalues of the adjacency matrix for the nonlocal connectivity. Also, the numerical experiments show that the LEs in Eq. (3.46) are indeed transverse to the sync-manifold since the corresponding CLVs are of the form

$$\mathbf{v}^{(0)}_{\kappa} = [v^{(\text{trans})}_{\kappa 1},...,v^{(\text{trans})}_{\kappa N},0,...,0]^{\top} \in T_{\boldsymbol{\phi}_{\text{ch}}(t)}(\mathbb{T}^{2N}) \tag{3.47}$$

where $\sum_{i=1}^{N} v^{(\text{trans})}_{\kappa i} = 0$ for $\kappa = 2,...,N$. Note that as N increases, the gap between the two different transverse Lyapunov exponent groups in Eq. (3.46) is decreasing (compare Fig. 3.8 (b) with Fig. 3.8 (c)). Moreover, we find another Lyapunov exponent for the synchronized population, associated with a perturbation along the sync-manifold as we predicted above: $\Lambda^{(0)}_{\text{perturb}} = -\frac{\nu}{N}\mathrm{Z} < 0$. Therefore, the nonlocal Poisson chimera states are also stable in both the directions transverse and parallel to the sync-manifold, and their properties are dominated by the structure of the nonlocal connectivity.

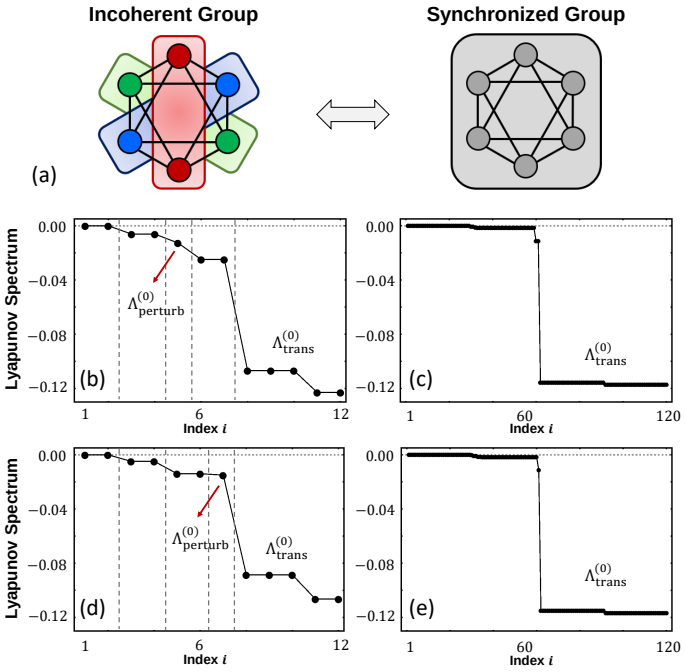

Fig. 3.8 (a) Schematic drawing of the two-population oscillators network with nonlocal coupling for $N = 6$. The same color in the incoherent group indicates that the oscillators marked by the same color are characterized by the same evolution dynamics. (b-c) The Lyapunov spectra for $A = 0.2$ with $N = 6$ and $N = 60$, respectively. (d-e) The Lyapunov spectra for $A = 0.35$ with $N = 6$ and $N = 60$, respectively.

Incoherent Population : Pairs of Two Nearly-degenerate Lyapunov Exponents

Next, we elucidate the Lyapunov exponents corresponding to the incoherent oscillators. As discussed above, the dimension reduction methods such as the OA ansatz and the WS transformation cannot be applied to the nonlocal intra-population network. Despite this, we can still reveal the properties of the Lyapunov exponents for the incoherent population.

In fact, the quotient dynamics for the incoherent oscillators in Eq. (3.44) is influenced by discrete symmetries arising due to the nonlocal topology, as schematically depicted in Fig. 3.8 (a). The nonlocal topology was defined ina way that each oscillator on the ring is disconnected only from the opposite one. Hence, the two incoherent oscillators $s_m(t)$ and $s_{m+N/2}(t)$ are governed by the same evolution equation[10]. Ref. [122] discusses that such discrete symmetries can cause nearly-degenerate Lyapunov exponents. Thus, we can anticipate $N/2$ pairs of two nearly identical Lyapunov exponents for the incoherent population (see Fig. 3.8 (b,d)). Furthermore, we numerically find these pairs of Lyapunov

[10]Note that the cluster pattern in Fig. 3.8 (a) is also an orbit partition. Hence, each oscillator in a cluster is affected by the same input from all the others.

exponents to be clearly negative. Therefore, unlike the global Poisson chimeras, which are neutrally stable, the incoherent dynamics of nonlocal Poisson chimeras is attracting. Thus, the dynamics asymptotically approaches a vicinity of the Poisson submanifold, even when initiated from an n-PIC. Note that there are two zero Lyapunov exponents arising from the two continuous symmetries: the phase shift ($\mathbf{v}_{\rm ps} = (\delta\phi_0, ..., \delta\phi_0)^\top$ where $|\delta\phi_0| \ll 1$) and the time shift ($\mathbf{v}_{\rm ts} \propto \dot{\phi}_{\rm ch} = \mathbf{f}(\phi_{\rm ch})$) symmetries, respectively, which in fact do not affect the stability of the trajectory. In Fig. 3.8 (c,e), it is shown that the nearly identical pairs of the Lyapunov exponents for the incoherent population are getting closer and closer to one another as N increases. Eventually, they form two almost continuous branches of the spectrum for large N. Nevertheless, they are slightly negative, which confirms that the large-sized nonlocal Poisson chimeras are still attracting.

In conclusion, the nonlocal topology adds a term to the governing equations of the system which can be interpreted as a topology-induced heterogeneity $\tilde{\omega}_m(t)$. Such a heterogeneity renders the OA manifold attracting, and leads to the attracting Poisson chimeras dynamics in a vicinity of the Poisson submanifold [97, 169, 168, 180]. Thus, the chimera dynamics asymptotically approaches a close vicinity of the Poisson submanifold and we obtain the attracting Poisson chimeras in the two-population network of the nonlocal intra-population connectivity.

3.3.3 Dynamical Variation: Stuart-Landau Oscillator Ensemble

In this section, we study the second way toward attracting Poisson chimera states. To do so, we impose a dynamical variation to Eq. (3.1). More precisely, we here consider a system of identical Stuart-Landau (SL) oscillators in two-population networks (all-to-all as in Fig. 5.1 (a)). Such a system has been studied recently in the thermodynamic limit [78, 79], in which attracting chimera states have been reported. In this chapter, the finite-sized ensemble is investigated and a full Lyapunov stability analysis is performed to give further evidence that the amplitude degrees of freedom are the key to rendering Poisson chimeras attracting. We will see below that the amplitude degrees of freedom introduce a small self-organized heterogeneity to the dynamics of incoherent phase variables.

In a system of identical Stuart-Landau (SL) oscillators, each oscillator is described by both a phase $\phi_i(t) \in \mathbb{T}$ and an amplitude variable $r_i(t) \in \mathbb{R}_{>0}$. For one population, the evolution of the amplitude variables is governed by

$$\partial_t r_i(t) = \varepsilon^{-1}(1-r_i^2)r_i + \frac{\mu}{N}\sum_{j=1}^{N} r_j\cos(\phi_j - \phi_i - \alpha) + \frac{\nu}{N}\sum_{j=1}^{N} r_{j+N}\cos(\phi_{j+N} - \phi_i - \alpha) \quad (3.48)$$

and the one of the phase variables follows

$$\partial_t \phi_i(t) = \omega - \sigma r_i^2 + \frac{\mu}{N}\sum_{j=1}^{N}\frac{r_j}{r_i}\sin(\phi_j - \phi_i - \alpha) + \frac{\nu}{N}\sum_{j=1}^{N}\frac{r_{j+N}}{r_i}\sin(\phi_{j+N} - \phi_i - \alpha) \qquad (3.49)$$

for $i = 1,...,N$. The dynamics of the oscillators in the second population can be described correspondingly. Below, we fix some parameters: $\sigma = 0.2$ and $\omega = 0$. Note that the system approaches the phase-reduced model, i.e., the Kuramoto-Sakaguchi phase oscillators (3.4-3.5) as $\varepsilon \to 0$, since then $r_i = r_0 \to 1$ for all $i = 1,...,2N$ [78], as we discussed in Chap. 2.

To study Poisson chimeras of the SL ensemble, we also start the dynamics from a PIC on the phase variables in Eq. (3.49). For the amplitude degrees of freedom (DOFs), we set $r_i(0) = 1$ for $i = 1,...,2N$[11]. The chimera trajectory evolving from such a PIC satisfies all the dynamical properties of Poisson chimeras according to their definition for the phase DOFs. Numerical integration of Eqs. (3.49-3.48) shows that one population remains perfectly synchronized and the other population holds the incoherent phase distribution to remain in the normalized Poisson kernel. Also, the stationary chimera states show the equally shifted instantaneous incoherent phase velocities within an oscillation period, which leads to the periodic order parameter motion for the small-sized stationary chimeras. Regarding the amplitude variables, all synchronized oscillators show homogeneous amplitude distribution $r_i(t) = 1$ for $i = 1,...,N$, and the amplitudes of the incoherent oscillators display a smooth curve as a function of sorted phase values, depending on the parameter ε [79]. This is called a *quasiphase oscillator regime* [182]. Indeed, varying the coupling strength ε as a bifurcation parameter, sufficiently small ε (here, we use $\varepsilon = 0.01$) exhibits a dynamics close to the one of the phase-reduced system. The evolution of the Kuramoto order parameter, defined using the phase variables, is very close to the motion depicted in Fig. 3.2. More specifically, the modulus of the Kuramoto order parameter is stationary for $A = 0.2$ and exhibits a (periodic) breathing motion for $A = 0.35$. For strong coupling strength ε with fixed $A = 0.2$, the stationary chimera, which can be obtained, e.g., for $\varepsilon = 0.1$, undergoes a Hopf bifurcation, giving rise to breathing chimeras, which are observed, e.g., for $\varepsilon = 0.15$, and is in line with findings reported in Ref. [78].

[11] Note that the Poisson chimeras are defined and characterized by solely the phase DOFs. Hence, we will investigate the properties of the phase DOFs to characterize the Poisson chimeras.

3.3.4 Lyapunov Stability Analysis: Poisson Chimeras of Stuart-Landau Oscillators

In this subsection, we investigate the spectral properties of Poisson chimera states of Sutart-Landau oscillators using Lyapunov stability analysis. First, we approximate the Lyapunov exponents for the synchronized population, for both the amplitude and the phase DOFs.

Network Symmetry Analysis: Application to Poisson Chimeras of Stuart-Landau Oscillators

Let us first consider the analysis of the amplitude DOFs. Using the same method as we employed above, the evolution of the amplitude DOFs can be re-expressed as

$$\partial_t r_i(t) = \mathrm{F}^{(\mathrm{amp})}(r_i(t)) + \sum_{j=1}^{2N} K_{ij}^{(\mathrm{amp})} B_{ij}^{(c)} \mathrm{H}^{(\mathrm{amp})}(r_j(t)) \tag{3.50}$$

for $i = 1,...,2N$. Here, the local dynamics is given as $\mathrm{F}^{(\mathrm{amp})}(r) = \varepsilon^{-1}(1-r^2)r + \frac{\mu}{N} r\cos\alpha$ and the coupling function is $\mathrm{H}^{(\mathrm{amp})}(r) = r$. This is a Pecora-type equation. Note that in order to obtain the approximated Lyapunov exponents, we assume that the phase variables in Eq. (3.50) are external forcing functions and treated them as constants in the amplitude DOF calculation. Thus, we define the coupling weight in Eq. (3.50) as $K_{ij}^{(\mathrm{amp})} = \frac{\mu}{N}\cos(\phi_j - \phi_i - \alpha)$ if i, j belong to the same population and $K_{ij}^{(\mathrm{amp})} = \frac{\nu}{N}\cos(\phi_j - \phi_i - \alpha)$ if i, j belong to the different populations.

Following the CS pattern of the chimera dynamics introduced in Sec. 3.2.2, we denote the amplitude degrees of freedom as $r_i(t) = R_0(t) = 1$ for the synchronized cluster and $r_{i+N}(t) = R_m(t)$ for the incoherent trivial clusters. The phase DOFs are written as $s_0 = \phi_i$ (sync.) and $s_m = \phi_{i+N}$ (incoh.) for $i = m = 1,...,N$. Then, the quotient dynamics of the amplitude DOFs for the synchronized population with the quotient adjacency matrix defined in Eq. (3.26) is governed by

$$\begin{aligned}
\partial_t R_0 &= \mathrm{F}^{(\mathrm{amp})}(R_0) + \frac{\mu}{N}\tilde{A}_{00}\mathrm{H}^{(\mathrm{amp})}(R_0)\cos\alpha + \frac{\nu}{N}\sum_{m'=1}^{N}\tilde{A}_{0m'}\mathrm{H}^{(\mathrm{amp})}(R_{m'})\cos(s_{m'} - s_0 - \alpha) \\
&= \left(\varepsilon^{-1}(1-R_0^2) + \frac{\mu}{N}\cos\alpha\right)R_0 + \frac{\mu}{N}(N-1)R_0\cos\alpha + \frac{\nu}{N}\sum_{m'=1}^{N} R_{m'}\cos(s_{m'} - s_0 - \alpha).
\end{aligned} \tag{3.51}$$

Imposing a small deviation on the CS dynamics, i.e., $\delta r_i(t) = r_i(t) - R_m(t)$ for $i \in C_m$ for $m = 0, 1, ..., N$, the coupled variational equations read

$$\begin{aligned}\partial_t \delta r_i(t) = & D\mathrm{F}^{(\mathrm{amp})}(R_0)\delta r_i + \frac{\mu}{N}\mathrm{C}_{00}\sum_{k\in C_0} B^{(c)}_{ik} D\mathrm{H}^{(\mathrm{amp})}(R_0)\delta r_k \\ & + \frac{\nu}{N}\sum_{m'=1}^{N}\sum_{k\in C_{m'}} B^{(c)}_{ik} D\mathrm{H}^{(\mathrm{amp})}(R_{m'})\mathrm{C}_{m'0}\delta r_k \end{aligned} \tag{3.52}$$

for each $i \in C_0$ and $\mathrm{C}_{m'm} = \cos(s_{m'} - s_m - \alpha)$ for $m, m' = 0, ..., N$. When we employ the cluster-based coordinates, the transversal variational equations in Eq. (3.22) read

$$\begin{aligned}\partial_t \xi^{(0)}_\kappa = & \sum_{i\in C_0} u^{(0)}_{\kappa i}\delta\dot{r}_i(t) = D\mathrm{F}^{(\mathrm{amp})}(R_0)\sum_{i\in C_0} u^{(0)}_{\kappa i}\delta r_i + \frac{\mu}{N} D\mathrm{H}^{(\mathrm{amp})}(R_0)\mathrm{C}_{00}\sum_{i\in C_0}\sum_{k\in C_0} u^{(0)}_{\kappa i} B^{(c)}_{ik}\delta r_k \\ & + \frac{\nu}{N}\sum_{i\in C_0}\sum_{m'=1}^{N}\sum_{k\in C_{m'}} u^{(0)}_{\kappa i} B^{(c)}_{ik} D\mathrm{H}^{(\mathrm{amp})}(R_{m'})\mathrm{C}_{m'0}\delta r_k \\ = & D\mathrm{F}^{(\mathrm{amp})}(R_0)\xi^{(0)}_\kappa + \frac{\mu}{N} D\mathrm{H}^{(\mathrm{amp})}(R_0)\mathrm{C}_{00}\sum_{i\in C_0}\sum_{k\in C_0}\sum_{\kappa'=1}^{|C_0|} u^{(0)}_{\kappa i} B^{(c)}_{ik} u^{(0)}_{\kappa' k}\xi^{(0)}_{\kappa'} \\ & + \frac{\nu}{N}\sum_{m'=1}^{N}\sum_{i\in C_0}\sum_{k\in C_{m'}}\sum_{\kappa'=1}^{|C_{m'}|} u^{(0)}_{\kappa i} B^{(c)}_{ik} u^{(m')}_{\kappa' k}\xi^{(m')}_{\kappa'}\mathrm{C}_{m'0} D\mathrm{H}^{(\mathrm{amp})}(R_{m'}) \end{aligned} \tag{3.53}$$

for $\kappa = 2, ..., N$. Due to the cluster-based coordinate vectors that make the adjacency matrix block-diagonalized, the last term becomes zero. Furthermore, they are chosen to be the eigenvectors of the adjacency matrix, which leads to $\sum_{i\in C_0}\sum_{k\in C_0} u^{(0)}_{\kappa i} B^{(c)}_{ik} u^{(0)}_{\kappa' k} = \lambda^{(0)}_\kappa \delta_{\kappa\kappa'}$ for $\kappa = 2, ..., N$. Finally, the $N-1$ transversal variational equations to the sync-manifold are given by

$$\begin{aligned}\partial_t \xi^{(0)}_\kappa &= \left(D\mathrm{F}^{(\mathrm{amp})}(R_0) + \frac{\mu}{N}\cos\alpha\,\lambda^{(0)}_\kappa D\mathrm{H}^{(\mathrm{amp})}(R_0)\right)\xi^{(0)}_\kappa \\ &= \left(\varepsilon^{-1}(1-3R_0^2) + \frac{\mu}{N}(1+\lambda^{(0)}_\kappa)\cos\alpha\right)\xi^{(0)}_\kappa \end{aligned} \tag{3.54}$$

For the global topology, we know $\lambda^{(0)}_\kappa = -1$. Thus, from Eq. (3.54), we obtain the approximate values of the $(N-1)$-fold degenerate transverse Lyapunov exponents in the amplitude DOFs as $\Lambda^{(\mathrm{amp},0)}_{\mathrm{trans},\kappa} \approx \varepsilon^{-1}(1-3R_0^2) < 0$ for $\kappa = 2, ..., N$.

For the Lyapunov exponent associated with the perturbation along the sync-manifold in the amplitude DOFs, we consider $R_0(t) \to R_0(t) + \delta R_0(t)$ with $|\delta R_0| \ll 1$ in Eq. (3.51).

Then, we obtain

$$\begin{aligned}\partial_t \delta R_0(t) &= D\mathrm{F}^{(\mathrm{amp})}(R_0)\delta R_0 + \frac{\mu}{N}\cos\alpha \tilde{A}_{00} D\mathrm{H}^{(\mathrm{amp})}(R_0)\delta R_0 \\ &= \left(\varepsilon^{-1}(1-3R_0^2)+\mu\cos\alpha\right)\delta R_0(t) \end{aligned} \tag{3.55}$$

which gives a slightly greater Lyapunov exponent value than the transverse ones as

$$\Lambda_{\mathrm{perturb}}^{(\mathrm{amp},0)} \approx \varepsilon^{-1}(1-3R_0^2)+\mu\cos\alpha < 0 \tag{3.56}$$

where $\Lambda_{\mathrm{trans}}^{(\mathrm{amp},0)} \lesssim \Lambda_{\mathrm{perturb}}^{(\mathrm{amp},0)}$ since $\mu\cos\alpha > 0$.

Next, we deal with the phase DOFs of the Stuart-Landau oscillators. To do so, we rewrite the governing equations for the phase DOFs as

$$\partial_t \phi_i(t) = \mathrm{F}^{(\mathrm{ph})}(\phi_i(t)) + \sum_{j=1}^{2N} K_{ij}^{(\mathrm{ph})} B_{ij}^{(c)} \mathrm{H}(\phi_j(t)-\phi_i(t)) \tag{3.57}$$

for $i = 1,...,2N$, where the uncoupled dynamics is governed by $\mathrm{F}^{(\mathrm{ph})}(\phi_i) = -\sigma r_i^2 - \frac{\mu}{N}\sin\alpha$ and the coupling function is defined as $\mathrm{H}(x) = \sin(x-\alpha)$. Here, we assume that the amplitude DOFs are constants, i.e., external forcing variables. The coupling weights are defined as $K_{ij}^{(\mathrm{ph})} = \frac{\mu}{N}\frac{r_j}{r_i}$ if i,j belong to the same population and $K_{ij}^{(\mathrm{ph})} = \frac{\nu}{N}\frac{r_j}{r_i}$ otherwise. The quotient dynamics of the synchronized and incoherent populations in the phase DOFs are obtained as

$$\begin{aligned}\partial_t s_0 &= -\sigma R_0^2 - \frac{\mu}{N}\sin\alpha - \frac{\mu}{N}\tilde{A}_{00}\sin\alpha + \frac{\nu}{N}\sum_{m'=1}^{N}\frac{R_{m'}}{R_0}\tilde{A}_{0m'}\sin(s_{m'}-s_0-\alpha) \\ \partial_t s_m &= -\sigma R_m^2 - \frac{\mu}{N}\sin\alpha + \frac{\nu}{N}\tilde{A}_{m0}\frac{R_0}{R_m}\sin(s_0-s_m-\alpha) + \frac{\mu}{N}\sum_{m'=1}^{N}\frac{R_{m'}}{R_m}\tilde{A}_{mm'}\sin(s_{m'}-s_m-\alpha) \\ &= \tilde{\Omega}_m(t) + \nu\frac{R_0}{R_m}\sin(s_0-s_m-\alpha) + \frac{\mu}{N}\sum_{m'=1}^{N}\sin(s_{m'}-s_m-\alpha) \end{aligned} \tag{3.58}$$

where $\tilde{\Omega}_m(t) = -\sigma R_m^2(t)$ for $m = 1,...,N$. The last line of Eq. (3.58) is our main point. The incoherent phase dynamics can be interpreted as globally coupled KS oscillators with a *self-organized heterogeneity* induced by the amplitude DOFs, i.e., $\tilde{\Omega}_m(t) := -\sigma R_m^2$ for $m = 1,...,N$. Below, we will numerically confirm that the incoherent population of the Poisson chimeras of the Stuart-Landau oscillators are attracting similarly for the attracting nonlocal Poisson chimeras in Sec. 3.3.1 whose dynamics is ruled by an effective heterogeneity as well, here introduced through the network topology.

Going further, we write the transversal variational equations as

$$\partial_t \eta_\kappa^{(0)} = \left(-\frac{\mu}{N}(N-1)\cos\alpha - \frac{\nu}{N}\tilde{Z} + \frac{\mu}{N}\lambda_\kappa^{(0)}\cos\alpha \right)\eta_\kappa^{(0)}. \tag{3.59}$$

Here, $\eta_\kappa^{(0)}(t) = \sum_{i\in C_0} u_{\kappa i}^{(0)}\delta\phi_i(t)$ for $\kappa = 2,...,N$ and the deviation along the CS dynamics is $\delta\phi_i(t) = \phi_i(t) - s_0(t)$ for $i \in C_0$, and the eigenvalues $\lambda_\kappa^{(0)} = -1$ for all κ. Then, we find that the phase DOFs in the synchronized population also have $(N-1)$-fold degenerate transverse Lyapunov exponents that read

$$\begin{aligned}\Lambda_{\text{trans},\kappa}^{(0)} &= -\mu\cos\alpha - \frac{\nu}{N}\sum_{m'=1}^{N}\frac{R_{m'}}{R_0}\cos(s_{m'} - s_0 - \alpha) \\ &= -\mu\cos\alpha - \frac{\nu}{N}\tilde{Z} < 0\end{aligned} \tag{3.60}$$

for $\kappa = 2,...,N$ where $\tilde{Z} = \sum_{m'=1}^{N}\frac{R_{m'}}{R_0}\cos(s_{m'} - s_0 - \alpha)$ should be considered as an external forcing field. Furthermore, the Lyapunov exponent due to a perturbation along the sync-manifold has the approximated value of $\Lambda_{\text{perturb}}^{(0)} = -\frac{\nu}{N}\tilde{Z} < 0$.

In Ref. [79], C. Laing showed that the eigenvalues determining the stability of chimeras in a two-population network in the thermodynamic limit are organized in two branches: One of the two is prominently negative and the other one has real parts close to zero (see Fig. 3 in Ref. [79]). Here, we briefly check this fact. Consider the real-valued coordinates of the SL variables

$$r_k(t)e^{i\phi_k(t)} = \frac{1}{\sqrt{2}}\big(a_k(t) + ib_k(t)\big) \tag{3.61}$$

for $k = 1,...,2N$. In the vector form, it reads $\mathbf{x}_k(t) = (a_k(t), b_k(t))^\top \in \mathbb{R}^2$. Then, they are governed by

$$\partial_t \mathbf{x}_i(t) = \mathbf{F}(\mathbf{x}_i(t)) + \sum_{j=1}^{2N} B_{ij}^{(c)} K_{ij}\mathbf{H}(\mathbf{x}_j(t)) \tag{3.62}$$

for $i = 1,...,2N$ where $B_{ij}^{(c)}$ and K_{ij} are defined in Eq. (3.25). The uncoupled local dynamics is represented by

$$\mathbf{F}(\mathbf{x}_i(t)) = \left[\begin{pmatrix}\varepsilon^{-1} & -\omega \\ \omega & \varepsilon^{-1}\end{pmatrix} + \frac{\mu}{N}\begin{pmatrix}\cos\alpha & \sin\alpha \\ -\sin\alpha & \cos\alpha\end{pmatrix}\right]\mathbf{x}_i(t) - \frac{\varepsilon^{-1}}{2}\begin{pmatrix}1 & -\varepsilon\sigma \\ \varepsilon\sigma & 1\end{pmatrix}|\mathbf{x}_i(t)|^2\mathbf{x}_i(t) \tag{3.63}$$

and the coupling function is written as

$$\mathbf{H}(\mathbf{x}_i(t)) = \begin{pmatrix} \cos\alpha & \sin\alpha \\ -\sin\alpha & \cos\alpha \end{pmatrix} \mathbf{x}_i(t) \tag{3.64}$$

for $i = 1,...,2N$. Considering the chimera state as a CS pattern dynamics, i.e., $\mathbf{x}_i(t) = \mathbf{s}_0$ (sync.) and $\mathbf{x}_{i+N}(t) = \mathbf{s}_m(t)$ (incoh.) for $i = m = 1,...,N$, the variational equations transversal to the synchronized cluster C_0 in the cluster-based coordinates are given by

$$\partial_t \eta_\kappa^{(\mathbf{0})} = \left[D\mathbf{F}(\mathbf{s}_0) + \frac{\mu}{N} \lambda_\kappa^{(0)} D\mathbf{H}(\mathbf{s}_0) \right] \eta_\kappa^{(\mathbf{0})} \tag{3.65}$$

for $\kappa = 2,...,N$ where the Jacobians of the dynamical functions in Eqs. (3.63-3.64) read

$$D\mathbf{F}(\mathbf{s}_0) = \begin{pmatrix} \varepsilon^{-1} & -\omega \\ \omega & \varepsilon^{-1} \end{pmatrix} + \frac{\mu}{N} \begin{pmatrix} \cos\alpha & \sin\alpha \\ -\sin\alpha & \cos\alpha \end{pmatrix} - \frac{\varepsilon^{-1}}{2} \begin{pmatrix} 1 & -\varepsilon\sigma \\ \varepsilon\sigma & 1 \end{pmatrix} \begin{pmatrix} 3s_{0_1}^2 + s_{0_2}^2 & 2s_{0_1}s_{0_2} \\ 2s_{0_1}s_{0_2} & 3s_{0_2}^2 + s_{0_1}^2 \end{pmatrix} \tag{3.66}$$

and

$$D\mathbf{H}(\mathbf{s}_0) = \begin{pmatrix} \cos\alpha & \sin\alpha \\ -\sin\alpha & \cos\alpha \end{pmatrix}. \tag{3.67}$$

For the synchronized Stuart-Landau oscillators, we have $r_k e^{i\phi_k} = e^{i\phi_0} = \frac{1}{\sqrt{2}}(a_0 + ib_0)$ for $k = 1,...,N$. Hence, the transversal variational equations are written as

$$\begin{aligned} \partial_t \eta_\kappa^{(\mathbf{0})} = & \left[\begin{pmatrix} \varepsilon^{-1} & -\omega \\ \omega & \varepsilon^{-1} \end{pmatrix} + \frac{\mu}{N}(1 + \lambda_\kappa^{(0)}) \begin{pmatrix} \cos\alpha & \sin\alpha \\ -\sin\alpha & \cos\alpha \end{pmatrix} \right. \\ & \left. - \frac{\varepsilon^{-1}}{2} \begin{pmatrix} 1 & -\varepsilon\sigma \\ \varepsilon\sigma & 1 \end{pmatrix} \begin{pmatrix} 2 + 4\cos^2\phi_0 & 4\cos\phi_0\sin\phi_0 \\ 4\cos\phi_0\sin\phi_0 & 2 + 4\sin^2\phi_0 \end{pmatrix} \right] \eta_\kappa^{(\mathbf{0})} \\ = & \mathbf{J}_{\text{trans}}^{(0)} \eta_\kappa^{(\mathbf{0})} \end{aligned} \tag{3.68}$$

for all the directions transverse to the sync-manifold, i.e., for $\kappa = 2,...,N$. Since it is a complete graph, the eigenvalues of the adjacency matrix are given by $\lambda_\kappa^{(0)} = -1$ for all κ. If

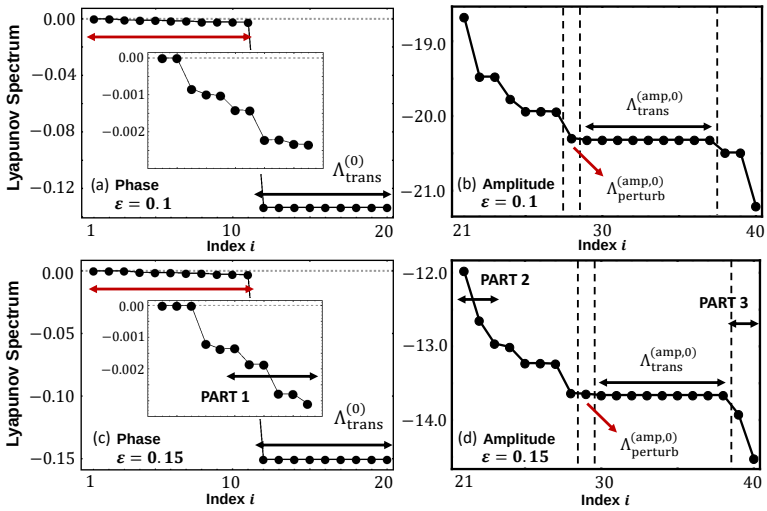

Fig. 3.9 Lyapunov exponents vs index of the strongly coupled SL oscillators with global intra-group coupling for $A = 0.2$, $N = 20$ and (a-b) $\varepsilon = 0.1$ (stationary) and (c-d) $\varepsilon = 0.15$ (breathing). (a,c) Lyapunov exponents of phase DOFs. The Insets show a magnification of the Lyapunov exponents corresponding to the incoherent phase DOFs. (b,d) Lyapunov exponents corresponding to amplitude DOFs.

we consider ϕ_0 as an external forcing function, then the eigenvalues of the matrix $\mathbf{J}^{(0)}_{\rm trans}$ are

$$\begin{aligned}\Lambda_1 &= -\frac{1+\sqrt{1-\varepsilon^2(3\sigma^2-4\sigma\omega+\omega^2)}}{\varepsilon}\\ \Lambda_2 &= \frac{-1+\sqrt{1-\varepsilon^2(3\sigma^2-4\sigma\omega+\omega^2)}}{\varepsilon}\end{aligned} \tag{3.69}$$

which gives $\Lambda_1 \sim -2\varepsilon^{-1}$ corresponding to the amplitude DOF branch and $\Lambda_2 \lesssim 0$ corresponding to the phase DOF branch for the synchronized oscillators.

For the numerical measurement of the Lyapunov exponents, we consider the real-valued coordinates of each Stuart-Landau oscillator defined in Eq. (3.61)[12]. In the coordinate systems, the perturbation vectors in the tangent space are written in the form

$$\mathbf{v}^{(i)} = (a_1,\ldots,,a_N,a_{N+1},\ldots,a_{2N},b_1,\ldots,b_N,b_{N+1},\ldots,b_{2N})^\top \in T_{\mathbf{x}_{\rm ch}(t)}(\mathbb{R}^{4N}). \tag{3.70}$$

Amplitude Degrees of Freedom

In Fig. 3.9, the Lyapunov exponents from numerical experiments along Poisson chimera reference trajectory for strong coupling $\varepsilon = 0.1$ (a,b) and 0.15 (c,d) are displayed. The Lyapunov exponents show two parts, one of which corresponds to the phase and the other to amplitude DOFs, respectively. The phase part is shown in the left column, the amplitude DOFs in the right one. First, consider the amplitude DOFs of the synchronized oscillators. Figure 3.9 (b) and (d) show strongly negative $(N-1)$-fold degenerate Lyapunov exponents, which are transverse to the sync-manifold. The approximate values of these Lyapunov exponents are $\Lambda^{(\mathrm{amp},0)}_{\mathrm{trans},\kappa} \approx \varepsilon^{-1}(1-3R_0^2) < 0$ for $\kappa = 2,\ldots,N$. The numerically obtained CLVs show that these Lyapunov exponents are indeed transverse to the sync-manifold as they have the following form

$$\mathbf{v}^{(\mathrm{amp},0)}_{\kappa} = \left(a^{(\mathrm{amp},0)}_{\kappa 1},\ldots,a^{(\mathrm{amp},0)}_{\kappa N},0,\ldots,0,b^{(\mathrm{amp},0)}_{\kappa 1},\ldots,b^{(\mathrm{amp},0)}_{\kappa N},0,\ldots,0\right)^{\top} \in \mathbf{T}_{\mathbf{x}_{\mathrm{ch}}(t)}(\mathbb{R}^{4N}) \tag{3.71}$$

where $\sum_{i=1}^{N} a^{(\mathrm{amp},0)}_{\kappa i} = \sum_{i=1}^{N} b^{(\mathrm{amp},0)}_{\kappa i} = 0$ for $\kappa = 2,\ldots,N$. In Fig. 3.9 (b,d), we observe another negative exponent, corresponding to Eq. (3.56), in the synchronized population of the amplitude DOFs associated with the perturbation along the sync-manifold. Its numerical value is slightly greater than those of the transverse Lyapunov exponent, as expected in Eq. (3.56). Hence, we conclude that in the amplitude DOFs, the synchronized manifold is stable in both transverse and parallel directions to the sync-manifold. We guess the other negative Lyapunov exponents in the amplitude DOFs are due to the incoherent oscillators via their quotient dynamics. Therefore, all the Lyapunov exponents of the amplitude DOFs are strongly negative, and all amplitude DOFs of Poisson chimeras are attracting.

Phase Degrees of Freedom

In Fig. 3.9 (a) and (c), the numerically obtained Lyapunov exponents are depicted for the phase degrees of freedom. They also have the $(N-1)$-fold degenerate transverse Lyapunov exponents whose values are approximated in Eq. (3.60). In addition, the LE corresponding to a perturbation along the sync-manifold has the value of $\Lambda^{(0)}_{\mathrm{perturb}} = -\frac{\nu}{N}\tilde{Z} < 0$. The numerically calculated CLVs show that $\Lambda^{(0)}_{\mathrm{trans},\kappa}$ and $\Lambda^{(0)}_{\mathrm{perturb}}$ are associated with the transverse and parallel perturbations to the sync-manifold, respectively.

[12] Note that this coordinate transformation is a unitary transformation; hence, it can uphold the information on Lyapunov exponents. Also, we measured the LEs in the original coordinate systems (phase and amplitude), and obtained the same result.

What makes Poisson chimeras of SL oscillators attracting is due to the incoherent LEs $\Lambda^{(\mathrm{incoh})}$ in Fig. 3.9 (see inset). In a rotating reference frame, the incoherent phase DOFs in Eq. (3.58) have the same form as those of the phase-reduced oscillators in Eqs. (3.27-3.28) except for the amplitude variables. As we discussed, they can be considered as a small self-organized heterogeneity $\tilde{\Omega}_m(t)$ in Eq. (3.58). In Fig. 3.9 (a,c), we find negative Lyapunov exponents in the incoherent phase DOFs. For the stationary chimera ($\varepsilon = 0.1$), we have two zero Lyapunov exponents arising from two continuous symmetries. For the breathing chimera ($\varepsilon = 0.15$), apart from the negative exponents, there are three zero Lyapunov exponents. The additional zero LE for the breathing chimeras arises from the Hopf frequency of the periodic motion. The stable Lyapunov exponents are expected to arise due to the role of the amplitude variables in the phase governing equations. The amplitude variables occur as a small self-organized heterogeneity, which in turn renders the Poisson chimeras attracting, in a similar way to the role of the generic heterogeneity in the OA manifold [97, 181, 62, 169, 102, 168, 180]. Hence, we conclude that the Poisson chimeras are attracting, compared to the KS phase-reduced Poisson chimera states because the amplitude variables introduce a self-organized heterogeneity in the phase governing equations. As a consequence, even if starting from an n-PIC, the chimera trajectories eventually approach a close vicinity of the Poisson submanifold, as is confirmed by the numerical simulations above[13].

3.4 Summary

In this chapter, we have dealt with chimera states in two-population networks of identical oscillators. For the identical Kuramoto-Sakaguchi phase oscillators, the order parameter dynamics of the incoherent oscillator population strongly depends on the initial condition and the population size. Once chimeras started from a special initial condition where all the initial phases of one population are in the Poisson kernel, i.e., the Poisson submanifold, the phases remain in the Poisson kernel for all times, and we called this chimera a Poisson chimera. Poisson chimeras show a rather simple motion of the incoherent oscillator population that is virtually indistinguishable from the continuum limit OA solution for sufficiently large population sizes. In contrast, the incoherent motion of a Poisson chimera with a small population size is drastically different from the simple OA dynamics. This difference is not due to finite-size fluctuations, but has a deterministic origin: The magnitude of the order parameter of the incoherent oscillator population shows not only the main motion

[13] Note that we also find the Poisson chimera state for the weak coupling strength $\varepsilon = 0.01$ is attracting. Furthermore, the system of the identical Stuart-Landau oscillators in two-population networks with the nonlocal intra-population connectivity also displays the attracting Poisson chimera states. For the detailed analysis, see Ref. [55].

close to the OA dynamics but also a superimposed secondary oscillation along the main motion. We demonstrated that this superposed oscillation is a consequence of the fact that the instantaneous frequencies of stationary Poisson chimeras exhibit a splay form. Furthermore, the splayed distribution of the instantaneous frequencies brings about that the period of the superposed oscillation tends to zero with increasing N, while the consideration of the WS global variables revealed how the amplitude of the secondary oscillation disappears with increasing N. Consequently, our investigations have revealed how the order parameter changes continuously from small-size chimeras to large-size chimeras up to the continuum limit, eventually showing the same dynamics as the OA dynamics at the continuum boundary.

In our numerical Lyapunov analysis, the stationary chimera states in a two-population network with global intra- and inter-population coupling topology, whether it is a Poisson or non-Poisson chimera, are neutrally stable in $N-1$ directions. It is important to note that the other negative Lyapunov exponent corresponds to the degree of coherence, specifically the macroscopic Watanabe-Strogatz radial variable. According to the Watanabe-Strogatz theory, this neutral stability primarily arises from the system's constants of motion.

Also, we examined two scenarios that render Poisson chimeras attracting, or at the very least, ensure their proximity to the Poisson submanifold. We introduced two distinct 'perturbations' to the identical Kuramoto-Sakaguchi phase oscillators within the global two-population network: a nonlocal intra-population topology and the inclusion of an amplitude degree of freedom using Stuart-Landau planar oscillators. Previous works have shown that the Ott-Antonsen manifold in the thermodynamic limit becomes attracting if the system demonstrates a certain level of heterogeneity. Our analysis has illustrated that the two perturbations we introduced can indeed be considered as forms of weak heterogeneity for the population of incoherent oscillators. In alignment with these considerations, the Lyapunov analysis has uncovered that systems involving nonlocally coupled phase oscillators and globally coupled Stuart-Landau amplitude oscillators exhibit negative Lyapunov exponents associated with the incoherent phase degrees of freedom. As a result, they follow an attracting trajectory leading to a Poisson chimera. Notably, even when initiated from non-Poisson initial conditions, the trajectory of the chimera evolves towards either the Poisson chimera state or asymptotically approaches a close vicinity of it.

Chapter 4

Coexistence Dynamics II: Chaotic Chimera Attractors

In Chap. 3, we discussed the chimera states in two-population networks with a particular focus on chimeras inside the Poisson submanifold and the OA manifold. Three types of stable chimera states were identified in two-population networks. First, we studied stationary chimera states where the order parameter of the incoherent population exhibits a steady motion as a fixed point of the OA equation in Eq. (3.10). Secondly, the so-called breathing chimeras, where the Kuramoto order parameter oscillates periodically, emerge at a supercritical Hopf bifurcation at which the stationary chimera state loses its stability [72, 74, 55]. In Chap. 3, we classified them as Poisson chimeras. Thirdly, outside the Poisson submanifold, one can obtain quasiperiodic chimeras or non-Poisson chimeras for nonuniform constants of motion [101].

On the other hand, a chaotic chimera motion requires more intricate configurations. It has been reported that the presence of heterogeneities [81, 183, 76], higher order interactions [80, 84] or higher-dimensional individual oscillators [82, 83] could induce a chaotic chimera state in terms of the macroscopic observables. Note that here the chaotic chimera states refer to the chaotic motion of macroscopic observable, e.g., the Kuramoto order parameter, the OA or the WS variables in large ensembles of oscillators. This has to be distinguished from chaotic (weak) chimeras in systems of just a few, e.g. three [184] or four oscillators [81].

In this chapter, we study a network of identical Kuramoto-Sakaguchi phase oscillators that exhibits chaotic chimera states. In particular, we will show that a triangular network, i.e., a three-population network, of identical Kuramoto-Sakaguchi oscillators possesses

The contents of this chapter were in part published previously in S. Lee and K. Krischer, Phys. Rev. E **107**, 054205 (2023) [56]. Note all figures and captions are reproduced from that reference.

macroscopic chaotic chimera attractors outside the OA manifold, coexisting with a periodic antiphase chimera state and a stationary chimera state both living in the OA manifold.

The chimera states in three-population networks of identical KS phase oscillators were previously studied only for symmetric solutions, which are here called *symmetric chimera states*. The symmetric chimera states were studied in the thermodynamic limit based on the OA equations and were restricted to the symmetry-reduced manifold where two populations behave identically [88, 89]. E. A. Martens reported in Ref. [88] that there are two types of symmetric chimera states: symmetric-DSD and symmetric-SDS chimera states, respectively[1] where 'D' and 'S' stand for partially incoherent and synchronized populations, respectively. On the symmetry-reduced manifold, both of these types of chimeras are stable in some range of the parameters and the order parameter (the radial OA variable) of the incoherent populations can be either stationary or breathing, similar to the Poisson chimeras in two-population networks. The author of Ref. [88] raised several questions: (i) The first concerns the stability of chimera states outside the symmetry-reduced manifold, and the possible existence of non-symmetric or symmetry-broken solutions, e.g., DSD$'$-chimeras, where the D$'$ indicates that the two desynchronized (i.e, incoherent) populations display a different motion of the order parameter. (ii) The second one relates to the existence of chaotic chimera dynamics, characterized by an aperiodic motion of the order parameter of the incoherent oscillators. In this chapter, we answer these questions and provide detailed dynamical properties of the observable chimera states, in particular, beyond the symmetry-reduced manifold, i.e., in the entire the phase space. Furthermore, we study their spectral properties,using Lyapunov analysis, as we did in the last chapter.

4.1 Governing Equations

We consider a system of identical Kuramoto-Sakaguchi phase oscillators in a triangular network of identical Kuramoto-Sakaguchi oscillators. Each oscillator is described by a phase variable $\phi_j^{(a)}(t) \in \mathbb{T}$ that is governed by

$$\partial_t \phi_j^{(a)} = \omega + \mathrm{Im}\left[H_a(t) e^{-i\phi_j^{(a)}}\right] = \omega + \sum_{b=1}^{3} G_{ab} \frac{1}{N} \sum_{k=1}^{N} \sin(\phi_k^{(b)} - \phi_j^{(a)} - \alpha) \qquad (4.1)$$

with $j = 1,...,N$ and $a,b = 1,2,3$. Here, $H_a(t)$ represents a mean-field forcing that globally affects an oscillator in population a and is defined by $H_a(t) := e^{-i\alpha}\big(\mu\Gamma_a(t) + \nu\Gamma_b(t) + \nu\Gamma_c(t)\big)$ where (a,b,c) is a permutation of $(1,2,3)$. As above, $\Gamma_a(t)$ denotes the Kuramoto

[1] Here, 'S' stands for a completely synchronized population while 'D' denotes a desynchronized population, i.e., the incoherent population.

order parameter of each population, which is defined as

$$\Gamma_a(t) = r_a(t)e^{i\Theta_a(t)} := \frac{1}{N}\sum_{j=1}^{N} e^{i\phi_j^{(a)}(t)}. \tag{4.2}$$

The phase-lag parameter α is written as $\alpha = \frac{\pi}{2} - \beta$. In this chapter, we fix $\beta = 0.025$. Note that we consider identical oscillators and set $\omega = 0$. The triangular network topology is defined by an all-to-all intra-population coupling strength, denoted by $\mu = 1$, and a global inter-population coupling strength given as $\nu = 1 - A$ where $A \in (0,1)$, and being always smaller than the intra-population coupling strength. Then, the coupling strength matrix is thus defined as [88, 89]

$$(G_{aa'}) = \begin{pmatrix} \mu & \nu & \nu \\ \nu & \mu & \nu \\ \nu & \nu & \mu \end{pmatrix} \tag{4.3}$$

for $a, a' = 1,2,3$.

To explore the macroscopic dynamics of the system, we study the dynamics on the levels of the OA and the WS reductions for the thermodynamic limit and for the finite-sized ensemble, respectively. First, the WS transformation is written as (cf. Eq. (2.74))

$$e^{i\phi_j^{(a)}} = e^{i\Phi_a}\frac{\rho_a + e^{i(\psi_j^{(a)} - \Psi_a)}}{1 + \rho_a e^{i(\psi_j^{(a)} - \Psi_a)}} \tag{4.4}$$

for $j = 1, ..., N$ and $a = 1,2,3$. As in Eq. (2.77), the relation between the WS macroscopic variables and the Kuramoto order parameter is given by

$$\Gamma_a(t) = \rho_a(t)e^{i\Phi_a(t)}\gamma_a(\rho_a, \Psi_a; t) \tag{4.5}$$

where γ_a is defined by

$$\begin{aligned} \gamma_a &= \frac{1}{\rho_a}(\zeta_a + i\xi_a) \\ &:= \frac{1}{\rho_a N}\sum_{k=1}^{N}\frac{2\rho_a + (1+\rho_a^2)\cos(\psi_k^{(a)} - \Psi_a)}{1 + 2\rho_a\cos(\psi_k^{(a)} - \Psi_a) + \rho_a^2} + i\frac{1}{\rho_a N}\sum_{k=1}^{N}\frac{(1-\rho_a^2)\sin(\psi_k^{(a)} - \Psi_a)}{1 + 2\rho_a\cos(\psi_k^{(a)} - \Psi_a) + \rho_a^2} \end{aligned} \tag{4.6}$$

for $a=1,2,3$. Then, the 9D WS macroscopic variables are governed by [101, 102, 74]

$$\begin{aligned}
\partial_t \rho_a &= \frac{1-\rho_a^2}{2}\sum_{a'=1}^{3} G_{aa'}\big(\zeta_{a'}\cos(\Phi_{a'}-\Phi_a-\alpha)-\xi_{a'}\sin(\Phi_{a'}-\Phi_a-\alpha)\big),\\
\partial_t \Psi_a &= \frac{1-\rho_a^2}{2\rho_a}\sum_{a'=1}^{3} G_{aa'}\big(\zeta_{a'}\sin(\Phi_{a'}-\Phi_a-\alpha)+\xi_{a'}\cos(\Phi_{a'}-\Phi_a-\alpha)\big),\\
\partial_t \Phi_a &= \frac{1+\rho_a^2}{2\rho_a}\sum_{a'=1}^{3} G_{aa'}\big(\zeta_{a'}\sin(\Phi_{a'}-\Phi_a-\alpha)+\xi_{a'}\cos(\Phi_{a'}-\Phi_a-\alpha)\big)
\end{aligned} \tag{4.7}$$

for $a=1,2,3$ where the uniform constants of motion can be taken as $\psi_j^{(a)}=-\pi+\frac{2\pi(j-1)}{N}$ for $j=1,...,N$.

In the thermodynamic limit, the 6D dynamics in the OA manifold can be obtained [88, 101, 102]

$$\begin{aligned}
\partial_t \rho_a &= \frac{1-\rho_a^2}{2}\sum_{a'=1}^{3} G_{aa'}\rho_{a'}\cos(\Phi_{a'}-\Phi_a-\alpha),\\
\partial_t \Phi_a &= \frac{1+\rho_a^2}{2\rho_a}\sum_{a'=1}^{3} G_{aa'}\rho_{a'}\sin(\Phi_{a'}-\Phi_a-\alpha)
\end{aligned} \tag{4.8}$$

where $\Gamma_a(t)=\rho_a(t)e^{i\Phi_a(t)}$ and $\gamma_a=1$ for $a=1,2,3$.

As mentioned above, one can consider a symmetric solution for chimera states, where two populations, let's say the first and the third one, behave identically: symmetric-SDS chimeras and symmetric-DSD chimera states. To understand their behavior, the previous works concentrated on the symmetry-reduced manifold, which will be lifted to the full-dimensional dynamics below. Here, we obtain the symmetry-reduced OA and WS governing equations for later reference in Sec. 4.3.

First, let us consider an SDS-type solution. For the OA dynamics, one can introduce the variables $\rho_1=\rho_3=1$, $\rho_2=\rho<1$, $\Phi_1=\Phi_3$, and $\varphi=\Phi_1-\Phi_2$, which are governed by [88]

$$\begin{aligned}
\partial_t \rho &= \frac{1-\rho^2}{2}\big(2(1-A)\sin(\varphi+\beta)+\rho\sin\beta\big)\\
\partial_t \varphi &= -(2-A)\cos\beta-(1-A)\rho\cos(-\varphi+\beta)+\frac{1+\rho^2}{2\rho}\big(2(1-A)\cos(\varphi+\beta)+\rho\cos\beta\big)
\end{aligned} \tag{4.9}$$

where $\beta=\frac{\pi}{2}-\alpha$ serves as the phase-lag parameter. For the WS variables, we can consider $\rho_1=\rho_3=1$, $\rho_2=\rho<1$, $\Phi_1=\Phi_3$, $\varphi=\Phi_1-\Phi_2$, and $\Psi=\Psi_1-\Psi_2$ with $\Psi_1=\Psi_3$. Then,

the symmetry-reduced SDS chimeras are governed by

$$\begin{aligned}
\partial_t \rho &= \frac{1-\rho^2}{2}\Big(\mu(\zeta\cos\alpha+\xi\sin\alpha)+2\nu\cos(\varphi-\alpha)\Big)\\
\partial_t \Psi &= -\frac{1-\rho^2}{2\rho}\Big(\mu(-\zeta\sin\alpha+\xi\cos\alpha)+2\nu\sin(\varphi-\alpha)\Big)\\
\partial_t \varphi &= -\mu\sin\alpha+\nu\Big(-\zeta\sin(\varphi+\alpha)+\xi\cos(\varphi+\alpha)\Big)-\nu\sin\alpha\\
&\quad -\frac{1+\rho^2}{2\rho}\Big(\mu(-\zeta\sin\alpha+\xi\cos\alpha)+2\nu\sin(\varphi-\alpha)\Big)
\end{aligned} \tag{4.10}$$

where the other variables are defined as

$$\zeta=\frac{1}{N}\sum_{k=1}^{N}\frac{2\rho+(1+\rho^2)\cos(\psi_k-\Psi)}{1+2\rho\cos(\psi_k-\Psi)+\rho^2},\quad \xi=\frac{1}{N}\sum_{k=1}^{N}\frac{(1-\rho^2)\sin(\psi_k-\Psi)}{1+2\rho\cos(\psi_k-\Psi)+\rho^2} \tag{4.11}$$

for $\psi_k=-\pi+(2\pi)\frac{k-1}{N}$, $k=1,...,N$, i.e., uniform constants of motion.

Secondly, the symmetry-reduced DSD chimeras can be represented as $\rho:=\rho_1=\rho_3<1$, $\rho_2=1$, and $\varphi:=\Phi_1-\Phi_2$ (with $\Phi_1=\Phi_3$). They follow

$$\begin{aligned}
\partial_t \rho &= \frac{1-\rho^2}{2}\Big((2-A)\rho\sin\beta+(1-A)\sin(-\varphi+\beta)\Big)\\
\partial_t \varphi &= -\frac{1+\rho^2}{2\rho}\Big((2-A)\rho\cos\beta+(1-A)\cos(-\varphi+\beta)\Big)+2(1-A)\rho\cos(\varphi+\beta)+\cos\beta.
\end{aligned} \tag{4.12}$$

The reduced WS dynamics for the DSD chimera states can be obtained by $\rho:=\rho_1=\rho_3<1$, $\rho_2=1$, $\varphi:=\Phi_1-\Phi_2$ (with $\Phi_1=\Phi_3$), $\Psi:=\Psi_1-\Psi_2$ (with $\Psi_1=\Psi_3$). Then, the governing equations are given as

$$\begin{aligned}
\partial_t \rho &= \frac{1-\rho^2}{2}\Big(\mu(\zeta\cos\alpha+\xi\sin\alpha)+\nu(\cos(\varphi+\alpha)+\zeta\cos\alpha+\xi\sin\alpha)\Big)\\
\partial_t \Psi &= \frac{1-\rho^2}{2\rho}\Big(\mu(-\zeta\sin\alpha+\xi\cos\alpha)+\nu(-\sin(\varphi+\alpha)-\zeta\sin\alpha+\xi\cos\alpha)\Big)\\
\partial_t \varphi &= \mu\sin\alpha-2\nu\Big(\zeta\sin(\varphi-\alpha)+\xi\cos(\varphi-\alpha)\Big)\\
&\quad +\frac{1+\rho^2}{2\rho}\Big(\mu(-\zeta\sin\alpha+\xi\cos\alpha)+\nu(-\sin(\varphi+\alpha)-\zeta\sin\alpha+\xi\cos\alpha)\Big)
\end{aligned} \tag{4.13}$$

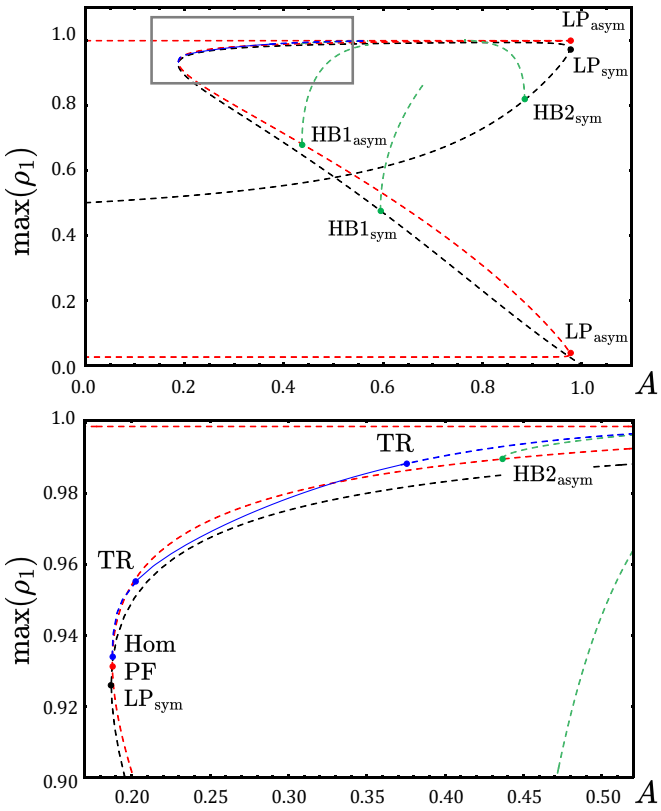

Fig. 4.1 Upper plate: Bifurcation diagram of DSD-type chimera states. Lower plate: Enlargement of the gray box in the upper plate. Dashed and solid lines indicate unstable and stable curves, respectively. Black: symmetric stationary DSD. Red: asymmetric stationary DSD′. Green: symmetric breathing chimeras. Blue: antiphase DSD′ chimera states.

4.2 Symmetry-broken Chimeras: Chaotic Chimera Attractors

In this section, we focus our attention on observable chimera states in the thermodynamic limit which could live on or off the Ott-Antonsen manifold. More specifically, we here discuss stable symmetry-broken DSD′ chimera states, which are connected to chaotic chimeras.

A bifurcation diagram of DSD-type chimera states is depicted in Fig. 4.1. The symmetric DSD chimera states (black) obey $\rho_1(t) = \rho_3(t) < 1$ while $\rho_2(t) = 1$ and $\Phi_1(t) = \Phi_3(t) \in \mathbb{T}$ and live in the symmetry-reduced manifold. Their dynamics restricted to this manifold was studied in Ref. [88]. In the symmetry-reduced manifold, the symmetric-DSD chimeras are found to be stable. However, if they are investigated beyond that manifold in the full-dimensional phase space, we find that all symmetric-DSD chimeras have at least one unstable direction transverse to the symmetry-reduced manifold. The transversal unstable direction

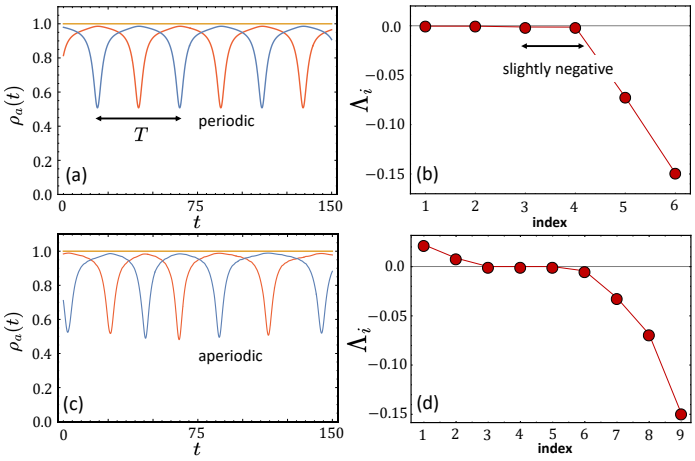

Fig. 4.2 (a) Radial variables of the 6D OA dynamics (red: first, blue: third population, and orange: second population) and (b) Lyapunov exponents along the antiphase chimera trajectory. (c) Radial variables of the 9D WS dynamics with uniform constants of motion and $N = 20$ and (d) and the corresponding Lyapunov exponents. In subfigures: $A = 0.35$ and all are measured after $t > 10^5$.

causes the two symmetric D-populations to move in opposite directions and thus break the symmetry. We will discuss details in Sec. 4.3.2. Not reported before are solutions of broken symmetry. We observe symmetry-broken DSD′ chimera states (blue) which are characterized by $\rho_1(t) \neq \rho_3(t) < 1, \Phi_1(t) \neq \Phi_3(t)$. The stable symmetry-broken chimera states appear with the two incoherent populations exhibiting periodic antiphase oscillations, i.e., $\rho_1(t) = \rho_3(t - \frac{T}{2})$ where T is the period of the oscillation. Thus, we call it an antiphase DSD′ chimera state from now on. In Fig. 4.2 (a), the time evolution of the three moduli of the OA variables, i.e, the Kuramoto order parameter, are shown. These periodic antiphase DSD′ chimeras are born near a double-homoclinic cycle of the stationary symmetric DSD chimeras, which is point-symmetric in the projection on the $\rho_1\rho_3$-plane with respect to the diagonal line ($\rho_1 = \rho_3$). In fact, the unstable antiphase DSD′ chimera state (blue, dashed) is born near a homoclinic bifurcation (Hom) that lies very close to a pitchfork bifurcation (PF) at which a pair of stationary DSD′ chimeras (red) bifurcates off the stationary symmetric-DSD chimera state (black). As the parameter A is increased, the antiphase DSD′ chimera states are stabilized (blue, solid) in a subcritical torus bifurcation (TR). Further increasing A, the antiphase DSD′ chimera state eventually becomes unstable, again via a subcritical torus bifurcation.

Note that such stable antiphase DSD′ chimera states are periodic solutions rather than a chaotic motion. It can be noticed by the fact that the dynamics inherits a spatiotemporal symmetry of the solution such that $\dot{\Phi}_a(t) = \dot{\Phi}_a(t - T), \dot{\rho}_a(t) = \dot{\rho}_a(t - T)$ for $a = 1, 3$ and

$\dot{\Phi}_2(t) = \dot{\Phi}_2(t - \frac{T}{2}), \dot{\Phi}_1(t) = \dot{\Phi}_3(t - \frac{T}{2})$ which leads to $\rho_1(t) = \rho_3(t - \frac{T}{2})$. Thus, the above antiphase DSD′ chimera states in the OA manifold possess just two effective degrees of freedom, and thus cannot be chaotic. This fact is numerically verified by determining the Lyapunov exponents (LEs), as shown in Fig. (4.2) (b). There are two zero Lyapunov exponents arising from two continuous symmetries: the time and the phase shift invariance, which does not affect the stability of the reference trajectory. All the other Lyapunov exponents are negative. Hence, the antiphase DSD′ chimera states in the OA manifold are indeed a stable chimera state, that is, a periodic antiphase chimera.

Next, we consider the finite-sized ensemble and the WS dynamics in Eq. (4.7) with uniform constants of motion, i.e., in the Poisson submanifold. The WS radial variables of the antiphase chimera state in a finite-sized system are shown in Fig. 4.2 (c). The chimera state also displays antiphase oscillation between two incoherent populations, similar to those of the OA dynamics in the thermodynamic limit depicted in Fig. (4.2) (a). However, the antiphase motion of the two WS radial variables for the incoherent populations is not periodic but rather aperiodic, which breaks the aforementioned spatiotemporal symmetry, i.e., $\rho_1(t) \neq \rho_3(t - \frac{T}{2})$. To further investigate this, we numerically determined the Lyapunov exponents, in particular for small system size N. The results are shown in Fig. 4.2 (d). There are clearly two positive Lyapunov exponents, which confirms that the antiphase chimera state in the WS dynamics for small N is chaotic within the Poisson submanifold. This conjecture is supported when its trajectory is traced in a Poincaré section defined by $\Psi_1 \equiv 2\pi$. In Fig. 4.3 (a), the chaotic motion of the antiphase chimera is depicted in the Poincaré section for $N = 30$, which exhibits scattered points on a band-like region, as expected for an aperiodic motion on a chaotic attractor.

Opposed to this, the dynamics of the antiphase chimera state in the WS dynamics for a large system, e.g., $N = 100$ oscillators, resides on a one-dimensional curve in the Poincaré section (Fig. 4.3 (b)). This suggests that the chaotic motion is restricted to small system sizes when uniform constants of motion are chosen. In Fig. 4.3 (c), the two largest Lyapunov exponents of the antiphase chimera states are depicted as a function of system size N. The values of the two positive Lyapunov exponents decrease until $N \approx 60$ where they become numerically zero. Hence, the chaotic behavior of the antiphase chimera state with uniform constants of motion (COM) disappears for large N. Such a small-size effect for the chaotic chimera dynamics is due to the influence of $\gamma_a \in \mathbb{C}$ on the dynamics of the WS variables. For small N, γ_a significantly affects the WS dynamics in Eq. (4.7) and makes the WS dynamics different from the OA dynamics. More precisely, the real and the imaginary part of γ_a show irregular time evolutions along the chaotic chimera trajectory, as depicted in Fig. 4.3 (d).

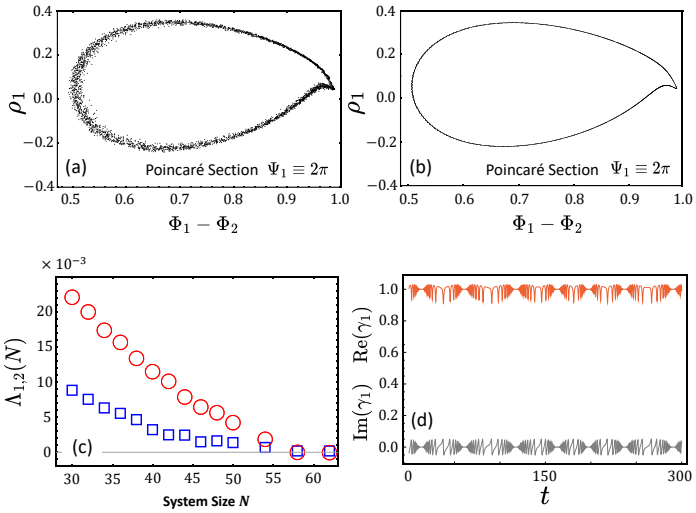

Fig. 4.3 Poincaré section of 9D WS dynamics with uniform constants of motion and $\Psi_1 \equiv 2\pi$ for (a) $N = 30$ and (b) $N = 100$. (c) The largest and the second largest LEs as a function of N for 9D WS dynamics. (d) Real (orange) and imaginary (gray) parts of γ_1 as a function of time after $t > 10^4$. All the results are obtained with uniform constants of motion of WS dynamics, and $A = 0.35$.

However, as $N \to \infty$, $\mathrm{Re}(\gamma_a) \to 1$ and $\mathrm{Im}(\gamma_a) \to 0$, so that Eq. (4.7) becomes identical to Eq. (4.8) and the aperiodic WS dynamics renders a periodic antiphase OA motion.

So far, we have investigated antiphase DSD′ chimeras in the OA manifold for infinite-N and in the Poisson submanifold (i.e., uniform COM for finite-N). Now, we explore the antiphase chimeras outside the OA manifold. First, the chaotic antiphase chimera states can be observed also in the microscopic dynamics of Eq. (4.1) when starting from random initial conditions picked from $\mathbb{T}^{3N}$. In Fig. 4.4 (a), the time evolution of the magnitudes of the Kuramoto order parameters in the microscopic dynamics, defined in Eq. (4.2), is shown for $N = 40$. Also, the radial variables of the WS dynamics is depicted in Fig. 4.4 (b) for $N = 40$ with nonuniform COM, defined by $\psi_j^{(a)} = (1-q)\frac{\pi}{2} + \frac{\pi q(j-1)}{N/2}$ and $\psi_{j+N/2}^{(a)} = -(1+q)\frac{\pi}{2} + \frac{\pi q(j-1)}{N/2}$ with $q = 0.85$ for $j = 1, \ldots, \frac{N}{2}$ and for $a = 1, 2, 3$ [101, 102]. The moduli of the Kuramoto order parameters display a qualitatively similar motion as the dynamics of the WS radial variables, but with further fluctuations superimposed. This is also expected from the impact of γ_a in Eq. (4.5). However, not like the WS dynamics with the uniform COM, the chaotic motion of the WS variables outside the Poisson submanifold persists for systems as large as $N = 4000$. To show this, we numerically determined the two largest Lyapunov exponents as a function of the system size N, as shown in Fig. 4.4 (c). For small N, they decrease as system size increases but then eventually saturate at a positive, non-zero value. From this, we can conjecture that the chaotic attractors exist outside the OA

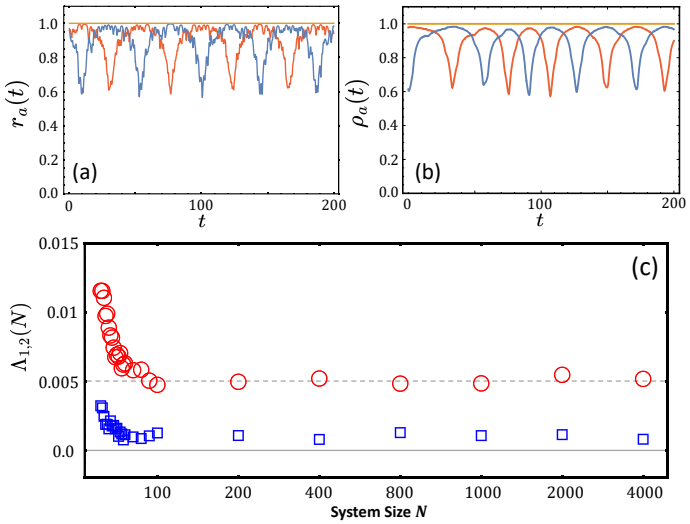

Fig. 4.4 (a) Moduli of the Kuramoto order parameters of the three populations for the microscopic dynamics (4.1) with $N = 40$ after $t > 10^5$. (b) Radial variables of the WS dynamics (4.7) with $N = 40$ after $t > 10^5$. (c) The largest and the second largest LEs as a function of N. The 9D WS dynamics is obtained with nonuniform constants of motion and the microscopic dynamics from a random initial condition. The parameter used here is $A = 0.3$.

manifold even in the thermodynamic limit. This conjecture is further supported when plotting the dynamics in a Poincaré section, as we did above. Cf. Fig. 4.3 (a). With nonuniform constants of motion, one obtains a similar scattered characteristic of the chimera trajectory in the WS dynamics, even for $N = 200$ (not shown here). Note that this chaotic motion is not microscopic chaos of a few oscillators but rather it presents macroscopic chaos of the Kuramoto order parameter dynamics [49, 50].

Hence, we demonstrated that a large system of identical Kuramoto-Sakaguchi phase oscillators in three-population networks exhibits the existence of periodic antiphase chimeras within the OA manifold and chaotic antiphase chimeras outside of it in the thermodynamic limit. Furthermore, in a broad range of parameter values, there is a stationary symmetric-SDS chimera state that coexists with these two states. For more information on the stability of the symmetric-SDS chimeras, see Sec. 4.3.1. We, thus, provide evidence for the coexistence of three distinguishable chimera states in the phase space.

4.3 Symmetric Chimeras

To assess the probability of observable chimera states, we performed a total of 200 simulations for the OA (Eq. (4.8)), the WS (Eq. (4.7)), and the microscopic (Eq. (4.1)) dynamics in

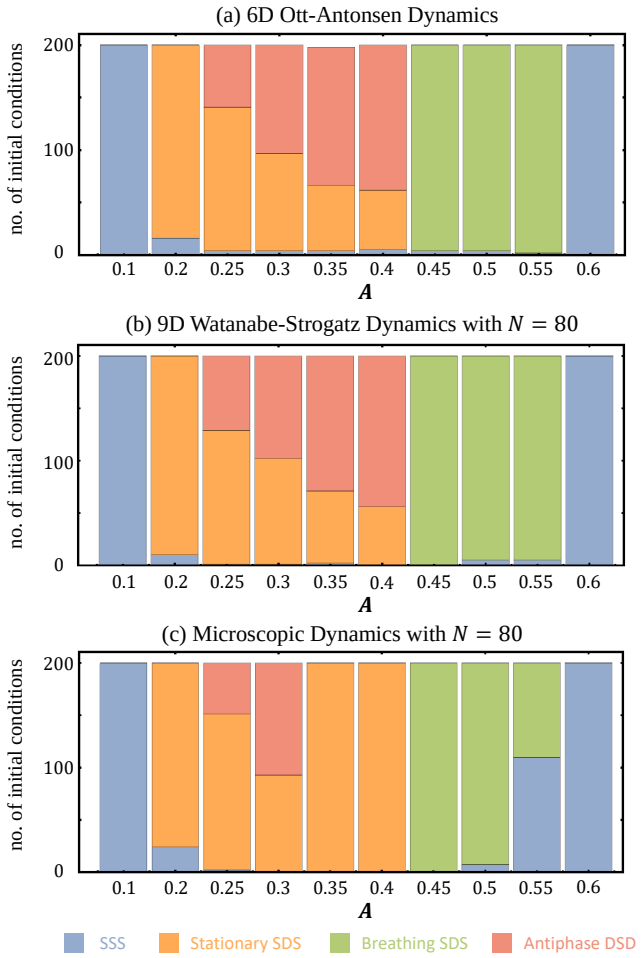

Fig. 4.5 The number of dynamical states at $t = 20,000$ starting from 200 random initial conditions for different values of A. (a) 6D Ott-Antonsen dynamics. (b) 9D Watanabe-Strogatz macroscopic dynamics with $N = 80$ and uniform constants of motion. (c) $3N$-dimensional microscopic dynamics with $N = 80$.

the full-dimensional phase space, i.e., beyond the symmetry-reduced manifold. Note that for the WS dynamics, we employed uniform COM with $N = 80$. Each simulation was initialized with random initial conditions for the relevant dynamical variables. Figure 4.5 depicts the number of dynamical states obtained after long time transient at some parameter values. In the range of approximately $0.2 \lesssim A \lesssim 0.4$, we observe the simultaneous presence of stationary symmetric-SDS chimeras and antiphase DSD$'$ chimeras in both the OA and the WS dynamics. In this case, the antiphase chimeras exhibit periodic behavior since they are in the OA manifold and the WS dynamics for large-sized ensembles in the Poisson submanifold, respectively. For the microscopic dynamics from random initial conditions corresponding to nonuniform COM, we find the coexistence of chaotic antiphase chimeras

with stationary symmetric-SDS chimera states, albeit within a slightly narrower parameter range. Additionally, we also encounter breathing symmetric-SDS chimeras for large values of A. Note that the stationary and breathing symmetric-DSD chimera states are not observed at all in this numerical experiment since they are unstable in the full phase space outside the symmetry-reduced manifold.

4.3.1 Symmetric-SDS Chimera States

Symmetric-SDS chimera states in three-population networks behave similarly to the Poisson/non-Poisson chimeras in two-population networks depending on the ICs, as discussed in Chap. 3. In this section, we discuss their dynamical and spectral properties. In the 6D OA manifold, the stationary symmetric-SDS chimeras appear as $\rho_1(t) = \rho_3(t) = 1$, $\rho_2(t) = \rho_0 < 1$, $\partial_t \Phi_a(t) = \Omega \in \mathbb{R}$ for $a = 1,2,3$. In Fig. 4.6 (a), the time evolution of $\rho_a(t)$ is shown. As ρ_a is stationary, this stationary symmetric-SDS chimera state is a fixed point solution in a reference frame rotating with Ω. Hence, linear stability can be easily studied by measuring the eigenvalues of the Jacobian matrix evaluated at that solution. In Fig. 4.6 (b), the six eigenvalues are plotted in the complex plane for $A = 0.35$ as an exmaple. The chimera state is found to be stable in the OA dynamics since all the eigenvalues have non-positive real parts, except for one eigenvalue corresponding to the phase-shift invariance: The eigenvalue $\lambda_1 = 0$ with the corresponding eigenvector $\delta x_1 = (0,0,0,\delta a,\delta a,\delta a)^\top$ where $\delta a = 1/\sqrt{3}$, i.e., all the mean phases Φ_a of three populations are perturbed by a constant shift. The pair of complex conjugate eigenvalues, $\lambda_2 = \overline{\lambda}_3$ corresponds to the eigenvector within the symmetry-reduced manifold: $\delta x_2 = \overline{\delta x_3} = (0,\delta a,0,\delta b,\delta c,\delta b)^\top$ for $\delta a, \delta c \in \mathbb{C}$ and $\delta b \in \mathbb{R}$. The real negative eigenvalue λ_4 is related to the perturbation transverse to the symmetry-reduced manifold in the angular direction: $\delta x_4 = (0,0,0,\delta a,0,-\delta a)^\top$ where $\delta a = 1/\sqrt{2}$. The last two eigenvalues $\lambda_5 = \lambda_6$ are real, negative and degenerate. In Fig. 4.6 (c), a bifurcation diagram of the stationary symmetric-SDS chimera state is depicted[2]. They are born in a limit point bifurcation (LP), creating a stable (red, solid) and an unstable (red, dashed) symmetric-SDS chimera branch. The stable stationary chimera state is destabilized in a supercritical Hopf bifurcation (HB), giving rise to a stable breathing symmetric-SDS chimera state (green, solid). This breathing chimera disappears in a homoclinic bifurcation as the parameter A is further increased while the period of the breathing chimera is soaring up to infinity.

[2]Note that the bifurcation diagram of the symmetric-SDS chimera states is qualitatively the same as bifurcation scenario for chimeras either in two-population networks [72, 74] or in three-population networks restricted to the symmetry-reduced manifold [88].

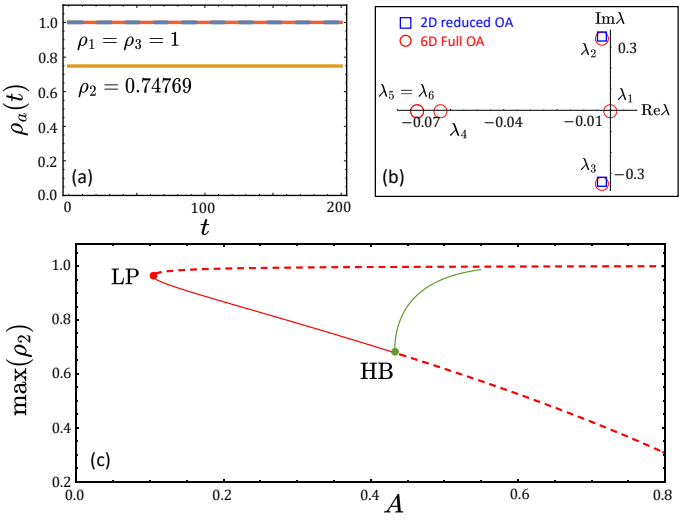

Fig. 4.6 Stationary SDS chimeras in the 6D OA dynamics. (a) Time evolution of the radial variables of 6D OA dynamics after a transient time of 10^5 units for $A = 0.35$. (b) The eigenvalues of the Jacobian matrix evaluated at the stationary SDS chimera fixed point solution shown in (a) in the complex plane. Red circles indicate the eigenvalues in the 6D OA dynamics, and the blue squares those in the 2D symmetry-reduced manifold. (c) Bifurcation diagram of SDS chimeras. The states are born in a limit point bifurcation (LP). The red dashed and solid curves indicate the location of unstable and stable stationary SDS chimeras, respectively. The green curve shows the maxima of the radial variable of a breathing chimera state emerging in a supercritical Hopf bifurcation (HB).

In Fig. 4.7, we explore the 9D WS dynamics in Eq. (4.7) for the stationary symmetric-SDS chimeras with uniform constants of motion. As is in Chap. 3, the macroscopic WS dynamics strongly depends on the system size N. For large N, the radial variables (Fig. 4.7 (a)) appears as a fixed point solution and is characterized by $\rho_1(t) = \rho_3(t) = 1$ (red and blue) and $\rho_2(t) = \rho_0 < 1$ (orange coinciding with black, see below). The angular variable is found to be $\partial_t \Phi_a(t) = \Omega$ for $a = 1,2,3$. The other WS angular variables read $\partial_t \Psi_a(t) = 0$ for $a = 1,3$, and $\partial_t \Psi_2(t) = \tilde{\Omega}$. For small N (Fig. 4.7 (b)), the WS radial variables are slightly fluctuating along the OA dynamics (orange not coinciding with black). However, such fluctuations are so small that they can be neglected. Such dependence on the system size is more clear for the Kuramoto order parameter, obtained from Eq. (2.77). For small N, the Kuramoto order parameter of the incoherent population displays a regular secondary oscillating motion along the OA dynamics ρ_0 (black, in Fig. 4.7 (b)). Such a regular secondary oscillation is suppressed as N increases (black, in Fig. 4.7 (a)), similar to the stationary Poisson chimeras in Chap. 3. Note that here also both the amplitude and the period are vanishing as N increases. This phenomenon can be understood in the same way as in Sec. 3.1.2 in Chap. 3. Here, we also find that the instantaneous phase velocity of each oscillator in the incoherent population

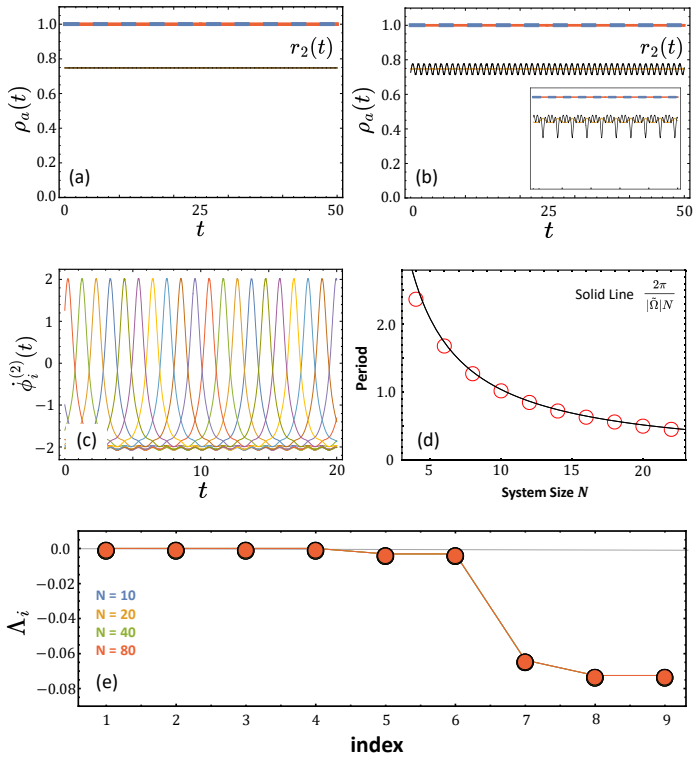

Fig. 4.7 Stationary SDS chimera states in the 9D Watanabe-Strogatz dynamics. (a,b) Time evolution of the radial macroscopic variables after a transient time of 10^5 units for $A = 0.35$. Blue and red lines indicate $\rho_1(t) = \rho_3(t) = 1$ and the orange line $\rho_2(t) < 1$. The black line shows the modulus of Kuramoto order parameter $r_2(t)$ calculated from the relation between Kuramoto order parameter and the WS variables with uniformly distributed constants of motion: (a) $N = 10$ and (b) $N = 40$. The inset of (b) shows the radial variables and Kuramoto order parameter with nonuniform constants of motion with $N = 10$. (c) Instantaneous phase velocities for $N = 10$ with uniform constants of motion. (d) Period of the modulus of the Kuramoto order parameter as a function of system size N. The red circles are numerically obtained periods and the black solid line is the curve $\frac{2\pi}{|\tilde{\Omega}|N}$. (e) Lyapunov exponents of the 9D macroscopic variables of the WS dynamics.

satisfies the three characteristics (see Fig. 4.7 (c)): (i) It is a periodic function with the period $T = \frac{2\pi}{|\tilde{\Omega}|}$, as shown in Eq. (3.15). (ii) All the oscillators have the same functional form since they are determined by the same three WS variables (ρ_0, Ω and $\tilde{\Omega}$). (iii) They are equally spaced within the time interval T due to the uniform constants of motion. These facts cause the periodic modulus of the Kuramoto order parameter with $r_2(t) = r_2\left(t - \frac{T}{N}\right) = r_2\left(t - \frac{2\pi}{|\tilde{\Omega}|N}\right)$ where the period $\frac{2\pi}{|\tilde{\Omega}|N}$ is decreasing as N increases. In Fig. 4.7 (d), the numerically measured periods of the modulus of the Kuramoto order parameter are depicted for different sizes N (red circles) and are compared with $\frac{2\pi}{|\tilde{\Omega}|N}$. The good agreement between the two curves supports

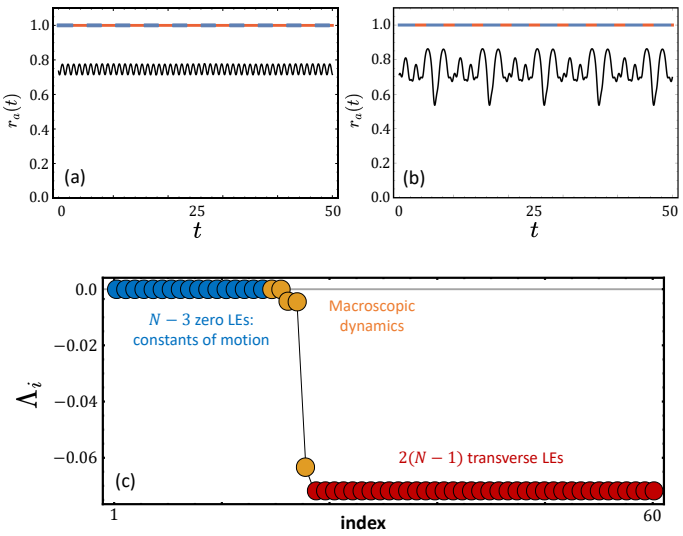

Fig. 4.8 Stationary SDS chimera states in $3N$-dimensional microscopic dynamics. (a,b) Time series of the moduli of the Kuramoto order parameters of the three populations with (a) PIC and (b) n-PIC for $N = 10$ and $A = 0.35$ after a transient time of 10^5 units. (c) Lyapunov exponents of the SDS chimeras initiated from a PIC for $N = 20$ and $A = 0.35$.

that the stationary symmetric-SDS chimera state for small N continuously approaches the OA dynamics as $N \to \infty$ in a similar as we discussed it for the Poisson chimeras in Sec. 3.1.2. Furthermore, as the Poisson chimeras in two-population do, the stationary symmetric-SDS chimeras in the 9D WS dynamics shows a strong dependence on the constants of motion (equivalently, an initial condition of the microscopic dynamics). The inset of Fig. 4.7 (b) shows the temporal evolution of the WS radial variables and the Kuramoto order parameter for slightly nonuniform COM. They exhibit non-Poisson chimera features as studied in Chap. 3. The stability of the symmetric-SDS chimeras is investigated, using the Lyapunov exponents, as shown in Fig. 4.7 (e). The stationary SDS chimeras in 9D WS dynamics are neutrally stable independently of N. Two zero Lyapunov exponents arise from the two continuous symmetries: the time shift and the phase shift invariance. Also, the breathing SDS chimeras possess an additional zero Lyapunov exponent due to the Hopf frequency.

Finally, the $3N$-dimensional microscopic dynamics are investigated, where we employ PICs and n-PICs as defined in Chap. 3. In Fig. 4.8 (a) and (b), the temporal evolutions of the moduli of Kuramoto order parameters calculated from Eq. (4.2) are shown for a PIC and an n-PIC, respectively, for $N = 10$. For a PIC, the order parameter dynamics shows the Poisson chimera characteristics as in Fig. 4.7 (b) since a PIC corresponds to uniform constants of motion. Thus, as the system size N increases, the amplitude and the period of the secondary oscillation of the modulus of the Kuramoto order parameter are decreasing and the

dynamics approaches the OA dynamics as $N \to \infty$. On the other hand, a non-Poisson chimera motion starting from an n-PIC is depicted in Fig. 4.8 (b), qualitatively similar to the inset of Fig. 4.7 (a), and corresponding to nonuniform constants of motion. The stability of the chimera states in the microscopic dynamics can be studied using Lyapuov exponents. Both PICs and n-PICs exhibit the same spectral characteristics, as depicted in Fig. 4.8 (c). Therein, stationary symmetric-SDS chimeras are found to be neutrally stable, characterized by $N-1$ zero Lyapunov exponents. This explains their strong dependence on the initial condition (or constants of motion), similar to the Poisson chimeras in two-population networks. More specifically, $N-3$ of the zero Lyapunov exponents (blue) arise from the $N-3$ constants of motion. The two other zero LEs (orange, zero) are expected to arise from the macroscopic dynamics. The two nearly identical and negative Lyapunov exponents (orange) describe the stability with respect to perturbations along the two synchronized populations, and the strongly negative one (orange) is related to the WS radial variable of the incoherent population. Also, there are $2(N-1)$-fold degenerate Lyapunov exponents (red), which are transveral LEs to the two synchronized populations. The corresponding covariant Lyapunov vectors (CLVs) are given by

$$\delta x_{\text{trans}} = (\delta a_1, ..., \delta a_N, 0, ..., 0, \delta b_1, ..., \delta b_N)^\top \quad \text{where} \quad \sum_{k=1}^{N} \delta a_k = \sum_{k=1}^{N} \delta b_k = 0, \tag{4.14}$$

which reveals that these Lyapunov exponents determine the stability transverse to the synchronized populations.

4.3.2 Symmetric-DSD Chimera States

As already discussed above, a stationary or breathing symmetric-DSD chimera state is stable in the symmetry-reduced manifold [88], but found to be unstable in the full-dimensional phase spac. Since we want to study unstable solutions, a very specific initial condition is required here as random initial conditions cannot approach the unstable solution. In the 6D OA dynamics, we use initial conditions characterized by $\rho_1(0) = \rho_3(0) = \rho_0 < 1$, $\rho_2(0) = 1$, $\Phi_1(0) = \Phi_3(0) = \varphi_0 \in \mathbb{T}$ and $\Phi_2(0) = 0$. Here, ρ_0 and φ_0 are the stable symmetric-DSD fixed point solution in the reduced manifold, i.e., a fixed point solution to Eq. (4.12). In Fig. 4.9 (a-b), a stationary symmetric-DSD chimera state from such an initial condition is shown. It is characterized by $\rho_1(t) = \rho_3(t) = \rho_0 < 1$, $\rho_2(t) = 1$, $\Phi_1(t) = \Phi_3(t) = \Omega t + \varphi_0$ and $\Phi_2(t) = \Omega t$. In a reference frame rotating with Ω, it is a fixed point solution. Hence, the linear stability results from the eigenvalues of the Jacobian matrix. In Fig. 4.9 (c), the eigenvalues are depicted in the complex plane. We have two eigenvalues with positive real

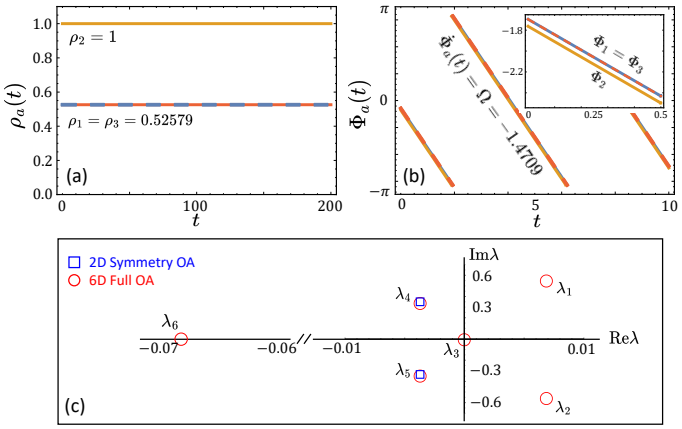

Fig. 4.9 Unstable stationary DSD chimera state in 6D OA dynamics. (a) Radial variables $\rho_2(t) = 1$ (orange line), $\rho_1(t) = \rho_3(t) = \rho_0 < 1$ (red and blue lines) as a function of time for $A = 0.55$. (b) Time series of the angular variables with the same color scheme as used in (a). In (a) and (b) the first 10^5 time units were discarded. (c) Eigenvalues of the Jacobian matrix evaluated at the DSD solution in the rotating reference frame.

parts: $\lambda_1 = \overline{\lambda}_2$ with corresponding eigenvectors $\delta x_1 = \overline{\delta x_2} = (\delta a, 0, -\delta a, \delta b, 0, -\delta b)^\top$ for $\delta a \in \mathbb{C}$ and $\delta b \in \mathbb{R}$. This demonstrates that the unstable directions are transverse to the symmetry-reduced manifold, i.e., the first and the third populations are opposite to each other.

On the level of the WS dynamics with the uniform COM, a specific initial condition is also required for the exploration of the unstable stationary symmetric-DSD chimera state. In the symmetry-reduced WS dynamics, Cf. Eq. (4.10), the symmetric-DSD chimeras are found to be stable. Then, we use $\rho_1(0) = \rho_3(0) = \rho(T), \rho_2(0) = 1, \Phi_1(0) = \Phi_3(0) = 0, \Phi_2(0) = \varphi(T)$, and $\Psi_1(0) = \Psi_3(0) = \Psi(T), \Psi_2(0) \in \mathbb{T}$ as an initial condition of Eq. (4.7) for $T \gg 1$. In Fig. 4.10 (a-c) the dynamics of a symmetric-DSD chimera state is shown, starting from the above initial condition. When introducing a small perturbation to the initial conditions in this system, the stationary symmetric-DSD chimera state emerges only temporarily, transitioning into a breathing symmetric-SDS chimera state through an antiphase oscillation (Fig. 4.10 (d)). The Lyapunov exponents of the stationary DSD chimeras in the 9D WS dynamics are shown in Fig. 4.11 (a). There are two positive Lyapunov exponents, namely Λ_1 and Λ_2. However, the presence of these positive exponents does not imply that the state shows a chaotic motion since the symmetric-DSD chimera state does not exhibit any chaotic behavior. Instead, it should be regarded as an unstable solution. Furthermore, the corresponding covariant Lyapunov vectors (CLVs) take the form $\delta x_{1,2} = (\delta a, 0, -\delta a, \delta b, 0, -\delta b, \delta c, 0, -\delta c)$. This

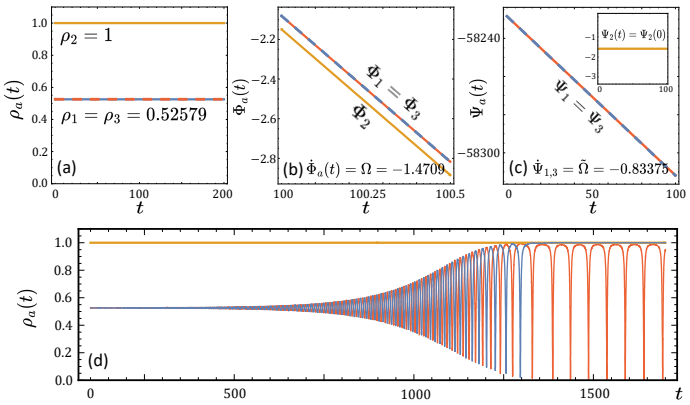

Fig. 4.10 Unstable stationary DSD chimera states in 9D WS dynamics. (a-c) Time evolution of the 9D Watanabe-Strogatz macroscopic variables after a transient time of 10^5 units with the same color scheme in Fig. 4.9. (d) Time evolution of the radial variables with a small perturbation on the specific initial condition. $A = 0.55$ and $N = 40$.

observation further confirms that the unstable directions of the stationary symmetric-DSD chimera state are transverse to the symmetry-reduced manifold.

In the microscopic dynamics, even when initialized with a precise PIC, we observe an unusual transient behavior. Initially, the system exhibits an oscillatory approach towards the stationary symmetric-DSD state and remains in its vicinity for several hundred time units. Subsequently, it transitions into a transient antiphase motion before ultimately settling into a breathing symmetric-SDS chimera state (Fig. 4.11 (c-d)). During our observations of the microscopic dynamics, we were unable to detect a symmetric-DSD chimera that persisted for a sufficiently long time to allow for the numerical experiments of Lyapunov exponents. Hence, we need to study the 9D WS variables $\rho_a(t)$, $\Psi_a(t)$ and $\Phi_a(t)$ and uniform constants of motion together with the inverse WS transformation from Eq. (4.4) for the exploration of the microscopic dynamics:

$$\phi_j^{(a)}(t) = \Phi_a(t) + 2\tan^{-1}\left(\frac{1-\rho_a(t)}{1+\rho_a(t)}\tan\left(\frac{\psi_j^{(a)} - \Psi_a(t)}{2}\right)\right) \tag{4.15}$$

for $j = 1,...,N$ and $a = 1,2,3$. Initially, we perform a numerical integration of the 9D WS equations using the given initial condition for the stationary symmetric-DSD chimeras. Subsequently, we employ the inverse WS transformation with the 9D WS macroscopic variables to derive the temporal evolution of the microscopic individual phases $\phi_j^{(a)}(t)$ for $a = 1,2,3$ and for $j = 1,...,N$. Then, the tangent space dynamics is governed by the Jacobian

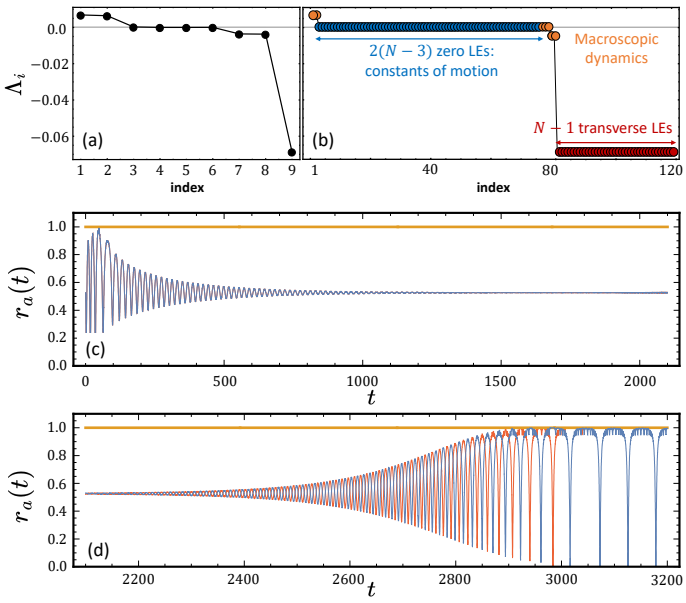

Fig. 4.11 (a) Lyapunov exponents of the 9D WS dynamics for $N = 40$ corresponding to Fig. 4.10 (a-c). (b) Lyapunov exponents of the $3N$-dimensional microscopic dynamics for $N = 40$. (c-d) Time evolution of the moduli of the Kuramoto order parameters for the $3N$-dimensional microscopic dynamics with $N = 40$ starting from a PIC. $A = 0.55$.

matrix defined by

$$(\mathbf{J})_{ij}(t) = \begin{pmatrix} \frac{\partial \dot{\phi}_i^{(1)}}{\partial \phi_j^{(1)}} & \frac{\partial \dot{\phi}_i^{(1)}}{\partial \phi_j^{(2)}} & \frac{\partial \dot{\phi}_i^{(1)}}{\partial \phi_j^{(3)}} \\ \frac{\partial \dot{\phi}_i^{(2)}}{\partial \phi_j^{(1)}} & \frac{\partial \dot{\phi}_i^{(2)}}{\partial \phi_j^{(2)}} & \frac{\partial \dot{\phi}_i^{(2)}}{\partial \phi_j^{(3)}} \\ \frac{\partial \dot{\phi}_i^{(3)}}{\partial \phi_j^{(1)}} & \frac{\partial \dot{\phi}_i^{(3)}}{\partial \phi_j^{(2)}} & \frac{\partial \dot{\phi}_i^{(3)}}{\partial \phi_j^{(3)}} \end{pmatrix} \tag{4.16}$$

evaluated at $\phi_j^{(a)}(t)$ for $i, j = 1, \ldots, 3N$ and for $a = 1, 2, 3$. Then, the Lyapunov exponents are obtained in the long time limit according to

$$\Lambda_i = \lim_{t \to \infty} \frac{1}{t} \log \frac{||\mathbf{M}(t, t_0)\delta\mathbf{u}_i(t_0)||}{||\delta\mathbf{u}_i(t_0)||} \tag{4.17}$$

where $\delta\mathbf{u}_i(t_0)$ belongs to each Oseledets' splitting for $i = 1, \ldots, 3N$, as discussed in Sec. 2.6.

In Fig. 4.11 (b), the Lyapunov exponents, obtained through the aforementioned numerical scheme, are depicted for the $3N$-dimensional microscopic dynamics. Among these exponents,

there are two positive values, and their corresponding CLVs take the following form:

$$\delta x_{1,2} = (\delta a_1, ..., \delta a_N, 0, ..., 0, \delta b_1, ..., \delta b_N)^\top \quad \text{where} \quad \delta b_i = -\delta a_i \tag{4.18}$$

for $i = 1, ..., N$, which again ensures that the unstable directions are transverse to the symmetry-reduced manifold. Furthermore, there exist $2(N-3)$ Lyapunov exponents with a value of zero (blue), which arise from the constants of motion associated with the two incoherent populations. Lastly, we have the CLVs that correspond to the $(N-1)$-fold degenerate transverse Lyapunov exponents (red) given by

$$\delta x_{\text{trans}} = (0, ..., 0, \delta a_1, ..., \delta a_N, 0, ..., 0)^\top \quad \text{where} \quad \sum_{k=1}^{N} \delta a_k = 0. \tag{4.19}$$

We anticipate that the remaining Lyapunov exponents, including three that have a value of zero (orange), originate from the WS macroscopic variables and perturbations along the synchronized population.

4.4 Summary

Our investigation has revealed that within three-population networks of identical Kuramoto-Sakaguchi phase oscillators, a diversity of qualitatively distinct chimera states not only exist but also coexist on a significant portion of the initial conditions in phase space. Previously, symmetric chimera states, specifically SDS and DSD-chimeras where two populations behave identically, were observed within the symmetry-reduced manifold. In this chapter, we have extended the dynamics beyond the confinements of symmetry and delved into a comprehensive analysis of the full-dimensional dynamics at both microscopic and macroscopic levels, employing the Watanabe-Strogatz and the Ott-Antonsen ansatz. When considering the full phase space, it becomes apparent that symmetric DSD chimeras, while unstable to transversal perturbations—perturbations wherein the two D-populations move in opposing directions—give rise to asymmetric DSD′ states. These asymmetric DSD′ chimeras exhibit stability across a wide parameter range. Notably, they are chaotic antiphase chimera attractors within finite-sized systems and in the thermodynamic limit outside the Ott-Antonsen manifold. Within the Ott-Antonsen manifold, the antiphase chaotic chimera assumes periodic behavior. Consequently, these two varieties of antiphase DSD′ chimeras coexist within the thermodynamic limit. Furthermore, these two chimera types coexist with a symmetric stationary SDS chimera state.

Chapter 5

Coexistence Dynamics III: Heteroclinic Switching between Saddle Chimeras

In the previous chapters, we show that the chimera states in two- and three-population networks exhibit a variety of dynamics distinguished by the motion of order parameters for the incoherent populations. In particular, we investigated stationary, breathing, quasiperiodic [72, 74, 101, 102] and also chaotic chimera states [56, 75, 80, 82–84]. In literature, more complicated forms of chimera states were observed in a variety of oscillator systems. Among them, we here concentrate on so-called alternating chimera states or switching chimeras. This state is characterized by repeatedly exchanging the coherent and the incoherent domains as time goes on. In previous works, alternating chimeras were known to occur either due to metastable states or heteroclinic cycles. For the metastable states, the alternating behavior is triggered by large enough fluctuations [185, 86, 77, 186]. In particular, an alternating chimera triggered by arbitrarily small noise with power-law scaling is said to exhibit critical switching [187]. For the latter, the switching chimera dynamics occurs between unstable states by forming a heteroclinic cycle of the saddle chimeras along which the trajectory evloves [91, 92, 94, 188–192]. For the previous works, e.g., in Refs. [91, 92, 94], the authors observed the heteroclinic switching dynamics between weak chimera states, arising from a system with higher-order interactions of small number of oscillators.

In this chapter, a heteroclinic switching between saddle chimera states in large systems of sinusoidally coupled oscillators will be discussed. More precisely, we consider a system of identical Kuramoto-Sakaguchi oscillators in a ring of six oscillator populations (see Fig. (5.1) and Eq. (5.4)). Each oscillator is globally coupled to all oscillators in the same population and

The contents of this chapter were in part published previously in S. Lee and K. Krischer, Chaos **33**, 063120 (2023) [57]. Note that all figures and their captions are reproduced from those in it.

it is connected to all the oscillators in the two nearest populations along the ring. With this topological setup, we study the dynamics both in the thermodynamic limit and in finite-sized ensembles using the Ott-Antonsen ansatz and the Watanabe-Strogatz reduction, respectively. Hence, we consider a system of sinusoidally coupled oscillators.

5.1 Governing Equations and Saddle Chimeras

A Kuramoto-Sakaguchi oscillator $\phi_j^{(a)}(t) \in \mathbb{T}$ in a ring of six populations is governed by

$$\begin{aligned}\partial_t \phi_j^{(a)} &= \omega_j^{(a)} + \mathrm{Im}\left[H_a(t) e^{-i\phi_j^{(a)}}\right] \\ &= \omega_j^{(a)} + \sum_{b=1}^{6} G_{ab} \frac{1}{N} \sum_{k=1}^{N} \sin(\phi_k^{(b)} - \phi_j^{(a)} - \alpha)\end{aligned} \tag{5.1}$$

with $j = 1,...,N$ (oscillator index) and $a = 1,...,6$ (population index). Again, an effective forcing function $H_a(t)$ globally affects the oscillators in population a and is defined by

$$H_a(t) := e^{-i\alpha} \sum_{b=1}^{6} G_{ab} \Gamma_b(t) \tag{5.2}$$

where $\Gamma_a(t) \in \mathbb{C}$ is the Kuramoto order parameter of each population defined as

$$\Gamma_a(t) := \frac{1}{N} \sum_{j=1}^{N} e^{i\phi_j^{(a)}(t)} \tag{5.3}$$

for $a = 1,...,6$. Here, the coupling matrix (G_{ab}) is given by[1]

$$G_{ab} = \begin{cases} \mu = 1, & \text{for } a = b \\ \\ \nu = 1 - A, & \text{for } a = b \pm 1 \mod 6 \end{cases} \tag{5.4}$$

with $a, b = 1,...,6$. A scheme of the six oscillator populations defined by the above coupling matrix is displayed in Fig. 5.1 (a). Here, the intra-population coupling strength is fixed as $\mu = 1$ and the inter-population coupling between the nearest neighboring populations is given as $\nu = 1 - A$ where $A \in [0,1]$. The phase-lag parameter α is written as $\alpha = \frac{\pi}{2} - \beta$ with a fixed value of $\beta = 0.008$ throughout this chapter unless otherwise noted. Note that where we consider heterogeneous ensembles, the heterogeneous natural frequencies $\omega_j^{(a)}$ of

[1] From here on, population indices are taken modulo 6.

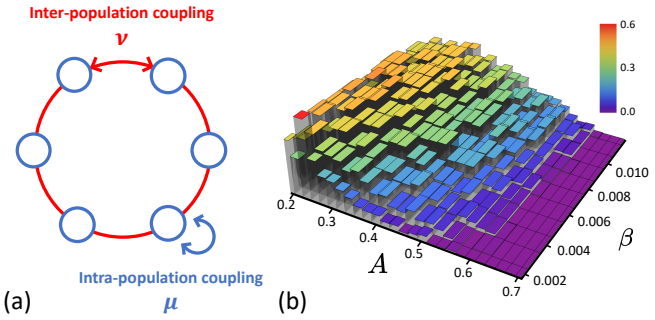

Fig. 5.1 (a) Schematic of the considered network topology. The intra-population coupling is all-to-all with strength $\mu = 1$ and the inter-population coupling is also all-to-all but only between the nearest-neighbor populations and with strength $\nu = 1 - A$. (b) A normalized histogram of occurrence of chimera states from 300 random initial conditions at $t = 5 \times 10^4$.

the oscillators are generated from a normalized distribution $g(\omega)$, for which we will consider a Cauchy-Lorentz distribution with half-width $\gamma \in \mathbb{R}$ and zero mean: $g(\omega) = \frac{\gamma}{\pi} \frac{1}{\omega^2+\gamma^2}$.

To investigate the macroscopic dynamics of the system, we first visit the thermodynamic limit, where we exploit the OA ansatz. Even though we were already well-trained in the derivation of the OA equations, we discuss the OA ansatz again since we here want to deal with not only the identical oscillator system but also the heterogeneous oscillators for later reference.

As we discussed in Sec. 2.4, the state function in the thermodynamic limit is a phase density function $f_a(\phi^{(a)}, \omega^{(a)}, t)$ governed by the continuity equation

$$\begin{aligned} \frac{\partial}{\partial t} f_a(\phi^{(a)}, \omega^{(a)}, t) &= -\frac{\partial}{\partial \phi^{(a)}} \left(f_a(\phi^{(a)}, \omega^{(a)}, t) v_a(\phi^{(a)}, \omega^{(a)}, t) \right) \\ v_a(\phi^{(a)}, \omega^{(a)}, t) &:= \omega^{(a)} + \mathrm{Im}\left[H_a(t) e^{-i\phi^{(a)}} e^{-i\alpha} \right] \end{aligned} \tag{5.5}$$

for $a = 1, \ldots, 6$, and the Kuramoto order parameter of each population reads

$$\Gamma_a(t) = \int_{\mathbb{R}} \int_{\mathbb{T}} f_a(\phi^{(a)}, \omega^{(a)}, t) e^{i\phi^{(a)}} d\phi^{(a)} d\omega^{(a)}. \tag{5.6}$$

Notice that the phase density function is 2π-periodic in the phase $\phi^{(a)}$ for each population. Therefore, one can rewrite it as Fourier series expansion. Then, in the Ott-Antonsen invariant manifold, all the Fourier harmonics can be expressed using only the first harmonic that describes the Kuramoto order parameter and is denoted as $Z_a(\omega^{(a)}, t) \in \mathbb{C}$. In the OA

manifold, all the higher Fourier coefficients are a power of the first coefficient:

$$f_a = \frac{g(\omega^{(a)})}{2\pi}\left(1+\sum_{n=1}^{\infty}\left[Z_a(\omega^{(a)},t)^n e^{-in\phi^{(a)}}+c.c\right]\right). \tag{5.7}$$

Substituting Eq. (5.7) into Eq. (5.5), we obtain the OA dynamics for the heterogeneous oscillators. Here, $z_a(t) := Z_a(i\gamma,t) = \Gamma_a(t)$ for $a = 1,...,6$ and they are governed by

$$\partial_t z_a(t) = -\gamma z_a + \frac{1}{2}H_a(t)e^{-i\alpha} - \frac{1}{2}z_a^2\,\overline{H_a(t)}e^{i\alpha}. \tag{5.8}$$

which can be rewritten in terms of the OA radial variables as

$$\begin{aligned}\partial_t\rho_a &= -\gamma\rho_a + \frac{1-\rho_a^2}{2}\sum_{b=1}^{6}G_{ab}\rho_b\cos(\varphi_b-\varphi_a-\alpha)\\ &= -\gamma\rho_a + \frac{1-\rho_a^2}{2}\Big(\nu\rho_{a+1}\cos(\varphi_{a+1}-\varphi_a-\alpha)\\ &\quad +\nu\rho_{a-1}\cos(\varphi_{a-1}-\varphi_a-\alpha)+\mu\rho_a\cos\alpha\Big).\end{aligned} \tag{5.9}$$

and the OA angular variables as

$$\begin{aligned}\partial_t\varphi_a &= \frac{1+\rho_a^2}{2\rho_a}\sum_{b=1}^{6}K_{ab}\rho_b\sin(\varphi_b-\varphi_a-\alpha)\\ &= \frac{1+\rho_a^2}{2\rho_a}\Big(\nu\rho_{a+1}\sin(\varphi_{a+1}-\varphi_a-\alpha)+\nu\rho_{a-1}\sin(\varphi_{a-1}-\varphi_a-\alpha)-\mu\rho_a\sin\alpha\Big)\end{aligned} \tag{5.10}$$

where $z_a(t) = \rho_a(t)e^{i\varphi_a(t)}$ for $a = 1,...,6$. For the moment, up to Sec. 5.3, we only consider a system of identical oscillator populations. Hence, firstly we set $\gamma = 0$. Then, as in Chap. 4, we denote a synchronized population as S, where $\rho_a = 1$ and all oscillators in population a share a common phase φ_a. Conversely, an incoherent population is denoted as D, with the mean phase $\varphi_a = \arg\Gamma_a$ for oscillators in population a when $0 < \rho_a < 1$.

From Eqs. (5.9-5.10), we can obtain a solution denoted as $S^6 = S\cdots S$ (6 times) which is characterized in terms of the OA variables: $\rho_a(t) = 1$ and $\varphi_a(t) = \Omega t + \frac{2\pi q}{6}a$ with the common frequency $\Omega = -(\mu + 2\nu\cos\left(\frac{\pi q}{3}\right))\sin\alpha$ for $a = 1,...,6$ and $q \in \{0,\pm1,\pm2\}$. This means that the distribution of mean phases of the populations follows either a twisted state on a ring [171] ($q \neq 0$) or they are all phase synchronized ($q = 0$). All S^6 states are fixed point solutions in a reference frame rotating with Ω, where we can study easily their linear

stability. The linear stability analysis verifies that the S^6 states with $q = 0, \pm 1$ are stable fixed points whereas those with $q = \pm 2$ are unstable.

Apart from S^6 states, there are fixed point solutions, in an appropriate rotating reference frame, corresponding to chimera states, i.e., the coexistence of synchrony and asynchrony. Examples are $(SD)^3 = SDSDSD$, $(DS^2)^2 = DS^2DS^2$ or $DS^5 = DSSSSS$ and so on. Note that the equations of motion (5.9-5.10) are dictated by the network structure. For example, they are invariant under the group $\mathbb{Z}_6 := \mathbb{Z}/6\mathbb{Z}$ such that cyclic permutations of the populations of those fixed points are also fixed points with the same properties [91]. Furthermore, the linear stability analysis for each chimera state above reveals that all of them have at least one eigenvalue with a positive real part, in most intervals of A. For example, the DS^5 chimera state has one positive real eigenvalue for $A = 0.3$. In conclusion, no linearly stable chimera fixed point solution exists for $A > 0.2$; all the chimera states are saddles.

Yet, in numerical integrations of Eqs. (5.9-5.10), chimera states are obtained. The histogram of the probability with which a DS^5 chimera or one of its symmetric counterparts was observed, is depicted in Fig. 5.1 (b). Trajectories of the OA equation initiated from 300 random initial conditions for $A \in [0.2, 0.7]$ and $\beta \in [0.002, 0.01]$ may approach one of the unstable chimera states in the long-term limit in a large region of the $A - \beta$ parameter plane. The results are intriguing: a considerable number of trajectories from random initial conditions settle down to the DS^5 chimera state or one of its symmetric counterparts, even though they are saddle chimeras. None other than a DS^5-type chimera was obtained in the simulations. Below, we will discuss the structure of the saddle chimeras that allows for this peculiar behavior in detail.

5.2 Heteroclinic Switching between Saddle Chimeras

5.2.1 Stationary Saddle Chimeras

As discussed above, the observation of the DS^5 chimera state or one of its $\mathbb{Z}_6$-symmetric counterparts, is intriguing since they are unstable solutions and we started our numerical simulations with random initial conditions in phase space. In these numerical experiments, for example, the six saddle chimeras can be obtained equally often from random initial conditions for $A \in (0.071, 0.45)$. To elucidate such a phenomenon, we here focus on DS^5 at $A = 0.3$ for the moment. The DS^5 chimera state for $A = 0.3$ is a stationary chimera state, i.e., a fixed point solution in an appropriate rotating reference frame. Here, the DS^5 chimera is characterized by the OA variables that satisfy $\rho_1(t) = \rho_0 < 1$, $\rho_a(t) = 1$ for $a = 2, \ldots, 6$. As mentioned above, all phases are locked at the common frequency Ω. Moreover, they follow

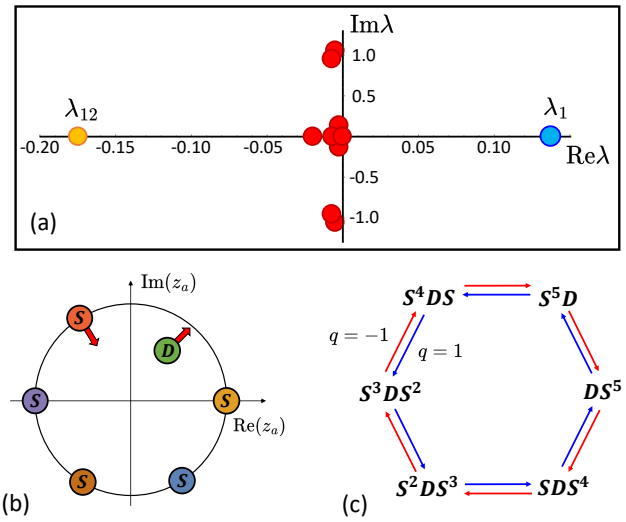

Fig. 5.2 (a) Eigenvalues of the Jacobian matrix evaluated at DS^5 in the complex plane for $A = 0.3$. (b) Schematic of the perturbation along the unstable eigenspace that raises the incoherent population up to sync and lowers the radial variable of one of the two neighboring synchronized populations. (c) Schematic of switching between saddle chimera states along the heteroclinic cycle $\mathbf{C}(\pm 1)$ defined in Eq. (5.12).

nearly a twisted state[2], and we can define a winding number of the phase variables along the six populations on a ring as

$$q := \frac{1}{2\pi} \sum_{a=1}^{6} \Delta_{a+1,a} \in \mathbb{Z} \tag{5.11}$$

where $\Delta_{a,b} := \varphi_a - \varphi_b$ with $\varphi_7 \equiv \varphi_1$. For the DS^5 chimeras, numerical observations show the winding number could be either $q = 1$ or $q = -1$, depending on a given initial condition. For the moment, we assume that $q = 1$ unless otherwise stated. As already mentioned, instability of the chimera state can be confirmed by linear stability analysis. In Fig. 5.2 (a), eigenvalues of the Jacobian matrix evaluated at DS^5 are depicted in the complex plane, which numerically confirms that the DS^5 chimera state is an unstable saddle chimera with a one-dimensional unstable manifold $W^u(\mathrm{DS}^5)$. We have one positive real eigenvalue $\lambda_1 > 0$ while all the other eigenvalues have negative real parts, except for one zero eigenvalue arising from the phase shift invariance. Since the DS^5 chimera state and its five symmetric counterparts are unstable fixed points, $\{\mathrm{DS}^5\} \subset [0,1]^6 \times \mathbb{T}^6$ is an invariant saddle point under

[2]This means the distribution of the phases $\varphi_a(t)$ along one cycle of the ring exhibits a twisted state, however, with small deviations, which arise from $\rho_1 \neq \rho_a = 1$ for $a = 2, \ldots, 6$. Hence, we can say it follows a nontrivial twisted state discussed in Append. A or Ref. [121]; cf. the S^6 state above for which $\rho_a = 1$ for $a = 1, \ldots, 6$.

the flow of Eqs. (5.9-5.10). Notably, the eigenvector corresponding to λ_1 has a form of[3] $\mathbf{v}_1 = (A_+, 0, 0, 0, 0, A_-)^\top \in \mathbb{R}^6$, together with $A_+ A_- < 0$. This is a key to the understanding of the observation of the saddle chimeras from random initial conditions. Looking at the form of the unstable eigendirection, we notice a small perturbation along the unstable manifold of DS^5 raises ($A_+ > 0$) the radial variable of the incoherent population $\rho_1 < 1$ while it lowers ($A_- < 0$) the radial variable of the nearest synchronized population $\rho_6 = 1$. This is schematically depicted in Fig. 5.2 (b). For $q = -1$, the radial parts of the eigenvector associated with the positive real eigenvalue has the form of $\mathbf{v}_1 = (A_+, A_-, 0, 0, 0, 0)^\top$, which also ensures that the unstable perturbation can result in the lowering in the radial variable of the nearest synchronized population on the opposite side of the D-population. This scenario also is found all the five other symmetric counterparts of DS^5.

In numerical simulations, one can easily find that imposing a small perturbation along the unstable eigendirection leads a DS^5 to a $\mathrm{S}^5\mathrm{D}$ state for $q = 1$ and to SDS^4 for $q = -1$. We can conjecture from this that the one-dimensional unstable manifold of DS^5 is connected to the stable manifold of $\mathrm{S}^5\mathrm{D}$ for $q = 1$, and therefore $W^u(\mathrm{DS}^5) \cap W^s(\mathrm{S}^5\mathrm{D}) \neq \emptyset$. Furthermore, both manifolds intersect the invariant subspace $\mathrm{Z_1S^4Z_6}$ where the populations two to five are synchronized and $\mathrm{Z}_{1,6}$ denotes the state of the first and the sixth populations, respectively. In this reduced subspace, DS^5 appears as a saddle and $\mathrm{S}^5\mathrm{D}$ as a sink. The above numerical studies strongly suggest our conjecture that *a heteroclinic cycle* of six saddle chimera states can be constructed as an invariant subspace of phase space, with, for example, a heteroclinic connection between DS^5 and $\mathrm{S}^5\mathrm{D}$. Here, the heteroclinic cycle of the winding number q is denoted by

$$\mathbf{C}(q) := \begin{cases} [\mathrm{DS}^5 \to \mathrm{S}^5\mathrm{D} \to \cdots \to \mathrm{SDS}^4 \to \mathrm{DS}^5], & \text{for } q = 1 \\ \\ [\mathrm{DS}^5 \to \mathrm{SDS}^4 \to \cdots \to \mathrm{S}^5\mathrm{D} \to \mathrm{DS}^5], & \text{for } q = -1 \end{cases} \tag{5.12}$$

where the winding number q takes over the role of a direction indicator of the heteroclinic switching. In Fig. 5.2 (c), the heteroclinic cycles $\mathbf{C}(\pm 1)$ are schematically illustrated. As it depicts, the heteroclinic switching between saddle chimera states strongly depends on the topology of the ring, i.e., the $\mathbb{Z}_6$ symmetry of the full system. For other chimera fixed points, such as $(\mathrm{SD})^3$ or $(\mathrm{DS}^2)^2$, we observe neither switching nor any long-term dynamics in numerical integrations of Eqs. (5.9-5.10) from random ICs. We guess it is because they

[3] Note that in fact the eigenvector has a form of $\mathbf{v}_1 = (A_+, 0, 0, 0, 0, A_-, \boldsymbol{\delta\varphi})^\top \in \mathbb{R}^6 \times \mathbb{R}^6$ where $A_+, A_- \in \mathbb{R}$ and $\boldsymbol{\delta\varphi} \in \mathbb{R}^6$ denotes a perturbation on phase variables. However, $\boldsymbol{\delta\varphi} \in \mathbb{R}^6$ does not prominently affect the switching dynamics between chimeras, and thus is not that relevant to the main issue in this context. From now on, we consider only the perturbations on the radial variables: $\mathbf{v}_1 = (A_+, 0, 0, 0, 0, A_-)^\top \in \mathbb{R}^6$.

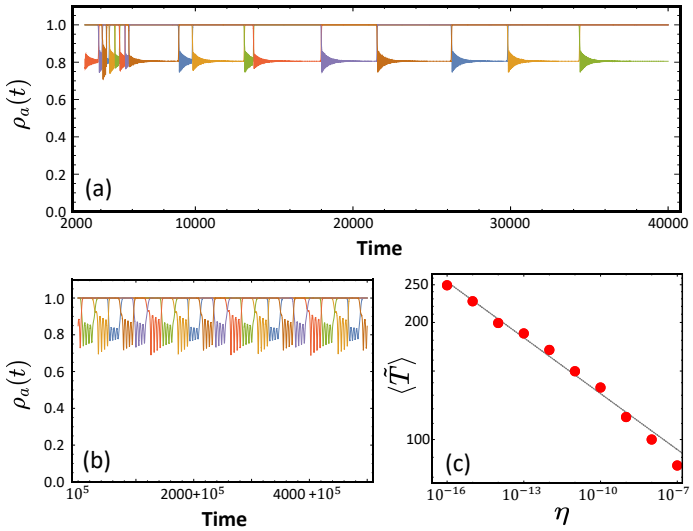

Fig. 5.3 (a) Time evolution of the radial variables of the OA dynamics from a random initial condition. (b) Time evolution of the radial variables of the OA dynamics with an imposed noise: $\eta = 10^{-15}$. (c) Log-log plot of the averaging switching period vs. the strength of the noise. The dashed line indicates $\langle \tilde{T} \rangle \sim \eta^{-0.048}$. Remaining parameters: $A = 0.3$ and $\beta = 0.008$.

have a higher-dimensional unstable manifold, which could prevent the saddle chimeras from forming an overall attracting heteroclinic cycle.

In Fig. 5.3 (a), an observable dynamics of Eqs. (5.9-5.10) is depicted. The chimera trajectory shows the switching between the six saddle chimera states. The lowering S-population and the raising D-population always occur between the nearest neighboring populations according to Eq. (5.12). Note that the average time interval between the switching increases, so that the trajectory eventually remains in one of the saddle chimera states for $t \gg 1$. During the switching period, the full symmetry of the system Eqs. (5.9-5.10) is recovered in terms of the long-term dynamics while each saddle chimera state characterizes a broken symmetry [187]. Finally, we can conclude that the formation of the heteroclinic cycle explains why the chimera states can be observed in a wide range of parameters, even though they are unstable saddle solutions.

As stated above, the trajectory along the heteroclinic switching between saddle chimera states eventually settles down to one of the six saddle chimera fixed points. In order for the switching dynamics between saddle chimera states to be persistent, we here impose a small

noise to the radial dynamics of each population [91, 187]:

$$\frac{d\rho_a}{dt} = \frac{1-\rho_a^2}{2} \sum_{b=1}^{6} G_{ab}\rho_b \cos(\varphi_b - \varphi_a - \alpha) - \eta |W_a(t)| \tag{5.13}$$

for $a = 1,...,6$. Here, $W_a(t)$ is Gaussian noise with unit standard deviation and $0 < \eta \ll 1$ is its strength. Note that we only consider a negative noise by taking the absolute value of $W_a(t)$ and then subtracting it from the governing equation. By doing so, we ensure $\rho_a(t) \leq 1$ for all times and for a to be physically meaningful: The order parameter should be less than or equal to unity in order to measure the degree of coherence among the oscillators in each population. In Fig. 5.3 (b), a persistent switching dynamics near the heteroclinic cycle of the saddle chimera states is shown for $\eta = 10^{-15}$. Furthermore, the average switching period $\langle \tilde{T} \rangle$ decreases with increasing noise strength η according to a power-law scaling, as illustrated in Fig. 5.3 (c). Hence, the switching dynamics is expected to persist near $\mathbf{C}(q)$ even at much smaller noise intensity than we could achieve due to the accuracy limit of the numerics. However, further increasing η beyond the highest value depicted in Fig. 5.3 (c) destroys the switching dynamics.

5.2.2 Breathing Saddle Chimeras

In Fig. 5.4 (a), a bifurcation diagram of the stationary DS^5 chimera state is depicted. For a comparatively small value of A, the stable (red, solid) and unstable (red, dashed) stationary DS^5 chimeras are born/destroyed in a saddle-node bifurcation (LP) denoted as $A_{LP} = 0.0678$ (see upper inset). The unstable DS^5 branch from the LP separates the basins of attraction of the stable DS^5 chimera state and the stable S^6 ($q = 0$) solution. Such an unstable chimera solution along the unstable branch from the LP is not observable at all in simulations and is not considered further in this work. On the contrary, one of the two branches of DS^5 states that emerge from the LP is actually stable within a narrow range of the parameter A. The stable DS^5 chimera, together with its symmetric counterparts, undergoes a destabilization in a transcritical bifurcation (BP) at $A_{BP} = 0.07008$. This bifurcation occurs through an interaction with a DS^4D' state (black), which consists of two incoherent populations having distinct values of their radial variables, $\rho_1 \neq \rho_6$. At A_{BP}, the stability of the DS^5 state is exchanged with that of the DS^4D' state. The unstable direction of the former is of the form $\mathbf{v} = (A_+, 0, 0, 0, 0, A_-)^\top$ as discussed above. However, in close vicinity to the bifurcation point, when a small perturbation is imposed on the unstable DS^5 chimera along this unstable eigendirection, the trajectory does not immediately transition to the next symmetric counterpart of DS^5 along $\mathbf{C}(q)$, but instead leads to the DS^4D' state. The

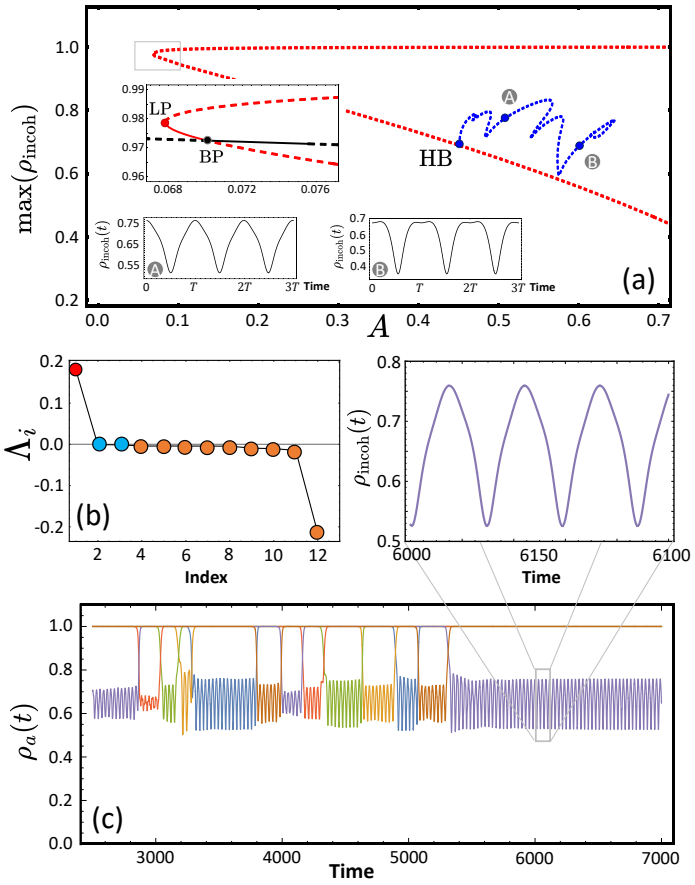

Fig. 5.4 (a) Bifurcation diagram of the stationary chimera state DS^5. Upper inset: Magnification close to LP. Lower insets: The time evolution of the radial variable of the incoherent population at points (A) and (B) of the bifurcation diagram corresponding to $A = 0.5$ and $A = 0.6$, respectively. Here, T is the period of the breathing chimera state. HB: Hopf bifurcation, LP: saddle-node bifurcation, and BP: transcritical bifurcation. Red: unstable stationary chimera state, Blue: unstable breathing chimera states. Note that the breathing chimera states undergo several saddle-node bifurcations. (b) Lyapunov exponents of the breathing chimera dynamics at $A = 0.5$. Red, blue, orange: positive, zero and negative LEs, respectively. (c) Switching dynamics of the radial variables of the OA dynamics as a function of time from a random initial condition at $A = 0.5$. Inset: Magnification of the times series around $t = 6150$.

emergence of the heteroclinic cycle is only observed after a series of subsequent bifurcations, wherein the DS^{4}D$'$ state interacts with various other solution branches. From $A = 0.15$ onwards, we consistently observe the dynamics of heteroclinic switching during numerical integration, as previously described (cf. Fig. 5.3 (a)).

The stationary saddle DS^5 chimeta state undergoes a Hopf bifurcation (HB) at $A_{\mathrm{HB}} = 0.451$. After the A_{HB}, the stationary saddle chimeras have more than one unstable direction,

which hinders them from forming an observable heteroclinic cycle. Therefore, no heteroclinic switching between stationary DS^5 chimeras is seen for $A > A_{\mathrm{HB}}$. For $A > A_{\mathrm{HB}}$, an unstable limit-cycle solution comes into being, which is characterized by $\rho_1(t) = \rho_1(t+T) < 1$ and $\rho_a = 1$ for $a = 2,\ldots,6$ (blue) where T denotes its period. The insets (A) and (B) depict example trajectories of the limit-cycle solutions. In both cases, the OA angular variables exhibit similar characteristics of a nontrivial twisted state with a winding number of $q = \pm 1$. This periodic breathing chimera solution also exhibits instability, determined by the presence of one positive real Floquet multiplier greater than unity. Similar to the stationary saddle SD^5 states, we observe the emergence of unstable breathing chimera solutions in the long-term dynamics, even when starting from random initial conditions. To understand this observation, we numerically determine the Lyapunov exponents and the covariant Lyapunov vectors along the observed breathing chimera trajectory, as discussed in Sec. 2.6. In Fig. 5.4 (b), the Lyapunov exponents of the observed breathing chimera trajectory are shown. The two zero LEs correspond to time and phase shift invariance. The positive Lyapunov exponent $\Lambda_1 > 0$ does not indicate a chaotic motion since the breathing chimera state is a periodic solution. Rather it indicates a local instability of the reference trajectory in phase space. Furthermore, the CLV corresponding to the positive LE Λ_1 has a form of $\mathbf{v}_1 = (A_+, A_-, 0, 0, 0, 0)^\top$. This reminds us of the unstable eigenvector of the stationary saddle chimera above, which also suggests that all the symmetric variants of the unstable breathing chimera can form a heteroclinic cycle of the type $\mathbf{C}(q)$. In Fig. 5.4 (c), we show a representative trajectory that was starting from a random IC, and exhibits switching dynamics near a heteroclinic cycle of the saddle limit-cycle chimeras along $\mathbf{C}(-1)$ for $A = 0.5$[4], thus supporting our conjecture.

5.2.3 Finite-sized Ensembles

Next, we shift our focus to populations of finite-N oscillators in a ring topology, as illustrated in Figure 5.1 (a). The macroscopic dynamics of each population can be explored by employing the Watanabe-Strogatz transformation, as we have so far done in the previous chapters. We already discussed that the WS dynamics with uniform constants of motion can be regarded as the finite-size counterpart of the Ott-Antonsen dynamics, i.e., the Poisson submanifold. Furthermore, we found that the qualitative behavior of both systems is highly similar to each other when $N \geq 10$, except for minor finite-size effects. Consequently, the heteroclinic switching between the stationary/breathing saddle chimeras observed in the OA manifold is also expected to appear within the corresponding finite-sized systems based on

[4] Compare the magnification of the limit-cycle in Fig. 5.4 (c) and the inset (A) in Fig. 5.4 (a).

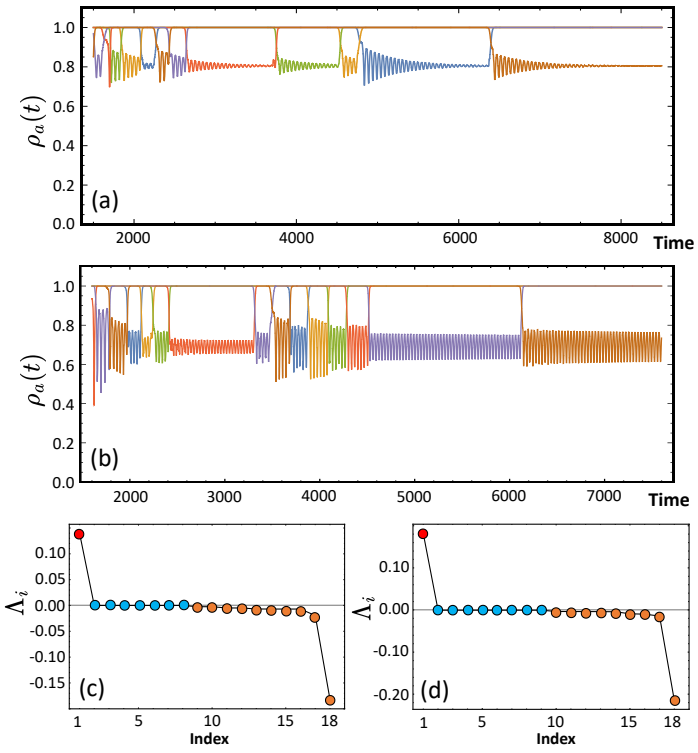

Fig. 5.5 Time evolution of the radial variables of the WS dynamics from a random initial condition: (a) $A = 0.3$ (stationary chimeras). (b) $A = 0.5$ (breathing chimeras). (c,d) Lyapunov exponents corresponding to the stationary and breathing chimeras for $A = 0.3$ and $A = 0.5$, respectively. The same color scheme as in Fig. 5.4. All simulations were done with uniform constants of motion and $N = 20$.

the WS dynamics. Below, we discuss the results obtained from Eq. (2.79) with G_{ab} defined in Eq. (5.4). In Fig. 5.5 (a) and (b), the WS macroscopic dynamics for $N = 20$ are depicted for the stationary (a) and the breathing (b) saddle chimeras, respectively. The radial $\rho_a(t)$ and the angular variables $\varphi_a(t)$ for $a = 1,\ldots,6$ show the same characteristics as the corresponding Ott-Antonsen variables in Sec. 5.2. Lyapunov spectral analysis can also be exploited to obtain stability information regarding the chimera trajectories of the WS dynamics, which is shown in Fig. 5.5 (c) and (d) for the states depicted in Fig. 5.5 (a) and (b) after settling down to one of the saddle chimeras, respectively. Likewise, both chimera trajectories exhibit one positive Lyapunov exponent, which does not indicate chaotic motion but rather verifies local instability along the reference trajectory. The CLV associated with this positive Lyapunov exponent takes the same form as the eigenvector corresponding to the positive eigenvalue in the case of the OA dynamics: it can be represented as $\mathbf{v}_1 = (A+,A_-,0,0,0,0)^\top$ and $\mathbf{v}_1 = (A+,0,0,0,0,A_-)^\top$ for $q = -1$ and $q = 1$, respectively, for the DS^5 chimeras with $A_+A_- < 0$. Note that the distinction between the stationary and breathing chimera dynamics

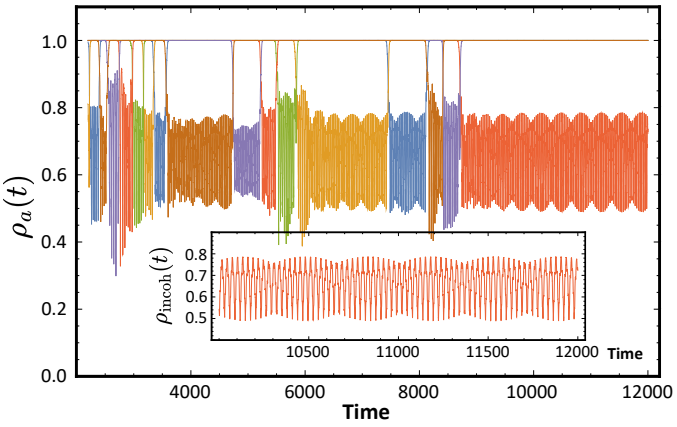

Fig. 5.6 Switching dynamics between quasiperiodic chimera states: Time evolution of the radial variables of the WS dynamics from a random initial condition with $A = 0.5$ and $N = 20$. The nonuniform constants of motion were obtained for $p = 0.85$.

appears in the number of zero Lyapunov exponents. The breathing chimera state possesses one additional zero Lyapunov exponent compared to the stationary chimeras due to the presence of the Hopf periodic motion.

In Chap. 3, we discussed the dynamics outside the Poisson submanifold[5], which can be constructed by considering nonuniform constants of motion in the WS dynamics. The nonuniform constants of motion here are generated from [102] $\psi_j^{(a)} = (1-p)\frac{\pi}{2} + \frac{\pi p(j-1)}{N/2}$ and $\psi_{j+N/2}^{(a)} = -(1+p)\frac{\pi}{2} + \frac{\pi p(j-1)}{N/2}$ with $p = 0.85$. One of the chimera states which cannot be captured by the OA dynamics (or the uniform constants of motion) is a quasiperiodic chimera state reported in Ref. [101]. For our network topology, we find the occurrence of heteroclinic switching dynamics between quasiperiodic chimera states using nonuniform constants of motion. Figure 5.6 presents an example of such heteroclinic switching dynamics for $p = 0.85$, $A = 0.5$, and $N = 20$. This finding underscores the robust nature of the heteroclinic cycle between saddle chimeras, which is primarily influenced by the symmetry inherent in the network topology.

5.3 Nonidentical Oscillators

In the subsequent sections, we study a system consisting of heterogeneous oscillators arranged in a ring configuration of six oscillator population as introduced above. Specifically, we introduce a heterogeneity parameter denoted as γ in Eqs. (5.9-5.10) for the OA dynamics

[5]Once again, note that in this thesis the Poisson submanifold is defined as a manifold for finite-N oscillators as close as possible to the OA manifold, using the uniform constants of motion.

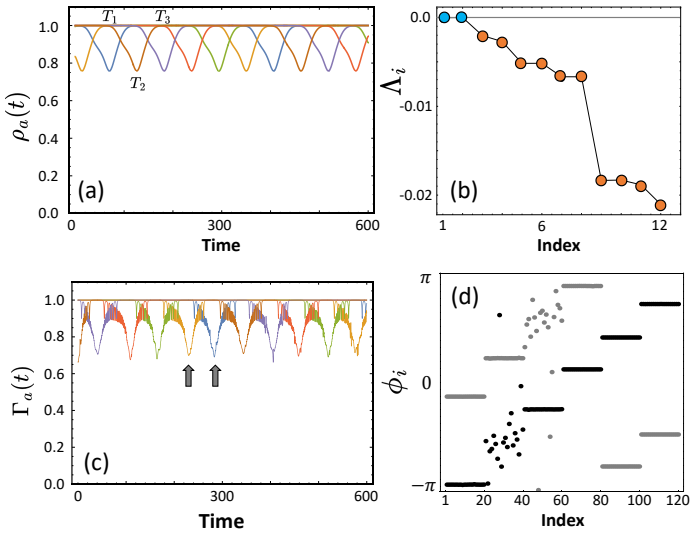

Fig. 5.7 (a) Time evolution of the radial variables of the OA dynamics after discarding transient behavior from a random initial condition. (b) Lyapunov exponents of the switching dynamics calculated along the switching trajectory. (c) Time evolution of moduli of the Kuramoto order parameters obtained from the microscopic dynamics with a random initial condition and $N = 20$. The two arrows indicate the instants in time at which the snapshot in (d) were taken. (d) Phase snapshots of the microscopic dynamics for $N = 20$ at two points indicated in (c). Other parameters: $\gamma = 10^{-6}$ and $A = 0.3$.

in the thermodynamic limit. It is worth noting that the OA manifold is known to exhibit asymptotic attractiveness for when considering heterogeneous oscillators, as discussed in Chap. 3 and in Refs. [169, 62, 97, 55]. For finite-sized systems, we numerically solve Eq. (5.1), where the natural frequency of each oscillator is derived from the Cauchy-Lorentz distribution, since the WS transformation does not work for the heterogeneous oscillators in each population.

5.3.1 Small heterogeneity: $\gamma = 10^{-6}$

First, we consider a case of a rather small heterogeneity characterized by $\gamma = 10^{-6}$. The Ott-Antonsen dynamics is then rendered attracting. Figure 5.7 (a) displays the time series of the OA radial variables for a system with a value of $\gamma = 10^{-6}$, starting from a random initial condition. Notably, persistent switching between chimera states is observed, a phenomenon that was previously observed only in the presence of low noise levels for strictly identical oscillators.

However, the switching dynamics looks different from that of the strictly identical oscillator systems. For most of the time, the chimera state exhibits a configuration consisting

of four S-populations and two D-populations[6]. See, for instance, the evolution of the 'brown' population during the time interval between T_1 and T_3 in Fig. 5.7 (a). Up to T_2, the 'blue' population becomes an S-population, while the 'brown' population becomes a D-population. Once the 'blue' population has achieved the S-state, the 'purple' population commences to be desynchronized. Hence, the trajectory corresponding to a precise DS^5 chimera state or its symmetric counterparts only occurs at specific periodic time instances, such as at T_2, rather than during continuous time intervals. Additionally, this persistent switching chimera dynamics is attracting, as supported by the numerical determination of the Lyapunov exponents. Figure 5.7 (b) shows the Lyapunov exponents obtained from a switching trajectory in (a), where all the Lyapunov exponents exhibit negative values, except for two zero Lyapunov exponents resulting from the time and the phase shift invariance of Eqs. (5.9-5.10).

For finite-sized ensembles, we need to directly investigate the microscopic dynamics in Eq. (5.1). First, the natural frequencies are generated from the Cauchy-Lorentz distribution according to

$$\frac{j-\frac{1}{2}}{N} = \int_{-\infty}^{\omega_j} g(\omega)d\omega = \int_{-\infty}^{\omega_j} \frac{\gamma}{\pi}\frac{1}{\omega^2+\gamma^2}d\omega = \frac{1}{2}+\frac{1}{\pi}\tan^{-1}\left(\frac{\tilde{\omega}_j}{\gamma}\right) \tag{5.14}$$

for $j = 1,...,N$, which produces $\{\omega_j = \gamma\tan\left(\frac{\pi(2j-1-N)}{2N}\right)\}_{j=1}^{N}$. By directly solving the microscopic dynamics in Eq. (5.1) with $\gamma = 10^{-6}$, we observe a switching dynamics in the magnitudes of the Kuramoto order parameters defined in Eq. (5.3). Figure 5.7 (c) displays the temporal evolution of the magnitudes of the Kuramoto order parameters, which apparently follows the same switching dynamics as depicted in Fig. 5.7 (a), albeit with superimposed fluctuations resulting from finite-size effects. Two snapshots of the microscopic phases at two instances along the dynamics in Fig. 5.7 (c) are depicted in Fig. 5.7 (d), which are indicated by the two arrows. At those time instances, there exist five S-populations and one D-population, precisely corresponding to the DS^5 chimera state. Similar to the DS^5 chimera state for the identical oscillator ensembles, the mean phases of the populations exhibit a nearly twisted state.

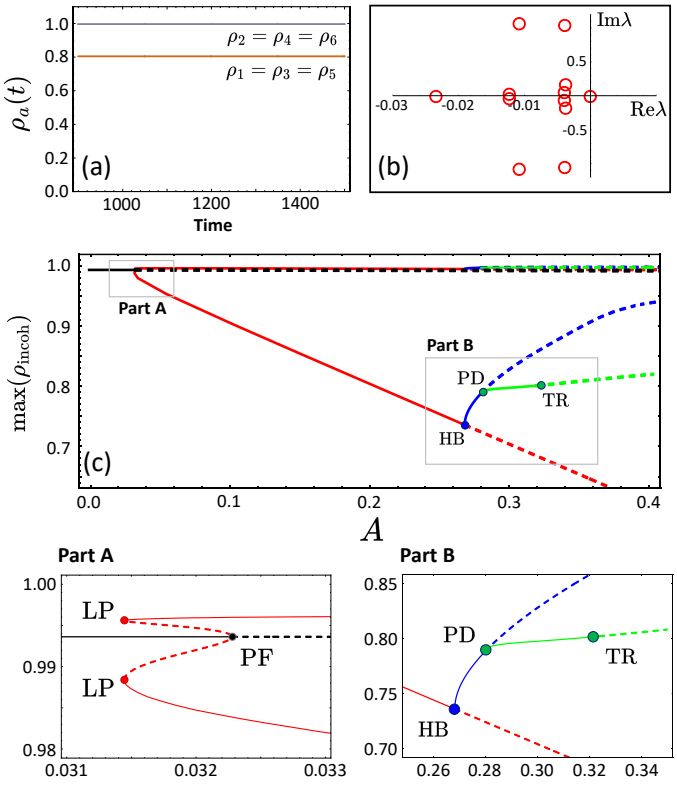

Fig. 5.8 (a) Time evolution of the radial variables for $(\mathrm{DS})^3$ chimeras at $A = 0.2$. (b) Eigenvalues of the Jacobian matrix evaluated at $(\mathrm{DS})^3$ in the complex plane at $A = 02$. (c) Bifurcation diagram of the $(\mathrm{DS})^3$ chimera state. Solid and dashed lines indicate stable and unstable states, respectively. Black, red, blue and green: uniform states, stationary, breathing and period-doubled chimera solutions, respectively.

5.3.2 Larger heterogeneity: $\gamma = 10^{-4}$

Stationary Chimera States

In this section, we introduce a relatively larger heterogeneity characterized by $\gamma = 0.0001$ in Eqs. (5.9-5.10). However, from numerical integration of them, no switching dynamics between chimera states is detected. Instead, we discover an attracting stationary chimera state, specifically of the $(\mathrm{DS})^3$ type. Our numerical integration of Eqs. (5.9-5.10) from random initial conditions does not reveal any other types of chimeras. Taking into account the symmetry of the network, we note that the clusters $C_1 = 1,3,5$ and $C_2 = 2,4,6$ are intertwined clusters [47], also known as an ISC set [46] (independently synchronizable

[6]Note that due to the small heterogeneity, the full synchronization of a population cannot be obtained. Despite this, we keep the same notation and refer to nearly synchronized populations with $\rho_a \in [0.995, 1)$ as S-populations.

cluster set). This implies that the stability of each cluster relies on the stability of the other cluster [46, 178].

In Fig. 5.8 (a), the OA radial variables of a stationary $(\mathrm{DS})^3$ chimera starting from a random initial condition are shown as a function of time for $A = 0.2$. It is characterized by $\rho_a(t) = \rho_\mathrm{D} < 1$ (incoherent populations) for $a = 1,3,5$ and $\rho_a(t) = \rho_\mathrm{S} \approx 1$ (nearly-synchronized populations) for $a = 2,4,6$. The phase variables are also locked at the common frequency, thus the chimera state is a fixed point solution. The OA phase variable differences between populations in the same cluster are found to be $\frac{2\pi}{3}$, i.e., $\varphi_{a+2} - \varphi_a = \frac{2\pi}{3}$. In Fig. 5.8 (b), the eigenvalues of the Jacobian matrix computed at the $(\mathrm{DS})^3$ chimera state are shown in the complex plane. Notably, all the eigenvalues exhibit negative real parts, except for a single zero eigenvalue associated with the phase shift invariance, not affecting the stability of the trajectory. This confirms the linear stability of the $(\mathrm{DS})^3$ chimera state, i.e., the attracting chimera state.

In Fig. 5.8 (c), a bifurcation diagram of the $(\mathrm{DS})^3$ chimera state is depicted. For a small A, a stable uniform solution (black) exists with $\rho_a = \rho_0 < 1$ for $a = 1,\ldots,6$ where the OA angular variables are equally spaced along one cycle of the ring. The uniform state possesses two identical clusters, denoted as C_1 and C_2. Then, this uniform state undergoes a destabilizing pitchfork bifurcation (PF) at $A_\mathrm{PF} = 0.0323$, during which one eigenvalue becomes positive. The corresponding eigenvector associated with the positive eigenvalue takes the form $\mathbf{v} = (\delta_+, \delta_-, \delta_+, \delta_-, \delta_+, \delta_-)^\top$, where $\delta_+\delta_- < 0$. This indicates that the uniform state becomes unstable along the transverse direction between the two clusters. As a result of the transverse instability, two symmetric solutions emerge from the uniform state in a pitchfork bifurcation (see Part A in Fig. 5.8). Both solutions exhibit a chimera state of the type $(\mathrm{DS})^3$ or $(\mathrm{SD})^3$, respectively, where each solution consists of one cluster of three nearly synchronized populations and the other cluster of three incoherent populations. Coming from low values of A, each of these two solution branches is born in a saddle-node bifurcation (LP) at $A_\mathrm{LP} = 0.03144$ together with a stable, stationary $(\mathrm{SD})^3$- respectively $(\mathrm{DS})^3$-chimera state. This chimera state is stable in a wide range of the parameter A as shown in Fig. 5.8 (c).

Breathing, Period-doubled and Quasiperiodic Chimera States

The stationary $(\mathrm{DS})^3$-type chimera states undergo a supercritical Hopf bifurcation (HB) at $A_\mathrm{HB} = 0.26812$, leading to the emergence of a periodic solution, that is, a stable breathing chimera state. The time evolution of the OA radial variables is depicted in Fig. 5.9 (a), while the corresponding Lyapunov spectrum is shown in Fig. 5.9 (b) for $A = 0.274$. In the breathing chimera state, the periodic motions within each cluster are shifted in time by $T/3$ and $2T/3$, where T indicates the period of the OA radial variable: $\rho_a(t) = \rho_{a+2}(t - \frac{T}{3}) = \rho_{a+4}(t - \frac{2T}{3})$

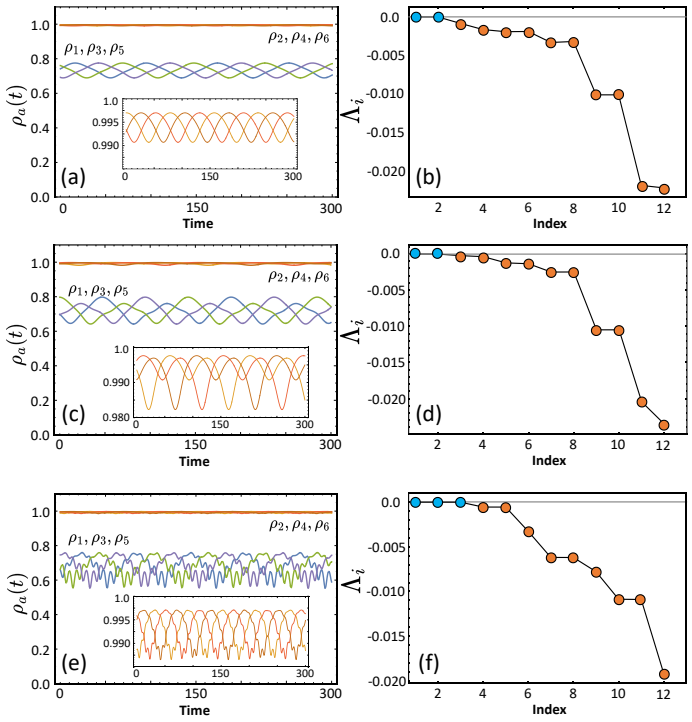

Fig. 5.9 Breathing (a,b), period-doubled (c,d) and quasiperiodic (e,f) chimera states for $A = 0.274$, $A = 0.3$ and $A = 0.34$, respectively. Left column: time series of the radial variables with insets of magnifying the dynamics of nearly-synchronized populations. Right column: Lyapunov exponents with the same color scheme as in Fig. 5.4.

for $a = 1, \ldots, 6$ (indices are taken modulo 6). Apart from the two zero Lyapunov exponents associated with phase and time shift invariance, all other Lyapunov exponents of the breathing $(\mathrm{DS})^3$-type chimera are negative, indicating that the chimera state is attracting. The chimera state exists within a narrow range of the parameter A. At $A_{\mathrm{PD}} = 0.27995$, a supercritical period-doubling bifurcation (PD) occurs, as shown in Part B of Fig. 5.8 (c). The period-doubled feature of the radial variables can be seen in panels (c-d) of Fig. 5.9 together with the stability of the period-doubled chimera trajectory. The radial variables exhibit the previously mentioned spatiotemporal symmetry, but with a period that is approximately twice compared to the ones of the breathing chimeras in Fig. 5.9 (a).

The period-doubled chimera state loses its stability in a supercritical torus bifurcation (TR) at $A_{\mathrm{TR}} = 0.31957$. For $A > A_{\mathrm{TR}}$, one can observe a quasiperiodic chimera dynamics on a torus, as shown in Fig. 5.9 (e-f) with an example trajectory and its stability. The quasiperiodic chimera is characterized by one additional zero Lyapunov exponent arising from the second incommensurate frequency. The rich dynamics of the $(\mathrm{DS})^3$-type chimera states can be better appreciated in a time-parametric plot where $\rho_1(t)$ is plotted vs. $\rho_3(t)$

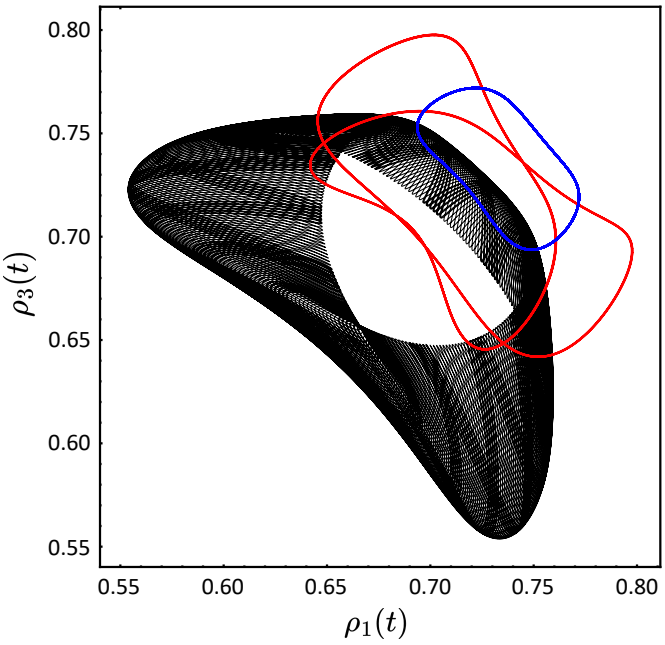

Fig. 5.10 Time-parametric plot of $\rho_1(t)$ vs. $\rho_3(t)$ for the time interval $\Delta t = 3000$ after discarding the transient behavior: breathing (blue), period-doubled (red) and quasiperiodic (black) chimera trajectories for $A = 0.274$, $A = 0.3$ and $A = 0.34$, respectively.

(Fig. 5.10): The breathing chimera state occurs as a single, closed-loop trajectory (blue) in the projected space, while the period-doubled chimera state (red) exhibits a double-wound loop. In contrast, the quasiperiodic motion on the torus (black) lacks the spatiotemporal symmetry observed in the other chimera states.

5.4 Summary

In this chapter, we investigated a system consisting of six populations of identical Kuramoto-Sakaguchi phase oscillators arranged in a ring geometry. When considering the thermodynamic limit, the Ott-Antonsen dynamics shows a diverse array of chimera solutions stemming from the system's symmetry, i.e., the cyclic permutations of the ring. The majority of these solutions, however, exhibit instability across nearly the entire parameter space. Among them, one type of chimeras, that is, DS^5 and its symmetric counterparts, has a one-dimensional unstable eigenspace as a fixed point solution in a rotating reference frame.

Interestingly, the six one-dimensional unstable manifolds of the saddle DS^5 chimeras connect them in a heteroclinic cycle. This structural arrangement causes the observation of chimera states through numerical integration, even when initiated from random initial

conditions. Intriguingly, the trajectories exhibit transient shifts between the saddle chimera states, a behavior that gains persistence when a weak noise is introduced to the radial dynamics. At a certain value of A, the stationary saddle chimeras undergo a Hopf bifurcation, resulting in the emergence of a heteroclinic orbit featuring saddle limit-cycles. Consequently, we observe switching dynamics between breathing chimeras. Notably, within finite-sized populations, an additional form of switching between quasiperiodic chimera states can emerge outside the OA manifold using nonuniform constants of motion in the WS theory.

Finally, we extended our exploration to oscillator ensembles with a distribution of heterogeneous natural frequencies. For a weak heterogeneity of natural frequencies, we observed an attracting switching dynamics between chimera states, which is persistent without any stochastic variables, and looks different from DS^5 for the identical oscillator ensembles. The numerically measured Lyapunov exponents confirmed that this persistent switching dynamics is indeed an attracting trajectory in phase space. Considering a stronger heterogeneity, we observed a prevalence of non-switching attracting chimera states exhibiting diverse symmetries and complex order parameter dynamics across a wide parameter range. The emergence of these various macroscopic dynamics occurred through Hopf, period-doubling, and torus bifurcations.

Chapter 6

Coexistence Dynamics IV: Chimeras of Generalized Kuramoto Oscillators

So far, in Chap. 3 to Chap. 5, we have explored a variety of dynamical behavior of chimera states in a system of identical Kuramoto-Sakaguchi oscillators. As seen in Sec. 2.5, such a phase oscillator defined on the unit circle of $\mathbb{C}^1$ or $\mathbb{R}^2$ can be extended to the so-called generalized Kuramoto oscillators defined on $\mathbb{S}^M$. In this chapter, we investigate possible chimera dynamics in a system of identical generalized Kuramoto-Sakaguchi oscillators in two-population networks, with a particular focus on $\mathbb{C}^2$ and $\mathbb{R}^4$. Here, we also find stationary and breathing chimera states, similar to what we studied in a system of usual KS oscillators in two-population networks. However, in higher dimensional spaces, we observe more than this since the Kuramoto order parameter vector consists of M components. Such a higher-dimensional complexity leads to more complex chimera states than those in the usual KS oscillators in two-population networks. To show this, we elucidate the detailed dynamical properties of observable chimera states as we vary the intra-population coupling strength.

We consider a system of generalized Kuramoto-Sakaguchi oscillators in a two-population network, each of which is described by a unit vector $\boldsymbol{x}_j(t) \in \mathbb{S}^M$, and governed by

$$\begin{aligned} \partial_t \boldsymbol{x}_j^{(1)} &= -\boldsymbol{x}_j^{(1)} \boldsymbol{H}_1^\dagger \boldsymbol{x}_j^{(1)} + \boldsymbol{H}_1 \\ \partial_t \boldsymbol{x}_j^{(2)} &= -\boldsymbol{x}_j^{(2)} \boldsymbol{H}_2^\dagger \boldsymbol{x}_j^{(2)} + \boldsymbol{H}_2 \end{aligned} \tag{6.1}$$

The contents of this chapter were in part published previously in S. Lee and K. Krischer, J. Phys. A: Math. Theor. **56**, 405001 (2023) [58]. All figures and their captions are reproduced from those in it.

for $j = 1, ..., N$. More specifically, we define the mean-field forcing for each population as

$$\boldsymbol{H}_a = \boldsymbol{K} \cdot \sum_{b=1}^{2} G_{ab} \boldsymbol{\Gamma}_b = \mu \boldsymbol{K} \cdot \boldsymbol{\Gamma}^{(a)} + \nu \boldsymbol{K} \cdot \boldsymbol{\Gamma}^{(b)} \in \mathbb{K}^M \tag{6.2}$$

for $(a,b) = (1,2)$ or $(2,1)$. As we did so far in the previous chapters, we assume that the forcing field depends only on the Kuramoto order parameter, i.e., a center of mass of the oscillators on $\mathbb{S}^M$, of each population, which reads

$$\boldsymbol{\Gamma}^{(a)}(t) = \frac{1}{N} \sum_{k=1}^{N} \boldsymbol{x}_k^{(a)}(t) \in \mathbb{K}^M \tag{6.3}$$

for $a = 1,2$. Throughout this chapter, we fix the inter-population coupling strength as $\mu = 1$ while the intra-population coupling strength is $\nu = 1 - A$ where A is the control parameter. As in Sec. 2.5, we specify the coupling matrix $\boldsymbol{K} \in \mathbb{K}^{M \times M}$ in Eq. (6.2) to be a given rotation matrices for the real spaces in Sec. 2.5 and $\boldsymbol{K} = e^{-i\alpha} I_M$ for $\mathbb{K} = \mathbb{C}$, respectively. Note that in this chapter, we also fix $\alpha = \frac{\pi}{2} - 0.005 < \alpha_{\mathrm{BF}}$.

6.1 Chimera Dynamics in Two-population Networks for $\mathbb{C}^2$

In this section, we study the observable chimera dynamics for $\mathbb{K} = \mathbb{C}$ with $M = 2$.

6.1.1 Stationary and Breathing Chimeras

To study the macroscopic dynamics of the chimera states in $\mathbb{C}^2$, we here need to explore the dynamics of the WS variable since the Kuramoto order parameter is given as $\boldsymbol{\Gamma}^{(a)}(t) = \boldsymbol{\psi}_a(t)$ for $a = 1,2$ in the thermodynamic limit[1]. For the moment, we focus on the thermodynamic limit for the exploration of chimera dynamics. As discussed in Sec. 2.5.2, the WS variables $\boldsymbol{\psi}_a$ for $a = 1,2$ in two-population networks are governed by

$$\partial_t \boldsymbol{\psi}_a = -\boldsymbol{\psi}_a \boldsymbol{H}_a^\dagger \boldsymbol{\psi}_a + \boldsymbol{H}_a = -\boldsymbol{\psi}_a \left(\mu \boldsymbol{\psi}_a^\dagger \boldsymbol{K}^\dagger + \nu \boldsymbol{\psi}_b^\dagger \boldsymbol{K}^\dagger \right) \boldsymbol{\psi}_a + \mu \boldsymbol{K} \boldsymbol{\psi}_a + \nu \boldsymbol{K} \boldsymbol{\psi}_b \tag{6.4}$$

for $(a,b) = (1,2)$ and $(2,1)$ in the thermodynamic limit.

[1] Definitely, it is whenever the constants of motion $\boldsymbol{x}_0$ are uniformly distributed on $\mathbb{S}^M$. See Sec. 2.5.

First, we examine the magnitude of the order parameter vectors: $|\boldsymbol{\psi}_a| := \sqrt{\langle \boldsymbol{\psi}_a | \boldsymbol{\psi}_a \rangle}$ for $a = 1, 2$. From Eq. (6.4), we can obtain the magnitude dynamics as

$$\begin{aligned} \partial_t |\boldsymbol{\psi}_1|^2 &= 2(1-|\boldsymbol{\psi}_1|^2)\left(\mu \cos\alpha |\boldsymbol{\psi}_1|^2 + \nu \mathrm{Re}\left[e^{-i\alpha}\langle \boldsymbol{\psi}_1 | \boldsymbol{\psi}_2 \rangle\right]\right) \\ \partial_t |\boldsymbol{\psi}_2|^2 &= 2(1-|\boldsymbol{\psi}_2|^2)\left(\mu \cos\alpha |\boldsymbol{\psi}_2|^2 + \nu \mathrm{Re}\left[e^{-i\alpha}\langle \boldsymbol{\psi}_2 | \boldsymbol{\psi}_1 \rangle\right]\right) \end{aligned} \tag{6.5}$$

and the cross term as

$$\begin{aligned} \partial_t \langle \boldsymbol{\psi}_1 | \boldsymbol{\psi}_2 \rangle = \mu\big((1-|\boldsymbol{\psi}_1|^2)e^{-i\alpha} + (1-|\boldsymbol{\psi}_2|^2)e^{i\alpha}\big)\langle \boldsymbol{\psi}_1 | \boldsymbol{\psi}_2 \rangle \\ + \nu e^{-i\alpha}(|\boldsymbol{\psi}_1|^2 - \langle \boldsymbol{\psi}_1 | \boldsymbol{\psi}_2 \rangle^2) + \nu e^{i\alpha}(|\boldsymbol{\psi}_2|^2 - \langle \boldsymbol{\psi}_1 | \boldsymbol{\psi}_2 \rangle^2). \end{aligned} \tag{6.6}$$

From the numerical integration of Eq. (6.4), we find the cross term can be represented by[2] $\langle \boldsymbol{\psi}_1 | \boldsymbol{\psi}_2 \rangle = |\boldsymbol{\psi}_1||\boldsymbol{\psi}_2| e^{i\Theta}$ where $\Theta \in \mathbb{R}$ is some angular variable, which we specify later. Then, setting $|\boldsymbol{\psi}_a| =: \rho_a$ for $a = 1, 2$, we obtain

$$\begin{aligned} \partial_t \rho_1 &= (1-\rho_1^2)\big(\mu \rho_1 \cos\alpha + \nu \cos(\Theta - \alpha)\big) \\ \partial_t \Theta &= \mu \sin\alpha(\rho_1^2 - 1) + \nu\Big(-2\rho_1 \sin(\Theta+\alpha) + \sin(\Theta-\alpha)\big(-\frac{1}{\rho_1} - \rho_1\big)\Big). \end{aligned} \tag{6.7}$$

where we put $\rho_2 = 1$ for the study of chimera states. Note that the above equations are equivalent to Eq. (3.10) in Chap. 3, i.e., the Ott-Antonsen equation of a system of identical usual KS oscillators in two-population networks.

In Fig. 6.1 (a), a bifurcation diagram of chimera states is depicted with A taken as bifurcation parameter. Stable (red solid) and unstable (red dashed) stationary chimera states are born/annihilated in a saddle-node bifurcation (LP) for a rather small value of A. The stable stationary chimera state undergoes a supercritical Hopf bifurcation (HB) at $A = A_{\mathrm{HB}}$, in which a breathing chimera state (green solid) emerges. Numerically integrating Eq. (6.4) [193], the stationary and breathing chimera states can be easily obtained for the corresponding parameter values. We assume that the first population is incoherent ($|\boldsymbol{\psi}_1(t)| < 1$) and the second population is synchronized ($|\boldsymbol{\psi}_2(t)| = 1$). Here, the following notations are introduced to denote components of each order parameter vector: $\boldsymbol{\psi}_1(t) = (z_1(t), z_2(t))^\top$ and $\boldsymbol{\psi}_2(t) = (w_1(t), w_2(t))^\top$ where $z_i(t), w_i(t) \in \mathbb{C}$ and $\theta_i(t) = \arg z_i(t) \in \mathbb{R}$ and $\phi_i(t) = \arg w_i(t) \in \mathbb{R}$ for $i = 1, 2$.

[2] Note that this representation does not hold in general

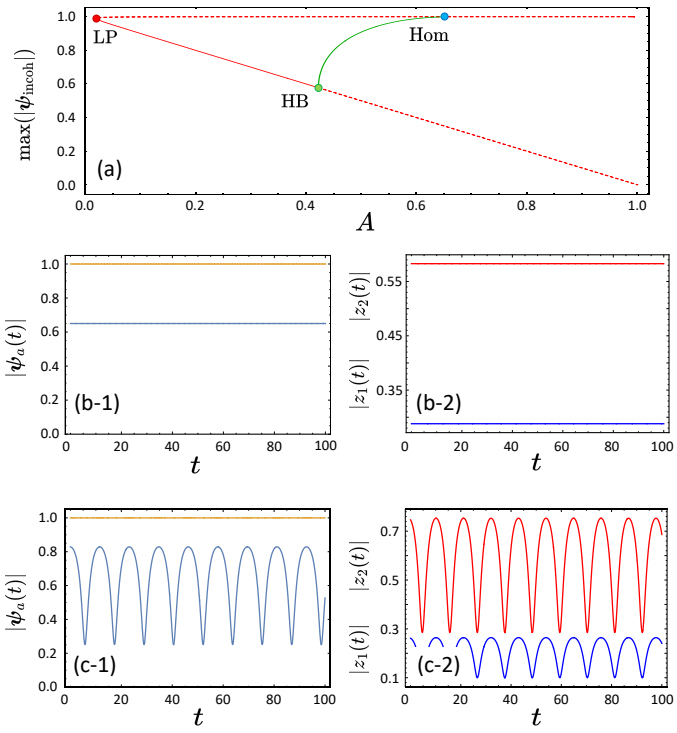

Fig. 6.1 (a) A bifurcation diagram of stable (solid curve) and unstable (dashed curve) chimera states from Eq. (6.7): stationary chimeras (red) and breathing chimera states (green). LP: limiting point bifurcation, HB: supercritical Hopf bifurcation, and Hom: homoclinic bifurcation. Lower panels: Time evolution of the magnitude of the order parameter vectors (the synchronized population $|\boldsymbol{\psi}_2|$ with orange color and the incoherent population $|\boldsymbol{\psi}_1|$ with light blue) in the left column and time evolution of the modulus of the components of the order parameter vector for the incoherent population $\boldsymbol{\psi}_1 = (z_1, z_2)^\top$ (the first component $|z_1|$ with red and the second component $|z_2|$ with blue) in the right column. (b) Stationary chimera states for $A = 0.35$. (c) Breathing chimera states for $A = 0.46$. The presented results are based on data obtained after disregarding the initial transient behavior for $t > 10^5$.

For $A \in (A_{\rm LP}, A_{\rm HB})$, we observe a stationary chimera dynamics where temporal evolutions of the magnitude of the order parameter vectors ($\boldsymbol{\psi}_2(t)$) and the components ($|z_1(t)|$ and $|z_2(t)|$) both exhibit steady motion, as depicted in Fig. 6.1 (b). The synchronized population ($\boldsymbol{\psi}_1(t)$), $|w_i(t)|$ also shows stationary behavior for $i = 1, 2$. Furthermore, the governing equations of $\boldsymbol{\psi}_a(t)$ has a continuous symmetry. Equation (6.4) is invariant under a unitary transformation defined by

$$\boldsymbol{u} = \begin{pmatrix} e^{-i\theta_1} & 0 \\ 0 & e^{-i\theta_2} \end{pmatrix} \tag{6.8}$$

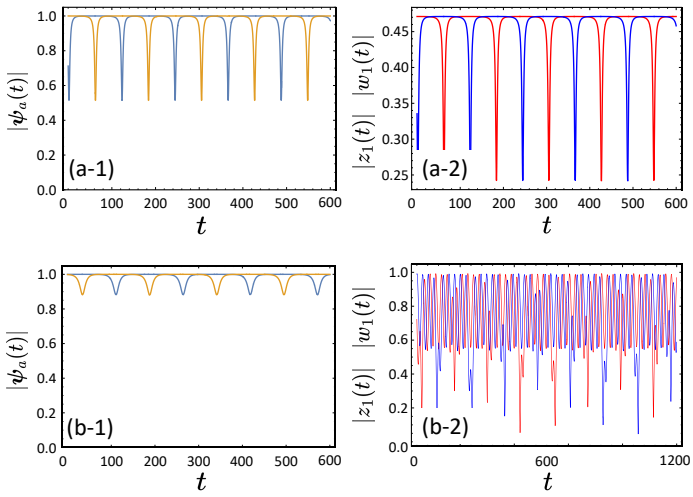

Fig. 6.2 Left column: Time evolution of the magnitude of the order parameters: $|\boldsymbol{\psi}_1(t)|$ (blue light) and $|\boldsymbol{\psi}_2(t)|$ (orange). Right column: Time evolution of the first component of the order parameter vectors: $|z_1(t)|$ (red) and $|w_1(t)|$ (blue). (a) The periodic alternating chimera is obtained at $A = 0.75$. (b) The aperiodic alternating chimera occurs at $A = 0.86$. The presented results are based on data obtained after disregarding the initial transient behavior for $t > 10^5$.

which means $F_a(\boldsymbol{u}\boldsymbol{\psi}_a) = \boldsymbol{u}F_a(\boldsymbol{\psi}_a)$ where $F_a(\boldsymbol{\psi}_a) := -\boldsymbol{\psi}_a\boldsymbol{H}_a^{\dagger}\boldsymbol{\psi}_a + \boldsymbol{H}_a$ for $a = 1,2$. This unitary transformation corresponds to the phase shift invariance of the KS model on the unit circle, which leads us to the phase difference $\Theta_i(t) := \phi_i(t) - \theta_i(t)$ for $i = 1,2$ between the components of the two order parameter vectors. These phase differences also demonstrate a steady motion as a function of time (not shown here) for a stationary chimera state. As the parameter A is increased, the stationary chimera gets destabilized in a supercritical Hopf bifurcation, from which a breathing chimera state emerges. The time evolution of the breathing chimera states is depicted in Fig. 6.1 (c) for $|\boldsymbol{\psi}_a|$ and $|z_i|$, respectively. Further increasing A, the breathing chimera state undergoes a homoclinic bifurcation (Hom) at which it disappears, together with an indefinite increase of its period.

6.1.2 Alternating and Aperiodic Chimeras

Exploring the magnitude of the order parameter vectors, the scenario of the emergence of chimera states for $\mathbb{C}^2$ shows nothing more than that observed in the system of identical usual KS oscillators on the unit circle of $\mathbb{C}^1$ (e.g., see Refs. [72, 74]). However, in the two-dimensional complex space $\mathbb{C}^2$, the higher-dimensional complexity of the order parameter produces additional complexities beyond this. For a given $A > A_{\mathrm{Hom}}$, a chimera state

is observed and characterized by a periodic alternation between the two order parameter vectors, as shown in Fig. 6.2 (a). Both the magnitude of the order parameter vectors (Fig. 6.2 (a-1)) and each component (Fig. 6.2 (a-2)) show the alternating dynamics, and satisfy $|\boldsymbol{\psi}_1(t)| = |\boldsymbol{\psi}_2(t-\frac{T}{2})|$ and $|z_i(t)| = |w_i(t-\frac{T}{2})|$ for $i = 1,2$, respectively. Such an alternating motion of chimera states was reported previously for a system of heterogeneous Kuramoto-Sakaguchi oscillators in two-population networks [77, 76]. Therein, the alternating chimeras emerge also after the homoclinic bifuration at which the breathing chimera state disappears.

As the parameter A is increased further, we observe a motion seemingly similar to the alternating chimera dynamics in terms of the magnitude of the order parameters, as depicted in Fig. 6.2 (b). The magnitude of the order parameters (Fig. 6.2 (b-1)) shows similar behavior to that of the periodic alternating chimera dynamics except for $\min_{t>0}|\boldsymbol{\psi}_a(t)|$. However, the chimera dynamics turns out to be entirely different in terms of its components. In Fig. 6.2 (b-2), an aperiodic time evolution of the first components of the order parameter vector for both populations is depicted. Such an aperiodic dynamics is numerically verified in Fig. 6.3 (a) using the Poincaré section defined by $\mathrm{Re}[z_2] \equiv 0$ where the chimera dynamics exhibits scattered points on the section, as anticipated for the aperiodic motion on a chaotic attractor. This conjecture is further supported by numerically measuring the Lyapunov exponents [122, 194, 195]. Such a chimera trajectory possesses two positive Lyapunov exponents (Fig. 6.3 (b)) as it is expected for an aperiodic motion and indicates a sensitive dependence of the reference trajectory on initial conditions. In Fig. 6.3 (b), two zero Lyapunov exponents arise from two continuous symmetries: time shift invariance and the unitary transformation in Eq. (6.8) corresponding to a phase shift invariance.

Now, we explain the emergence of the aperiodic chimera state from the periodic alternating chimera state as A is increased. In Fig. 6.4 (a), we present a bifurcation diagram that illustrates the parameter points at which the periodic alternating (A_{Hom}) and aperiodic (A_c) chimera states emerge, respectively. Numerical integration of Eq. (6.4) reveals that two conserved quantities exist along the chimera trajectory in phase space for $A < A_c$. To find them, we first consider the unitary transformation in Eq. (6.8) under which the dynamics is invariant. This transformation leads us to defining the phase difference of each component between the two order parameter vectors: $\Theta_i(t) := \phi_i(t) - \theta_i(t)$ for $i = 1,2$. Then, the first conserved quantity is given by

$$C_1(\Theta_1, \Theta_2; t) := \sin(\Theta_1(t) - \Theta_2(t)). \tag{6.9}$$

This quantity is conserved as $C_1(t) = 0$ for all t along the chimera trajectory for a given $A < A_c$; for example, the stationary, breathing and periodic alternating chimera states all preserve $C_1(t)$ as zero along each trajectory. Secondly, from the numerical integration of

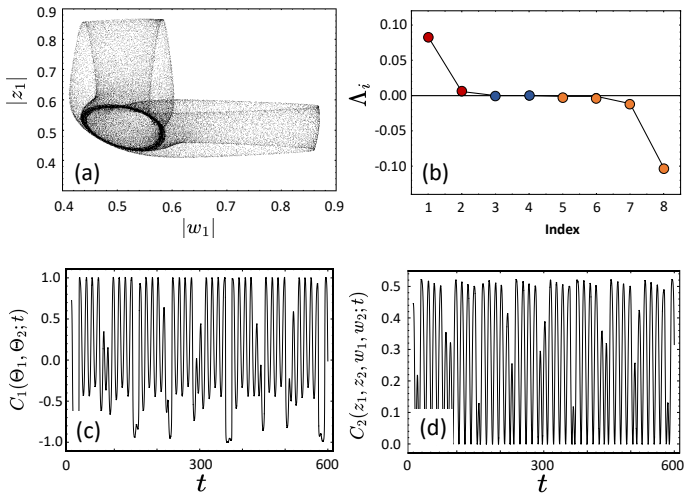

Fig. 6.3 (a) Poincaré map of the first components of the order parameters: $|z_1|$ vs. $|w_1|$ measured on the section defined by $\mathrm{Re}[z_2] \equiv 0$. (b) Lyapunov exponents measured along the reference trajectory in (a): Positive exponents (red), zero exponents (blue) and negative exponents (orange). (c-d) Time evolution of the broken conserved quantities of the trajectory in (a) (see main text). The parameter is $A = 0.86$ and the transient behavior was discarded ($t > 10^5$).

Eq. (6.4) for $A < A_c$, we also find the relation between the cross term and the magnitude of the order parameter vectors: $\langle \boldsymbol{\psi}_1 | \boldsymbol{\psi}_2 \rangle = |\boldsymbol{\psi}_1||\boldsymbol{\psi}_2| e^{i\Theta}$ where $\Theta := \Theta_1 = \Theta_2$ due to $C_1 = 0$. This relation gives the second conserved quantity:

$$C_2(z_1, z_2, w_1, w_2; t) := \big(|z_1(t)||w_2(t)| - |z_2(t)||w_1(t)|\big)^2 \tag{6.10}$$

and $C_2(t) = 0$ for all t along a chimera trajectory as long as $A < A_c$. Interestingly, these two conserved quantities are broken and show irregular time evolution whenever the chimera trajectory is observed for $A > A_c$. To give an example, the time evolution of $C_1(t)$ and $C_2(t)$ is depicted in Fig. 6.3 (c-d) for the chimera trajectory of Fig. 6.2 (b). To confirm this scenario, we numerically measure $\sup_{t\in[t_0,t_1]} |C_1(t)|$ and $\sup_{t\in[t_0,t_1]} |C_2(t)|$ as a function of the parameter A where $t_0 = 2 \times 10^4$ and $t_1 = 10^5$. We numerically find that the stationary, breathing and periodic alternating chimeras for $A < A_c$ have the two quantities conserved along their chimera dynamics whereas the conserved quantities are broken from A_c on for the aperiodic chimera state, as shown in Fig. 6.4 (b).

In this scenario, we find another notable observation with respect to the breathing chimera state. There is a global bifurcation for the breathing chimera state involving the completely incoherent state, i.e., $|\boldsymbol{\psi}_1| = 0$ [76]. Figure 6.4 (c) illustrates the maximum and minimum

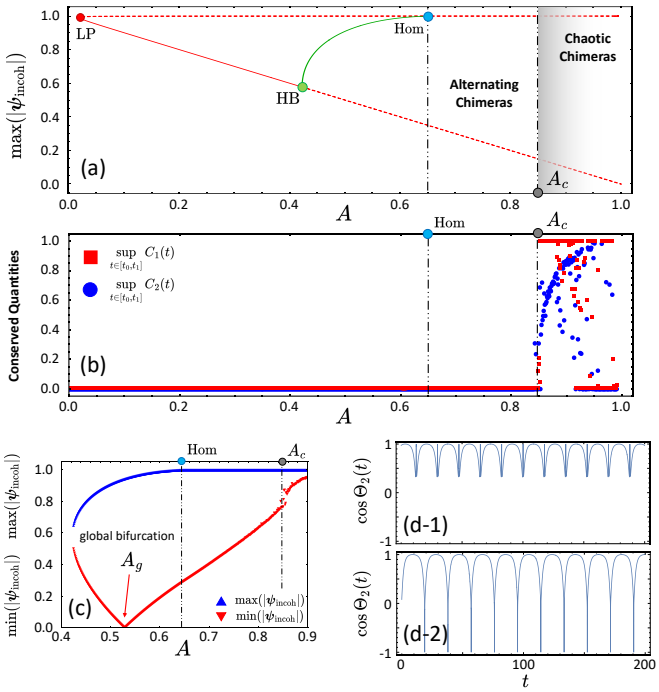

Fig. 6.4 (a) A re-plot of the bifurcation diagram in Fig. 6.1 (a) with the periodic alternating chimeras and the chaotic chimeras. (b) Conserved quantities as a function of the parameter A: $t_0 = 20,000$ and $t_1 = 10^5$. (c) Maximum (blue) and minimum (red) values of the magnitude of the order parameter vectors as a function of the parameter A. (d) Time evolution of $\cos\Theta_2(t)$ before (upper, $A = 0.52$) and after (lower, $A = 0.53$) the global bifurcation. A_c denotes a parameter point from which on the chaotic chimera emerges.

values of the magnitude of the order parameter vector for the incoherent population. As A increases, for small values of A, $\min(|\boldsymbol{\psi}_{\text{incoh}}|)$ decreases continuously until it reaches $A = A_g$. At this point, it touches a value of zero, corresponding to the completely incoherent state. Beyond this point, the minimum value of the order parameter magnitude begins to increase continuously, eventually seamlessly connecting with that of the periodic alternating chimera state for $A > A\text{Hom}$. With further increase in A, we encounter the emergence of the aperiodic chimera state at A_c, accompanied by a discontinuous jump in $\min(|\boldsymbol{\psi}_{\text{incoh}}|)$ to higher values. At the global bifurcation point A_g, the behavior of the breathing chimera undergoes a significant change in its phase variable. In Fig. 6.4 (d), we depict the time evolution of $\cos\Theta(t)$ for the breathing chimera state before (d-1) and after (d-2), i.e., after the global bifurcation. For $A < A_g$, the phase variable $\Theta(t)$ of the breathing chimera states evolves within a limited interval smaller than $\mathbb{T} = [0, 2\pi]$ (libration). However, after touching the incoherent state for $A > A_g$, the phase $\Theta(t)$ of the breathing chimera states monotonically increases over time, sweeping across the entire range of $\mathbb{T}$ (rotation).

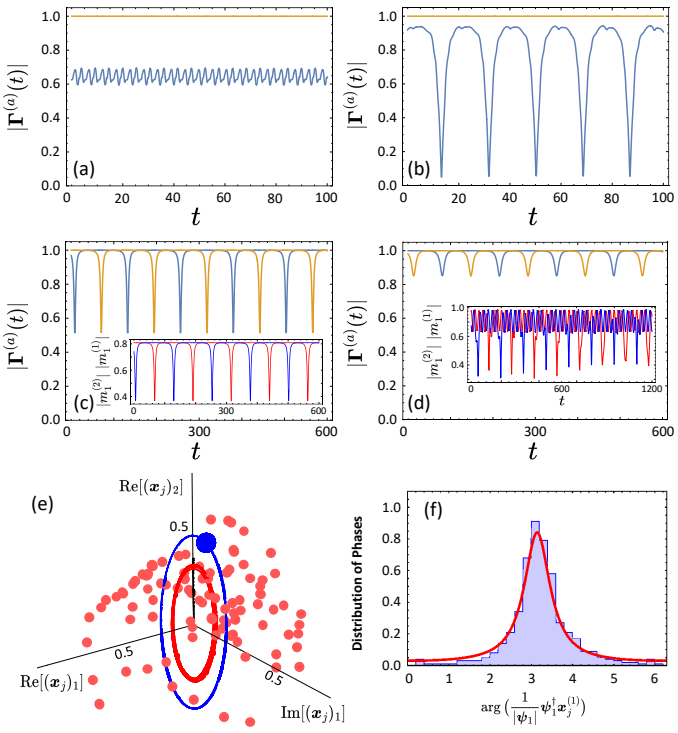

Fig. 6.5 (a-d) Time evolution of the magnitude of the order parameter vectors defined in Eq. (6.3) from solving Eq. (6.1) with $N = 30$: the first population $|\mathbf{\Gamma}^{(1)}(t)|$ (light blue) and the second population $|\mathbf{\Gamma}^{(2)}(t)|$ (orange). (a) The stationary chimera state with $A = 0.35$. (b) The breathing chimera state with $A = 0.55$. (c) The periodic alternating chimera state with $A = 0.75$. (d) The chimera state of the broken conserved quantities with $A = 0.86$. Insets of (c-d): Time evolution of $\mathbf{\Gamma}_1^{(1)}(t)$ (blue) and $\mathbf{\Gamma}_1^{(2)}(t)$ (red). (e) Snapshot of the oscillators with $N = 100$. Blue dot: synchronized oscillators $\boldsymbol{x}_j^{(2)}$. Red dots: incoherent oscillators $\boldsymbol{x}_j^{(1)}$. Blue curve: $\mathbf{\Gamma}^{(2)}(t)$. Red curve: $\mathbf{\Gamma}^{(1)}(t)$. (f) The histogram of the distribution of the phases $\left\{\arg\left(\frac{1}{|\boldsymbol{\psi}_1|}\boldsymbol{\psi}_1^\dagger \boldsymbol{x}_j^{(1)}\right)\right\}_{j=1}^N$ for $N = 500$ and $A = 0.35$. Red curve indicates the normalized Poisson kernel in Eq. (6.14). The presented results are based on data obtained after disregarding the initial transient behavior for $t > 10^4$.

6.1.3 Chimera States in Microscopic Dynamics

In this section, we investigate the microscopic dynamics of the system of generalized Kuramoto-Sakaguchi oscillators in two-population networks. Here, we directly perform numerical integrations of Eq. (6.1) for $\mathbb{C}^2$.

Figure 6.5 (a-d) displays the temporal evolution of the magnitude of the Kuramoto order parameter $|\mathbf{\Gamma}^{(a)}(t)|$, as defined in Eq.(6.3), for each population $a = 1, 2$. All the presented outcomes are obtained from random initial conditions of $\boldsymbol{x}_j^{(a)}(0)$, satisfying

$\left\langle \boldsymbol{x}^{(a)}j(0)\middle|\boldsymbol{x}^{(a)}j(0)\right\rangle = 1$ for $j = 1,...,N$ and $a = 1,2$. For a given value of $A \in (A_{\mathrm{LP}}, A_{\mathrm{HB}})$, i.e., in a region where stationary chimeras exist, the order parameter vector exhibits fluctuations, as we expect for finite-sized systems (Fig.6.5 (a)). Similarly, in Fig. 6.5 (b), the typical dynamics of breathing chimera states exhibit superposed fluctuations caused by finite-size effects when $A \in (A_{\mathrm{HB}}, A_{\mathrm{Hom}})$. Additionally, the microscopic dynamics reveals the occurrence of alternating chimeras (Fig. 6.5 (c)) for a given parameter $A \in (A_{\mathrm{Hom}}, A_c)$. The alternating chimera state exhibits alternating motion in both the magnitude and individual components of the order parameter vectors between the two populations (as depicted in the inset of Fig. 6.5 (c)). Notably, in the microscopic dynamics, we numerically verify that these three types of chimera states also possess conserved quantities along their trajectories in phase space. The quantities defined by

$$\begin{aligned} C_1(t) &:= \sin(\Theta_1(t) - \Theta_2(t)) \\ C_2(t) &:= \left(|m_1^{(1)}(t)||m_2^{(2)}(t)| - |m_2^{(2)}(t)||m_1^{(1)}(t)|\right)^2 \end{aligned} \tag{6.11}$$

remains always zero (not shown). Here, $\boldsymbol{\Gamma}^{(1)} = (m_1^{(1)}, m_2^{(1)})^\top \in \mathbb{C}^2$ and $\boldsymbol{\Gamma}^{(2)} = (m_1^{(2)}, m_2^{(2)})^\top \in \mathbb{C}^2$ are the Kuramto order parameters in Eq. (6.3), and $\Theta_i = \arg m_i^{(2)} - \arg m_i^{(1)}$ for $i = 1,2$. When the parameter A exceeds A_c, the chimera states undergo a breakdown of their conserved quantities. Figure 6.5 (d) depicts the time evolution of the order parameters for a chimera trajectory with a given parameter $A > A_c$. Clearly, the conserved quantities are no longer maintained (not shown here). Furthermore, the components of the order parameter vectors no longer exhibit alternation between the two populations but instead display aperiodic dynamics (as shown in the inset of Fig. 6.5 (d)). Therefore, our observation of chimera states in the thermodynamic limit can also be confirmed in ensembles of a finite number of oscillators. Figure 6.5 (e) shows a snapshot of 100 oscillators, corresponding to the stationary chimera state. The synchronized oscillators altogether (depicted as blue dots) exhibit identical behavior along the trajectory of the order parameter $\boldsymbol{\Gamma}^{(2)}(t)$ (represented by the blue curve). On the other hand, the incoherent oscillators (depicted as red dots) are dispersed, and their order parameter $\boldsymbol{\Gamma}^{(1)}(t)$ (indicated by the red curve) has a lower magnitude compared to $\boldsymbol{\Gamma}^{(2)}(t)$.

Finally, one can study the distribution of the incoherent oscillators along the direction of $\boldsymbol{\psi}_1$ as follows. In this context, we consider a stationary chimera state for a specific value of $A \in (A_{\mathrm{LP}}, A_{\mathrm{HB}})$, where the magnitude of $\boldsymbol{\psi}_1$ reaches a steady value after a transient behavior. To begin, let us introduce angular variables for the incoherent oscillators along the direction of the order parameter: $e^{i\varphi(t)} := \frac{1}{|\boldsymbol{\psi}_1|}\boldsymbol{\psi}_1^\dagger \boldsymbol{x}^{(1)}(t)$ and $e^{i\varphi_0} := \frac{1}{|\boldsymbol{\psi}_1|}\boldsymbol{\psi}_1^\dagger \boldsymbol{x}_0^{(1)}$ in the thermodynamic

limit. Using the generalized Watanabe-Strogatz transformation in Eq. (2.86), we obtain

$$e^{i\varphi} := \frac{1}{|\boldsymbol{\psi}_1|}\boldsymbol{\psi}_1^\dagger \boldsymbol{x}^{(1)} = \frac{1}{|\boldsymbol{\psi}_1|}\frac{\boldsymbol{\psi}_1^\dagger \boldsymbol{A}_1 \boldsymbol{x}_0^{(1)} + |\boldsymbol{\psi}_1|^2}{|\boldsymbol{\psi}_1| e^{i\varphi_0} + 1} \tag{6.12}$$

with $\boldsymbol{A} = \boldsymbol{H}^{1/2}\boldsymbol{U}$ and $\boldsymbol{H}^{1/2}\boldsymbol{\psi}_1 = \boldsymbol{\psi}_1$ where we can set $\boldsymbol{U} = I_M$ as long as $\boldsymbol{x}_0^{(1)}$ are uniformly distributed on $\mathbb{S}^M$. Algebraically rearranging Eq. (6.12), we obtain

$$e^{i\varphi_0} = \frac{e^{i\varphi} - |\boldsymbol{\psi}_1|}{1 - |\boldsymbol{\psi}_1| e^{i\varphi}}. \tag{6.13}$$

Denoting $\varphi = T(\varphi_0)$ and $\varphi_0 = T^{-1}(\varphi)$ (inverse transformation), it leads to $d(T_*\mu)(\varphi) = f(\varphi)d\varphi$ where $f(\varphi) := \frac{1}{2\pi}\partial_\varphi T^{-1}(\varphi)$ is the phase density function, and $d\mu(\varphi_0) = \frac{1}{2\pi}d\varphi_0$ since $\boldsymbol{x}_0^{(1)}$ are uniformly distributed on $\mathbb{S}^M$. Then, we obtain

$$\begin{aligned} f(\varphi) &= \frac{1}{2\pi}\partial_\varphi T^{-1}(\varphi) = \frac{1}{2\pi i}\left(\frac{ie^{i\varphi}}{e^{i\varphi} - |\boldsymbol{\psi}_1|} + \frac{i|\boldsymbol{\psi}_1| e^{i\varphi}}{1 - |\boldsymbol{\psi}_1| e^{i\varphi}}\right) \\ &= \frac{1}{2\pi}\frac{1 - |\boldsymbol{\psi}_1|^2}{1 - 2|\boldsymbol{\psi}_1|\cos\varphi + |\boldsymbol{\psi}_1|^2} \end{aligned} \tag{6.14}$$

which is the normalized Poisson kernel distribution. This is reminiscent of the Ott-Antonsen manifold, which applies to the usual Kuramoto-Sakaguchi oscillators on the unit circle in $\mathbb{C}^1$, where the phases of the oscillators follow the normalized Poisson kernel as described in Eq. (2.55). In the case of higher dimensions, such as $\mathbb{C}^2$, we observe that the oscillator distribution along the generalized WS variable also satisfies the normalized Poisson kernel. In Fig. 6.5 (f), the histogram of the distribution (represented by the blue bars) of $\varphi_j := \frac{1}{|\boldsymbol{\psi}_1|}\boldsymbol{\psi}_1^\dagger \boldsymbol{x} j^{(1)}\, j = 1^N$ is displayed for $N = 500$ and $A = 0.35$. The numerical results obtained from the finite-sized ensemble align well with the analytical prediction (illustrated by the red curve) given by Eq. (6.14).

6.2 Chimera Dynamics in Two-population Networks for $\mathbb{R}^4$

In this section, we investigate the system of identical generalized Kuramoto-Sakaguchi oscillators in two-population networks for $\mathbb{K} = \mathbb{R}$ in the thermodynamic limit as a comparison to Sec. 6.1. The WS variables $\boldsymbol{\psi}_a(t) \in \mathbb{R}^M$ are governed by

$$\partial_t \boldsymbol{\psi}_a = -\boldsymbol{\psi}_a \boldsymbol{H}_a^\dagger \boldsymbol{\psi}_a + \boldsymbol{H}_a = -\boldsymbol{\psi}_a \boldsymbol{H}_a^\top \boldsymbol{\psi}_a + \boldsymbol{H}_a \tag{6.15}$$

for $a = 1,2$ where $\dagger = \top$ (i.e., hermitian adjoint=transpose) for $\mathbb{K} = \mathbb{R}$. In this system, it is worth noting that the mean-field forcing is expected to differ. This is because the Kuramoto order parameter does not exactly coincide with the WS variable as described in Eq. (2.103). Instead, we use $\boldsymbol{\Gamma}^{(a)}(t) = h(|\boldsymbol{\psi}_a|^2, M)\boldsymbol{\psi}_a(t)$. Thus, we have to consider

$$\boldsymbol{H}_a := \mu \boldsymbol{K} h(|\boldsymbol{\psi}_a|^2, M)\boldsymbol{\psi}_a(t) + \nu \boldsymbol{K} h(|\boldsymbol{\psi}_b|^2, M)\boldsymbol{\psi}_b(t) \tag{6.16}$$

for $(a,b) = (1,2)$ or $(2,1)$. Here, the coupling matrix $\boldsymbol{K}$ is a suitable rotational matrix introduced in Sec. 2.5. In this section, we use the following notations: $\boldsymbol{\psi}_1 = (x_1, ..., x_M)^\top$ and $\boldsymbol{\psi}_2 = (y_1, ..., y_M)^\top$ where $x_i, y_i \in \mathbb{R}$ for $i = 1, ..., M$.

To gain an overview of the observable chimera states, our initial focus is on exploring the reduced dynamics, i.e., the dynamics of the magnitude of $\boldsymbol{\psi}_a$. Considering Eq. (6.15), we obtain

$$\begin{aligned}
\partial_t \rho_1 &= \frac{1-\rho_1^2}{\rho_1}\left(\mu h(\rho_1^2, M)\rho_1^2 \cos\alpha + \nu h(\rho_2^2, M)\xi\right) \\
\partial_t \rho_2 &= \frac{1-\rho_2^2}{\rho_2}\left(\mu h(\rho_2^2, M)\rho_2^2 \cos\alpha + \nu h(\rho_1^2, M)\left(\xi \cos 2\alpha + \sin 2\alpha \sqrt{\rho_1^2\rho_2^2 - \xi^2}\right)\right)
\end{aligned} \tag{6.17}$$

for the magnitude of the order parameter vectors and

$$\begin{aligned}
\partial_t \xi = {} & \mu h(\rho_1^2, M)\left(\xi(1-\rho_1^2)\cos\alpha + \sin\alpha\sqrt{\rho_1^2\rho_2^2 - \xi^2}\right) \\
& + \mu h(\rho_2^2, M)\left(\xi(1-\rho_2^2)\cos\alpha - \sin\alpha\sqrt{\rho_1^2\rho_2^2 - \xi^2}\right) \\
& + \nu h(\rho_1^2, M)\left((\rho_1^2 - \xi^2)\cos 2\alpha - \sin 2\alpha\sqrt{\rho_1^2\rho_2^2 - \xi^2}\right) + \nu h(\rho_2^2, M)(\rho_2^2 - \xi^2)
\end{aligned} \tag{6.18}$$

for the cross term. Here, $\rho_a := |\boldsymbol{\psi}_a|$ for $a = 1,2$ and $\xi := \langle \boldsymbol{\psi}_1 | \boldsymbol{K} | \boldsymbol{\psi}_2 \rangle$ indicates the cross term. Note that the behavior of the magnitude of $\boldsymbol{\psi}_a$ depends on the dimension M, cf. the complex space as in Eq. (6.7).

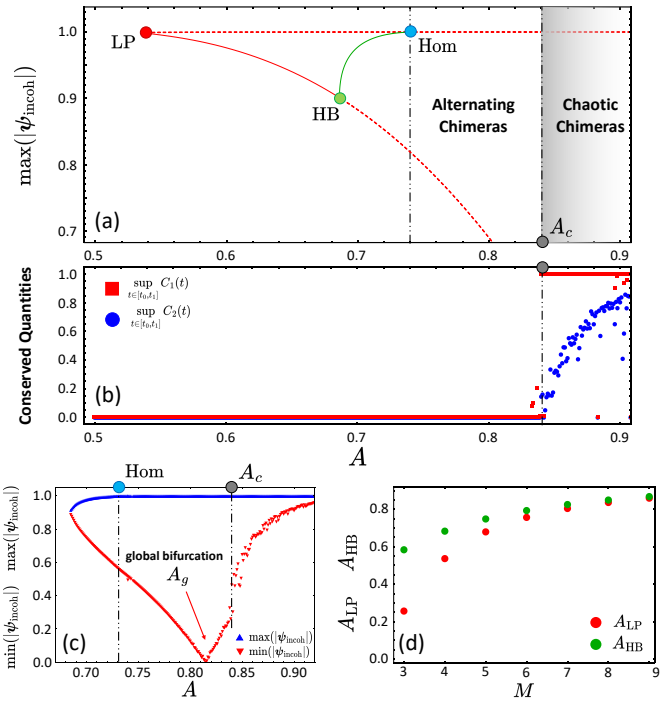

Fig. 6.6 (a) Bifurcation diagram of stable (solid curve) and unstable (dashed curve) chimera states in two-population networks. Red: stationary chimeras and Green: breathing chimera states. LP: limiting point bifurcation, HB: supercritical Hopf bifurcation, Hom: homoclinic bifurcation, and A_c from which on a chaotic chimera appears. (b) Conserved quantities as a function of the parameter A. $t_0 = 20,000$ and $t_1 = 10^5$. (c) Maximum and minimum values of the magnitude of the WS variable $\boldsymbol{\psi}_1$ as a function of the parameter A. All the results are obtained for $\mathbb{R}^4$. (d) Bifurcation points A_{LP} and A_{HB} as a function of the dimension M.

To obtain Eqs. (6.17-6.18), we consider

$$
\begin{aligned}
\partial_t|\boldsymbol{\psi}_1|^2 &= \partial_t(\boldsymbol{\psi}_1^\dagger\boldsymbol{\psi}_1)\\
&= -\mu h_1\left(\boldsymbol{\psi}_1^\dagger \boldsymbol{K}\boldsymbol{\psi}_1\boldsymbol{\psi}_1^\dagger - \boldsymbol{\psi}_1^\dagger\boldsymbol{K}^\dagger\right)\boldsymbol{\psi}_1 - \nu h_2\left(\boldsymbol{\psi}_1^\dagger\boldsymbol{K}\boldsymbol{\psi}_2\boldsymbol{\psi}_1^\dagger - \boldsymbol{\psi}_2^\dagger\boldsymbol{K}^\dagger\right)\boldsymbol{\psi}_1\\
&\quad -\mu h_1\boldsymbol{\psi}_1^\dagger\left(\boldsymbol{\psi}_1\boldsymbol{\psi}_1^\dagger\boldsymbol{K}^\dagger\boldsymbol{\psi}_1 - \boldsymbol{K}\boldsymbol{\psi}_1\right) - \nu h_2\boldsymbol{\psi}_1^\dagger\left(\boldsymbol{\psi}_1\boldsymbol{\psi}_2^\dagger\boldsymbol{K}^\dagger\boldsymbol{\psi}_1 - \boldsymbol{K}\boldsymbol{\psi}_2\right)\\
&= 2(1-|\boldsymbol{\psi}_1|^2)\left(\mu h_1\left\langle\boldsymbol{\psi}_1\middle|\frac{\boldsymbol{K}+\boldsymbol{K}^\dagger}{2}\middle|\boldsymbol{\psi}_1\right\rangle + \nu h_2\langle\boldsymbol{\psi}_1|\boldsymbol{K}|\boldsymbol{\psi}_2\rangle\right)\\
\partial_t|\boldsymbol{\psi}_2|^2 &= \partial_t(\boldsymbol{\psi}_2^\dagger\boldsymbol{\psi}_2)\\
&= 2(1-|\boldsymbol{\psi}_2|^2)\left(\mu h_2\left\langle\boldsymbol{\psi}_2\middle|\frac{\boldsymbol{K}+\boldsymbol{K}^\dagger}{2}\middle|\boldsymbol{\psi}_2\right\rangle + \nu h_1\left\langle\boldsymbol{\psi}_1\middle|\boldsymbol{K}^\dagger\middle|\boldsymbol{\psi}_2\right\rangle\right)\\
\partial_t\langle\boldsymbol{\psi}_1|\boldsymbol{K}|\boldsymbol{\psi}_2\rangle &= -\mu h_2\left(|\boldsymbol{\psi}_1|^2\cos\alpha\langle\boldsymbol{\psi}_1|\boldsymbol{K}|\boldsymbol{\psi}_2\rangle - \langle\boldsymbol{\psi}_1|\boldsymbol{\psi}_2\rangle\right) - \nu h_2\left(\langle\boldsymbol{\psi}_1|\boldsymbol{K}|\boldsymbol{\psi}_2\rangle^2 - |\boldsymbol{\psi}_2|^2\right)\\
&\quad -\mu h_2\left(|\boldsymbol{\psi}_2|^2\cos\alpha\langle\boldsymbol{\psi}_1|\boldsymbol{K}|\boldsymbol{\psi}_2\rangle - \left\langle\boldsymbol{\psi}_1\middle|\boldsymbol{K}^2\middle|\boldsymbol{\psi}_2\right\rangle\right)\\
&\quad -\nu h_1\left(\langle\boldsymbol{\psi}_1|\boldsymbol{K}|\boldsymbol{\psi}_2\rangle\left\langle\boldsymbol{\psi}_1\middle|\boldsymbol{K}^\dagger\middle|\boldsymbol{\psi}_2\right\rangle - |\boldsymbol{\psi}_1|^2\cos 2\alpha\right)
\end{aligned}
\tag{6.19}
$$

where $h_a := h(|\boldsymbol{\psi}_a|^2, M)$ for $a = 1,2$. Then, we consider the cross term with the coupling matrix as a variable, i.e., $\xi := \langle \boldsymbol{\psi}_1 | \bar{\boldsymbol{K}} | \boldsymbol{\psi}_2 \rangle = |\boldsymbol{\psi}_1||\boldsymbol{\psi}_2| \cos\theta$ which leads to

$$\begin{aligned}
\langle \boldsymbol{\psi}_1 | \boldsymbol{\psi}_2 \rangle &= |\boldsymbol{\psi}_1||\boldsymbol{\psi}_2| \cos(\theta - \alpha) = \xi \cos\alpha + \sin\alpha \sqrt{|\boldsymbol{\psi}_1|^2 |\boldsymbol{\psi}_2|^2 - \xi^2} \\
\left\langle \boldsymbol{\psi}_1 \middle| \boldsymbol{K}^\dagger \middle| \boldsymbol{\psi}_2 \right\rangle &= |\boldsymbol{\psi}_1||\boldsymbol{\psi}_2| \cos(\theta - 2\alpha) = \cos 2\alpha \xi + \sin 2\alpha \sqrt{|\boldsymbol{\psi}_1|^2 |\boldsymbol{\psi}_2|^2 - \xi^2} \\
\langle \boldsymbol{\psi}_1 | \boldsymbol{K}^2 | \boldsymbol{\psi}_2 \rangle &= |\boldsymbol{\psi}_1||\boldsymbol{\psi}_2| \cos(\theta + \alpha) = \cos\alpha \xi - \sin\alpha \sqrt{|\boldsymbol{\psi}_1|^2 |\boldsymbol{\psi}_2|^2 - \xi^2}.
\end{aligned} \tag{6.20}$$

Note that for even M, we can easily find $\left\langle \boldsymbol{\psi}_a \middle| \frac{\boldsymbol{K}+\boldsymbol{K}^\dagger}{2} \middle| \boldsymbol{\psi}_a \right\rangle = \cos\alpha |\boldsymbol{\psi}_a|^2$. However, for odd M, we find that chimera states only live in the $M^\perp$-plane. Hence, we assume $\left\langle \boldsymbol{\psi}_a \middle| \frac{\boldsymbol{K}+\boldsymbol{K}^\dagger}{2} \middle| \boldsymbol{\psi}_a \right\rangle = \cos\alpha |\boldsymbol{\psi}_a|^2$ for $a = 1,2$. Finally, plugging Eq. (6.20) into Eq. (6.19), we obtain Eqs. (6.17-6.18) in Sec. 6.2.

Here, we only focus on the dynamics for $\mathbb{R}^4$ unless stated otherwise. A bifurcation diagram from Eqs. (6.17-6.18) is depicted in Fig. 6.6 (a), assuming $\rho_2 = 1$. Similar to Fig. 6.4 (a), stable (red, solid) and unstable (red, dashed) chimeras are created in a saddle-node (LP) bifurcation, however, at a rather large value of A_{LP} compared to the case of $\mathbb{C}^2$. Likewise, the stable stationary chimera state undergoes a supercritical Hopf bifurcation at which a stable limit-cycle solution, i.e., a breathing chimera state (green, solid) emerges. Increasing A, the breathing chimera disappears in a homoclinic bifurcation as its period is soaring up. Moreover, we also observe periodic alternating chimera states in the full component-dynamics from numerical integrations of Eq. (6.15). For a given $A \in (A_{\mathrm{Hom}}, A_c)$, a periodic alternating chimera state is found, which also apparently satisfies $\boldsymbol{\psi}_1(t) = \boldsymbol{\psi}_2(t - \frac{T}{2})$ and $x_i(t) = y_i(t - \frac{T}{2})$ for $i = 1,\ldots,4$ where T is the period. We also find two conserved quantities along the trajectory of the stationary, breathing, and periodic alternating chimera states, as we did so for the complex spaces. The conserved quantities are here defined as follows. First, we define angular variables $\theta_1 := \tan^{-1}\frac{x_2}{x_1}$, $\theta_2 := \tan^{-1}\frac{x_4}{x_3}$, $\phi_1 := \tan^{-1}\frac{y_2}{y_1}$, $\phi_2 := \tan^{-1}\frac{x_4}{x_3}$. Then, instead of using the unitary transformation, we here notice that Equation (6.15) is equivariant under a rotational transformation

$$Q := \begin{pmatrix} R(-\theta_1) & \mathbf{0} \\ \mathbf{0} & R(-\theta_2) \end{pmatrix} \quad \text{where} \quad R(\theta) = \begin{pmatrix} \cos\theta & \sin\theta \\ -\sin\theta & \cos\theta \end{pmatrix} \tag{6.21}$$

and $Q \in \mathbb{R}^{4\times4}$, $R(\theta) \in \mathbb{R}^{2\times2}$, and $\mathbf{0} \in \mathbb{R}^{2\times2}$ is the zero-matrix. Therefore, the phase differences are defined as $\Theta_1 := \phi_1 - \theta_1$ and $\Theta_2 := \phi_2 - \theta_2$. The first conserved quantity is written

by

$$C_1 := \sin\left(\Theta_1 - \Theta_2\right) \tag{6.22}$$

and $C_1(t) = 0$ for all t along the chimera trajectory for $A < A_c$. The second conserved quantity reads

$$C_2 := \sum_{k=1}^{4} x_k^2 \sum_{k=1}^{4} y_k^2 - \left(\sqrt{x_1^2+x_2^2}\sqrt{y_1^2+y_2^2} + \sqrt{x_3^2+x_4^2}\sqrt{y_3^2+y_4^2}\right)^2 \tag{6.23}$$

which arises from the relation

$$\langle \boldsymbol{\psi}_1 | \boldsymbol{\psi}_2 \rangle = |\boldsymbol{\psi}_1||\boldsymbol{\psi}_2| \cos\Theta = \sqrt{x_1^2+x_2^2}\sqrt{y_1^2+y_2^2}\cos\Theta + \sqrt{x_3^2+x_4^2}\sqrt{y_3^2+y_4^2}\cos\Theta \tag{6.24}$$

where $\Theta := \Theta_1 = \Theta_2$ since $C_1 = 0$. To show how the aperiodic dynamics occurs, we also measure $\sup_{t\in[t_0,t_1]} C_1(t)$ and $\sup_{t\in[t_0,t_1]} C_1(t)$ as a function of the parameter A with $t_0 = 2\times 10^4$ and $t_1 = 10^5$. Figure 6.6 (b) shows that these two quantities conserve a value of zero along the chimera trajectory for $A < A_c$. Moreover, they are broken along a chimera trajectory for $A > A_c$ (Fig. 6.6 (b)). For $A > A_c$, a chimera state shows componentwise aperiodic motion of the WS variables, similar to the ones in $\mathbb{C}^2$ shown in Fig. 6.3.

A global bifurcation involving the completely incoherent state also occurs for the real spaces. However, this global bifurcation is observed for the periodic alternating chimera state for $A > A_{\mathrm{Hom}}$ rather than the breathing chimeras. In Fig. 6.6 (c), the maximum and the minimum values of $|\boldsymbol{\psi}_{\mathrm{incoh}}|$ are shown versus the parameter A. With increasing A, the breathing chimera state exhibits a continuous decrease in $\min|\boldsymbol{\psi}_{\mathrm{incoh}}|$, eventually seamlessly connecting to that of the periodic alternating chimera state for $A > A_{\mathrm{Hom}}$. These chimera states are characterized by the phase variable $\Theta(t)$ evolving within a smaller interval than $\mathbb{T}$ (libration), similar to the behavior depicted in Fig.6.4 (d-1). As A is further increased, the alternating chimera state touches the completely incoherent state, and its phase variable monotonically increases with time (rotation), analogous to the scenario shown in Fig.6.4 (d-2).

Finally, we note that the chimera dynamics in terms of the WS variables depends on the dimension M of the real space. For small A, the emergence of the chimera states in low-dimensional real spaces follows the scenario that the stationary chimera state is born/annihilated in a saddle-node bifurcation (A_{LP}) which undergoes a supercritical Hopf bifurcation at $A = A_{\mathrm{HB}}$. However, Figure 6.6 (d) shows that the length of the parameter interval $(A_{\mathrm{LP}}, A_{\mathrm{HB}})$ decreases as M increases. This observation suggests that obtaining stationary chimera states becomes more challenging in higher-dimensional real spaces.

Moreover, it is difficult to observe other types of chimera states within our numerical capabilities in higher-dimensional real spaces.

6.3 Summary

In this chapter, we explored a system comprised of identical higher-dimensional Kuramoto-Sakaguchi oscillators situated on the surface of the unit sphere within two-population networks. First, we introduced a suitable coupling matrix for both the real and complex spaces, analogous to the phase-lag parameter for the conventional KS model on the unit circle. This parameter assumes significance in determining the Benjamin-Feir instability.

For the 2D complex space $\mathbb{C}^2$, particularly in the context of the thermodynamic limit, we observed the emergence and annihilation of stationary chimeras at a saddle-node bifurcation. The stable chimera states undergo a supercritical Hopf bifurcation, giving rise to stable breathing chimera states. Notably, these breathing chimera states underwent a global bifurcation involving the completely incoherent state, leading to a shift from libration to rotation in their phase variable dynamics. Then, the breathing chimera states encounter a homoclinic bifurcation, after which we observe a periodic alternating chimera dynamics. It is important to highlight that all three varieties of chimera states presented above were characterized by two conserved quantities throughout their phase space trajectories. However, a further reduction in coupling strength resulted in the breaking of these conserved quantities, leading to componentwise aperiodic dynamics within the chimera trajectory. This scenario of the emergence of chimera states in the thermodynamic limit can be substantiated by studying a finite-sized ensemble of identical generalized KS oscillators in two populations on $\mathbb{C}^2$.

Finally, we proceeded to compare the results from $\mathbb{C}^2$ with the dynamics exhibited in $\mathbb{R}^4$ within the thermodynamic limit. Remarkably, chimera states within the real space followed a similar scenario, encompassing stationary and breathing chimeras, the presence of conserved quantities, and ultimately, the breaking of these conserved quantities to become componentwise aperiodic chimera dynamics. Notably, in this context, the global bifurcation manifested within the realm of alternating chimera states rather than simple breathing chimera states.

Chapter 7

Conclusion

As we discussed earlier in the thesis, many natural phenomena cannot be explained, unlike the doctrine of reductionism, in terms of a simple extrapolation of the properties of the building blocks, which constitute the complex system. Thus, understanding the complex system necessarily requires us to investigate collective behavior described in terms of the macroscopic observable, as well as the properties of individual building blocks. In this thesis, we focused on the collective/emergent phenomena in a system of coupled Kuramoto-Sakaguchi oscillators, with a particular focus on *coexistence dynamics* of coherence and incoherence. This coexistence pattern is called a *chimera state* and is simultaneously composed of a coherently oscillating part and an incoherently oscillating part, and constitutes a symmetry broken state. We studied the dynamical and spectral properties of chimera states in *a network of networks*, where a system consists of more than one interacting population in each of which there are numerous Kuramoto-Sakaguchi oscillators. In these systems, the chimera state emerges through the breaking of the permutation symmetries of populations in a given topology, i.e., elements of the automorphism group of the graph. We know that the chimera states are not only just theoretically interesting concepts but also appear in many natural phenomena and in man-made systems [165, 166, 196–202].

In this thesis, we theoretically and numerically elucidate some interesting and important properties of chimera states. To do so, we first started in Chap. 2 with discussions about the theoretical principles by which one can investigate dynamical and spectral properties of chimera patterns as collective behavior in a network of networks. Therein, we studied how to construct an ensemble of Kuramoto-Sakaguchi phase oscillators, starting from a single oscillator as a building block of the system. Next, we revisited dimension reduction methods of sinusoidally coupled systems, which allows for the description of the system's macroscopic dynamics in terms of a few dynamical variables, for both standard and higher-dimensional Kuramoto oscillator ensembles. Moreover, we reviewed Lyapunov stability analysis which

has been exploited throughout the thesis in order to investigate spectral properties of chimera states.

For the exploration of chimera states, we considered two aspects in this thesis: (a) How the complexity of the network topology, i.e., topology of a network of networks, affects observable chimera dynamics and (b) how the macroscopic dynamics of chimera states behaves, i.e., the dynamics of the Kuramoto order parameter. In Chap. 3, we investigated a system of identical Kuramoto-Sakaguchi oscillators in *two-population networks*, as the first example of *a network of networks*. This network topology can be considered the simplest network where one can explore chimera dynamics of coupled oscillators. In this system, chimera states consist of one synchronized population, where the modulus of the Kuramoto order parameter is unity, and one other incoherent population where the modulus of the Kuramoto order parameter is less than unity, showing various dynamics depending on a given parameter. This system exhibits the simplest chimera dynamics in the Ott-Antonsen manifold and in a finite-sized system with uniform constants of motion, i.e., with a PIC. Such simplest chimeras appear as an equilibrium solution in terms of its Kuramoto order parameter in the OA manifold, i.e., a stationary chimera state, while it accompanies a regular, secondary oscillation superimposed to the OA solution for the finite-sized ensembles. We also observed a breathing chimera state in the simplest form as a stable limit-cycle solution of the OA equation and also in a finite-sized ensemble with uniform constants of motion or PICs after a supercritical Hopf bifurcation. On the other hand, we further supported that outside the OA manifold or with n-PICs, chimera states show an irregular dynamics of the Kuramoto order parameter that cannot be understood in terms of the OA dynamics. Moreover, we explained how such irregular dynamics appears in terms of Lyapunov stability analysis. It is due to many neutrally stable directions arising from constants of motion of the dynamics and we confirmed it by investigating Lyapunov exponents and covariant Lyapunov vectors. Finally, we studied how the complexity of topology in two-population networks and how higher-dimensional complexity, namely, amplitude oscillators, influences the chimera dynamics by considering nonlocal intra-population topology and a system of Stuart-Landau oscillators, respectively. Both cases render the chimera states attracting in phase space.

Next, for the second example of *a network of networks*, we increased the complexity of the network topology, i.e., we considered a system of identical Kuramoto-Sakaguchi oscillators in *three-population networks* in Chapt. 4. In this system, we observed symmetric chimera states, namely, SDS and DSD chimeras where two populations behave identically in terms of their order parameter dynamics. The symmetric chimera states appear in various forms of Kuramoto order parameter dynamics such as stationary and breathing chimeras, depending on a parameter set. Furthermore, the three-population network of KS oscillators

can show a symmetry-broken chimera state in a form of DSD′ in full-dimensional phase space. The symmetry-broken chimera states arise from the transverse perturbations to the symmetric DSD-chimeras wherein the two D-populations move in opposite directions and are characterized by a periodic alternation of the two Kuramoto order parameters for the two incoherent populations. However, when we consider the system outside the OA manifold using nonuniform constants of motion or n-PICs, the symmetry-broken chimera states constitute a chaotic attractor where the Kuramoto order parameter dynamics shows aperiodic motion. Moreover, we found that the chaotic chimera attractor coexists with a periodic DSD′ chimera state and a stationary SDS chimera state in phase space. Consequently, the simple transition from two- to three-population networks results in an enriched Kuramoto order parameter dynamics. In particular, symmetry-broken chimeras emerge from the breaking of the cyclic permutations of the populations via transverse perturbations. Hence, we can expect that the more complex the topology is, the richer the Kuramoto order parameter dynamics can be. If such a simple transition from two- to three-population networks brings forth various chimera dynamics concerning its Kuramto order parameter, how much more diverse can the dynamics become in more complex topologies of networks?

In Chap. 5, we further increased the complexity of the network topology to *a ring of six oscillator populations*. This complex network topology gives rise to a rather different chimera dynamics, namely, a heteroclinic switching between saddle chimera states. The observable saddle chimera states are characterized by one incoherent and five synchronized populations and found to be unstable by linear stability analysis. However, they can form a heteroclinic cycle in phase space due to cyclic permutation symmetries of the ring of six populations and their stable/unstable manifold structure. The heteroclinic switching dynamics shows stationary and breathing chimera dynamics inside the OA manifold as well as quasiperiodic motions of the Kuramoto order parameter for the incoherent population outside the OA manifold. The saddle chimera states emerge from the breaking of the cyclic permutations of the populations in a ring while the heteroclinic switching dynamics restores the broken symmetry in terms of the long-term dynamics. The robust presence of heteroclinic cycles displaying diverse Kuramoto order parameter dynamics stands out distinctly when compared to the dynamics observed in alternative network topologies. In scenarios involving 3, 4, 5, 7, and 8 populations arranged in a ring, we did not detect any instances of switching dynamics between chimera states initiated from random initial conditions. The reason why others do not exhibit the switching dynamics of chimera states is now unclear and can be further investigated in the future. Thus, one could say that the ring of six oscillator populations has not only more symmetries than two- or three-population networks but also has an appropriate symmetry that can bring forth the switching chimera dynamics. Thus, we learned that not

only the complexity of the topology but also an appropriate symmetry of the topology is of great importance when it comes to the Kuramoto order parameter dynamics of the chimera states in a network of networks.

Finally, in Chap. 6, we considered a system of higher-dimensional Kuramoto-Sakaguchi oscillators in two-population networks. In this chapter, we studied how the higher-dimensional complexity affects the chimera dynamics, not the complexity of its topology. Note that in Chap. 3, we considered a system of Stuart-Landau oscillators in two-population networks as another higher-dimensional complexity. We demonstrated here that not only the topological complexity but also the higher-dimensional complexity of the oscillator ensembles gives rise to more complex motions of order parameter dynamics. Due to the higher-dimensional nature of the Kuramoto order parameter vectors, we observed a periodic alternation of magnitudes of the Kuramoto order parameter vectors, and they also show componentwise aperiodic dynamics by the breaking of the conserved quantities.

In this thesis, we thoroughly explored the coexistence dynamics of a system of identical Kuratmo-Sakaguchi oscillators, considering various network topologies and higher-dimensional complexities. In a network of networks, chimera states emerge via the breaking of permutation symmetries of the populations in a given topology. Note that the chimera states were originally observed in a ring geometry, arising from the breaking of the translational invariance. Thus, introducing more complex network topology gives rise to various complex chimera motions in terms of the Kuramoto order parameter for the incoherent populations. Starting from two-population networks, we visited three-population networks that exhibit symmetric and symmetry-broken chimera states, and move further to a ring of six oscillator populations where the heteroclinic switching chimera dynamics can be detected due to cyclic permutations of populations in a ring. Thus, we studied various chimera patterns whose order parameter dynamics is dominated by network symmetry, and explored how such network topology affects the observable chimera patterns as macroscopic dynamics.

Such studies enhanced our understanding of chimera dynamics and can lead us to a variety of future explorations for coexistence dynamics of coherence and incoherence in physics, biology, chemical oscillations, and even to engineering systems. Nowadays, investigations of chimera states become of great importance in many interdisciplinary fields. For example, scientists, mathematicians, and engineers gathered at the workshop named *Chimera States: From theory and experiments to technology and living systems* and discussed/shared their impressive studies of chimera patterns [203]. As implied by the workshop's title, delving into chimera states can pave the way for insights and practical applications related to the collective and emergent behaviors of coupled oscillators in various fields, including living systems, technology, and experimental and theoretical research. Particularly, it does not stop

at a theoretical/mathematical play but rather it goes further to understandings of emergent behaviors in nature and man-made systems. Therefore, as the next step, it is possible to explore numerous real-world phenomena that demonstrate the coexistence of incoherent and coherent oscillations such as unihemispheric sleep, onset of epileptic seizure, symmetry-breaking cluster patterns in a complex network, coexistence patterns in neural networks, chemical oscillation or quantum-mechanical systems, as introduced in Ref. [203], and their fundamental characteristics by leveraging the dynamics and the properties of chimera states as discussed throughout this thesis.

Appendix A

Collective Dynamics I: Nontrivial Twisted States

In this thesis, our main concerns are chimera states in a network of networks where each network consists of globally coupled identical oscillators. In all-to-all coupling or a system on a network topology, there is no spatial information but rather they are coupled via a topology defined by $G_{ij} = \frac{1}{L}$ and a given adjacency matrix $G_{ij} = A_{ij}$, respectively. On the other hand, for Eq. (2.9), another situation can be considered to introduce a geometrical coupling scheme. To give a concrete example, we here discuss a system of (spatially) nonlocally coupled Stuart-Landau oscillators on a ring geometry. In this system, the oscillators, geometrically arranged on a ring, show collective dynamics in the form of a spatiotemporal pattern. The coupling function is given by a nonconstant, piece-wise smooth function $G_{jk} = G(x_j - x_k)$ where $x_j = \frac{L(j-1)}{N-1}$ for $j = 1,...,N$. Moreover, it has been observed that the system of nonlocally coupled oscillators can also exhibit chimera states with various coupling functions [54, 66, 67, 71, 170]. In fact, the chimera states were originally observed in such a system [53].

In a ring of nonlocally coupled oscillators, there exists a significant form of collective dynamics called a twisted state [118, 204, 171, 205, 206]. The 'traditional' twisted state, which we call a *trivial twisted state* (TTS), is characterized by the fact that the phase difference between adjacent oscillators is always the same along the ring. The phase distribution gains an integer multiple of 2π when it is traced along the ring. This means the phase profile satisfies $\phi(x,t) = \frac{2\pi q}{L}x + \Omega t$ where Ω is a collective frequency and L is the length of the medium. The phase gradient is everywhere constant, given by $\partial_x \phi(x,t) = \frac{2\pi q}{L}$ with a winding number

The contents of this section are written by revisiting S. Lee and K. Krischer, Phys. Rev. E **106**, 044210 (2022) [121]. All figures and captions are reproduced directly from it.

$q \in \mathbb{Z}$ where $\partial_x := \frac{\partial}{\partial x}$. For the TTS, the amplitude variables are distributed homogeneously on the ring, which then follows $r(x,t) = r_0 \approx 1$ for all $x \in [0,L] =: \mathbb{D}$. Hence, the TTS can be studied in the phase-reduced model as we discussed in Sec. 2.2.

In this Appendix, we explore another type of twisted states in a ring of nonlocally coupled oscillators. It is called a *nontrivial twisted state* (NTS) [121], compared to the *trivial twisted state* (TTS) characterized above. What looks different is that the NTS is characterized by a non-constant gradient of the phase profile, that is, $\partial_x \phi(x,t) \neq$ const. and an inhomogeneous amplitude profile $r(x,t) \neq$ const. for all $x \in \mathbb{D}$. Due to the inhomogeneous amplitude profile, the NTS cannot be treated in the framework of the phase model as introduced in Sec. 2.2. Hence, we need to study the Stuart-Landau oscillators themselves. Furthermore, the NTS solution occurs as a coherent traveling wave of the system [60], with a fixed shape and a constant speed. Nevertheless, we can define a winding number for the NTS since the phase still advances by a multiple of 2π as going once around the ring. A similar observation to the NTS was reported in Ref. [207].

A.1 Nontrivial Twisted State

A.1.1 Governing Equation and Observable Collective Dynamics

To observe an NTS, we consider a system of nonlocally coupled, identical Stuart-Landau oscillators along a 1D ring of length $|\mathbb{D}| = L$. The building block of this system is represented by a complex-valued dynamical oscillator $W(x,t) = r(x,t)e^{i\phi(x,t)} \in \mathbb{C}$ for $x \in \mathbb{D}$. The oscillator field is governed by

$$\begin{aligned}\frac{\partial}{\partial t}W(x,t) &= \mathscr{F}(W(x,t)) + \varepsilon e^{-i\alpha(H(x,t))}H(x,t) \\ &= (1+i\omega)W(x,t) - |W(x,t)|^2 W(x,t) + \varepsilon e^{-i\alpha(H(x,t))}\int_0^L G(x-x')W(x',t)dx'\end{aligned} \tag{A.1}$$

with periodic boundary condition, i.e., $W(0,t) = W(L,t)$ for all t. The (uncoupled) local dynamics of a building block is given by a Stuart-Landau oscillator $\mathscr{F}(W) = (1+i\omega)W - |W|^2 W$ [69, 68, 65]. Note that Eq. (A.1) can be obtained from Eq. (2.7) with an appropriate set of parameters. Here, the phase-lag is not just a constant but rather the nonlinear phase-lag function is assumed to be $\alpha(H(x,t)) = \alpha_0 + \alpha_1 |H(x,t)|^2$ with real parameters α_0, $\alpha_1 \in \mathbb{R}$. The coupling strength is denoted by $\varepsilon \in \mathbb{R}$ and the natural frequency of the identical oscillators is set to $\omega = 0$.

Now, we are ready to specify a nonlocal coupling function $G(y)$ for $|y| < L/2$. To do so, we first assume that an oscillator located at $x \in \mathbb{D}$ is nonlocally influenced by the forcing field $H(x,t)$. Also, the forcing field is assumed to be governed by an auxiliary equation that reads [63, 208, 209]

$$\tau \frac{\partial}{\partial t} H(x,t) = \frac{1}{\kappa^2} \frac{\partial^2}{\partial x^2} H(x,t) - H(x,t) + W(x,t) \tag{A.2}$$

which characterizes the nonlocal coupling feature of the system. The parameter $\kappa^{-1} \in \mathbb{R}$ determines the interaction range with the dimension of length while the parameter τ indicates the characteristic time scale of the forcing field $H(x,t)$ in the auxiliary equation. In the limit of $\tau \to 0$, the forcing field then satisfies an inhomogenous Helmholtz equation with the periodic boundary condition, $H(0,t) = H(L,t)$ and $\partial_x H(0,t) = \partial_x H(L,t)$ such that

$$\frac{\partial^2}{\partial x^2} H(x,t) - \kappa^2 H(x,t) = -\kappa^2 W(x,t). \tag{A.3}$$

This gives the nonlocal coupling function $G(y)$ as the Green's function of it, i.e.,

$$G(y) = \frac{\kappa}{2\sinh(\kappa L/2)} \cosh\Big(\kappa(|y| - L/2) \Big) \tag{A.4}$$

for $|y| \leq L/2$ so that the normalization condition $\int_{-L/2}^{L/2} G(y)dy = 1$ holds. Finally, the forcing field can be rewritten as an integral convolution operator which reads

$$H(x,t) = (\mathscr{G}W)(x,t) := \int_0^L G(x-x')W(x',t)dx'. \tag{A.5}$$

Note that κ^{-1} characterizes the length of the medium. In the limit of $\kappa L \to \infty$, the coupling kernel becomes $G(x) = \kappa e^{-\kappa|x|}/2$, as used in [53]. In the following (up to Sec. A.3), we use the following parameter values: $\varepsilon = 1$, $\kappa = 4.874$, $L = 1$, $\alpha_0 = -0.4\pi$ and $\alpha_1 = -(\pi/2 + \alpha_0)/0.36$. In this setup, the coupling strength ε cannot be considered small, which would justify the use of the phase-reduced model. Hence, not only the phase variables but also the amplitude variables may display nontrivial dynamics.

For the exploration of the NTS, we consider the microscopic dynamics of the finite-size approximation with $N = 200$ oscillators. The discrete system of nonlocally coupled Stuart-Landau oscillators is governed by

$$\partial_t \phi_j(t) = \omega + \frac{\varepsilon}{r_j} \mathrm{Im}\left[H_j(t) e^{-i\phi_j} e^{-i\alpha(H_j(t))} \right] \tag{A.6}$$

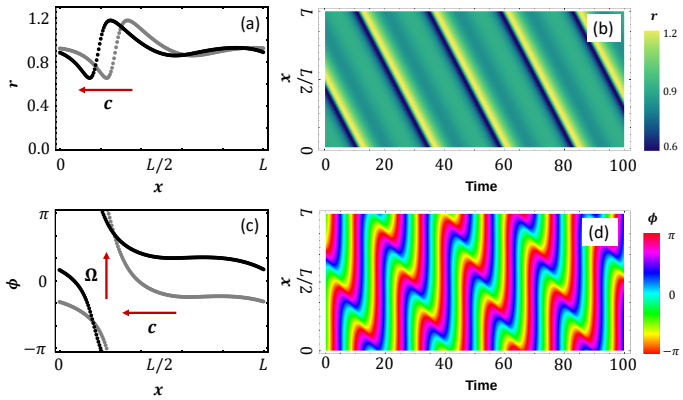

Fig. A.1 Nontrivial twisted state dynamics obtained from a random initial condition. (a) Amplitude profiles at $t = 10^4$ (gray) and $t+2$ (black), (b) spatio-temporal evolution of the amplitude ($t \geq 10^5$), (c) phase profiles at $t = 10^4$ (gray) and $t+2$ (black), (d) spatio-temporal evolution of the phase ($t \geq 10^5$). Other parameter values: $\varepsilon = 1$, $\kappa = 4.874$, $L = 1$, $\alpha_0 = -0.4\pi$ and $\alpha_1 = -(\pi/2 + \alpha_0)/0.36$.

and

$$\partial_t r_j(t) = r_j - r_j^3 + \varepsilon \mathrm{Re}\left[H_j(t) e^{-i\phi_j} e^{-i\alpha(H_j(t))}\right] \tag{A.7}$$

where $r_j(t)e^{i\phi_j(t)} = W(x_j,t)$ and $H_j(t) = H(x_j,t)$ for $x_j = \frac{L(j-1)}{N-1}$ for $j = 1,2,\ldots,N$.

In Fig. A.1, an example of observed nontrivial twisted states is depicted: the amplitude dynamics $r_j(t)$ (a,b) and the phase dynamics $\phi_j(t)$ (c,d) are shown, respectively. First, the amplitude profile forms a smooth time-dependent curve as a function of the spatial variable $x \in \mathbb{D}$ for a fixed t while it travels along the ring with that shape fixed and a constant speed, i.e., it constitues a traveling wave solution. Second, the phase snapshots in Fig. A.1 (c) show that the phase profile is also smooth along the ring for a fixed t. Moreover, the phases of the oscillators are uniformly rotating with a common collective frequency Ω as well as traveling with the lateral speed c (Fig. A.1 (c,d)). In a rotating reference frame, an NTS appears as a traveling wave solution due to the phase shift-invariance of the system. Note that the phase profile does not have a constant-valued gradient as a function of x but rather we find $\partial_x \phi(x,t) \neq$ const., which makes an NTS different from a TTS. In spite of this, we can define the winding number of the phase distribution as follows. The phase difference modulo 2π in the interval $[-\pi,\pi)$ is written as $\Delta_{i,j} := \phi_i - \phi_j$ with $\phi_{N+1} \equiv \phi_1$. Then, it follows that we can define the winding number as

$$q = \frac{1}{2\pi} \sum_{j=1}^{N} \Delta_{j+1,j} \in \mathbb{Z}. \tag{A.8}$$

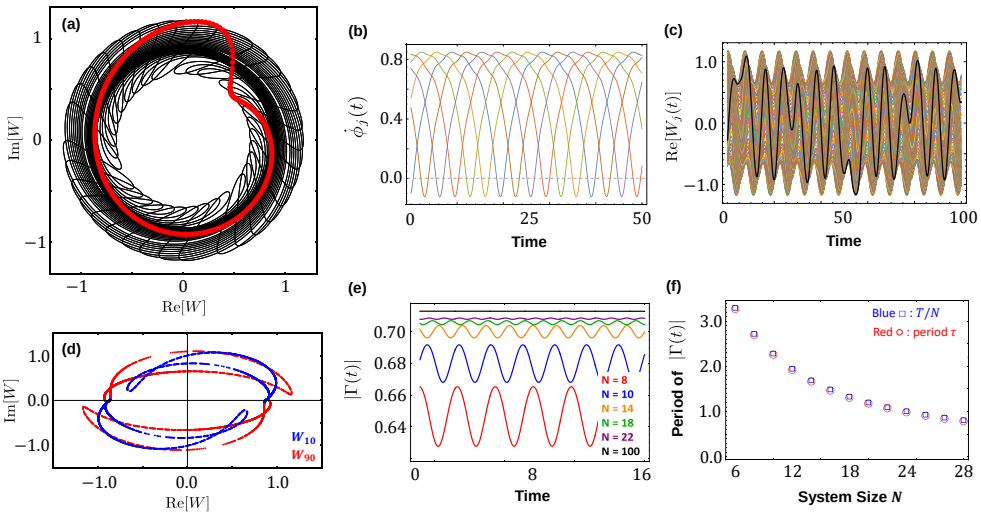

Fig. A.2 (a) Red curve: Snapshot of the amplitude profile of an NTS on the ring, i.e., $r(\frac{2\pi}{L}x)\cos(\frac{2\pi}{L}x)$ vs. $r(\frac{2\pi}{L}x)\sin(\frac{2\pi}{L}x)$ for $x \in [0,L]$ and $N = 200$; black line: trajectory of the first oscillator in the complex plane: $\mathrm{Re}[W_1(t)]$ vs. $\mathrm{Im}[W_1(t)]$); (b) Instantaneous phase velocity of the individual oscillators as a function of time for $N = 6$. (c) Time evolution of $\mathrm{Re}[W(t)]$ for $N = 200$. The black line highlights the time series of one of the oscillators. (d) Poincaré map of W_{10} (blue, dark gray) and W_{90} (red, light gray) in the complex plane where the Poincaré section is defined by $\phi_1(t) \equiv 0 \pmod{2\pi}$. (e) Modulus of the global Kuramoto order parameter as a function of time for different system sizes N (increasing from bottom to top). All numerical values shown for $t \geq 10^4$. (f) Period of the modulus of the global Kuramoto order parameter as a function of the system size N. The numerically obtained value (red circle) coincides with T/N (blue square).

Depending on an initial condition, we can numerically obtain $q = \pm 1$ for a nontrivial twisted state with $\Delta_{j+1,j} \neq \text{const}$ at this parameter set. For example, in Fig. A.1, $q = -1$.

The NTS is not just a traveling wave solution but it is a *coherent traveling wave*. The coherent traveling wave is defined as a traveling wave solution that exhibits locally coherent phases everywhere [60]. To see this, we introduce the local order parameter $z(x,t)$ for the NTS as a function of x. The local order parameter characterizes the degree of coherence of oscillator phases in a small neighborhood of a given $x \in \mathbb{D}$, which is defined by [71, 210]

$$z(x,t) = \lim_{N\to\infty} \frac{1}{|B_\delta^N(x)|} \sum_{j\in B_\delta^N(x)} e^{i\phi_j(t)} \tag{A.9}$$

with $B_\delta^N(x) = \{j : 1 \leq j \leq N, |x - x_j| < \delta\}$ for small enough $0 < \delta \ll 1$. Equation (A.9) provides a definition of the local order parameter and how to calculate it numerically from the finite-sized microscopic dynamics. In the continuum limit, Equation (A.9) is equivalent

to

$$z(x,t) = \frac{1}{2\delta}\int_{x-\delta}^{x+\delta} e^{i\phi(x',t)}dx' \tag{A.10}$$

for $0 < \delta \ll 1$ [118, 69]. Thus, the local order parameter demonstrates a coarse-grained observable that is continuous both in x and t, and thus characterizes a local degree of coherence in a small neighborhood around $x \in \mathbb{D}$ [61, 60, 101]. Note that in general $\phi(x,t)$ is not continuous. For the NTS, we obtain $|z(x,t)| = 1$ for all $x \in \mathbb{D}$ and all t, confirming that the NTS is an everywhere coherent traveling wave solution as a TTS is.

We now investigate the microscopic dynamical properties of the NTS. In Fig. A.2 (a), the trajectory of an oscillator in the NTS (black line) is shown together with a snapshot of the amplitude profile (red curve) in the complex plane. The trajectories encircle the origin, but exhibit a backward motion in its phase when the amplitude goes through a pronounced deformation from a circular structure (cf. also Fig. A.1 (d)). The reversal of the direction of the phase change is due to the negative values the instantaneous phase velocity attains when the amplitude variable goes through the hump (Fig. A.2 (b)). In Fig. A.2 (b), the time evolution of the instantaneous frequency of each oscillator is depicted. They are equally shifted in the time interval of the period T where $\dot{\phi}_j(t) = \dot{\phi}_j(t-T)$ for $j = 1,...,N$. The time evolution of $\mathrm{Re}(W)$ of the oscillators is shown in Fig. A.2 (c). The real part of each individual Stuart-Landau oscillator displays an irregular oscillation (illustrated by the black highlighted curve) whereas the motion of the entire oscillators fills the figure with a periodically oscillating envelope. In Fig. A.2 (d), the motions of two representative oscillators (W_{10} and W_{90}) are depicted on the Poincaré section defined by $\phi_1(t) \equiv 0 \pmod{2\pi}$. The trajectory of the oscillator on the section forms closed curves, as expected for a quasi-periodic motion in phase space.

To study the macroscopic dynamical properties of the NTS, we obtain the modulus of the *global Kuramoto order parameter* defined as

$$\Gamma(t) := \frac{1}{L}\int_0^L e^{i\phi(x,t)}dx \tag{A.11}$$

which corresponds to

$$\Gamma(t) := \frac{1}{N}\sum_{j=1}^{N} e^{i\phi_j(t)} \tag{A.12}$$

in the finite-sized ensemble. In Fig. A.2 (e), the modulus of the global Kuramoto order parameter $|\Gamma|$ is shown as a periodic motion for small system size N. Also, we notice that the period and amplitude of it decrease as N increases. After all, $|\Gamma|$ eventually reaches a

constant value, and $\Gamma(t)$ rotates uniformly with Ω, i.e., $\Gamma(t) = |\Gamma| e^{i\Omega t}$. This reminds us of the order parameter behavior of the Poisson chimeras in two-population networks in Sec. 3. In Fig. A.2 (b), we find that the instantaneous phase velocities $\{\dot{\phi}_i(t)\}_{i=1}^N$ of all oscillators are periodic functions with the same period $T \approx 23$, and they have identical shapes yet equally shifted in the time interval of T. Hence, we can assume that $\dot{\phi}_i(t - \frac{j}{N}T) = \dot{\phi}_{i+j}(t)$ for an arbitrary $j \in \{1, ..., N\}$, which gives $\phi_i(t - \frac{T}{N}) = \phi_{i+1}(t) + \Theta_0$ for $i = 1, ..., N$ with a common constant shift $\Theta_0 \in \mathbb{R}$ and $\phi_1 \equiv \phi_{N+1}$. Substituting this into Eq. (A.11), we obtain

$$|\Gamma(t)| = \left| \frac{1}{N} \sum_{j=1}^{N} e^{i\phi_{j+1}(t)} \right| = \left| \frac{e^{-i\Theta_0}}{N} \sum_{j=1}^{N} e^{i\phi_j(t-\frac{T}{N})} \right| = |\Gamma(t - \frac{T}{N})| = |\Gamma(t - \tau)| \tag{A.13}$$

which eventually leads to $|\Gamma(t)| = |\Gamma(t - \tau)|$ for $\forall_t$ where $\tau = \frac{T}{N}$. The modulus of the global Kuramoto order parameter is $\frac{T}{N}$-periodic. This conjecture can be further verified by measuring the period of $|\Gamma|$ numerically from Eq. (A.11) and comparing it with $\tau = T/N$ where T is the period of each instantaneous phase velocity in Fig. A.2 (f). In fact, this reveals the difference between an NTS and a TTS in terms of the macroscopic dynamics. The global Kuramoto order parameter $|\Gamma(t)| = 0$ for all $N \in \mathbb{N}$ for a TTS.

A.1.2 Linear Stability of the Nontrivial Twisted States

In this section, we study the stability of the NTS both for a continuous system and a discrete ensemble. First, in the continuous system, the NTS is treated as a stationary solution for both the phase and amplitude profiles in a reference frame moving with the constant lateral speed c and uniformly rotating with Ω. Here, we assume that

$$W(x,t) = W_0(\xi) e^{i\Omega t} \tag{A.14}$$

where $\xi = x - ct$. Then the winding number of the NTS is obtained by

$$q = \frac{1}{2\pi} \sum_{j=1}^{N} (\Phi_{j+1} - \Phi_j) \tag{A.15}$$

where $\Phi_j = \arg W_0(\xi_j)$ at $\xi_j = \frac{(j-1)}{N-1} \in \mathbb{D}$ for $j = 1, ..., N$. The stationary profile of the NTS satisfies

$$-c\partial_\xi W_0(\xi) = (1 + i\Delta) W_0(\xi) - |W_0(\xi)|^2 W_0(\xi) + \varepsilon e^{-i\alpha((\mathcal{G}W_0)(\xi))} (\mathcal{G}W_0)(\xi) \tag{A.16}$$

where $\partial_\xi := \frac{d}{d\xi}$ and $\Delta = \omega - \Omega$ is a real unknown constant. Here, the integral convolution operator is written as

$$(\mathscr{G}W_0)(\xi) = H_0(\xi) = \int_0^L G(\xi - \xi')W_0(\xi')d\xi' \tag{A.17}$$

where $G(y)$ is defined in Eq. (A.4).

As we did in Sec. 2.3, the linear stability of the stationary solution can be investigated by linearizing the evolution equation around the stationary wave profile and then determining the eigenvalues of the Jacobian matrix evaluated at the stationary solution. To this end, we introduce a coordinate transformation

$$W_0(\xi) = X_0(\xi) + iY_0(\xi) \tag{A.18}$$

where $\mathrm{Re}W_0 = X_0$ and $\mathrm{Im}W_0 = Y_0$ are real-valued functions that are periodic in ξ: $X_0(\xi + L) = X_0(\xi)$ and $Y_0(\xi + L) = Y_0(\xi)$. Then, the stationary wave solution satisfies

$$-c\partial_\xi \begin{pmatrix} X_0 \\ Y_0 \end{pmatrix} = \left[\begin{pmatrix} 1 & -\Delta \\ \Delta & 1 \end{pmatrix} - (X_0^2 + Y_0^2)I_2 \right] \begin{pmatrix} X_0 \\ Y_0 \end{pmatrix} + \varepsilon \begin{pmatrix} \cos\alpha & \sin\alpha \\ -\sin\alpha & \cos\alpha \end{pmatrix} \begin{pmatrix} (\mathscr{G}X_0)(\xi) \\ (\mathscr{G}Y_0)(\xi) \end{pmatrix} \tag{A.19}$$

where $\alpha = \alpha_0 + \alpha_1 |H_0(\xi)|^2$ and $I_2 \in \mathbb{R}^{2\times 2}$ is the identity matrix. To obtain the linearized equation, we impose a small deviation onto $W_0(\xi)$: $v_1(\xi,t) = X(\xi,t) - X_0(\xi)$ and $v_2(\xi,t) = Y(\xi,t) - Y_0(\xi)$ with $|v_i| \ll 1$ for $i = 1,2$. By treating ξ here as a time-independent spatial variable, we obtain the linearized equation as

$$\frac{d\mathbf{V}}{dt} = \mathbf{L}\mathbf{V} \tag{A.20}$$

where $\mathbf{V} = (\mathbf{v_1}, \mathbf{v_2})^\top$ and $\mathbf{L} := \mathbf{M} + \mathbf{K}$ is a time-independent linear operator whose point and continuous spectra $\sigma(\mathbf{L}) = \sigma_{\mathrm{pt}}(\mathbf{L}) \cup \sigma_{\mathrm{cont}}(\mathbf{L})$ determine the linear stability of the profiles of the NTS. To numerically obtain the spectra, we uniformly discretize operators calculated at each $\xi = \xi_j$ for $j = 1, \ldots, M$ with $M \gg 1$ [63]. The multiplication operator then reads

$$(\mathbf{M}\mathbf{V})(\xi) = \mathbf{M}(\xi)\mathbf{V}(\xi) = \left[\begin{pmatrix} c\mathbf{D} + \mathbf{2Y_0^2} & -\Delta \\ \Delta & c\mathbf{D} + \mathbf{2X_0^2} \end{pmatrix} + \begin{pmatrix} \mathrm{Re}\,\eta(\xi) & \mathrm{Im}\,\eta(\xi) \\ \mathrm{Im}\,\eta(\xi) & \mathrm{Re}\,\eta(\xi) \end{pmatrix} \right] \mathbf{V}(\xi) \tag{A.21}$$

where $\eta(\xi) = 1 - 3(X_0^2 + Y_0^2) - i2X_0Y_0 \in \mathbb{C}^{M\times M}$ and $\mathbf{D} \in \mathbb{C}^{M\times M}$ is a differential operator[1]. From the numerical evaluation, we observe that the multiplication operator $\mathbf{M}$ only has a discretization of continuous spectrum branches $\sigma(\mathbf{M}) = \sigma_{\text{cont}}(\mathbf{M})$ [61]. On the other hand, the compact integral operator $\mathbf{K}$ is given by

$$(\mathbf{KV})(\xi) = \varepsilon\Big(\mathbf{A}(\xi) + \mathbf{2}\alpha_1\mathbf{B}(\xi)\Big)\begin{pmatrix}(\mathscr{G}v_1)(\xi)\\(\mathscr{G}v_2)(\xi)\end{pmatrix},$$

$$\mathbf{A}(\xi) = \begin{pmatrix}\cos\alpha & \sin\alpha\\ -\sin\alpha & \cos\alpha\end{pmatrix},\quad \alpha = \alpha_0 + \alpha_1|H_0(\xi)|^2,$$

$$\mathbf{B}(\xi) = \begin{pmatrix}-\sin\alpha & \cos\alpha\\ -\cos\alpha & -\sin\alpha\end{pmatrix}\begin{pmatrix}\mathrm{Re}^2H_0 & 0\\ 0 & \mathrm{Im}^2H_0\end{pmatrix} + \mathrm{Im}H_0\mathrm{Re}H_0\begin{pmatrix}\cos\alpha & -\sin\alpha\\ -\sin\alpha & -\cos\alpha\end{pmatrix},$$

$$(\mathscr{G}v_i)(\xi) = \int_0^L G(\xi-\xi')v_i(\xi')d\xi',\quad i = 1,2 \tag{A.22}$$

where $\mathrm{Re}^2H_0 = (\mathrm{Re}H_0)^2$ and $\mathrm{Im}^2H_0 = (\mathrm{Im}H_0)^2$ are also discretized with the same method [63].

In Fig. A.3 (a), the eigenvalues of the linear operator $\mathbf{L}$ are shown in the complex plane. Note that the eigenvalues with large imaginary parts outside of the continuous branches are spurious eigenvalues due to the numerical evaluation, especially in the discretization of the differential operator [212]. The two (discretized forms of) continuous branches correspond to phase and amplitude variables, respectively. These continuous branches obtained from the entire linear operator, i.e., $\sigma_{\text{cont}}(\mathbf{L})$ coincide with the eigenvalues of the multiplication operator, i.e., $\sigma(\mathbf{M})$. Thus, the continuous branches are invariant under the compact operator $\mathbf{K}$ [61, 60]. In Fig. A.3 (b), a magnification of (a) is shown for the eigenvalues with the small imaginary part. There are a few scattered eigenvalues (blue) in $\sigma(\mathbf{L})$. Since $\sigma_{\text{pt}}(\mathbf{L}) = \sigma(\mathbf{L}) \setminus \sigma(\mathbf{M}) = \sigma(\mathbf{L}) \setminus \sigma_{\text{cont}}(\mathbf{L})$, we can identify them as the point spectrum [61, 60]. The point spectrum has one zero eigenvalue arising from the translational invariance, not affecting the stability of the solution. All other eigenvalues have a negative real part, ensuring that the observed NTS is linearly stable. Note that an unstable TTS exists at the same parameter value where the stable NTS occurs. The linearized operator for the TTS has two complex conjugate eigenvalues with positive real parts. It is therefore an unstable solution (Fig. A.3 (c)).

[1] For the numerical calculation, we exploit the differential operator in Ref. [211].

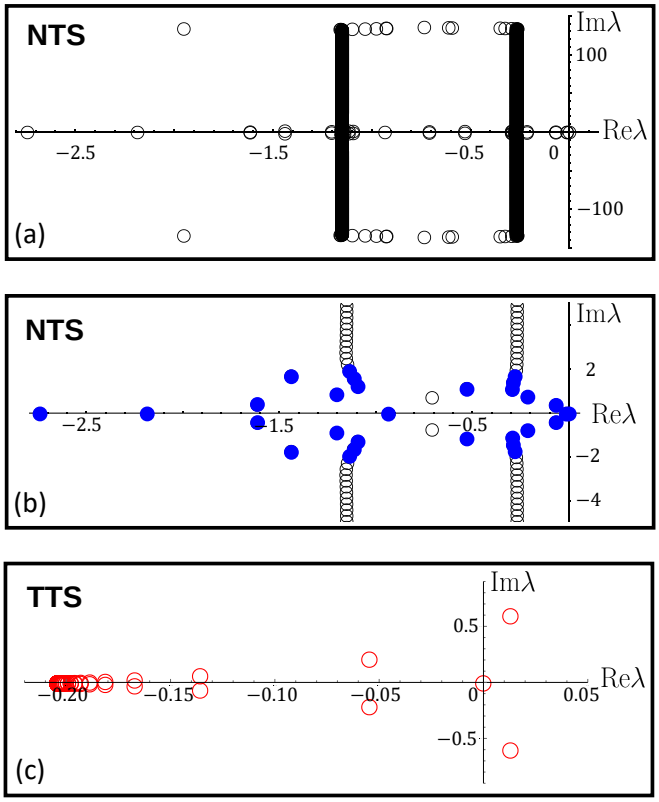

Fig. A.3 (a) Eigenvalues of the linearized system around the NTS solution in a reference frame moving with c and rotating with Ω. (b) Magnification of (a) to highlight the eigenvalues with small imaginary part. The blue filled dots indicate the eigenvalues which do not coincide with the eigenvalues of the multiplication operator, i.e. $\sigma(\mathbf{L}) \setminus \sigma(\mathbf{M})$, and the black dots display a discretization of the continuous spectrum. These eigenvalues are obtained from the discretization of the linear operator with $M = 2^{10}$. (c) Some eigenvalues of the unstable, coexisting TTS near the origin of the complex plane. The parameters are specified in Sec. A.1.1.

Next, we investigate the stability of the NTS in a finite-sized system. For a finite-sized ensemble, an NTS cannot be represented as a stationary solution in an appropriate reference frame. Hence, to study its spectral properties, we exploit the Lyapunov stability analysis in Sec. 2.6. Let us say an NTS is our time-evolving reference trajectory in the phase space. In Sec. 2.6, we studied that the tangent space dynamics is governed by the Jacobian matrix, which reads

$$(\mathbf{J})_{ij} = \left(\begin{array}{c|c} \frac{\partial \dot{\phi}_i}{\partial \phi_j} & \frac{\partial \dot{\phi}_i}{\partial r_j} \\ \hline \frac{\partial \dot{r}_i}{\partial \phi_j} & \frac{\partial \dot{r}_i}{\partial r_j} \end{array}\right) \in \mathbb{R}^{2N\times 2N}, \quad i,j = 1,...,N. \tag{A.23}$$

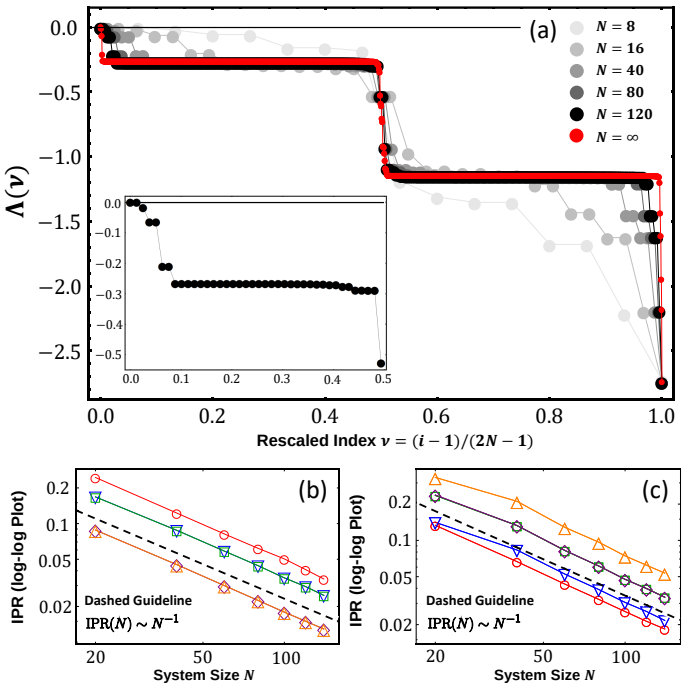

Fig. A.4 (a) Lyapunov exponents of the NTS as a function of the re-scaled index ν for various system sizes. The red dots reproduce the real parts of the eigenvalues obtained from the continuum limit analysis. The inset depicts the first half of the Lyapunov spectrum for $N = 40$. (b) and (c) The IPR as a function of system size N corresponding to the discrete Lyapunov exponents around $\nu = 0.0$ and $\nu = 1.0$, respectively.

Then, we can follow the instruction of Sec. 2.6: Defining the tangent linear propagator $\mathbf{M}(t,t_0) = \mathbf{O}(t)\mathbf{O}^{-1}(t_0)$ where $\mathbf{O}(t)$ is the fundamental matrix solution of $\dot{\mathbf{O}}(t) = \mathbf{J}(t)\mathbf{O}(t)$ with the identity matrix $\mathbf{O}(0) = I_{2N}$, we obtain the Lyapunov exponents Λ_i as an exponential growth rate

$$\Lambda_i = \lim_{t\to\infty} \frac{1}{t} \log \frac{||\mathbf{M}(t,t_0)\mathbf{u}(t_0)||}{||\mathbf{u}(t_0)||} \tag{A.24}$$

along the perturbation vector in the tangent space $\mathbf{T}_{\mathbf{x}^{\mathrm{NTS}}(t)}(\mathbb{R}^{2N})$ where $\mathbf{x}^{\mathrm{NTS}}(t)$ is a given NTS reference trajectory in phase space, and $\mathbf{u}(t_0)$ is an initial perturbation vector belonging to each Oseledets' splitting for $i = 1,\ldots,2N$.

In Fig. A.4 (a), Lyapunov spectra $\Lambda(\nu)$ are depicted for different system sizes N as a function of the re-scaled index $\nu = \frac{i-1}{2N-1}$ (black and gray tone) together with the real part of $\sigma(\mathbf{L})$ from the above analysis in the continuum limit (red points). Regardless of the system size, there are two zero Lyapunov exponents which arise from the two continuous symmetries: the time shift invariance due to the autonomous governing equations, and the phase shift invariance, $W \to We^{i\chi}$ for $\chi \in \mathbb{R}$ as discussed in Sec. 2.1. These two perturbations do not affect the stability of the NTS reference trajectory. Except for these two zero LEs, all other

Lyapunov exponents are negative. The negative Lyapunov exponents confirm that a local perturbation to the NTS trajectory exponentially decays to the trajectory and thus the NTS solution is stable. Furthermore, comparing the Lyapunov exponents with $\sigma(\mathbf{L})$, we classify the LEs into two groups: discrete Lyapunov exponents and continuous branches, respectively. In Fig. A.4 (a), some of the exponents approach continuous branches with nearly identical values as N increases, whereas others remain discrete outside of the continuous branches. This implies that for $N \to \infty$ the Lyapunov spectrum converges to the real part of $\sigma(\mathbf{L})$ in the continuum limit, which resembles the spectral properties of chimera states reported in Ref. [71].

One further remark on the Lyapunov analysis is concerned with the collective Lyapunov modes. The traveling wave solution in fact is dominated by some collective modes since all elements behave in the same way and the ensemble of them forms a propagating structure. To capture the collective modes of the wave, we also exploit the Lyapunov analysis. Using the CLVs, we can measure the time-averaged *inverse participation ratios* (IPRs) as a function of N, which are defined by [213]

$$\mathrm{IPR}^{(i)}(N) = \left\langle \exp\left(\frac{1}{q-1} \log \sum_{j=1}^{2N} \left| v_j^{(i)}(t) \right|^{2q} \right) \right\rangle_t \tag{A.25}$$

where $q = 2$ and $\mathrm{IPR}^{(i)} \in [(2N)^{-1}, 1]$ and $v_j^{(i)}$ is the j^{th} component of the CLV $\mathbf{v}^{(i)} \in \mathbf{T}_{\mathbf{x}^{\mathrm{NTS}}(t)}(\mathbb{R}^{2N})$ corresponding to a certain Lyapunov exponent $\Lambda_i(N)$ in Eq. (A.24) for $i = 1, \ldots, 2N$. The IPR gives a way to capture the so-called collective Lyapunov modes. A CLV is a collective Lyapunov mode if $\mathrm{IPR}^{(i)}(N) \sim \frac{1}{N}$ as $N \to \infty$, which means the CLV evenly spreads out through all the oscillators [213]. In contrast, when $\mathrm{IPR}^{(i)}(N) \sim$ const. as N increases, the vector is well localized.

In Fig. A.4 (b-c), the IPRs are depicted as a function of N for the first and the last few Lyapunov modes, i.e., the discrete LEs near $\nu \gtrsim 0.0$ and $\nu \lesssim 1.0$, respectively. We numerically find $\mathrm{IPR}(N) \sim \frac{1}{N}$ as N increases. Therefore, these modes are the collective Lyapunov modes. Also the discrete LEs around $\nu = \frac{i-1}{2N-1} \approx 0.5$ show the same scaling, so that they too are collective Lyapunov modes. All these numerical observations lead us to the conclusion that an NTS trajectory is indeed dominated by collective modes as anticipated for a traveling wave solution.

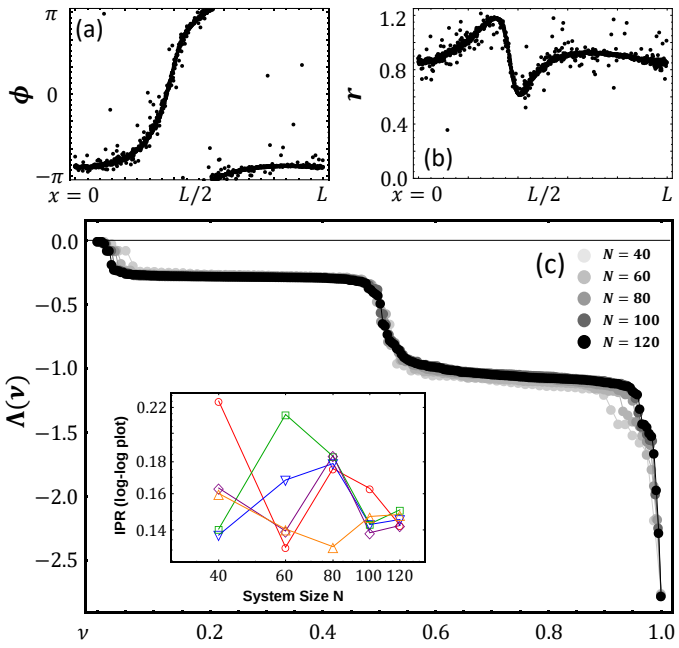

Fig. A.5 NTS in a system with heterogeneous natural frequencies ($\gamma = 0.002$). (a) Phase snapshot and (b) amplitude snapshot with $N = 1600$. (c) Lyapunov exponents for $N = 40, 60, 80, 100$, and 120. Inset: IPR as a function of the system size for the first five modes in $\nu \geq 0.5$.

A.2 Nonidentical Oscillators

Thus far, we have discussed the NTS in a system of identical Stuart-Landau oscillators on a ring. Would an NTS remain, if a heterogeneity is imposed on the natural frequencies of Stuart-Landau oscillators, which seems more realistic than identical oscillator systems? In this section, we demonstrate the robustness of the NTS against adding a small heterogeneity to the natural frequencies. To this end, we consider the Cauchy-Lorentz distribution

$$g(\omega) = \frac{\gamma}{\pi} \frac{1}{\omega^2 + \gamma^2} \tag{A.26}$$

that leads us to

$$\frac{j - \frac{1}{2}}{N} = \int_{-\infty}^{\tilde{\omega}_j} g(\omega) d\omega = \frac{1}{2} + \frac{1}{\pi} \tan^{-1}\left(\frac{\tilde{\omega}_j}{\gamma}\right) \tag{A.27}$$

for $j = 1, ..., N$ and for $\gamma = 0.002$ (a small heterogeneity). Note that since the system is not all-to-all coupled, we need to mix the natural frequencies obtained above to assign randomly distributed natural frequencies to the oscillators.

The system of nonlocally coupled Stuart-Landau oscillators with natural frequency heterogeneity also shows an NTS solution. In Fig. A.5 (a-b), snapshots of phase and amplitude profiles are depicted for the heterogeneous Stuart-Landau oscillators. They look similar to the NTS in Fig. A.1, and also the amplitude and phase variables travel along the ring while the phase variables are rotating, yet not with the same angular frequency. However, the NTS with heterogeneity is not a coherent wave solution, i.e., $|z(x,t)| \neq 1$ for all $x \in \mathbb{D}$ but rather it is a partially coherent wave solution ($0 < |z(x,t)| < 1$ for all $x \in \mathbb{D}$) that resembles a partially coherent twisted state reported in Refs. [204, 117, 118]. To investigate the spectral properties of the partially coherent NTS, we measure the Lyapunov exponents, which are shown in Fig. A.5 (c). In spite of the heterogeneity, the NTS remains a stable solution. All Lyapunov exponents are negative as in the identical system, except for the two zero exponents which also correspond to the two continuous symmetries. Hence, we can say that the NTS solution is robust to a small heterogeneity of the natural frequencies. Note that we cannot capture the collective modes of the partially coherent NTS by the Lyapunov analysis, i.e., the collective Lyapunov modes, as apparent from the inset in Fig. A.5 (c). The incoherent dynamics of the individual oscillators seems to overshadow the collective response of the oscillators.

A.3 Bifurcation Scenario

Trivial twisted states and nontrivial twisted state with winding number $q = 1$

In this section, we perform a bifurcation analysis of the TTS and the NTS, based on pseudo-arclength continuation with the Newton-Raphson method as in Refs. [214–216].

First, we discuss how the TTS solution behaves when the coupling strength ε varies. In Fig. A.6 (a), the bifurcation diagram of the stable (gray) and the unstable (black) TTS are depicted. The TTS is found to be unstable for small values of ε and becomes stabilized at a comparatively large value of ε via a subcritical Hopf bifurcation (HB), i.e., there is no stable periodic motion after the HB. Furthermore, the velocity c of the TTS depends linearly on ε since the homogeneous amplitudes $r_j = r_0 \approx 1$ for all j and the phase differences of adjacent oscillators are the same as $\Delta_{j,j+1} = \frac{2\pi}{N}$ (TTS). Then, the coupling term in Eq. (A.6) is identical for all oscillators (the same $r_j = r_0$ for all j) and scales linearly with ε. This predicts a linear increase of $|c|$ with ε. The branch of unstable TTS continues actually up to $\varepsilon = 0$ at which also $c = 0$.

Secondly, for the NTS, the corresponding bifurcation curve is depicted by the red (stable) and blue (unstable) lines in Fig. A.6 (a). For small values of ε, an unstable NTS exists. As ε increases further, it is stabilized in a Hopf bifurcation (A) where a pair of complex conjugate

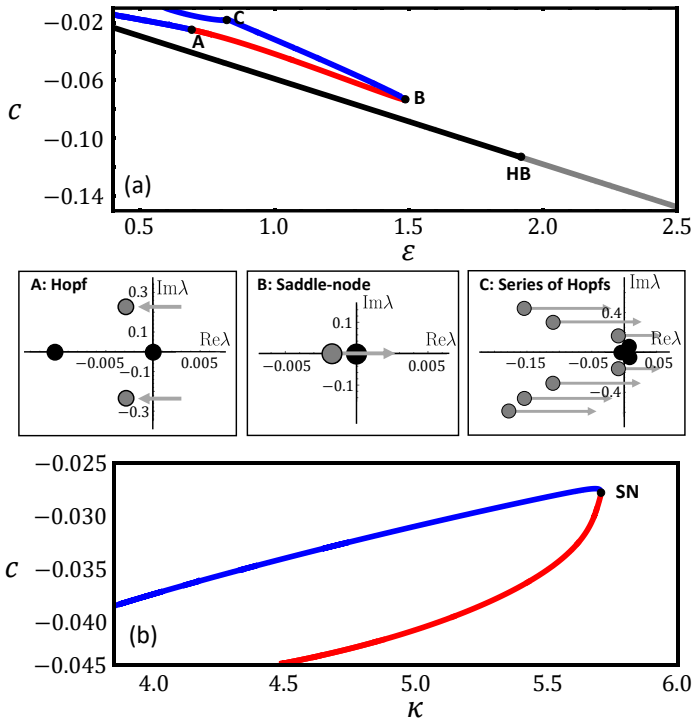

Fig. A.6 (a) Bifurcation diagrams of the TTS (black and gray lower lines; black: unstable states, gray: stable states) and NTS (blue and red upper lines; blue: unstable states, red; stable states) with ε the speed c characterizing the NTS solution. The panels in the middle row depict some of the eigenvalues of the linearized equation around the wave profiles in the complex plane close to points (A-C) in (a). (b) Bifurcation diagram of the NTS solution with κ as bifurcation parameter. The color code is as in (a). The remaining parameters are the same as in Fig. A.1.

eigenvalues crosses the imaginary axis in the complex plane (see the left panel in the middle row of Fig. A.6). Beyond the Hopf bifurcation (A), the stable NTS exists in a large range of the parameter ε. Along this stable curve, the difference between the maximum and minimum values of the amplitude hump increases with increasing ε. Note that apart from the NTS and the TTS, we find that the fully synchronized state is stable for $\varepsilon \gtrapprox 0.773$. Thus, the NTS coexists with the uniform oscillation in most of its existence range. Further increasing ε, the NTS solution is annihilated in a saddle-node bifurcation (SN) at point B (see the middle panel in the middle row), and the fully synchronized state is the only stable state until the TTS is stabilized in HB at somewhat larger values of ε. Along the unstable branch, the NTS is more and more destabilized in a series of Hopf bifurcations starting at C. At the same time, the amplitude profile becomes flatter and flatter approaching the uniform profile as c approaches zero.

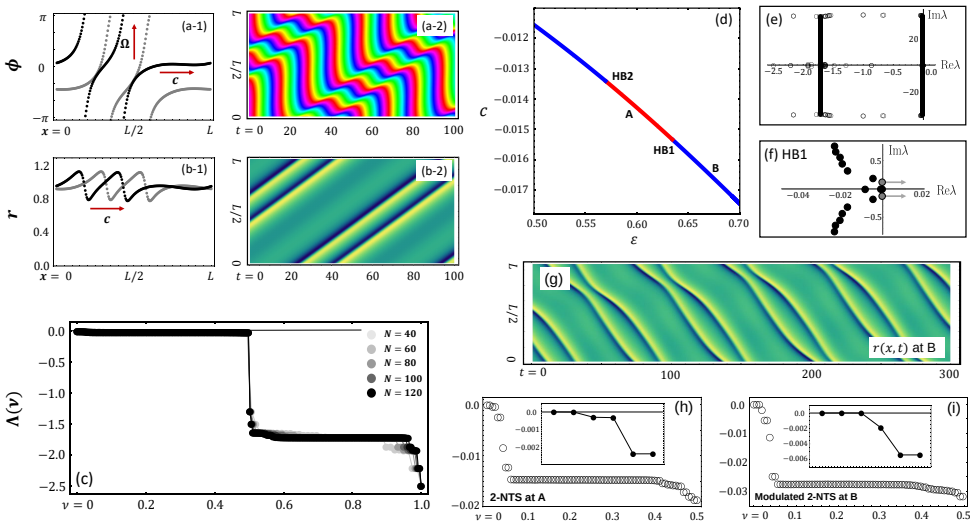

Fig. A.7 (a-b) Phase and amplitude dynamics of the NTS with $|q| = 2$ for $N = 200$, and $\varepsilon = 0.6$. The other parameters and the color code is the same as in Fig. A.1. (c) Lyapunov exponents of the 2-NTS for $N = 40, 60, 80, 100$ and 120. (d) Bifurcation diagrams of the 2-NTS with ε as bifurcation parameter and the propagation speed c characterizing the NTS with the same color scheme as in Fig. A.6. (e) Full eigenvalue spectrum in the complex pane of the Jacobian matrix evaluated at the stationary 2-NTS at A. (f) The eigenvalues near zero in the complex plane at the Hopf bifurcation (HB1). (g) Temporal evolution of the amplitude profile of the modulated 2-NTS at B after HB1; $\varepsilon = 0.67$. (h-i) The first half of the Lyapunov exponents of 2-NTS and modulated 2-NTS for $N = 80$, respectively. Insets show a magnification close to the origin and highlight the first six Lyapunov exponents.

Finally, a bifurcation diagram of the NTS with the parameter κ reveals that the solution is restricted to a certain interaction range, or a certain length of the system (Fig. A.6 (b)).

Nontrivial twisted states with winding number $q = 2$

So far, we have discussed an NTS with a winding number $|q| = 1$ only. However, just like a TTS, an NTS also shows a winding number $|q| = 2$, which is here called 2-NTS. In Fig. A.7 (a-b), snapshots and the time evolutions of the phase and the amplitude profiles are depicted for a stable 2-NTS solution. Here, the amplitude profile has two humps and the phase profile winds twice along the ring, gaining in total 4π along the full cycle of the ring. The 2-NTS solution is also a stable solution, numerically verified by the Lyapunov exponents in Fig. A.7 (c). However, it is less stable than the 1-NTS; the first half of the Lyapunov exponents are closer to zero than those of the 1-NTS (compare Fig. A.7 (c),(h) to Fig. A.4 (a)). This can be also verified by determining the eigenvalues of the linearized equation in the continuum limit analysis (Fig. A.7 (e)): One of the continuous branches of the 2-NTS is closer to the

imaginary axis than that of the 1-NTS. The stable 2-NTS can be obtained in some nonzero parameter range of ε in Fig. A.7 (d), which is, however, smaller than that of the 1-NTS.

In Fig. A.7 (d), we see that the 2-NTS is destabilized at both ends of the existence interval via Hopf bifurcations (HB1 and HB2). Moreover, we have conducted numerical simulations to confirm that one of the bifurcations (HB1) is indeed a supercritical Hopf bifurcation. Prior to HB1, the 2-NTS solution demonstrates a stationary amplitude profile in a moving reference frame (Fig. A.7 (b-2)). Beyond HB1, a 2-NTS state is still observed. However, now its amplitude profile oscillates periodically. For this case, the 2-NTS solution appears as a modulated traveling wave solution (Fig. A.7 (g)). The modulated NTS features three zero Lyapunov exponents, two of which arise from the continuous symmetries, the third originating from the modulation frequency (Fig. A.7 (i)).

A.4 Summary

In this Appendix, we presented a novel form of collective behavior within a circular arrangement of Stuart-Landau oscillators that are connected nonlocally. This distinctive phenomenon, labeled as a nontrivial twisted state, is distinguished by its uneven amplitude and phase gradient profiles, along with a designated winding number denoted as q. This winding number is indicative of the twisted state and signifies a coherent progressive wave structure. Taking a broader perspective, at a macroscopic level, the absolute value of the local order parameter within the nontrivial twisted state (referred to as NTS) remains consistently at 1 across all points x within the interval $[0, L]$, and at all times t. In contrast, the global order parameter, as defined by the global Kuramoto order parameter equation, maintains a value greater than 0 but less than 1 for all time instances. By way of comparison, the conventional trivial twisted state features a uniform amplitude profile and a constant phase gradient, resulting in a global order parameter of 0 ($|\Gamma(t)| = 0$), while still keeping the absolute value of the local order parameter at 1 ($|z(x,t)| = 1$) for all values of x and t. The investigation involving linear stability analysis, Lyapunov analysis, and bifurcation analysis collectively revealed that NTS solutions displaying a winding number of $|q| = 1$ or 2 emerge as attractor states. These states persist over extensive ranges of parameter configurations and various initial conditions.

Chapter 8

Publication List

From Jeonbuk National University in S. Korea

[1] **Twisted states in low-dimensional hypercubic lattices**

- **Seungjae Lee**, Young Sul Cho, and Hyunsuk Hong
- Phys. Rev. E **98**, 062221 (2018)
- `https://journals.aps.org/pre/abstract/10.1103/PhysRevE.98.062221`

[2] **Stable chimeras of non-locally coupled Kuramoto-Sakaguchi oscillators in a finite array**

- **Seungjae Lee** and Young Sul Cho
- Journal-Korean Physical Society, **78**, 476 (2021)
- `https://link.springer.com/article/10.1007/s40042-021-00068-4`

From Technische Universität München in Deutschland

[1] **Attracting Poisson chimeras in two-population networks**

- **Seungjae Lee** and Katharina Krischer
- Chaos **31**, 113101 (2021)
- `https://aip.scitation.org/doi/10.1063/5.0065710`

[2] **Nontrivial twisted states in nonlocally coupled Stuart-Landau oscillators**

- **Seungjae Lee** and Katharina Krischer
- Phys. Rev. E **106**, 044210 (2022)

- https://journals.aps.org/pre/abstract/10.1103/PhysRevE.106.044210

[3] **Chaotic chimera attractors in a triangular network of identical oscillators**

- **Seungjae Lee** and Katharina Krischer
- Phys. Rev. E **107**, 054205 (2023)
- https://journals.aps.org/pre/abstract/10.1103/PhysRevE.107.054205

[4] **Heteroclinic switching between chimeras in a ring of six oscillator populations**

- **Seungjae Lee** and Katharina Krischer
- Chaos **33**, 063120 (2023)
- https://doi.org/10.1063/5.0147228

[5] **Chimera dynamics of generalized Kuramoto-Sakaguchi oscillators in two-population networks**

- **Seungjae Lee** and Katharina Krischer
- J. Phys. A: Math. Theor. **56**, 405001 (2023)
- https://iopscience.iop.org/article/10.1088/1751-8121/acf4d6

[6] **Volcano Transition in a System of Generalized Kuramoto Oscillators with Random Frustrated Interactions**

- **Seungjae Lee**, Yeonsu Jeong, Seung-Woo Son and Katharina Krischer
- J. Phys. A: Math. Theor. **57**, 085702 (2024)
- https://iopscience.iop.org/article/10.1088/1751-8121/ad2226

References

[1] The American Heritage Dictionary of the English Language (https://www.ahdictionary.com/).

[2] S. Haro, *Emergence and Reduction in Physics*. 2017.

[3] J. Lennox, *God's Undertaker: Has Science Buried God?* Lion, 2009.

[4] R. Westfall, *The Life of Isaac Newton*. Canto Classics, Cambridge University Press, 2015.

[5] R. Westfall, *Never at Rest: A Biography of Isaac Newton*. Cambridge paperback library, Cambridge University Press, 1983.

[6] M. Kline, *Mathematics: The Loss of Certainty*. Galaxy book, Oxford University Press, 1982.

[7] L. Smolin, *Three Roads to Quantum Gravity*. SCIENCE MASTERS, Orion, 2014.

[8] "https://en.wikipedia.org/wiki/Spherical_cow,"

[9] S. Weinberg, *Dreams Of A Final Theory: The Search for The Fundamental Laws of Nature*. Random House, 2010.

[10] S. Rose, *Lifelines: Life Beyond the Gene*. Oxford University Press, 2003.

[11] R. Dawkins, *A Devil's Chaplain: Reflections on Hope, Lies, Science, and Love*. Houghton Mifflin Harcourt, 2004.

[12] "33 Best Sir Isaac Newton Quotes: https://graciousquotes.com/isaac-newton/ and Top 100 Isaac Newton Quotes https://quotefancy.com/isaac-newton-quotes,"

[13] F. Dyson, "The Scientist As Rebel," *The American Mathematical Monthly*, vol. 103, no. 9, pp. 800–805, 1996.

[14] S. H. Strogatz, "Love affairs and differential equations," *Mathematics Magazine*, vol. 61, no. 1, pp. 35–35, 1988.

[15] P. W. Anderson, "More is different: broken symmetry and the nature of the hierarchical structure of science.," *Science*, vol. 177, no. 4047, pp. 393–396, 1972.

[16] S. Strogatz, S. Walker, J. M. Yeomans, C. Tarnita, E. Arcaute, M. De Domenico, O. Artime, and K.-I. Goh, "Fifty years of 'More is different'," *Nature Reviews Physics*, vol. 4, pp. 508–510, Aug 2022.

[17] K. Christensen and N. Moloney, *Complexity and Criticality*. Advanced physics texts, Imperial College Press, 2005.

[18] M. Newman, *Networks: An Introduction*. OUP Oxford, 2010.

[19] A. BarabÃ¡si and M. PÃ3sfai, *Network Science*. Cambridge University Press, 2016.

[20] R. Baxter, *Exactly Solved Models in Statistical Mechanics*. Elsevier Science, 2016.

[21] "`https://besharamagazine.org/science-technology/dr-vasileios-basios-the-century-of-complexity/`,"

[22] C. Huygens, *Oeuvres Complètes de Christiaan Huygens*, vol. 8. M. Nijhoff, 1899.

[23] K. Czolczynski, P. Perlikowski, A. Stefanski, and T. Kapitaniak, "HUYGENS'ODD SYMPATHY EXPERIMENT REVISITED," *International Journal of Bifurcation and Chaos*, vol. 21, no. 07, pp. 2047–2056, 2011.

[24] A. R. Willms, P. M. Kitanov, and W. F. Langford, "Huygens' clocks revisited," *Royal Society open science*, vol. 4, no. 9, p. 170777, 2017.

[25] A. Pikovsky, M. Rosenblum, and J. Kurths, *Synchronization: A Universal Concept in Nonlinear Sciences*. Cambridge: Cambridge University Press, 2001.

[26] S. H. Strogatz, *Sync*. New York: Hyperion, 2003.

[27] L. Larger, B. Penkovsky, and Y. Maistrenko, "Laser chimeras as a paradigm for multistable patterns in complex systems," *Nature Communications*, vol. 6, p. 7752, Jul 2015.

[28] J. Shena, J. Hizanidis, P. Hövel, and G. P. Tsironis, "Multiclustered chimeras in large semiconductor laser arrays with nonlocal interactions," *Phys. Rev. E*, vol. 96, p. 032215, Sep 2017.

[29] K. Wiesenfeld and J. W. Swift, "Averaged equations for Josephson junction series arrays," *Phys. Rev. E*, vol. 51, pp. 1020–1025, Feb 1995.

[30] S. A. Marvel and S. H. Strogatz, "Invariant submanifold for series arrays of Josephson junctions," *Chaos*, vol. 19, no. 1, p. 013132, 2009.

[31] S. H. Strogatz and I. Stewart, "Coupled oscillators and biological synchronization," *Scientific american*, vol. 269, no. 6, pp. 102–109, 1993.

[32] A. Winfree, *The Geometry of Biological Time*. Interdisciplinary Applied Mathematics, Springer New York, 2013.

[33] R. E. Mirollo and S. H. Strogatz, "Synchronization of Pulse-Coupled Biological Oscillators," *SIAM Journal on Applied Mathematics*, vol. 50, no. 6, pp. 1645–1662, 1990.

[34] J. Fell and N. Axmacher, "The role of phase synchronization in memory processes," *Nature Reviews Neuroscience*, vol. 12, pp. 105–118, Feb 2011.

[35] M. Breakspear, "Dynamic models of large-scale brain activity," *Nature Neuroscience*, vol. 20, pp. 340–352, Mar 2017.

[36] P. Ashwin, S. Coombes, and R. Nicks, "Mathematical Frameworks for Oscillatory Network Dynamics in Neuroscience," *The Journal of Mathematical Neuroscience*, vol. 6, p. 2, Jan 2016.

[37] P. S. Skardal and A. Arenas, "Memory selection and information switching in oscillator networks with higher-order interactions," *Journal of Physics: Complexity*, vol. 2, no. 1, p. 015003, 2020.

[38] J. Pantaleone, "Stability of incoherence in an isotropic gas of oscillating neutrinos," *Phys. Rev. D*, vol. 58, p. 073002, Aug 1998.

[39] B. Zhu, J. Schachenmayer, M. Xu, F. Herrera, J. G. Restrepo, M. J. Holland, and A. M. Rey, "Synchronization of interacting quantum dipoles," *New Journal of Physics*, vol. 17, p. 083063, sep 2015.

[40] B. A. Carreras, V. E. Lynch, I. Dobson, and D. E. Newman, "Complex dynamics of blackouts in power transmission systems," *Chaos: An Interdisciplinary Journal of Nonlinear Science*, vol. 14, pp. 643–652, 09 2004.

[41] A. E. Motter, S. A. Myers, M. Anghel, and T. Nishikawa, "Spontaneous synchrony in power-grid networks," *Nature Physics*, vol. 9, pp. 191–197, Mar 2013.

[42] Y. Kuramoto, *Chemical Oscillations, Waves, and Turbulence*. Dover Publications, 2003.

[43] "From Kuramoto to Crawford: exploring the onset of synchronization in populations of coupled oscillators," *Physica D: Nonlinear Phenomena*, vol. 143, no. 1, pp. 1–20, 2000.

[44] S. H. Strogatz and R. E. Mirollo, "Stability of incoherence in a population of coupled oscillators," *Journal of Statistical Physics*, vol. 63, pp. 613–635, May 1991.

[45] K. Okuda, "Variety and generality of clustering in globally coupled oscillators," *Physica D: Nonlinear Phenomena*, vol. 63, no. 3, pp. 424–436, 1993.

[46] Y. S. Cho, T. Nishikawa, and A. E. Motter, "Stable chimeras and independently synchronizable clusters," *Phys. Rev. Lett.*, vol. 119, p. 084101, 2017.

[47] L. M. Pecora, F. Sorrentino, A. M. Hagerstrom, T. E. Murphy, and R. Roy, "Cluster synchronization and isolated desynchronization in complex networks with symmetries," *Nat. Commun.*, vol. 5, p. 4079, 2014.

[48] F. Sorrentino, L. Pecora, A. M. Hagerstrom, T. E. Murphy, and R. Roy, "Complete characterization of the stability of cluster synchronization in complex dynamical networks," *Sci. Adv.*, vol. 2, p. e1501737, 2016.

[49] N. Nakagawa and Y. Kuramoto, "From collective oscillations to collective chaos in a globally coupled oscillator system," *Physica D: Nonlinear Phenomena*, vol. 75, no. 1, pp. 74–80, 1994.

[50] N. Nakagawa and Y. Kuramoto, "Anomalous Lyapunov spectrum in globally coupled oscillators," *Physica D: Nonlinear Phenomena*, vol. 80, no. 3, pp. 307–316, 1995.

[51] D. Pazó, "Thermodynamic limit of the first-order phase transition in the Kuramoto model," *Phys. Rev. E*, vol. 72, p. 046211, Oct 2005.

[52] F. A. Rodrigues, T. K. D. Peron, P. Ji, and J. Kurths, "The Kuramoto model in complex networks," *Physics Reports*, vol. 610, pp. 1–98, 2016.

[53] Y. Kuramoto and D. Battogtokh, "Coexistence of coherence and incoherence in nonlocally coupled phase oscillators," *Nonlinear Phenom. Complex Syst.*, vol. 5, p. 380, 2002.

[54] D. M. Abrams and S. H. Strogatz, "Chimera States for Coupled Oscillators," *Phys. Rev. Lett.*, vol. 93, p. 174102, Oct 2004.

[55] S. Lee and K. Krischer, "Attracting Poisson chimeras in two-population networks," *Chaos*, vol. 31, no. 11, p. 113101, 2021.

[56] S. Lee and K. Krischer, "Chaotic chimera attractors in a triangular network of identical oscillators," *Phys. Rev. E*, vol. 107, p. 054205, May 2023.

[57] S. Lee and K. Krischer, "Heteroclinic switching between chimeras in a ring of six oscillator populations," *Chaos: An Interdisciplinary Journal of Nonlinear Science*, vol. 33, 06 2023. 063120.

[58] S. Lee and K. Krischer, "Chimera dynamics of generalized Kuramoto–Sakaguchi oscillators in two-population networks," *Journal of Physics A: Mathematical and Theoretical*, vol. 56, p. 405001, sep 2023.

[59] M. J. Panaggio and D. M. Abrams, "Chimera states: coexistence of coherence and incoherence in networks of coupled oscillators," *Nonlinearity*, vol. 28, pp. R67–R87, feb 2015.

[60] O. E. Omel'chenko, "The mathematics behind chimera states," *Nonlinearity*, vol. 31, pp. R121–R164, apr 2018.

[61] O. E. Omel'chenko, "Coherence-incoherence patterns in a ring of non-locally coupled phase oscillators," *Nonlinearity*, vol. 26, pp. 2469–2498, jul 2013.

[62] C. R. Laing, "The dynamics of chimera states in heterogeneous Kuramoto networks," *Physica D: Nonlinear Phenomena*, vol. 238, no. 16, pp. 1569–1588, 2009.

[63] L. Smirnov, G. Osipov, and A. Pikovsky, "Chimera patterns in the Kuramoto–Battogtokh model," *Journal of Physics A: Mathematical and Theoretical*, vol. 50, p. 08LT01, jan 2017.

[64] G. C. Sethia, A. Sen, and G. L. Johnston, "Amplitude-mediated chimera states," *Phys. Rev. E*, vol. 88, p. 042917, Oct 2013.

[65] G. Bordyugov, A. Pikovsky, and M. Rosenblum, "Self-emerging and turbulent chimeras in oscillator chains," *Phys. Rev. E*, vol. 82, p. 035205, Sep 2010.

[66] M. Wolfrum and O. E. Omel'chenko, "Chimera states are chaotic transients," *Phys. Rev. E*, vol. 84, p. 015201, Jul 2011.

[67] O. E. Omel'chenko, M. Wolfrum, and Y. L. Maistrenko, "Chimera states as chaotic spatiotemporal patterns," *Phys. Rev. E*, vol. 81, p. 065201, Jun 2010.

[68] M. I. Bolotov, L. A. Smirnov, G. V. Osipov, and A. S. Pikovsky, "Breathing chimera in a system of phase oscillators," *JETP Letters*, vol. 106, pp. 393–399, Sep 2017.

[69] M. Bolotov, L. Smirnov, G. Osipov, and A. Pikovsky, "Simple and complex chimera states in a nonlinearly coupled oscillatory medium," *Chaos*, vol. 28, no. 4, p. 045101, 2018.

[70] M. I. Bolotov, L. A. Smirnov, E. S. Bubnova, G. V. Osipov, and A. S. Pikovsky, "Spatiotemporal Regimes in the Kuramoto–Battogtokh System of Nonidentical Oscillators," *Journal of Experimental and Theoretical Physics*, vol. 132, pp. 127–147, Jan 2021.

[71] M. Wolfrum, O. E. Omel'chenko, S. Yanchuk, and Y. L. Maistrenko, "Spectral properties of chimera states," *Chaos*, vol. 21, no. 1, p. 013112, 2011.

[72] D. M. Abrams, R. Mirollo, S. H. Strogatz, and D. A. Wiley, "Solvable Model for Chimera States of Coupled Oscillators," *Phys. Rev. Lett.*, vol. 101, p. 084103, Aug 2008.

[73] E. Montbrió, J. Kurths, and B. Blasius, "Synchronization of two interacting populations of oscillators," *Phys. Rev. E*, vol. 70, p. 056125, Nov 2004.

[74] M. J. Panaggio, D. M. Abrams, P. Ashwin, and C. R. Laing, "Chimera states in networks of phase oscillators: The case of two small populations," *Phys. Rev. E*, vol. 93, p. 012218, Jan 2016.

[75] E. A. Martens, C. Bick, and M. J. Panaggio, "Chimera states in two populations with heterogeneous phase-lag," *Chaos*, vol. 26, no. 9, p. 094819, 2016.

[76] S. Guo, M. Yang, W. Han, and J. Yang, "Dynamics in two interacting subpopulations of nonidentical phase oscillators," *Phys. Rev. E*, vol. 103, p. 052208, May 2021.

[77] C. R. Laing, "Disorder-induced dynamics in a pair of coupled heterogeneous phase oscillator networks," *Chaos: An Interdisciplinary Journal of Nonlinear Science*, vol. 22, no. 4, p. 043104, 2012.

[78] C. R. Laing, "Chimeras in networks of planar oscillators," *Phys. Rev. E*, vol. 81, p. 066221, Jun 2010.

[79] C. R. Laing, "Dynamics and stability of chimera states in two coupled populations of oscillators," *Phys. Rev. E*, vol. 100, p. 042211, Oct 2019.

[80] D. Pazó and E. Montbrió, "Low-Dimensional Dynamics of Populations of Pulse-Coupled Oscillators," *Phys. Rev. X*, vol. 4, p. 011009, Jan 2014.

[81] O. Burylko, E. A. Martens, and C. Bick, "Symmetry breaking yields chimeras in two small populations of Kuramoto-type oscillators," *Chaos*, vol. 32, no. 9, p. 093109, 2022.

[82] S. Olmi, "Chimera states in coupled Kuramoto oscillators with inertia," *Chaos*, vol. 25, no. 12, p. 123125, 2015.

[83] S. Olmi, E. A. Martens, S. Thutupalli, and A. Torcini, "Intermittent chaotic chimeras for coupled rotators," *Phys. Rev. E*, vol. 92, p. 030901, Sep 2015.

[84] C. Bick and P. Ashwin, "Chaotic weak chimeras and their persistence in coupled populations of phase oscillators," *Nonlinearity*, vol. 29, p. 1468, mar 2016.

[85] S. Guo, M. Yang, W. Han, and J. Yang, "Dynamics in two interacting subpopulations of nonidentical phase oscillators," *Phys. Rev. E*, vol. 103, p. 052208, May 2021.

[86] A. Buscarino, M. Frasca, L. V. Gambuzza, and P. Hövel, "Chimera states in time-varying complex networks," *Phys. Rev. E*, vol. 91, p. 022817, Feb 2015.

[87] C. R. Laing, K. Rajendran, and I. G. Kevrekidis, "Chimeras in random non-complete networks of phase oscillators," *Chaos*, vol. 22, p. 013132, 2012.

[88] E. A. Martens, "Bistable chimera attractors on a triangular network of oscillator populations," *Phys. Rev. E*, vol. 82, p. 016216, Jul 2010.

[89] E. A. Martens, "Chimeras in a network of three oscillator populations with varying network topology," *Chaos*, vol. 20, no. 4, p. 043122, 2010.

[90] C. R. Laing, "Chimeras on a ring of oscillator populations," *Chaos: An Interdisciplinary Journal of Nonlinear Science*, vol. 33, no. 1, p. 013121, 2023.

[91] C. Bick, "Heteroclinic switching between chimeras," *Phys. Rev. E*, vol. 97, p. 050201, May 2018.

[92] C. Bick, "Heteroclinic Dynamics of Localized Frequency Synchrony: Heteroclinic Cycles for Small Populations," *Journal of Nonlinear Science*, vol. 29, pp. 2547–2570, Dec 2019.

[93] C. Bick, T. Böhle, and C. Kuehn, "Multi-population phase oscillator networks with higher-order interactions," *Nonlinear Differential Equations and Applications NoDEA*, vol. 29, no. 6, p. 64, 2022.

[94] C. Bick and A. Lohse, "Heteroclinic Dynamics of Localized Frequency Synchrony: Stability of Heteroclinic Cycles and Networks," *Journal of Nonlinear Science*, vol. 29, pp. 2571–2600, Dec 2019.

[95] S. A. Marvel, R. E. Mirollo, and S. H. Strogatz, "Identical phase oscillators with global sinusoidal coupling evolve by Möbius group action," *Chaos*, vol. 19, no. 4, p. 043104, 2009.

[96] E. Ott and T. M. Antonsen, "Low dimensional behavior of large systems of globally coupled oscillators," *Chaos*, vol. 18, no. 3, p. 037113, 2008.

[97] E. Ott and T. M. Antonsen, "Long time evolution of phase oscillator systems," *Chaos*, vol. 19, no. 2, p. 023117, 2009.

[98] S. Watanabe and S. H. Strogatz, "Integrability of a globally coupled oscillator array," *Phys. Rev. Lett.*, vol. 70, pp. 2391–2394, Apr 1993.

[99] S. Watanabe and S. H. Strogatz, "Constants of motion for superconducting Josephson arrays," *Physica D: Nonlinear Phenomena*, vol. 74, no. 3, pp. 197–253, 1994.

[100] E. Stein and R. Shakarchi, *Complex Analysis*. Princeton lectures in analysis, Princeton University Press, 2010.

[101] A. Pikovsky and M. Rosenblum, "Partially Integrable Dynamics of Hierarchical Populations of Coupled Oscillators," *Phys. Rev. Lett.*, vol. 101, p. 264103, Dec 2008.

[102] A. Pikovsky and M. Rosenblum, "Dynamics of heterogeneous oscillator ensembles in terms of collective variables," *Physica D: Nonlinear Phenomena*, vol. 240, no. 9, pp. 872–881, 2011.

[103] C. Bick, M. Goodfellow, C. R. Laing, and E. A. Martens, "Understanding the dynamics of biological and neural oscillator networks through exact mean-field reductions: a review," *The Journal of Mathematical Neuroscience*, vol. 10, p. 9, May 2020.

[104] T. Tanaka, "Solvable model of the collective motion of heterogeneous particles interacting on a sphere," *New Journal of Physics*, vol. 16, p. 023016, feb 2014.

[105] A. Winfree, *Timing of Biological Clocks*. Henry Holt and Company, 1986.

[106] S. Thornton and J. Marion, *Classical Dynamics of Particles and Systems*. Brooks/Cole, 2004.

[107] H. Goldstein, C. Poole, and J. Safko, *Classical Mechanics*. Pearson Education, 2014.

[108] G. Fowles and G. Cassiday, *Analytical Mechanics*. International student edition, Thomson Brooks/Cole, 2005.

[109] J. Walker, D. Halliday, R. Resnick, and a. O. M. C. Safari, *Fundamentals of Physics*. John Wiley & Sons Australia, Limited, 2004.

[110] V. García-Morales and K. Krischer, "The complex Ginzburg–Landau equation: an introduction," *Contemporary Physics*, vol. 53, no. 2, pp. 79–95, 2012.

[111] S. H. Strogatz, *Nonlinear Dynamics and Chaos: With Applications to Physics, Biology, Chemistry, and Engineering (2nd ed.)*. Boca Raton: CRC Press, 2015.

[112] L. Perko, *Differential Equations and Dynamical Systems*. New York, NY: Springer, 2001.

[113] S. Wiggins, P. Holmes, F. John, W. Jager, J. Marsden, L. Sirovich, and M. Golubitsky, *Introduction to Applied Nonlinear Dynamical Systems and Chaos*. Texts in Applied Mathematics, Springer New York, 1990.

[114] Y. A. Kuznetsov, "Andronov-Hopf bifurcation," *Scholarpedia*, vol. 1, no. 10, p. 1858, 2006. revision #90964.

[115] *Dynamical Systems II: A Concise Graduate Course, author=Christian Kuehn*. AMS Open Math Notes, 2018.

[116] I. S. Aranson and L. Kramer, "The world of the complex Ginzburg-Landau equation," *Rev. Mod. Phys.*, vol. 74, pp. 99–143, Feb 2002.

[117] M. I. Bolotov, L. A. Smirnov, E. S. Bubnova, G. V. Osipov, and A. S. Pikovsky, "Spatiotemporal Regimes in the Kuramoto–Battogtokh System of Nonidentical Oscillators," *Journal of Experimental and Theoretical Physics*, vol. 132, pp. 127–147, Jan 2021.

[118] D. Bolotov, M. I. Bolotov, L. A. Smirnov, G. V. Osipov, and A. S. Pikovsky, "Twisted States in a System of Nonlinearly Coupled Phase Oscillators," *Regular and Chaotic dynamics*, vol. 24, no. 6, pp. 717 – 724, 2019.

[119] K. Höhlein, F. P. Kemeth, and K. Krischer, "Lyapunov spectra and collective modes of chimera states in globally coupled Stuart-Landau oscillators," *Phys. Rev. E*, vol. 100, p. 022217, Aug 2019.

[120] J. Gómez-Gardeñes, Y. Moreno, and A. Arenas, "Paths to Synchronization on Complex Networks," *Phys. Rev. Lett.*, vol. 98, p. 034101, Jan 2007.

[121] S. Lee and K. Krischer, "Nontrivial twisted states in nonlocally coupled Stuart-Landau oscillators," *Phys. Rev. E*, vol. 106, p. 044210, Oct 2022.

[122] A. Pikovsky and A. Politi, *Lyapunov Exponents: A Tool to Explore Complex Dynamics*. Cambridge: Cambridge University Press, 2016.

[123] F. Ginelli, H. Chaté, R. Livi, and A. Politi, "Covariant Lyapunov vectors," *Journal of Physics A: Mathematical and Theoretical*, vol. 46, p. 254005, jun 2013.

[124] P. V. Kuptsov and U. Parlitz, "Theory and Computation of Covariant Lyapunov Vectors," *Journal of Nonlinear Science*, vol. 22, pp. 727–762, Oct 2012.

[125] Y. Kuramoto and H. Nakao, "On the concept of dynamical reduction: the case of coupled oscillators," *Philosophical Transactions of the Royal Society A*, vol. 377, no. 2160, p. 20190041, 2019.

[126] J. A. Acebrón, L. L. Bonilla, C. J. Pérez Vicente, F. Ritort, and R. Spigler, "The Kuramoto model: A simple paradigm for synchronization phenomena," *Rev. Mod. Phys.*, vol. 77, pp. 137–185, Apr 2005.

[127] E. M. Izhikevich and B. Ermentrout, "Phase model," *Scholarpedia*, vol. 3, no. 10, p. 1487, 2008. revision #129938.

[128] H. Nakao, "Phase reduction approach to synchronisation of nonlinear oscillators," *Contemporary Physics*, vol. 57, no. 2, pp. 188–214, 2016.

[129] Y. Kuramoto, "Self-entrainment of a population of coupled non-linear oscillators," in *International Symposium on Mathematical Problems in Theoretical Physics* (H. Araki, ed.), (Berlin, Heidelberg), pp. 420–422, Springer Berlin Heidelberg, 1975.

[130] D. Efimov, P. Sacré, and R. Sepulchre, "Controlling the phase of an oscillator: A phase response curve approach," pp. 7692–7697, 2009.

[131] C. C. Canavier, "Phase response curve," *Scholarpedia*, vol. 1, no. 12, p. 1332, 2006. revision #91651.

[132] K. Josic, E. T. Shea-Brown, and J. Moehlis, "Isochron," *Scholarpedia*, vol. 1, no. 8, p. 1361, 2006. revision #182469.

[133] J. T. Ariaratnam and S. H. Strogatz, "Phase Diagram for the Winfree Model of Coupled Nonlinear Oscillators," *Phys. Rev. Lett.*, vol. 86, pp. 4278–4281, May 2001.

[134] R. Gallego, E. Montbrió, and D. Pazó, "Synchronization scenarios in the Winfree model of coupled oscillators," *Phys. Rev. E*, vol. 96, p. 042208, Oct 2017.

[135] M. Bennett and K. Wiesenfeld, "Averaged equations for distributed Josephson junction arrays," *Physica D: Nonlinear Phenomena*, vol. 192, no. 3, pp. 196–214, 2004.

[136] J. W. Swift, S. H. Strogatz, and K. Wiesenfeld, "Averaging of globally coupled oscillators," *Physica D: Nonlinear Phenomena*, vol. 55, no. 3, pp. 239–250, 1992.

[137] S. Nichols and K. Wiesenfeld, "Ubiquitous neutral stability of splay-phase states," *Phys. Rev. A*, vol. 45, p. 12, 1992.

[138] D. G. Aronson, M. Golubitsky, and J. Mallet-Paret, "Ponies on a merry-go-round in large arrays of Josephon junctions," *Nonlinearity*, vol. 4, p. 903, 1991.

[139] I. Kra and S. R. Simanca, "On circulant matrices," *Notices of the AMS*, vol. 59, no. 3, pp. 368–377, 2012.

[140] H. Karner, J. Schneid, and C. W. Ueberhuber, "Spectral decomposition of real circulant matrices," *Linear Algebra and Its Applications*, vol. 367, pp. 301–311, 2003.

[141] C. J. Goebel, "Comment on "Constants of motion for superconductor arrays"," *Physica D: Nonlinear Phenomena*, vol. 80, no. 1, pp. 18–20, 1995.

[142] E. Ott, B. R. Hunt, and T. M. Antonsen, "Comment on "Long time evolution of phase oscillator systems" [Chaos 19, 023117 (2009)]," *Chaos: An Interdisciplinary Journal of Nonlinear Science*, vol. 21, no. 2, p. 025112, 2011.

[143] H. Daido, "Onset of cooperative entrainment in limit-cycle oscillators with uniform all-to-all interactions: bifurcation of the order function," *Physica D: Nonlinear Phenomena*, vol. 91, no. 1, pp. 24–66, 1996.

[144] A. Pikovsky and M. Rosenblum, "Partially integrable dynamics of ensembles of nonidentical oscillators," 2010.

[145] V. Jaćimović and A. Crnkić, "Low-dimensional dynamics in non-Abelian Kuramoto model on the 3-sphere," *Chaos: An Interdisciplinary Journal of Nonlinear Science*, vol. 28, 08 2018. 083105.

[146] H. K. Lee, H. Hong, and J. Yeo, "Improved numerical scheme for the generalized Kuramoto model," *Journal of Statistical Mechanics: Theory and Experiment*, vol. 2023, no. 4, p. 043403, 2023.

[147] W. Zou, S. He, D. V. Senthilkumar, and J. Kurths, "Solvable Dynamics of Coupled High-Dimensional Generalized Limit-Cycle Oscillators," *Phys. Rev. Lett.*, vol. 130, p. 107202, Mar 2023.

[148] S. Chandra, M. Girvan, and E. Ott, "Continuous versus Discontinuous Transitions in the *D*-Dimensional Generalized Kuramoto Model: Odd *D* is Different," *Phys. Rev. X*, vol. 9, p. 011002, Jan 2019.

[149] A. Crnkić, V. Jaćimović, and M. Marković, "On synchronization in Kuramoto models on spheres," *Analysis and Mathematical Physics*, vol. 11, no. 3, p. 129, 2021.

[150] M. A. M. de Aguiar, "Generalized frustration in the multidimensional Kuramoto model," *Phys. Rev. E*, vol. 107, p. 044205, Apr 2023.

[151] M. A. Lohe, "Systems of matrix Riccati equations, linear fractional transformations, partial integrability and synchronization," *Journal of Mathematical Physics*, vol. 60, 07 2019. 072701.

[152] A. E. D. Barioni and M. A. de Aguiar, "Complexity reduction in the 3D Kuramoto model," *Chaos, Solitons & Fractals*, vol. 149, p. 111090, 2021.

[153] A. E. D. Barioni and M. A. de Aguiar, "Ott-Antonsen ansatz for the D-dimensional Kuramoto model: A constructive approach," *Chaos: An Interdisciplinary Journal of Nonlinear Science*, vol. 31, no. 11, p. 113141, 2021.

[154] M. Lipton, R. Mirollo, and S. H. Strogatz, "The Kuramoto model on a sphere: Explaining its low-dimensional dynamics with group theory and hyperbolic geometry," *Chaos: An Interdisciplinary Journal of Nonlinear Science*, vol. 31, 09 2021. 093113.

[155] M. Lohe, "Higher-dimensional generalizations of the Watanabe-Strogatz transform for vector models of synchronization," *Journal of Physics A: Mathematical and Theoretical*, vol. 51, no. 22, p. 225101, 2018.

[156] S. Chandra, M. Girvan, and E. Ott, "Complexity reduction ansatz for systems of interacting orientable agents: Beyond the Kuramoto model," *Chaos: An Interdisciplinary Journal of Nonlinear Science*, vol. 29, 05 2019. 053107.

[157] G. L. Buzanello, A. E. D. Barioni, and M. A. M. de Aguiar, "Matrix coupling and generalized frustration in Kuramoto oscillators," *Chaos: An Interdisciplinary Journal of Nonlinear Science*, vol. 32, 09 2022. 093130.

[158] J. Sakurai, *Advanced Quantum Mechanics*. A-W series in advanced physics, Addison-Wesley Publishing Company, 1967.

[159] M. A. Lohe, "Higher-dimensional generalizations of the Watanabe–Strogatz transform for vector models of synchronization," *Journal of Physics A: Mathematical and Theoretical*, vol. 51, p. 225101, may 2018.

[160] K. S. Miller, "On the Inverse of the Sum of Matrices," *Mathematics Magazine*, vol. 54, no. 2, pp. 67–72, 1981.

[161] S. Hassani, *Mathematical Physics: A Modern Introduction to Its Foundations*. Springer International Publishing, 2013.

[162] G. Arfken, *Mathematical Methods for Physicists*. Elsevier Science, 2013.

[163] V. Oseledets, "A multiplicative ergodic theorem. Characteristic Liapunov, exponents of dynamical systems," *Trans. Mosc. Math. Soc.*, vol. 19, p. 197, 1968.

[164] J. P. Eckmann, "Ergodic theory of chaos and strange attractors," *Rev. Mod. Phys.*, vol. 57, p. 3, 1985.

[165] T. Bountis, V. G. Kanas, J. Hizanidis, and A. Bezerianos, "Chimera states in a two-population network of coupled pendulum-like elements," *Eur. Phys. J. Special Topics*, vol. 223, p. 721, 2014.

[166] E. A. Martens, A. F. S. Thutupalli, and O. Hallatschek, "Chimera states in mechanical oscillator networks," *Proceedings of the National Academy of Sciences*, vol. 110, p. 10563, 2013.

[167] E. A. Martens, M. J. Panaggio, and D. M. Abrams, "Basin of attraction for chimera states," *New. J. Phys.*, vol. 18, p. 022002, 2016.

[168] I. V. Tyulkina, D. S. Goldobin, L. S. Klimenko, and A. Pikovsky, "Dynamics of Noisy Oscillator Populations beyond the Ott-Antonsen Ansatz," *Phys. Rev. Lett.*, vol. 120, p. 264101, 2018.

[169] B. Pietras and A. Daffertshofer, "Ott-Antonsen attractiveness for parameter-dependent oscillatory systems," *Chaos*, vol. 26, p. 103101, 2016.

[170] D. M. Abrams and S. H. Strogatz, "CHIMERA STATES IN A RING OF NON-LOCALLY COUPLED OSCILLATORS," *International Journal of Bifurcation and Chaos*, vol. 16, no. 01, pp. 21–37, 2006.

[171] S. Lee, Y. S. Cho, and H. Hong, "Twisted states in low-dimensional hypercubic lattices," *Phys. Rev. E*, vol. 98, p. 062221, Dec 2018.

[172] Y. S. Cho, "Concurrent formation of nearly synchronous clusters in each intertwined cluster set with parameter mismatches," *Phys. Rev. E*, vol. 99, p. 052215, 2019.

[173] V. Nicosia, M. Valencia, M. Chavez, and A. Díaz-Guilera, "Remote synchronization reveals network symmetries and functional modules," *Phys. Rev. Lett.*, vol. 110, p. 174102, 2013.

[174] M. T. Schaub, N. O'Clery, Y. N. Billeh, J. Delvenne, R. Lambiotte, and M. Barahona, "Graph partitions and cluster synchronization in networks of oscillators," *Chaos*, vol. 26, p. 094821, 2016.

[175] F. P. Kemeth, S. W. Haugland, and K. Krischer, "Symmetries of chimera states," *Phys. Rev. Lett.*, vol. 120, p. 214101, 2018.

[176] B. D. MacArthur, R. J. Sánchez-García, and J. W. Anderson, "Symmetry in complex networks," *Discrete Applied Mathematics*, vol. 156, p. 3525, 2008.

[177] S. Kudose, "EQUITABLE PARTITIONS AND ORBIT PARTITIONS," 2009.

[178] `https://github.com/tnishi0/grouping-clusters/`.

[179] A. Pikovsky and M. Rosenblum, "Self-organized partially synchronous dynamics in populations of nonlinearly coupled oscillators," *Physica D*, vol. 238, p. 27, 2009.

[180] V. Vlasov, M. Rosenblum, and A. Pikovsky, "Dynamics of weakly inhomogenous oscillator populations: perturbation theory on top of Watanabe-Strogatz integrability," *J. Phys. A: Math. Theor.*, vol. 49, p. 31LT02, 2016.

[181] C. R. Laing, "Chimera states in heterogeneous networks," *Chaos*, vol. 19, p. 013113, 2009.

[182] P. Clusella and A. Politi, "Between phase and amplitude oscillators," *Phys. Rev. E*, vol. 99, p. 062201, Jun 2019.

[183] C. Bick, M. J. Panaggio, and E. A. Martens, "Chaos in Kuramoto oscillator networks," *Chaos*, vol. 28, no. 7, p. 071102, 2018.

[184] Y. Maistrenko, S. Brezetsky, P. Jaros, R. Levchenko, and T. Kapitaniak, "Smallest chimera states," *Phys. Rev. E*, vol. 95, p. 010203, Jan 2017.

[185] N. Semenova, A. Zakharova, V. Anishchenko, and E. Schöll, "Coherence-Resonance Chimeras in a Network of Excitable Elements," *Phys. Rev. Lett.*, vol. 117, p. 014102, Jul 2016.

[186] R. Ma, J. Wang, and Z. Liu, "Robust features of chimera states and the implementation of alternating chimera states," *Europhysics Letters*, vol. 91, no. 4, p. 40006, 2010.

[187] Y. Zhang, Z. G. Nicolaou, J. D. Hart, R. Roy, and A. E. Motter, "Critical Switching in Globally Attractive Chimeras," *Phys. Rev. X*, vol. 10, p. 011044, Feb 2020.

[188] S. W. Haugland, L. Schmidt, and K. Krischer, "Self-organized alternating chimera states in oscillatory media," *Scientific Reports*, vol. 5, p. 9883, Apr 2015.

[189] R. J. Goldschmidt, A. Pikovsky, and A. Politi, "Blinking chimeras in globally coupled rotators," *Chaos: An Interdisciplinary Journal of Nonlinear Science*, vol. 29, no. 7, p. 071101, 2019.

[190] P. Ebrahimzadeh, M. Schiek, P. Jaros, T. Kapitaniak, S. van Waasen, and Y. Maistrenko, "Minimal chimera states in phase-lag coupled mechanical oscillators," *The European Physical Journal Special Topics*, vol. 229, pp. 2205–2214, Sep 2020.

[191] S. Brezetsky, P. Jaros, R. Levchenko, T. Kapitaniak, and Y. Maistrenko, "Chimera complexity," *Phys. Rev. E*, vol. 103, p. L050204, May 2021.

[192] M. Komarov and A. Pikovsky, "Effects of nonresonant interaction in ensembles of phase oscillators," *Phys. Rev. E*, vol. 84, p. 016210, Jul 2011.

[193] W. R. Inc., "Mathematica, Version 12.0." Champaign, IL, 2022: Numerical integration was performed in *NDSolve* with *IDA*.

[194] F. Ginelli, H. Chaté, R. Livi, and A. Politi, "Covariant Lyapunov vectors," *J. Phys. A: Math. Theor.*, vol. 46, p. 254005, 2013.

[195] P. V. Kuptsov and U. Parlitz, "Theory and computation of covariant Lyapunov vectors," *J. Nonlinear Sci.*, vol. 22, p. 727, 2012.

[196] L. Schmidt, K. Schönleber, and K. Krischer, "Coexistence of synchrony and incoherence in oscillatory media under nonlinear global coupling," *Chaos*, vol. 24, p. 013102, 2014.

[197] J. D. Hart, K. Bansal, T. E. Murphy, and R. Roy, "Experimental observation of chimera and cluster states in a minimal globally coupled network," *Chaos*, vol. 26, p. 094801, 2016.

[198] M. Wickramasinghe and I. Z. Kiss, "Spatially Organized Dynamical States in Chemical Oscillator Networks: Synchronization, Dynamical Differentiation, and Chimera Patterns," *PLoS One*, vol. 8, p. e80586, 2013.

[199] J. F. Totz, J. Rode, M. R. Tinsley, K. Showalter, and H. Engel, "Spiral wave chimera states in large populations of coupled chemical oscillators," *Nature Physics*, vol. 14, p. 282, 2018.

[200] A. M. Hagerstrom, T. E. Murphy, R. Roy, P. Hövel, I. Omelchenko, and E. Schöll, "Experimental observation of chimeras in coupled-map lattices," *Nature Physics*, vol. 8, p. 658, 2012.

[201] M. R. Tinsley, S. Nkomo, and K. Showalter, "Chimera and phase-cluster states in populations of coupled chemical oscillators," *Nature Physics*, vol. 8, p. 662, 2012.

[202] N. Rattenborg, C. Amlaner, and S. Lima, "Behavioral, neurophysiological and evolutionary perspectives on unihemispheric sleep," *Neurosci. Biobehav. Rev.*, vol. 24, p. 87, 2000.

[203] "Chimera states: From theory and experiments to technology and living systems," MPIPKS, Dresden, Germany, May 2022. `https://www.pks.mpg.de/de/chimer22`.

[204] O. E. Omel'chenko, M. Wolfrum, and C. R. Laing, "Partially coherent twisted states in arrays of coupled phase oscillators," *Chaos: An Interdisciplinary Journal of Nonlinear Science*, vol. 24, no. 2, p. 023102, 2014.

[205] D. A. Wiley, S. H. Strogatz, and M. Girvan, "The size of the sync basin," *Chaos: An Interdisciplinary Journal of Nonlinear Science*, vol. 16, no. 1, p. 015103, 2006.

[206] T. Girnyk, M. Hasler, and Y. Maistrenko, "Multistability of twisted states in non-locally coupled Kuramoto-type models," *Chaos: An Interdisciplinary Journal of Nonlinear Science*, vol. 22, no. 1, p. 013114, 2012.

[207] L. Smirnov and A. Pikovsky, "Travelling chimeras in oscillator lattices with advective–diffusive coupling," *Philosophical Transactions of the Royal Society A*, vol. 381, no. 2245, p. 20220076, 2023.

[208] S.-i. Shima and Y. Kuramoto, "Rotating spiral waves with phase-randomized core in nonlocally coupled oscillators," *Phys. Rev. E*, vol. 69, p. 036213, Mar 2004.

[209] C. R. Laing, "Chimeras in networks with purely local coupling," *Phys. Rev. E*, vol. 92, p. 050904, Nov 2015.

[210] O. E. Omel'chenko, "Mathematical Framework for Breathing Chimera States," *Journal of Nonlinear Science*, vol. 32, p. 22, Jan 2022.

[211] L. Trefethen, *Spectral Methods in MATLAB*. Philadelphia: SIAM, 2000.

[212] O. E. Omel'chenko, "Travelling chimera states in systems of phase oscillators with asymmetric nonlocal coupling," *Nonlinearity*, vol. 33, p. 611, dec 2019.

[213] K. A. Takeuchi and H. Chaté, "Collective lyapunov modes," *Journal of Physics A: Mathematical and Theoretical*, vol. 46, p. 254007, jun 2013.

[214] C. R. Laing, "Numerical Bifurcation Theory for High-Dimensional Neural Models," *The Journal of Mathematical Neuroscience*, vol. 4, p. 13, Jul 2014.

[215] C. R. Laing, "Interpolating between bumps and chimeras," *Chaos: An Interdisciplinary Journal of Nonlinear Science*, vol. 31, no. 11, p. 113116, 2021.

[216] C. R. Laing and O. Omel'chenko, "Moving bumps in theta neuron networks," *Chaos: An Interdisciplinary Journal of Nonlinear Science*, vol. 30, no. 4, p. 043117, 2020.